

# **Improving the sustainability of organic and perovskite photovoltaic cells**



**Chankyu Kwak**

The department of Chemical and Biological Engineering  
University of Sheffield

Thesis submitted for the degree of Doctor of Philosophy

August 2016



## **Acknowledgements**

I first would like to thank my supervisor Dr. Alan Dunbar for giving me the chance to study this research. I am lucky to have such a great supervisor, who also serves as a wonderful mentor. While I have studied for my degree with your tutelage, I improved my logical and critical thinking, and have come one step closer to becoming a knowledgeable researcher. I learned invaluable information from you, and with your guidance. Also, thanks to Darren Watters for assistance with teaching me how to make devices and useful talks about experiments. Particular thanks to Hunan Yi for help and advice for synthesis with discussion about data.

Thanks also to our group PhD students: Hatice Burak, Gabriel Perez, Edwin Pineda, Konstantinos Tsevas, and Noura Alhazmi.

I also have to thank my friends here and away. To list a few: Jay Park, Beomseok Lee, Eurin Park, Dongkyu Kim, Woong Jeon, Daigeun Kim, and Taehyeok Lee in Sheffield. Tae Hyeon Kim, ONOM, Ja Young Cheon, and all friends in Korea. Jay and Beomseok are the best flat mates and good advisors. Additionally, I really appreciate all friends for always encouraging me to overcome the difficulties of living abroad and spending time discussing my work. You are all wonderful friends and great people. Thanks all again.

Lastly, and most significantly, I would like to thank my parents, older sister, brother in law and cousin Yoojin. My parents, especially my mother has sacrificed so much for me and I could have many wonderful opportunities in life. My father is special mentor for me. He always assists me to get over a difficulty. My sister and brother in law, they still may not "get" me or my work, but will always be there for me. YJ have helped me from when I came to England. Thanks for putting up with my irrational fits and for loving me unconditionally. It was with your support that I have made it through this process.

## Abstract

Many researchers have studied conjugated polymer-based photovoltaic cells and perovskite-based photovoltaic cells. They have shown lower efficiencies than inorganic photovoltaic cells so far. However, they are attractive because of their potential low cost and easy process. In order to fabricate organic photovoltaic cells, organic solvents are typically used, which results in significant waste solvent being produced. These are moderately expensive and many are toxic. Perovskite photovoltaics commonly incorporate lead, which is toxic and may hinder their adoption. This thesis aims reduce the need for organic solvents during organic photovoltaic cell manufacture by employing water-soluble conjugated polymers as an alternative. It also seeks to improve the efficiency of the devices such the less solvents are required per Watt produced. Reducing the usage of organic solvents would reduce fabrication and solvent treatment costs. Bismuth perovskites are also studied for use in perovskite photovoltaic cells to replace the toxic lead with a less toxic material.

The poly(3,4-ethylenedioxythiophene):poly(styrenesulfonate) (PEDOT:PSS) hole transporting layer used in both types of solar cells has been characterised in order to understand the influence of moisture and oxygen in air on the layer. Eight different thermally annealed PEDOT:PSS films were fabricated namely: as cast, 50, 75, 100, 125, 150, 175, and 200 °C. UV-vis absorption and conductivity were measured. Absorption intensity increased very slightly as thickness increased.

In order to develop fabrication skills and understand the principles of these devices, P3HT bulk-heterojunction photovoltaic cells were prepared. The devices were fabricated with different blend ratios both in air and in an oxygen free glovebox. P3HT:PCBM blend ratios of 1:0.6 and 1:0.8 showed the best efficiencies.

In this thesis, the synthesis of a new low band gap polyelectrolyte based on fluorene and dithiano-benzothiadiazole is described. Poly[(9,9-bis(4-sulfonatobutyl sodium) fluorene-alt-phenylene)-ran-(4,7-di-2-thienyl-2,1,3-benzothiadiazole-alt-phenylene)] is an anionic charged conjugated polyelectrolyte and was synthesised via Suzuki-cross coupling. Sulfonate groups were introduced to help the low band gap polyelectrolyte to dissolve in water. The aim was a new bulk-heterojunction

material to be applied in organic photovoltaic cells. It has a strong absorption peak at 372 nm, a weaker one at 530 nm and a photoluminescence emission peak at 647 nm. Although the conjugated polyelectrolyte did not show any photovoltaic effects as an active layer, it resulted in an improvement of efficiency when used as an additive in the PEDOT:PSS hole transporting layer in the devices. There is an efficiency gain as a result of improved carrier generation and charge transport across the interface into the hole transporting layer which is optimised at a CPE concentration close to 5 mg/ml. Improving the efficiency will improve the sustainability of the devices by reducing the materials required and waste produced per Watt of power produced.

Although lead-based perovskites have shown high performance in photovoltaic cells, they have led to concerns regarding their toxicity. Hybrid perovskites with reduced lead content are currently being investigated as a strategy to overcome this issue and to this end we evaluate the use of bismuth as a possible candidate for lead substitution. A series of hybrid perovskite films with the general composition  $\text{MA}(\text{Pb}_y\text{Bi}_{1-y})\text{I}_{3-x}\text{Cl}_x$  were characterised by their basic optical and structural properties using UV-vis spectroscopy, scanning electron microscopy and grazing incidence wide angle X-ray scattering. The bismuth perovskite precursors form a perovskite crystal structure upon annealing, with a corresponding optical bandgap, for  $\text{MABiI}_3$ , of around 2 eV. Whilst the structural and optical characterisation is promising, preliminary photovoltaic cell tests show power conversion efficiencies below 0.01% with a maximum  $V_{\text{OC}}$  of 0.78 V. It was suggested that such low overall efficiencies reflect a competition between precursor conversion and material de-wetting from the substrate that occurs during perovskite formation, the overall outcome of which is severely limited photocurrent. In the context of current processing methods, these factors may limit the general applicability of hybrid bismuth perovskites in photovoltaic applications. A blend ratio of 3:1  $\text{MAI}:\text{BiCl}_3$  used to make a perovskite based photovoltaic cell and annealed at 90 °C showed the best results in this research but it was very low efficiency.

## **Publication**

A. T. Barrows, A. J. Pearson, C. K. Kwak, A. D. F. Dunbar, A. R. Buckley and D. G. Lidzey, “Efficient planar heterojunction mixed-halide perovskite solar cells deposited via spray-deposition”, *Energy & Environmental Science*, 7, 2944-2950 (2014)

C. K. Kwak, A. T. Barrows, A. J. Pearson, D. G. Lidzey, and A. D. F. Dunbar, “An Xray Scattering and Electron Microscopy Study of Bismuth Perovskites for Solar Cell Applications”, submitted 2016

C. K. Kwak, G. E. Perez, B. G. Freestone, S. A. Al-Isaee, A. Iraqi, D. G. Lidzey, and A. D. F. Dunbar, “Improved efficiency in organic solar cells via conjugated polyelectrolyte additive in the hole transporting layer”, *Journal of Materials Chemistry C*, 4, 10722-10730 (2016)

## **Conference**

Materials Research Society spring meeting & exhibits, San Francisco, April 2015 (poster)

## **Award**

2016 Foxwell Memorial Prize

## Abbreviation

AFM	atomic force microscopy
AM 1.5	air mass 1.5
a-Si	amorphous silicon
BHJ	bulk heterojunction
CB	chlorobenzene
CNT	carbon nanotube
CPE	conjugated polyelectrolytes
CV	cyclic voltammetry
DI	de-ionised
DNA	deoxyribonucleic acid
EA	elemental analysis
EDG	electron donating group
$E_g$	band gap
EWG	electron withdrawing group
EQE	external quantum efficiency
FF	fill factor
FRET	fluorescence resonance energy transfer
GIWAXS	grazing-incidence wide-angle x-ray scattering
GPC	gel permeation chromatography
HOMO	high occupied molecular orbital
ICBA	indene-C60 Bisadduct
IR	infra-red
$I_{sc}$	short circuit current
ITO	indium tin oxide
$J_{sc}$	short circuit current density
MA	methylamine
MAI	methylammonium iodide
$\mu$ CP	micro-contact printing
$\mu$ c-Si	microcrystalline silicon
NMR	nuclear magnetic resonance
OLED	organic light emitting diode
OPVC	organic photovoltaic cell
OTFT	organic thin film transistor
P3HT	poly(3-hexylthiophene)
PCBM	[6,6]-phenyl-C61 butyric acid methyl ester
PC <sub>71</sub> BM	[6,6]-phenyl-C71-butylric acid methyl ester

PCDTBT	poly[N-9''-hepta-decanyl-2,7-carbazole-alt-5,5-(4',7'-di-2-thienyl-2',1',3'-benzothiadiazole)]
PCE	power conversion efficiency
PEDOT	poly(3,4-ethylenedioxythiophene)
PFN	Poly [(9,9-bis(3'-(N,N-dimethylamino)propyl)-2,7-fluorene)-alt-2,7-(9,9-dioctylfluorene)]
PL	photoluminescence
Poly-Si	polycrystalline silicon
PPVC	perovskite photovoltaic cell
PSS	poly(styrenesulfonate)
PT	polythiophene
PTB7	Poly[[4,8-bis[(2-ethylhexyl)oxy]benzo[1,2-b:4,5-b']dithiophene-2,6-diyl][3-fluoro-2-[(2-ethylhexyl)carbonyl]thieno[3,4-b]thiophenediyl]]
Spiro-OMeTAD	2,2',7,7'-tetrakis-(N,N-di-p-methoxyphenylamine)9,9'-spirobifluorene
UPS	ultraviolet photoelectron spectroscopy
UV	ultra violet
V <sub>oc</sub>	open circuit voltage

LIST OF CONTENTS	Page
Acknowledgements -----	I
Abstract -----	II
Publications, conference, and award -----	IV
Abbreviation -----	V
List of contents -----	VII
<b>1. Introduction</b> -----	<b>1</b>
1.1. Objectives and aims -----	1
1.2. Origin of photovoltaic cells -----	2
1.2.1. Photovoltaic cells based on inorganic materials -----	3
1.2.2. Photovoltaic cells based on organic materials -----	5
1.3. Conjugated polymers -----	6
1.3.1. Conjugated polyelectrolytes -----	7
1.3.2. Conjugated polyelectrolytes use in water for photovoltaic cells -----	8
1.4. Perovskite photovoltaic cells -----	8
1.4.1. Origin of perovskite -----	8
1.4.2. Organic-metal halide perovskite photovoltaic cells -----	9
1.5. References -----	11
<b>2. Theory</b> -----	<b>17</b>
2.1. Synthesis -----	17
2.1.1. Electrophilic aromatic substitution -----	17
2.1.2. Nucleophilic substitution -----	20
2.1.3. Suzuki-Miyaura cross coupling -----	24
2.2. Photovoltaic cell -----	26
2.2.1. Solar radiation -----	26
2.3. Theory of I-V characterisation in photovoltaic cells -----	28
2.3.1. The effect of light -----	28
2.3.2. Short circuit current and open circuit voltage -----	30
2.3.3. Maximum power ( $P_{mp}$ ), maximum current ( $I_{mp}$ ), and maximum voltage ( $V_{mp}$ ) -----	31
2.3.4. Fill factor -----	31
2.3.5. The effects of parasitic (series and shunt) resistances -----	32
2.3.6. Power conversion efficiency of photovoltaic cells -----	33
2.4. Organic bulk-heterojunction (BHJ) photovoltaic cells -----	34
2.4.1. The operation of organic BHJ photovoltaic cells -----	34
2.4.2. How BHJ photovoltaic cells work -----	35
2.5. Low band gap polymers -----	36

2.6. Perovskite photovoltaic cells -----	39
2.6.1. Formation of perovskite -----	39
2.6.2. How perovskite photovoltaic cells work -----	40
2.7. References -----	41
<b>3. Literature review -----</b>	<b>45</b>
3.1. Introduction -----	45
3.2. Photovoltaic cells via bulk-heterojunction -----	45
3.2.1. PEDOT:PSS for HTL in OPVCs -----	46
3.3. Use of conjugated polymers for BHJ photovoltaic cells -----	47
3.3.1. Poly(3-hexylthiophene) based photovoltaic cells -----	48
3.3.2. Low band gap polymer based photovoltaic cells -----	49
3.4. Use of conjugated polyelectrolytes for photovoltaic cells -----	54
3.4.1. Synthesis of conjugated polyelectrolytes -----	55
3.4.2. Conjugated polyelectrolyte photovoltaic cells -----	56
3.4.3. Use of conjugated polyelectrolyte as interfacial layer in photovoltaic cells -----	57
3.5. Perovskite photovoltaic cells -----	59
3.5.1. Methylammonium lead trihalide based perovskite -----	59
3.5.2. Formamidinium lead trihalide perovskite -----	60
3.6. References -----	60
<b>4. Fabrication and characterisation of P3HT photovoltaic cells -----</b>	<b>67</b>
4.1. Introduction -----	67
4.2. Experimental -----	67
4.2.1. Materials -----	67
4.2.2. Fabrication of thin films for characterisation of PEDOT:PSS -----	68
4.2.3. Fabrication of photovoltaic cells -----	68
4.2.4. Instruments for characterisation of thin films and devices -----	69
4.3. Study of PEDOT:PSS -----	69
4.3.1. Conductivity of PEDOT:PSS films under various annealing temperature -----	70
4.3.2. Absorption of PEDOT:PSS thin film under different thickness -----	73
4.4. Study on BHJ OPVCs using P3HT:PCBM -----	74
4.4.1. Different blend ratio of P3HT:PCBM based OPVCs -----	74
4.4.2. Comparing fabrication of OPVCs in the glovebox and atmosphere -	79
4.4.3. Fabrication of OPVCs with only Al cathode layer -----	81
4.5. Conclusions -----	83
4.6. References -----	85
<b>5. Synthesis of conjugated polyelectrolyte -----</b>	<b>87</b>
5.1. Introduction -----	87
5.1.1. Synthesis of conjugated polyelectrolyte -----	87
5.2. Experimental -----	88
5.2.1. Materials -----	88
5.2.2. Instruments for characterisation of monomers and a polymer -----	89

5.2.3. Synthesis of monomers and conjugated polyelectrolyte -----	89
5.3. Results and discussion -----	94
5.3.1. NMR analysis of monomers and PSFP-DTBTP -----	94
5.3.2. FT-IR spectrum of PSFP-DTBTP -----	99
5.3.3. Optical properties of PSFP-DTBTP -----	101
5.3.4. Cyclic voltammetry measurement of PSFP-DTBTP -----	103
5.4. Conclusions -----	105
5.5. References -----	105
<b>6. Polymer photovoltaic cells with conjugated polyelectrolyte -----</b>	<b>109</b>
6.1. Introduction -----	109
6.2. Experimental -----	110
6.2.1. Materials -----	110
6.2.2. Organic photovoltaic cells fabrication (PSFP-DTBTP used as active layer) -----	110
6.2.3. Organic photovoltaic cells fabrication (PSFP-DTBTP used as HTL or additive in HTL) -----	111
6.2.4. Preparation of films for characterisation -----	112
6.2.5. Instruments -----	112
6.3. Use PSFP-DTBTP in active layer -----	113
6.3.1. Thickness change of PEDOT:PSS HTL caused by spin casting subsequent water soluble layers -----	113
6.3.2. Fabrication of water based photovoltaic cells -----	114
6.4. Use PSFP-DTBTP in HTL -----	115
6.4.1. Optical characterisation of conjugated polyelectrolyte with PEDOT:PSS and PCDTBT:PC <sub>71</sub> BM -----	116
6.4.2. FT-IR spectra of CPE and HTL layers -----	118
6.4.3. The characterisation of band gaps of each layer -----	119
6.4.4. Work function of HTLs -----	120
6.4.5. Photovoltaic properties of devices with CPE additive in HTL -----	120
6.4.6. Conductivity of HTLs -----	124
6.4.7. Photoluminescence characterisation of HTL and active layer -----	125
6.4.8. AFM characterisation of HTLs -----	127
6.4.9. Photovoltaic properties of device with CPE HTL -----	128
6.5. Conclusions -----	130
6.6. References -----	131
<b>7. Perovskite photovoltaic cells -----</b>	<b>135</b>
7.1. Introduction -----	135
7.2. Experimental -----	137
7.2.1. Materials -----	137
7.2.2. Synthesis of methylamine iodide (MAI) -----	137
7.2.3. Mixed perovskite precursor by various blend ratio -----	137
7.2.4. Thin films fabrication for SEM, EDS, and GIWAXS -----	138
7.2.5. Thin films fabrication for UV-vis absorption spectroscopy -----	139
7.2.6. Device fabrication and characterisation -----	139

7.2.7. Instruments -----	140
7.3. Results and discussion -----	140
7.3.1. UV-vis absorption of perovskites -----	141
7.3.2. SEM and EDS characterisation of perovskite thin films -----	142
7.3.3. GIWAXS characterisation of perovskite thin films -----	149
7.3.4. Photovoltaic properties of perovskite PVCs -----	153
7.4. Conclusions -----	156
7.5. References -----	157
<b>8. Conclusions and further work -----</b>	<b>161</b>
8.1. Conclusions -----	161
8.2. Further work -----	163

# 1. Introduction

## 1.1. Objectives and aims

Solar energy is a very attractive energy source because it is a stable source of renewable energy and a sustainable fossil fuel alternative, and as such it is studied widely (Thompson and Frechet, 2008a). The advantages of organic polymer-based photovoltaic cells (OPVCs) and perovskite photovoltaic cells (PPVCs) are that they offer a low cost, simple to process, light weight, mechanically flexible route to solar cell manufacture. Furthermore, PPVCs have attracted much interest due to their outstanding efficiency (Snaith, 2013, Sondergaard et al., 2012, Espinosa et al., 2012, Azzopardi et al., 2011, Dennler et al., 2009, Gunes et al., 2007, Yu et al., 1995, Facchetti, 2011, Shaheen et al., 2005, Brabec, 2004). Although, OPVCs have the many advantages mentioned above, they still need to improve to compare with inorganic solar cells. The power conversion efficiency (PCE) of OPVC is about 8% for bulk heterojunction (BHJ) solar cells based on a blend of conjugated polymer and fullerene derivative [6,6]-phenyl-C61 butyric acid methyl ester (PCBM) (He et al., 2011) as the active layer. In order to approach over 10% efficiency, it is necessary to understand the fundamental active layer morphology and electronic interaction between donor and acceptor (Scharber et al., 2006).

Reduction of organic solvent use and harmful materials in OPVCs and PPVCs are necessary to help the environment (Capello et al., 2007, Ohlson and Hogstedt, 1981). In particular, although PPVCs showed good performance, toxicity of lead is an issue that still needs to be addressed in PPVCs (Flora et al., 2012, Landrigan, 1989). In order to reduce the effects of these harmful materials, less harmful alternatives can be used instead and/or the performance of the devices improved such that less smaller areas of photovoltaic need to be manufactured.

The aim of this PhD research is the development of more sustainable PVCs through using less harmful materials in and during the fabrication of the active layer and/or interfacial layers in PVCs and also by increasing their efficiency. In order to improve their sustainability the research has investigated less toxic materials for both OPVC and PPVC.

In OPVCs, to reduce the use of organic solvent and harmful materials, water-soluble conjugated polymers (known as conjugated polyelectrolytes) were synthesised and then utilised in OPVCs. The efficiency of the OPVCs produced were determined. Fluorene, thiophene, and benzothiadiazole groups were introduced in the synthesis steps for the polyelectrolyte because these polymers absorb light from 300 to 600 nm in wavelength. This project focussed on the synthesis of suitable polymers and their subsequent characterization through various methods (e.g. conductivity, absorption, and morphology). The main difference between conventional conjugated polymers in OPVC and conjugated polyelectrolytes is that it is possible to dissolve the polyelectrolytes in water. Therefore, removing the need to produce the environmental pollutants that results from using organic solvents. The fabrication process was optimised using conjugated polyelectrolytes both as an active layer and as an interfacial layer. When using it as an interfacial layer organic solvents are still needed to make the active layer but by achieving a higher overall efficiency than previously report the overall environmental impact of OPVCs can be reduced by increasing their efficiency.

In PPVCs, to reduce the use of toxic materials such as lead and caesium in perovskite, bismuth was introduced as the metal cation. Bismuth is less toxic than lead, therefore it will reduce the use of harmful lead in perovskite. Bismuth perovskite was applied as an active layer and its structure and morphology was studied. Various molar ratios of bismuth perovskite precursor were applied to find optimised molar ratio.

## **1.2. Origin of photovoltaic cells**

Increasing energy demands and concern about climate change in the world have focussed study on renewable, clean and abundant energy sources, of which solar cells are a good example. The energy demands in the world are about  $\sim 1.3 \times 10^{13}$  W, while the Earth receives  $\sim 1.2 \times 10^{17}$  W of solar energy per year (Energy, 2005, Tao, 2008). This is 10,000 times larger than the amount of energy that people use. In particular, the Sun provides more energy to our planet in one hour,  $4.3 \times 10^{20}$  J, than the current worldwide annual energy consumption  $4.1 \times 10^{20}$  J (Energy, 2005).

The photovoltaic effect was defined by A. E. Becquerel, a French physicist, in 1839 (Becquerel, 1839). He observed the generation of current upon illuminating platinum electrodes covered with silver chloride in an acidic solution. The first solid state photovoltaic cell was developed by C. Fritts, an American inventor, in 1883 (Fritts, 1883). This photovoltaic cell was made by selenium wafer with a thin layer of gold. R. Ohl patented the modern junction semiconductor photovoltaic cell in 1946 (Ohl, 1946) and the first silicon photovoltaic cell was realised by D. Chapin, C. S. Fuller and G. Pearson in 1954 (Chapin et al., 1954). They worked on silicon p–n junction photocells that reached 6% efficiency and showed significant improvement compared to the selenium cells that measured 0.5% efficiency. The efficiency of PVCs has improved since 1954 and it is now over 40% (NREL, 2015).

### **1.2.1. Photovoltaic cells based on inorganic materials**

Inorganic photovoltaic cells (IPVCs) have shown good results in that they have achieved high PCE about 46%, confirmed by the National Renewable Energy Laboratory, due to the excellent charge carrier mobility and the environmental stability of inorganic materials (NREL, 2015, Green et al., 2016). Since the first photovoltaic cells were reported (1946), IPVCs have improved tremendously as reported over the last 50 years. Various kinds of IPVCs have been discovered and been developed such as single-crystal silicon (sc-Si) cells, polycrystalline silicon (poly-Si) cells and heterojunction with intrinsic thin layer (HIT) cells all using crystalline Si. Thin-film photovoltaic cell based on CdTe, copper indium gallium diselenide (CIGS), amorphous silicon (a-Si), and microcrystalline ( $\mu$ c-Si) and others have also been developed (Miles et al., 2007, Schropp et al., 2007, Slaoui and Collins, 2007). The best research-cell efficiencies for each type and material of photovoltaic cells are shown in **Figure 1-1** reported by National Renewable Energy Laboratory (NREL) in 2015.

The best PCE in crystalline silicon cell is from single crystalline cells, it has approached 24.7% (non-concentrator) and 27.6% (concentrator) for about 20 years. However, the efficiency of poly-Si cells is shown to be 20.4% in 2004. The PCE of a-Si cells have gradually increased from 1976 to 2012 and it reached 13.4% (LG Electronics), while that of CIGS cells has reached 20.4% (EMPA). The advantage of poly-Si cells is that they are less expensive to buy and manufacture. The advantage of a-Si is that they can be

deposited in thin films on a variety of substrates at low temperatures and the thin film reduces the cost of an individual solar panel. Among the many photovoltaic cells, the highest PCE photovoltaic cells are multijunction cells. The multijunction photovoltaic cells are built up of multiple p-n junctions using different semiconductor materials (e.g. GaAs/CIS). They can respond to several ranges of wavelength by using different materials to produce electric current. They have been developed PCE over 40% (Green et al., 2016).

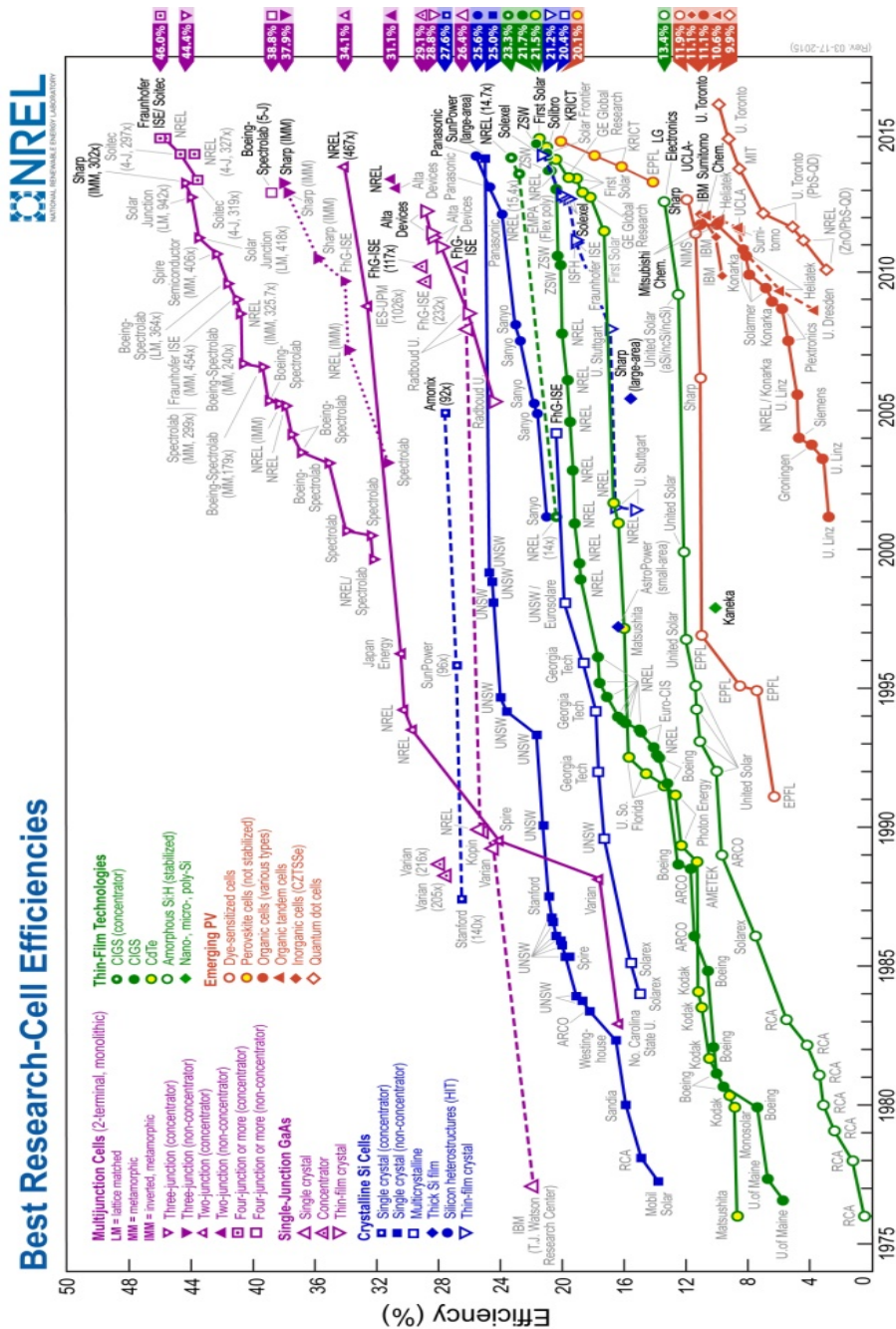
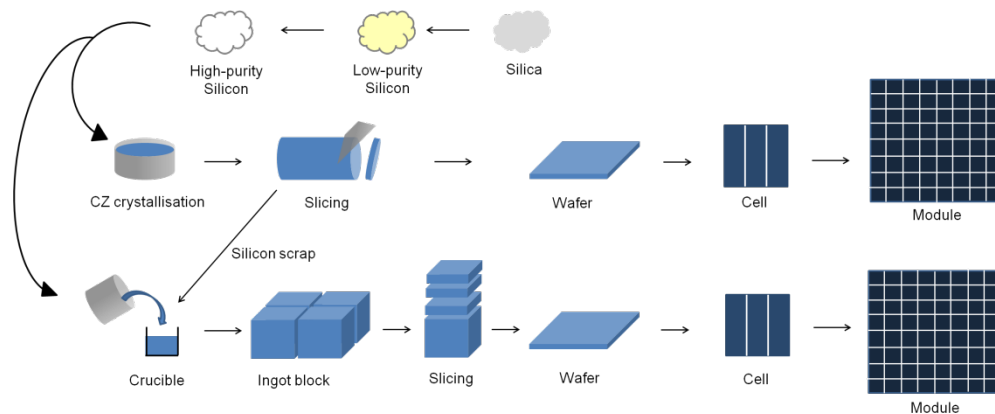


Figure 1-1 The best efficiencies of various kinds of photovoltaic cells (NREL, 2015).

The Shockley-Queisser (S-Q) limit is the maximum theoretical efficiency for photovoltaic cells using a single p-n junction. According to the S-Q limit, the maximum efficiency for a single junction device is around 33%, see **Figure 2-29(a)** in the section 2.5. However, multijunction photovoltaic cells are able to achieve over 33% efficiency and approach up to a PCE of 86% in infinite junctions (Green, 2003).

Silicon-based PVCs lead the PVC market and dominate about 90% of the total PVC production (SolarCellCentral.com). Even if IPVCs show good efficiencies and account for 90%, the main drawback is their production cost due to expensive component materials and fabrication process for the devices. Highly purified silicon wafer is made by various steps from raw material in order to make good efficiency of photovoltaic cells and it leads to increasing cost. **Figure 1-2** shows the steps for preparing photovoltaic cells (Saga, 2010). This is an energy intensive and therefore expensive process (cost of polysilicon is around €15 per kilogram).



**Figure 1-2** The procedure of preparing inorganic photovoltaic cells (Saga, 2010).

### 1.2.2. Photovoltaic cells based on organic materials

Conjugated polymer-based photovoltaic cells are becoming attractive as renewable energy sources for energy generation due to the ability to tune their design for efficient energy harvesting. Because conjugated polymers are generally able to absorb a wider range of visible light by applying donor and acceptor groups in the polymer chain when compared to other organic materials such as monomers and oligomers. The solid red-circles and line in **Figure 1-1** indicates the PCE of a diverse range of organic based photovoltaic cells (NREL, 2015). The best result for organic cells was 11.1% in 2012. Although the efficiency of organic photovoltaic

cells has improved from 2001 to 2009, it has strikingly increased for the last 4 years, while other technologies have not been able to show this rate of improvement in the same period. The main advantages of organic photovoltaic cells are low-cost, flexibility, and their simple production process (Li, 2012, Dennler et al., 2009, Thompson and Frechet, 2008b, Yu et al., 1995). Organic materials are cheaper than inorganic materials and it is possible to process them using diverse techniques such as solution process, spin casting, roller casting and inkjet printing. Often several components can be deposited in one step by taking advantage of self-organised processing. These techniques help reduce the price of devices, decrease processing time and also make large area coating feasible. Conjugated polymers and fullerenes are generally used as the active layer and organic solvents such as chlorobenzene or dichlorobenzene are needed to dissolve these materials. The solvents needed for the production of OPVCs are fairly expensive and dangerous both environmentally and from a health and safety point of view. In the laboratory scale, organic solvents are inevitably used for OPVCs from a few microlitres to a few millilitres. Therefore it will be helpful to use water-soluble or alcohol-soluble materials to reduce organic solvent use were the production of OPVCs to be scaled up to an industrial process.

### **1.3. Conjugated polymers**

The term ‘conjugation or conjugated’ refers to a system having connected p-orbitals by alternating single and multiple bonds with delocalised electrons within the molecules. Conjugated polymers have alternate p-orbitals with single and multiple bonds and this results in their characteristic conductivity and fluorescence. This is because electrons in p-orbitals are able to absorb energy and become excited to higher energy state similar to the conduction band in a semiconducting crystal and so they can cause conductivity and fluorescence. Fluorescent conjugated polymers have attracted much interest due to their thermal stability, strong emission properties, good process ability and wide range of potential application as organic light emitting diodes (OLED) (Huyal et al., 2008), organic thin film transistors (OTFT) (Li et al., 2006), organic photovoltaic cells (Staniec et al., 2011), and chemical and biosensors (Thomas et al., 2007, Liu and Bazan, 2004a). In particular, conjugated polymers used in photovoltaic cells have drawn much interest as renewable energy sources due to fast electron transport, low-costs, ease of synthesis and the ability to tune their properties by altering their structure.

The most valuable advantage of conjugated polymers is that a many different conjugated polymers can be synthesised and it is easy to change their character (solubility, conductivity, band gap, and so on) by introducing various chemical groups.

### 1.3.1. Conjugated polyelectrolytes

Conjugated polyelectrolytes (water-soluble conjugated polymers) are conjugated polymers that contain charged side chains which give them water-solubility. Conjugated polyelectrolytes have been synthesised with polar ionic functional groups, such as anionic carboxylates (Kim et al., 2005), sulfonates (Vetrichelvan et al., 2006), and cationic quaternary ammonium salts (Liu and Bazan, 2004b) within their polymer backbones. The hydrophobic nature of conjugated polymer main chains makes it difficult to dissolve in water because of  $\pi$ - $\pi$  interactions between adjacent polymer backbones causing polymer aggregations. However, by attaching charged side chains it is possible to improve water solubility and therefore it is possible to expand the application of conjugated polymer to various areas.

Conjugated polyelectrolytes have  $\pi$ - $\pi$  conjugation and show photophysical properties that are similar to conjugated polymer. However, their polarity in solution makes polyelectrolytes show different fluorescent properties compared to their corresponding polymer due to hydrogen bonding with solvents or reagents, even though their polymer backbones are same. The charged side chains of polyelectrolytes lead to aggregation with other materials. Positive-charged conjugated polyelectrolytes can induce electrostatic assembly with negatively charged materials. These properties allow them to be used in applications such as biosensors for DNA and protein. Ho et al. suggested a DNA sensor using electrostatic interaction with polythiophene and target DNA without additional fluorophore and quencher (Ho et al., 2002). Gaylord et al. also synthesised water-soluble conjugated poly phenylene fluorene as DNA sensors and then detected the target DNA through FRET with fluorescein (Gaylord et al., 2002). Kwak et al. reported protein sensor using micro-contact printing ( $\mu$ CP) through water-soluble conjugated poly(*para*-phenylene) with fluorescein-labelled streptavidin (Kwak et al., 2010).

From previous reports, conjugated polymers/polyelectrolytes have been used as biosensor probe (*in vitro* and *in vivo*) (Yang et al., 2013, Li and Liu, 2012, Lee et

al., 2012) because conjugated polyelectrolytes show high fluorescence, good stability and low cytotoxicity. In particular, conjugated polyelectrolytes are biocompatible for *in vivo* experiments on mice or rabbits (Ding et al., 2011). Therefore, they are low toxicity materials and could therefore be used in photovoltaic cells as more environmentally friendly materials than the currently used polymers.

### **1.3.2. Conjugated polyelectrolytes use in water for photovoltaic cells**

Concern for the environment is one of the most important issues in the world. The use of organic solvents in various fields causes health and environmental problems (Li, 1993, Narayan et al., 2005). In particular, persistent exposure leads to occupational diseases such as Parkinson's disease, malignant lymphoma, and so on (Ohlson and Hogstedt, 1981, Hardell et al., 1981). Therefore, researchers in chemistry have tried to change from using organic solvents to using water where possible. The advantages of water are that it has low cost, is safe, and is easy to recycling.

For use in the OPVCs in this study, conjugated polyelectrolyte was synthesised. The conjugated polyelectrolyte was applied as an active layer and also as a hole transporting layer in the devices. Unfortunately, the conjugated polyelectrolyte did not show any photovoltaic ability within the active layer. However, it showed good ability as an additive in HTL in the devices. Although when used as an additive, organic solvents were needed for fabrication of photovoltaic cells, water was used as the solvent for conjugated polyelectrolyte. In addition, there was no further organic solvent use (i.e. chlorobenzene, methanol, and so on) therefore the reported improvement of PCE compared to previous reports (Lee et al., 2008, Li et al., 2007) means that for the same power output less materials overall would be required, therefore improving the environmental benefits of OPVCs.

## **1.4. Perovskite photovoltaic cells**

### **1.4.1. Origin of perovskite**

Perovskite was discovered in Ural Mountains by Gustav Rose in 1839 and was named after the Russian mineralogist Lew A. Perowski. Perovskite initially denotes calcium titanium oxide ( $\text{CaTiO}_3$ ), but the term perovskite is used to describe any

compound which has a crystal structure similar to  $\text{CaTiO}_3$  following the pioneering synthesis of perovskite by Goldschmidt in 1926. Perovskites have the chemical formula  $\text{ABX}_3$  structure which consists of cations, A and B, of two different sizes, and anion X. The ideal structure of  $\text{ABX}_3$  perovskite is cubic where B cation coordinates corner sharing ( $\text{BX}_6$ ) octahedral structure with anion X and A cation neutralise total charge in 12-fold coordination. In perovskite, various divalent metal ions are accepted for B cation (Cu, Ni, Co, Fe, Mn, Cr, Pd, Cd, Ge, Sn, Pb, Eu or Yb) (Mitzi, 1999, Liang et al., 1998, Baikie et al., 2013). **Figure 1-3** shows general perovskite structure  $\text{ABX}_3$ .

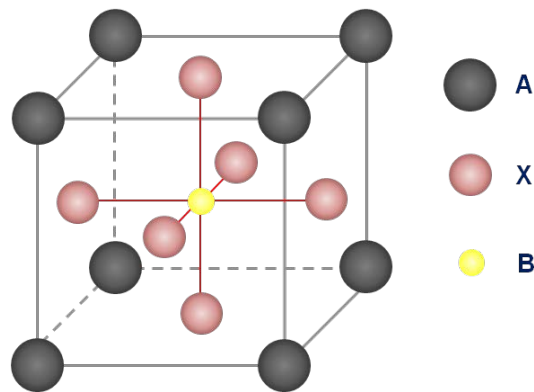


**Figure 1-3** The perovskite lattice structure of  $\text{ABX}_3$  (Eperon et al., 2014).

#### 1.4.2. Organic-metal halide perovskite photovoltaic cells

As shown in **Figure 1-1**, the perovskite photovoltaic cells have rapidly improved since 2010 and they have achieved over 20% PCE (Yang et al., 2015). Perovskites are one of the most interesting materials in the photovoltaic cells field due to their fast development and high efficiency. The first perovskite solar cell was reported by Kojima et al. in 2009 (Kojima et al., 2009). They used methylammonium lead halide perovskites ( $\text{CH}_3\text{NH}_3\text{PbX}_3$ , X= Br, or/and I) as the light harvester in sensitized solar cells.  $\text{CH}_3\text{NH}_3\text{PbI}_3$  or  $\text{CH}_3\text{NH}_3\text{PbBr}_3$  were respectively coated on mesoporous  $\text{TiO}_2$  with liquid electrolyte between electrodes.

Advantages of perovskite photovoltaic cells are low-cost technology (Snaith, 2013), easily tuning band gap of perovskite (Kulkarni et al., 2014), and wide range of absorption wavelengths up to 800 nm (Eperon et al., 2014), and available versatile structures of devices such as sensitised PPVC architecture and planar PPVC architecture which are originated in dye-sensitised PVC and planar heterojunction PVC respectively.

#### 1.4.2.1. Sensitised perovskite photovoltaic cells

A sensitised-perovskite photovoltaic cell is a type of dye-sensitised photovoltaic cell which includes a perovskite as the active layer and it is coated on a mesoporous  $\text{TiO}_2$  layer. The general structure of these devices are anode/n-type contact/ $\text{TiO}_2$ :perovskite/p-type contact/cathode as shown in **Figure 1-4**. Sun light is harvested by perovskite and dissociated electrons and holes are extracted by n-type and p-type contacts respectively. **Figure 1-4** shows the architecture of sensitised perovskite photovoltaic cell (Gamliel and Etgar, 2014).

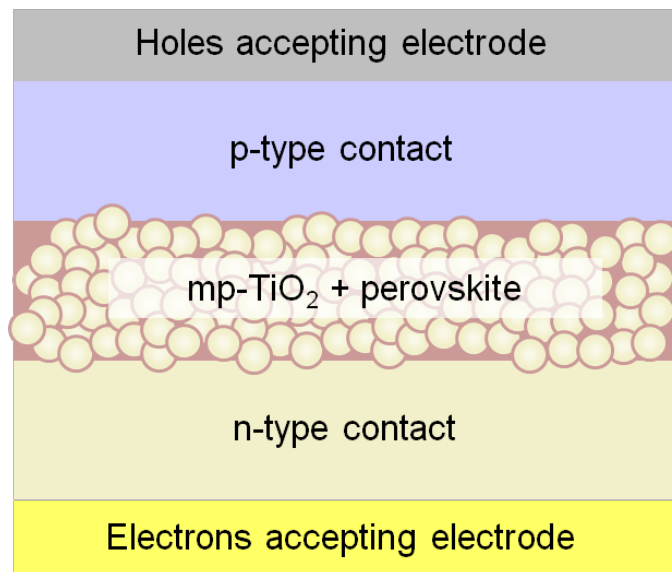


**Figure 1-4** Structure of sensitised perovskite photovoltaic cell.

#### 1.4.2.2. Planar perovskite photovoltaic cells

An interesting and remarkable feature of perovskite photovoltaic cells is that they can also be used in planar photovoltaic architectures. The advantages of planar architectures are that their processing is simple and the planar architecture removes infiltration problems of the perovskite and the hole transport material into the porous  $\text{TiO}_2$  in sensitised perovskite photovoltaic cells (Gamliel and Etgar, 2014). This leads to less recombination and better reproducibility. The two types of architecture of planar perovskite photovoltaic cells are shown in **Figure 1-5**(a) and (b). **Figure 1-5**(a) shows the architecture having FTO/Metal oxide ( $\text{TiO}_2$ )/perovskite/hole transporting layer (Spiro-OMeTAD)/electrode (Au). Dissociated electrons and holes pass through the metal oxide into the FTO and the hole transporting layer to the electrode (Au). Another architecture of planar

perovskite photovoltaic cell is ITO/hole transporting layer (PEDOT:PSS)/perovskite/electron transporting layer (PCBM)/electrode (Al). The dissociated electrons and holes move in the opposite direction to those in the former architecture.

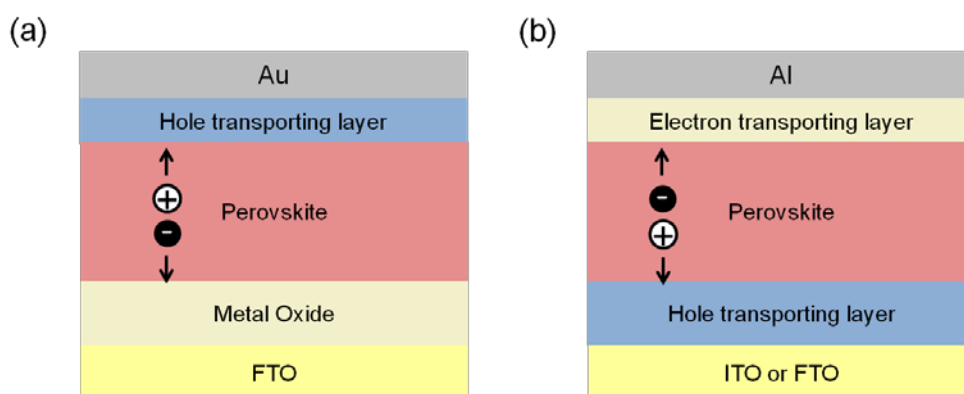


**Figure 1-5** The two types of planar perovskite photovoltaic cells architecture.

For PPVCs in this study, planar PPVC architecture was used. Bismuth was replacement of lead. Bismuth is less toxic than lead due to great insolubility of bismuth salts and it prevents their absorption (DiPalma, 2001). Bismuth-based perovskite structure was studied in different molar ratios of methylammonium iodide and bismuth halide.

Theory and literature related to research will be explained in the **Chapter 2** and **3**, respectively. **Chapter 4, 5, 6,** and **7** will deal with experiment of research project. General P3HT PVC will be explained in **Chapter 4**, synthesis of conjugated polyelectrolyte and study of OPVC with conjugated polyelectrolyte will be dealt with in the **Chapter 5,** and **6**. In **Chapter 7**, bismuth-based perovskite will be introduced.

## 1.5. References

- AZZOPARDI, B., EMMOTT, C. J. M., URBINA, A., KREBS, F. C., MUTALE, J. & NELSON, J. 2011. Economic assessment of solar electricity production from organic-based photovoltaic modules in a domestic environment. *Energy & Environmental Science*, 4, 3741-3753.

- BAIKIE, T., FANG, Y., KADRO, J. M., SCHREYER, M., WEI, F., MHAISALKAR, S. G., GRAETZEL, M. & WHITE, T. J. 2013. Synthesis and crystal chemistry of the hybrid perovskite (CH<sub>3</sub>NH<sub>3</sub>)PbI<sub>3</sub> for solid-state sensitised solar cell applications. *Journal of Materials Chemistry A*, 1, 5628-5641.
- BECQUEREL, E. 1839. *Comptes Rendus*, 9, 561.
- BRABEC, C. J. 2004. Organic photovoltaics: technology and market. *Solar Energy Materials and Solar Cells*, 83, 273-292.
- CAPELLO, C., FISCHER, U. & HUNGERBUHLER, K. 2007. What is a green solvent? A comprehensive framework for the environmental assessment of solvents. *Green Chemistry*, 9, 927-934.
- CHAPIN, D. M., FULLER, C. S. & PEARSON, G. L. 1954. A New Silicon P-N Junction Photocell for Converting Solar Radiation into Electrical Power. *Journal of Applied Physics*, 25, 676-677.
- DENNLER, G., SCHARBER, M. C. & BRABEC, C. J. 2009. Polymer-Fullerene Bulk-Heterojunction Solar Cells. *Advanced Materials*, 21, 1323-1338.
- DING, D., LI, K., ZHU, Z., PU, K. Y., HU, Y., JIANG, X. & LIU, B. 2011. Conjugated polyelectrolyte-cisplatin complex nanoparticles for simultaneous in vivo imaging and drug tracking. *Nanoscale*, 3, 1997-2002.
- DIPALMA, J. R. 2001. Bismuth Toxicity, Often Mild, Can Result in Severe Poisonings. *Emergency Medicine News*, 23, 16.
- ENERGY, U. S. D. O. 2005. *Basic Research Needs for Solar Energy Utilization*.
- EPERON, G. E., STRANKS, S. D., MENELAOU, C., JOHNSTON, M. B., HERZ, L. M. & SNAITH, H. J. 2014. Formamidinium lead trihalide: a broadly tunable perovskite for efficient planar heterojunction solar cells. *Energy & Environmental Science*, 7, 982-988.
- ESPINOSA, N., HOSEL, M., ANGMO, D. & KREBS, F. C. 2012. Solar cells with one-day energy payback for the factories of the future. *Energy & Environmental Science*, 5, 5117-5132.
- FACCHETTI, A. 2011. pi-Conjugated Polymers for Organic Electronics and Photovoltaic Cell Applications. *Chemistry of Materials*, 23, 733-758.
- FLORA, G., GUPTA, D. & TIWARI, A. 2012. Toxicity of lead: A review with recent updates. *Interdiscip Toxicol*, 5, 47-58.
- FRITTS, C. E. 1883. On a new form of selenium cell, and some electrical discoveries made by its use. *American Journal of Science*, 26, 465-472.
- GAMLIEL, S. & ETGAR, L. 2014. Organo-metal perovskite based solar cells: sensitized versus planar architecture. *Rsc Advances*, 4, 29012-29021.

- GAYLORD, B. S., HEEGER, A. J. & BAZAN, G. C. 2002. DNA detection using water-soluble conjugated polymers and peptide nucleic acid probes. *Proceedings of the National Academy of Sciences of the United States of America*, 99, 10954-10957.
- GREEN, M. A. 2003. *Third generation photovoltaics : advanced solar energy conversion*, Berlin ; New York, Springer.
- GREEN, M. A., EMERY, K., HISHIKAWA, Y., WARTA, W. & DUNLOP, E. D. 2016. Solar cell efficiency tables (version 47). *Progress in Photovoltaics*, 24, 3-11.
- GUNES, S., NEUGEBAUER, H. & SARICIFTCI, N. S. 2007. Conjugated polymer-based organic solar cells. *Chemical Reviews*, 107, 1324-1338.
- HARDELL, L., ERIKSSON, M., LENNER, P. & LUNDGREN, E. 1981. Malignant lymphoma and exposure to chemicals, especially organic solvents, chlorophenols and phenoxy acids: a case-control study. *Br J Cancer*, 43, 169-76.
- HE, Z. C., ZHONG, C. M., HUANG, X., WONG, W. Y., WU, H. B., CHEN, L. W., SU, S. J. & CAO, Y. 2011. Simultaneous Enhancement of Open-Circuit Voltage, Short-Circuit Current Density, and Fill Factor in Polymer Solar Cells. *Advanced Materials*, 23, 4636-+.
- HO, H. A., BOISSINOT, M., BERGERON, M. G., CORBEIL, G., DORE, K., BOUDREAU, D. & LECLERC, M. 2002. Colorimetric and fluorometric detection of nucleic acids using cationic polythiophene derivatives. *Angewandte Chemie-International Edition*, 41, 1548-1551.
- HUYAL, I. O., KOLDEMIR, U., OZEL, T., DEMIR, H. V. & TUNCEL, D. 2008. On the origin of high quality white light emission from a hybrid organic/inorganic light emitting diode using azide functionalized polyfluorene. *Journal of Materials Chemistry*, 18, 3568-3574.
- KIM, I. B., DUNKHORST, A. & BUNZ, U. H. F. 2005. Nonspecific interactions of a carboxylate-substituted PPE with proteins. A cautionary tale for biosensor applications. *Langmuir*, 21, 7985-7989.
- KOJIMA, A., TESHIMA, K., SHIRAI, Y. & MIYASAKA, T. 2009. Organometal Halide Perovskites as Visible-Light Sensitizers for Photovoltaic Cells. *Journal of the American Chemical Society*, 131, 6050-+.
- KULKARNI, S. A., BAIKIE, T., BOIX, P. P., YANTARA, N., MATHEWS, N. & MHAISALKAR, S. 2014. Band-gap tuning of lead halide perovskites using a sequential deposition process. *Journal of Materials Chemistry A*, 2, 9221-9225.

- KWAK, C. K., KIM, D. G., KIM, T. H., LEE, C. S., LEE, M. & LEE, T. S. 2010. Simultaneous and Dual Emissive Imaging by Micro-Contact Printing on the Surface of Electrostatically Assembled Water-Soluble Poly(p-phenylene) Using FRET. *Advanced Functional Materials*, 20, 3847-3855.
- LANDRIGAN, P. J. 1989. Toxicity of Lead at Low-Dose. *British Journal of Industrial Medicine*, 46, 593-596.
- LEE, J. K., MA, W. L., BRABEC, C. J., YUEN, J., MOON, J. S., KIM, J. Y., LEE, K., BAZAN, G. C. & HEEGER, A. J. 2008. Processing additives for improved efficiency from bulk heterojunction solar cells. *Journal of the American Chemical Society*, 130, 3619-3623.
- LEE, K., LEE, J., JEONG, E. J., KRONK, A., ELENITOBA-JOHNSON, K. S., LIM, M. S. & KIM, J. 2012. Conjugated polyelectrolyte-antibody hybrid materials for highly fluorescent live cell-imaging. *Adv Mater*, 24, 2479-84.
- LI, C. J. 1993. Organic-Reactions in Aqueous-Media - with a Focus on Carbon-Carbon Bond Formation. *Chemical Reviews*, 93, 2023-2035.
- LI, G., YAO, Y., YANG, H., SHROTRIYA, V., YANG, G. & YANG, Y. 2007. "Solvent annealing" effect in polymer solar cells based on poly(3-hexylthiophene) and methanofullerenes. *Advanced Functional Materials*, 17, 1636-1644.
- LI, K. & LIU, B. 2012. Polymer encapsulated conjugated polymer nanoparticles for fluorescence bioimaging. *Journal of Materials Chemistry*, 22, 1257-1264.
- LI, Y. F. 2012. Molecular Design of Photovoltaic Materials for Polymer Solar Cells: Toward Suitable Electronic Energy Levels and Broad Absorption. *Accounts of Chemical Research*, 45, 723-733.
- LI, Y. N., WU, Y. L. & ONG, B. S. 2006. Polyindolo[3,2-b]carbazoles: A new class of p-channel semiconductor polymers for organic thin-film transistors. *Macromolecules*, 39, 6521-6527.
- LIANG, K., MITZI, D. B. & PRIKAS, M. T. 1998. Synthesis and Characterization of Organic-Inorganic Perovskite Thin Films Prepared Using a Versatile Two-Step Dipping Technique. *Chemistry of Materials*, 10, 403-411.
- LIU, B. & BAZAN, G. C. 2004a. Homogeneous fluorescence-based DNA detection with water-soluble conjugated polymers. *Chemistry of Materials*, 16, 4467-4476.
- LIU, B. & BAZAN, G. C. 2004b. Interpolyelectrolyte complexes of conjugated copolymers and DNA: Platforms for multicolor biosensors. *Journal of the American Chemical Society*, 126, 1942-1943.

- MILES, R. W., ZOPPI, G. & FORBES, I. 2007. Inorganic photovoltaic cells. *Materials Today*, 10, 20-27.
- MITZI, D. B. 1999. Synthesis, Structure, and Properties of Organic-Inorganic Perovskites and Related Materials. *Progress in Inorganic Chemistry*. John Wiley & Sons, Inc.
- NARAYAN, S., MULDOON, J., FINN, M. G., FOKIN, V. V., KOLB, H. C. & SHARPLESS, K. B. 2005. "On water": Unique reactivity of organic compounds in aqueous suspension. *Angewandte Chemie-International Edition*, 44, 3275-3279.
- NREL. 2015. [http://www.nrel.gov/ncpv/images/efficiency\\_chart.jpg](http://www.nrel.gov/ncpv/images/efficiency_chart.jpg) [Online]. National Renewable Energy Laboratory. Available: [http://www.nrel.gov/ncpv/images/efficiency\\_chart.jpg](http://www.nrel.gov/ncpv/images/efficiency_chart.jpg).
- OHL, R. 1946. *LIGHT-SENSITIVE ELECTRIC DEVICE Filed*.
- OHLSON, C. G. & HOGSTEDT, C. 1981. Parkinson's disease and occupational exposure to organic solvents, agricultural chemicals and mercury--a case-referent study. *Scand J Work Environ Health*, 7, 252-6.
- SAGA, T. 2010. Advances in crystalline silicon solar cell technology for industrial mass production. *Npg Asia Materials*, 2, 96-102.
- SCHARBER, M. C., WUHLBACHER, D., KOPPE, M., DENK, P., WALDAUF, C., HEEGER, A. J. & BRABEC, C. L. 2006. Design rules for donors in bulk-heterojunction solar cells - Towards 10 % energy-conversion efficiency. *Advanced Materials*, 18, 789-+.
- SCHROPP, R. E. I., CARIUS, R. & BEAUCARNE, G. 2007. Amorphous silicon, microcrystalline silicon, and thin-film polycrystalline silicon solar cells. *Mrs Bulletin*, 32, 219-224.
- SHAHEEN, S. E., GINLEY, D. S. & JABBOUR, G. E. 2005. Organic-based photovoltaics. toward low-cost power generation. *Mrs Bulletin*, 30, 10-19.
- SLAOUI, A. & COLLINS, R. T. 2007. Advanced inorganic materials for photovoltaics. *Mrs Bulletin*, 32, 211-218.
- SNAITH, H. J. 2013. Perovskites: The Emergence of a New Era for Low-Cost, High-Efficiency Solar Cells. *Journal of Physical Chemistry Letters*, 4, 3623-3630.
- SOLARCELLCENTRAL.COM. <http://solarcellcentral.com/index.html> [Online]. Available: <http://solarcellcentral.com/index.html>.
- SONDERGAARD, R., HOSEL, M., ANGMO, D., LARSEN-OLSEN, T. T. & KREBS, F. C. 2012. Roll-to-roll fabrication of polymer solar cells. *Materials Today*, 15, 36-49.

- STANIEC, P. A., PARNELL, A. J., DUNBAR, A. D. F., YI, H. N., PEARSON, A. J., WANG, T., HOPKINSON, P. E., KINANE, C., DALGLIESH, R. M., DONALD, A. M., RYAN, A. J., IRAQI, A., JONES, R. A. L. & LIDZEY, D. G. 2011. The Nanoscale Morphology of a PCDTBT: PCBM Photovoltaic Blend. *Advanced Energy Materials*, 1, 499-504.
- TAO, M. 2008. Inorganic Photovoltaic Solar Cells: Silicon and Beyond. *The Electrochemical Society Interface*, 30.
- THOMAS, S. W., JOLY, G. D. & SWAGER, T. M. 2007. Chemical sensors based on amplifying fluorescent conjugated polymers. *Chemical Reviews*, 107, 1339-1386.
- THOMPSON, B. C. & FRECHET, J. M. 2008a. Polymer-fullerene composite solar cells. *Angew Chem Int Ed Engl*, 47, 58-77.
- THOMPSON, B. C. & FRECHET, J. M. J. 2008b. Organic photovoltaics - Polymer-fullerene composite solar cells. *Angewandte Chemie-International Edition*, 47, 58-77.
- VETRICHELVAN, M., LI, H. R., RAVINDRANATH, R. & VALIYAVEETIL, S. 2006. Synthesis and comparison of the structure-property relationships of symmetric and asymmetric water-soluble poly(p-phenylene)s. *Journal of Polymer Science Part a-Polymer Chemistry*, 44, 3763-3777.
- YANG, G., LIU, L., LV, F. & WANG, S. 2013. Conjugated polyelectrolyte materials for promoting progenitor cell growth without serum. *Sci Rep*, 3, 1702.
- YANG, W. S., NOH, J. H., JEON, N. J., KIM, Y. C., RYU, S., SEO, J. & SEOK, S. I. 2015. High-performance photovoltaic perovskite layers fabricated through intramolecular exchange. *Science*, 348, 1234-1237.
- YU, G., GAO, J., HUMMELEN, J. C., WUDL, F. & HEEGER, A. J. 1995. Polymer Photovoltaic Cells - Enhanced Efficiencies Via a Network of Internal Donor-Acceptor Heterojunctions. *Science*, 270, 1789-1791.

## 2. Theory

### 2.1. Synthesis

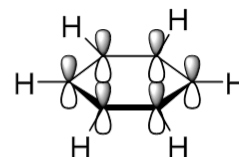
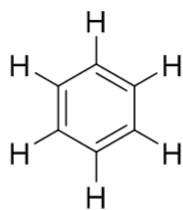
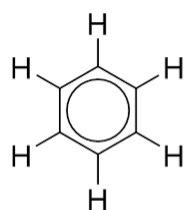
Some of the synthesis methods and theories described here for the study of synthesis of conjugated polyelectrolyte are taken from the texts Organic Chemistry (Klein, 2015, Clayden et al., 2012, McMurry, 1996) and Design and Synthesis of Conjugated Polymers (Leclerc and Morin, 2010).

Synthesis is an important part of the research process to achieve better results from photovoltaic cells using low band gap polymers. In order to synthesise low band gap conjugated polyelectrolytes in this study, which are able to absorb sunlight at long wavelengths (around 600 nm), an electrophilic substitution reaction, sultone ring open reaction, and Suzki-Miyaura cross coupling (polymerisation) using palladium catalyst were used.

#### 2.1.1. Electrophilic aromatic substitution (for bromination)

Electrophilic aromatic substitution is a significant reaction for aromatic compounds because functional side groups such as halogen, alkyl, sulfonyl, nitryl and acyl groups can be attached to conjugated polymer backbone using electrophilic aromatic substitution.

Before dealing with electrophilic aromatic reactions, the term aromatic is briefly explained. In general aromatic means materials which have scent and chemically aromatic refers to chemicals which have conjugated structures similar to benzene present. Benzene is a symmetrical planar hexagon having six carbons ( $sp^2$ ) and six hydrogens (Hückel's  $4n + 2$  rule). Therefore, a benzene ring forms conjugation as explained in **Chapter 1**. A remarkable feature of benzene is that all the carbon bond lengths are 139 pm which falls between the single bond (154 pm) and double bond (134 pm) lengths. The structure of benzene is illustrated in **Figure 2-1**. Alternating single and double bonds of benzene structure was firstly suggested by German chemist Friedrich August Kekulé in 1865 (Kekulé, 1866, Kekulé, 1872).



Two ways of drawing benzene

The  $\pi$  system

**Figure 2-1** Structure of benzene (Clayden et al., 2012, Kekulé, 1872, Kekulé, 1866).

Alternating double and single bonds make the electrons delocalise in the materials, therefore benzene is stabilised by conjugation. Benzene stability is higher than expected and this is proven by the energy of hydrogenation of benzene. Hydrogenation is the addition of hydrogen to materials. **Figure 2-2** shows energy diagram of hydrogenation heats for cyclohexene, 1,3-cyclohexadiene, and benzene. Hydrogenation heat of an unsaturated compound is the most direct way to measure its resonance energy (Rogers and McLafferty, 1971). Cyclohexene has one double bond ( $\text{CH}_2=\text{CH}_2$ ). The double bond is changed to a single bond during hydrogenation and the enthalpy is changed during the reaction. The enthalpy change of this reaction by hydrogen is  $-120 \text{ kJ/mol}$ . From this enthalpy change, the hydrogenation heat of 1,3-cyclohexadiene was expected to be  $-240 \text{ kJ/mol}$ . The observed hydrogenation heat of 1,3-cyclohexadiene was  $-232 \text{ kJ/mol}$  and it was not very different from the expected value (Clayden et al., 2012, McMurry, 1996). As shown in **Figure 2-2**, however, the expected hydrogenation heat of benzene is  $-360 \text{ kJ/mol}$ , but the actual heat of hydrogenation is  $-208 \text{ kJ/mol}$ . The energy difference ( $152 \text{ kJ/mol}$ ) between the expected value and the actual value is called the stabilisation energy of benzene and this value is associated with aromaticity.

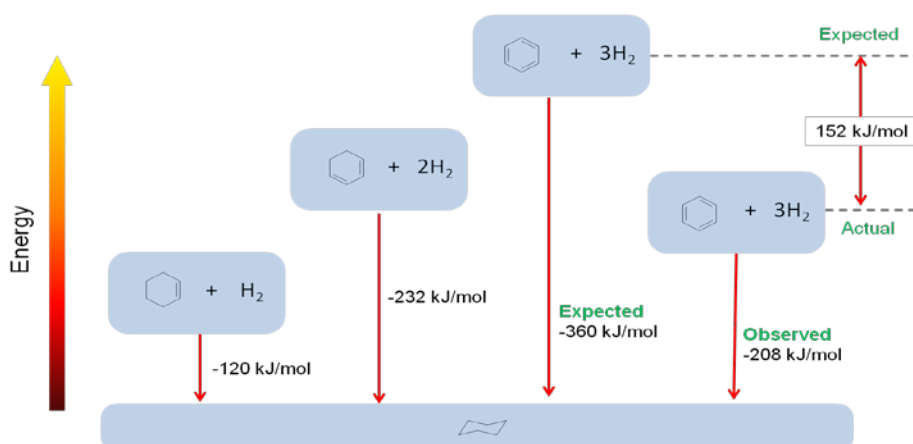


**Figure 2-2** Energy diagram of hydrogenation heats for cyclohexene, 1,3-cyclohexadiene, and benzene (Klein, 2015).

**Table 2-1** summarises the expected and observed hydrogenation heats of cyclohexene, 1,3-cyclohexadiene, and benzene.

**Table 2-1** Hydrogenation heats of cyclohexene, 1,3-cyclohexadiene, and benzene

materials	Expected hydrogenation heats	Observed hydrogenation heats
Cyclohexene	-120 kJ/mol	-120 kJ/mol
1,3-cyclohexadiene	-240 kJ/mol	-232 kJ/mol
Benzene	-360 kJ/mol	-208 kJ/mol

A benzene ring has a high electron density due to its six  $\pi$  electrons. Therefore, benzene reacts as an electron donor to electrophilic materials (electron acceptor) during electrophilic aromatic substitution. In order to understand electrophilic aromatic substitution, this reaction is compared with an electrophilic addition reaction. Alkenes react easily with electrophiles such as hydrochloric acid (HCl) or bromine ( $\text{Br}_2$ ) and the alkane is produced by an additional reaction. If HCl is added into the alkene, the electrophile  $\text{H}^+$  combines with a carbon which is double bonded and the other carbon becomes a carbocation. Then the  $\text{Cl}^-$  ion attacks the carbocation.

When  $\text{Br}_2$  is added into the cyclohexene, trans-1,2-dibromo-cyclohexane is produced. The reaction mechanism is same with HCl additional reaction above mentioned and it is rapidly processed. When  $\text{Br}_2$  is added into the benzene, hydrogen is replaced by bromine. However, a Lewis acid catalyst such as  $\text{FeBr}_3$  or  $\text{AlCl}_3$  is needed in order for the electrophilic aromatic substitution to occur. Because the reactivity of benzene is lower than the alkene due to the stability of its aromatic ring. The mechanism of both electrophilic addition and electrophilic substitution is illustrated in **Figure 2-3**.

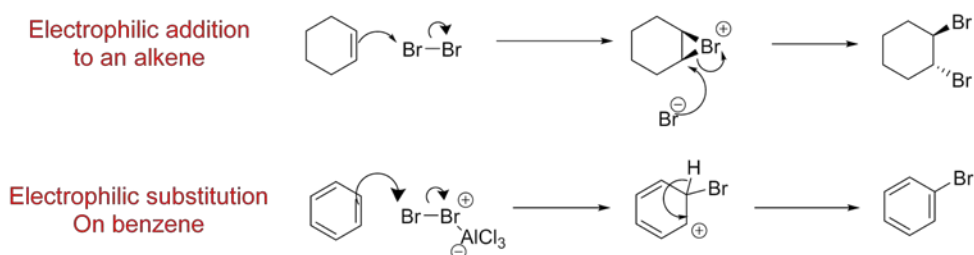


**Figure 2-3** The mechanism of electrophilic addition on cycloalkene and electrophilic substitution on benzene (Clayden et al., 2012).

As shown in **Figure 2-3** the catalyst,  $\text{AlCl}_3$  or  $\text{FeBr}_3$ , makes a complex with  $\text{Br}_2$ , so the electrophilicity of complexed  $\text{Br}_2$  is increased compared to  $\text{Br}_2$  and it acts like  $\text{Br}^+$  in electrophilic substitution. Then the  $\pi$  electrons of the benzene attack the polarised bromine and it forms an intermediate carbocation. In contrast with electrophilic addition,  $\text{H}^+$  is eliminated from the benzene intermediate carbocation and it forms an aromatic (benzene) ring again in order to preserve delocalisation and stability in electrophilic substitution. The mechanism and energy diagram of electrophilic aromatic substitution is shown in **Figure 2-4**.

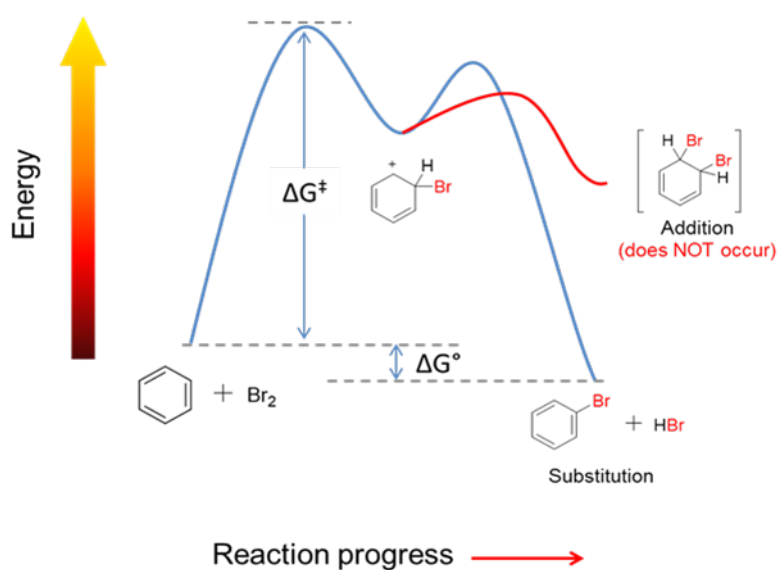


**Figure 2-4** Energy diagram of electrophilic substituted bromination of benzene (McMurry, 1996).

### 2.1.2. Nucleophilic substitution (for fluorene and sultone reaction)

Polyfluorene (fluorene) is a polycyclic aromatic hydrocarbon. Polyfluorene (fluorene) is obtained from coal tar and discovered by M. Berthelot in 1883 (W. R. Hodgkinson, 1883). A term 'fluorene' is related to its fluorescence. Because of this blue fluorescence, fluorene has been applied in various fields such as electroluminescence devices (Jiang et al., 2000), and photovoltaic cells (Yohannes et al., 2004). **Figure 2-5** shows fluorene.

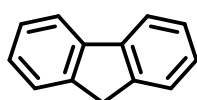


**Figure 2-5** The structure of fluorene.

Sultone is any heterocyclic ester of the hydroxy sulfonic acids. It is similar to lactone. The term of sultone and structure was first introduced in 1888 by H. Erdmann to explain the aromatic ring including hydroxyl sulfonic acid, 1,8-naphthosultone (Erdmann, 1888, Mondal, 2012) in **Figure 2-6**.

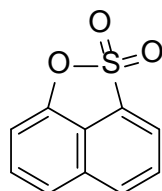


**Figure 2-6** The structure of 1,8-naphthosultone.

Sultone is an interesting heterocyclic compound which permits the attachment of alkyl chains accompanying the sulfonic acid groups. In this research, sulfoalkyl groups from sultone were introduced to enhance water-solubility of conjugated polymer.

Sultone and fluorene reaction is based on nucleophilic substitution and product was 2,7-dibromo-9,9-bis(4-sulfonatobutyl)fluorene disodium in the research. Therefore, in this part, nucleophilic substitution will be mentioned. Nucleophilic substitution is a fundamental technique in organic synthesis. **Figure 2-7** shows the structure of 2,7-dibromo-9,9-bis(4-sulfonatobutyl)fluorene disodium.

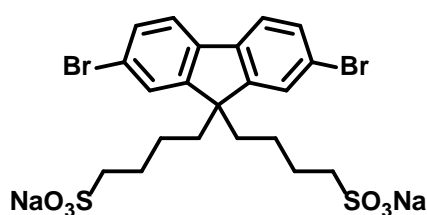


**Figure 2-7** The structure of 2,7-dibromo-9,9-bis(4-sulfonatobutyl)fluorene disodium

In this chapter, the mechanism of nucleophilic substitution will be explained. Nucleophilic substitution ( $S_N$ ) is the reaction where one group is replaced by a nucleophile. In general,  $S_N$  is easily achieved with alkyl halide because the carbon linked to the halogen is slightly positively charged due to electronegativity of halogen. In **Figure 2-8**, a nucleophile attacks the positive carbon and the halogen is replaced by the nucleophile.



**Figure 2-8** The mechanism of  $S_N2$  reaction with methyl iodide and hydroxide (Clayden et al., 2012).

In **Figure 2-8**, the reaction rate is determined by the concentration of  $\text{OH}^-$  and  $\text{MeI}$ . In other words, if the amounts of reactant or nucleophile are increased, their reaction is rapidly processed. This  $S_N$  reaction mechanism was suggested by E. D. Hugh, and C. Ingold in 1937 and it explains both the reaction rate and stereochemistry. This reaction is named an  $S_N2$  reaction because it is a substitution reaction which is, nucleophilic, and bimolecular.

The most important feature of  $S_N2$  reactions are that the reaction progressed in one step and it is affected by steric hindrance. As shown in **Figure 2-9**, the new bonding with an incoming nucleophile is produced and another bonding is cleaved in same time. The incoming nucleophile attacks the carbon on the opposite side to that linked with the halide (electron withdrawing group or leaving group) and then it enters the transition state. In a transition state, carbon and three substituents are in a planar arrangement. The nucleophile is connected with the carbon and the halide group is disconnected.

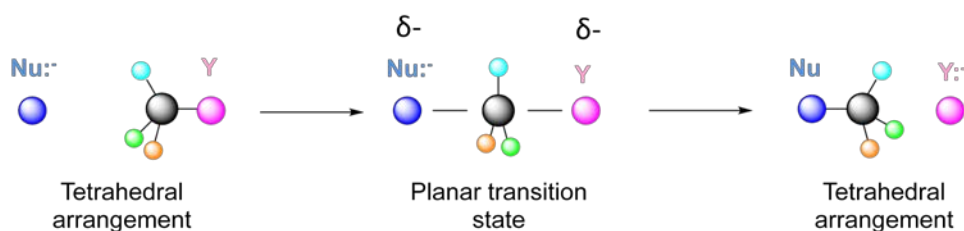


**Figure 2-9** The mechanism of  $S_N2$  reaction. The nucleophile attacks carbon through  $180^\circ$  opposite direction of leaving group (McMurry, 1996).

Steric effects (hindrance) are important factors in deciding whether a reaction is  $S_N2$  or  $S_N1$ . In  $S_N2$  reactions, since the incoming nucleophile has partial bond formation with the alkyl halide in transition state, it is sensible that a hindered, bulky substrate should prevent easy approach of the nucleophile, making bond formation difficult. **Figure 2-10** shows steric hindrance to the  $S_N2$  reaction.

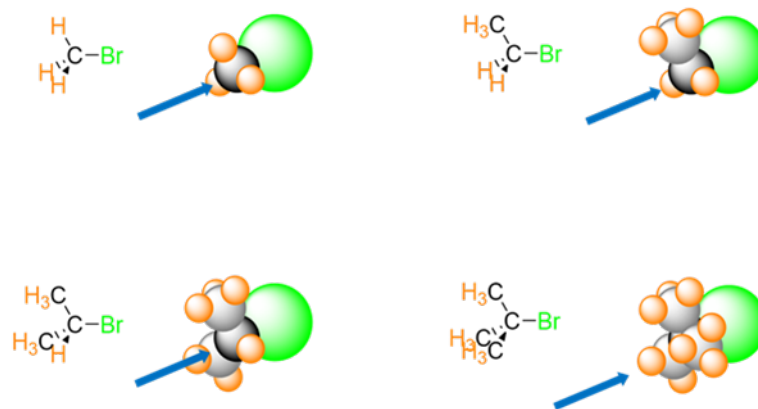


**Figure 2-10** Steric hindrance of  $S_N2$  reaction. (a) bromomethane has the fastest  $S_N2$  reaction rate, the reaction rates of (b) bromoethane, (c) bromopropane (secondary), and (d) 2-bromo-2-methylpropane (tertiary) are gradually reduced due to steric hindrance (McMurry, 1996).



**Figure 2-11** The mechanism of  $S_N1$  reaction (Clayden et al., 2012).

Another nucleophilic substitution mechanism is illustrated in **Figure 2-11**. This nucleophilic substitution is processed by two steps. There is loss of halogen (leaving) group and it forms an intermediate carbocation and then the nucleophile attacks the intermediate carbocation. In the reaction, reaction rate is only determined by concentration of the reactant. Therefore, the reaction is named as  $S_N1$  from substitution, nucleophilic, and unimolecular. The main difference with an  $S_N2$  reaction is that  $S_N1$  reaction is a stepwise process due to steric hindrance. As a result,  $S_N1$  reaction produces a racemic mixture and it is described in **Figure 2-12**.

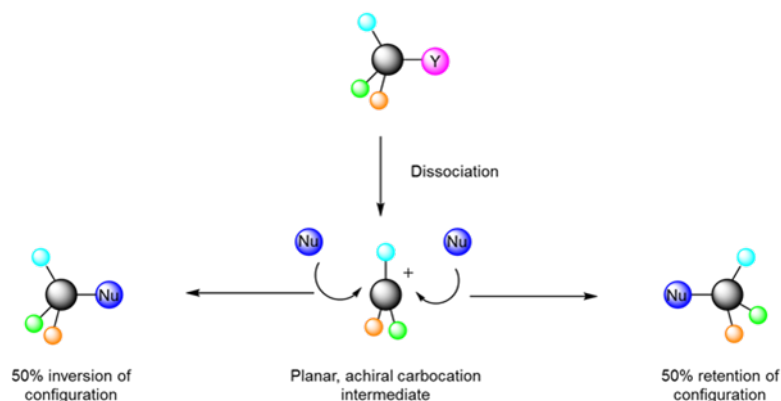


**Figure 2-12** Stereochemistry of  $S_N1$ . This reaction produces racemic structure via carbocation intermediate (McMurry, 1996).

In the reaction, tertiary alkyl halides react most quickly, but methyl and primary alkyl halide are unreactive via  $S_N1$ . Tertiary alkyl halides show the fastest reaction because a nucleophile is not directly attacking the reactant due to steric hindrance. Therefore, the leaving group is cleaved first; then the resulting intermediate carbocation reacts with a nucleophile.

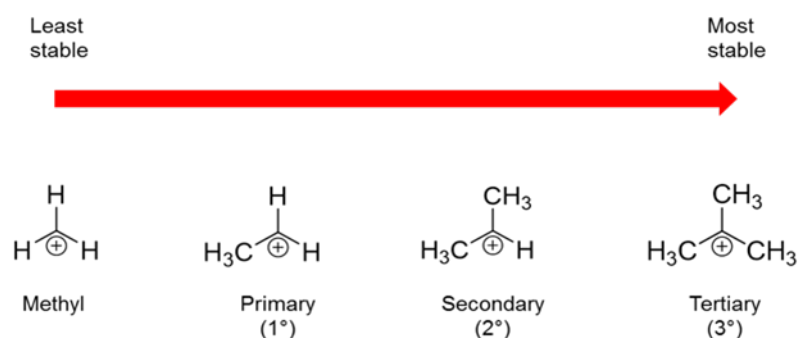


**Figure 2-13** The stability of methyl, primary, secondary, and tertiary carbocation (Klein, 2015).

In the  $S_N1$  reaction, the dominant factor is the stability of the carbocation. **Figure 2-13** shows the stability of the carbocations. As shown in **Figure 2-13**, the carbocations are stabilised by neighboring alkyl groups. Formation of tertiary carbocation is more stable and faster than other carbocation in  $S_N1$  reactions.

### 2.1.3. Suzuki-Miyaura cross coupling

Conjugated polymers can be directly or indirectly connected by conjugation of aromatic units or double or triple bonds. In order to synthesise the conjugated polymer, several synthesis techniques are used such as Stille, Sonogashira, Heck, Suzuki-Miyaura cross coupling and so on. The common feature of these coupling reactions is using palladium (Pd) catalyst. Among many cross coupling reactions using Pd catalyst, Suzuki-Miyaura cross coupling is frequently used for synthesis of aromatic-aromatic single bond reactions. In this research, Suzuki-Miyaura cross coupling was used for synthesis of a conjugated polyelectrolyte.

Suzuki-Miyaura cross coupling was first invented by Suzuki, Miyaura, and colleagues in 1979. It allows the connection of two specific  $sp^2$ -hybridized C atoms more efficiently and under milder conditions. It has been used worldwide for a few decades and it is often simply called “Suzuki coupling”.

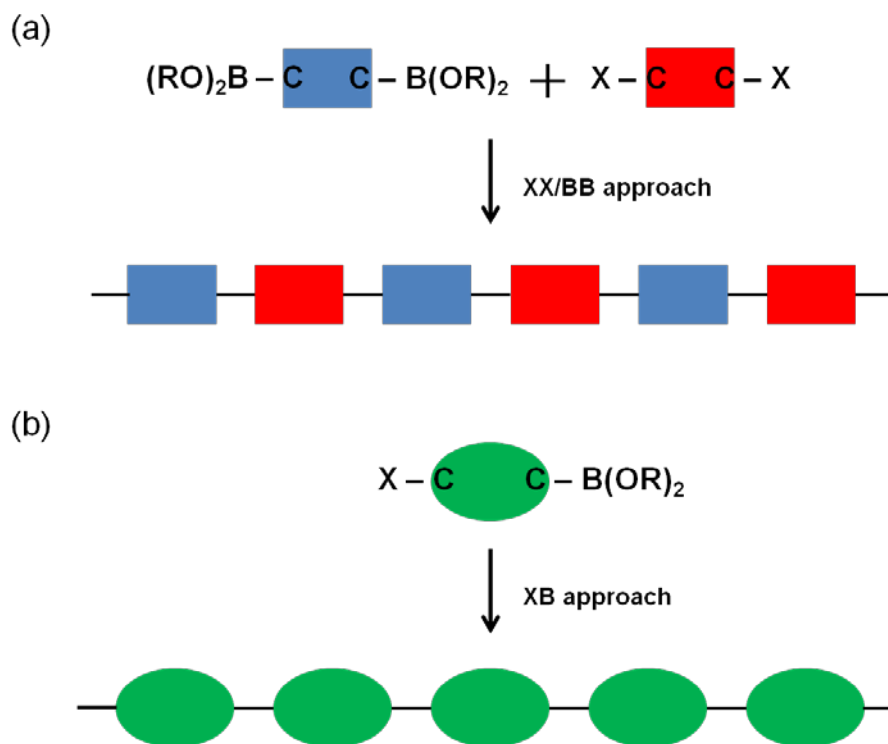


**Figure 2-14** The two different types (a) XX/BB and (b) XB approaches to Suzuki coupling. X is halogen group such as Br, Cl, and I, but Br is commonly used (Leclerc and Morin, 2010). X is halogen and B is boronic acid.

Suzuki coupling is the reaction in which aryl halides and organoboronic acids are reacted in the presence of Pd catalyst. Although lots of conditions for Suzuki coupling such as solvents, catalysts, and bases are important, in this chapter, the reaction mechanism will be dealt with. This is stepwise growth type reaction and the chemical equation is illustrated in **Figure 2-14**.

As shown in **Figure 2-14**, it is possible to approach with two types of XX/BB and XB. X and B are functional groups in the monomer including boronic acid and halogen, respectively. XX/BB type needs two different materials aryl halide and aryl boronic acid resulting in polyarylene backbone. The polyarylene made by AA/BB type is an alternating polymer and it allows that various aromatic groups are applied. However, AB type is only making one kind of repeating unit.

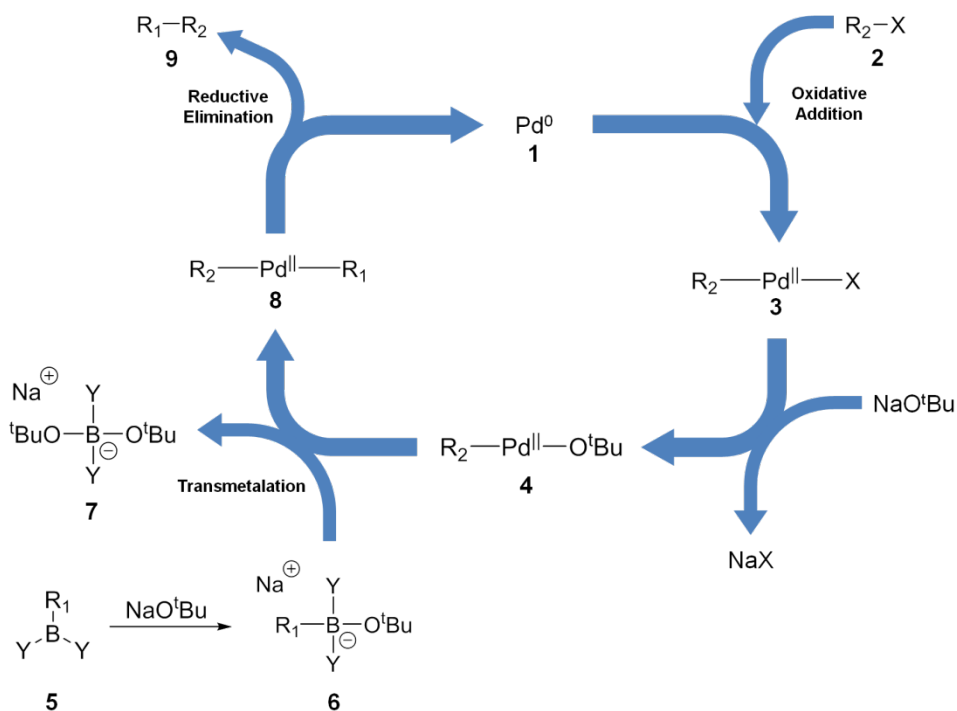


**Figure 2-15** Suzuki Coupling full mechanism with NaO<sup>t</sup>Bu (Leclerc and Morin, 2010).

The mechanism of Suzuki coupling is shown in **Figure 2-15**. The first step is that Pd catalyst is oxidative addition to halide then it forms the R<sub>2</sub>-Pd-X formation (3). The halide is replaced by NaO<sup>t</sup>Bu and R<sub>2</sub>-Pd-O<sup>t</sup>Bu intermediate (4) is formed. Boron part is changed by NaO<sup>t</sup>Bu to R<sub>1</sub>-BY<sub>2</sub>-O<sup>t</sup>Bu (6). (4) is transmetalated with (6) and it forms R<sub>1</sub>-Pd-R<sub>2</sub> (8). Pd catalyst is restored by reductive elimination and (8) is changed to R<sub>1</sub>-R<sub>2</sub>. The Suzuki coupling was applied to final step of synthesis for conjugated polyelectrolyte in the research and the procedure of synthesis is described in **Chapter 5**.

## 2.2 Photovoltaic cell

In this section, the basic principles of photovoltaic cells are described and general fabrication mechanisms are explained. The various theories are taken from textbooks (Nelson, 2003, Wenham, 2007).

### 2. 2. 1. Solar radiation

In order to find suitable polymers and achieve good efficiency for PVCs, understanding solar radiation is an important factor. Even if solar radiation is

constant, the radiation which reaches the Earth's surface is altered due to atmospheric effects such as absorption and scattering. The atmospheric effects may cause reduction of the incident light available to terrestrial PVs. **Figure 2-16** shows the spectra of the solar radiation of outside the atmosphere (AM 0), and the Earth's surface (AM 1.5) (NREL).

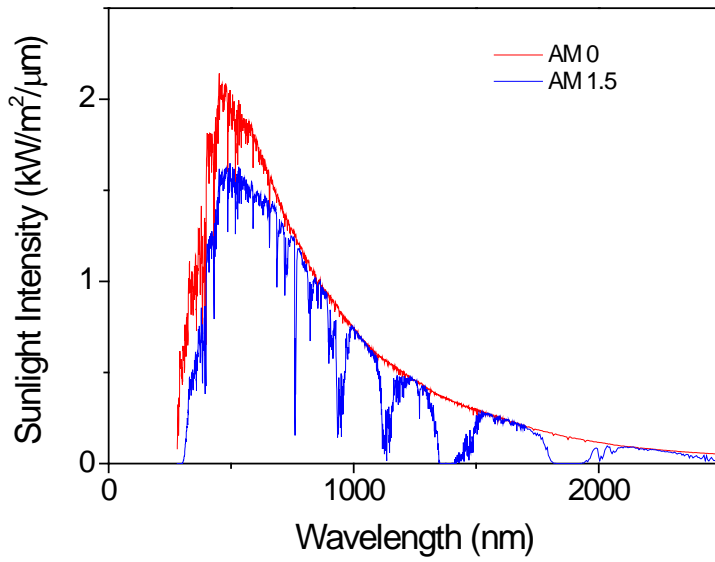


**Figure 2-16** The solar radiation of outside the atmosphere (AM 0, red), and the Earth's surface (AM 1.5, blue) (NREL).

According to the blue line (AM 1.5) in **Figure 2-16**, the solar radiation has been absorbed and scattered by O<sub>3</sub>, O<sub>2</sub>, H<sub>2</sub>O, and CO<sub>2</sub> as well as air molecules and dust in the atmosphere. These factors cause significant reduction in the sunlight intensity. As shown in **Figure 2-16**, sunlight intensity is reduced in the atmosphere, however lots of photons still reach the surface of the Earth at around 0.5 μm. Therefore when materials can absorb light at around 0.5 μm, they can capture more of the available photons and convert them to current.

The term Air Mass (AM) refers to the direct path length which the sunlight must pass through the atmosphere on way to reach the Earth's surface when the sun is vertically upwards. The equation of AM is defined as:

$$AM = \frac{1}{\cos\theta} \quad (2.1)$$

The AM relies on the angle of the sun. When  $\theta$  is zero from overhead, AM equals 1. AM 1.5 ( $\theta$  is  $48.2^\circ$  from overhead) and is used as the standard sunlight spectrum for photovoltaic cell testing. In order to achieve a standard test of photovoltaic cells, standard test conditions have been specified. They are a cell temperature of  $25^\circ\text{C}$  and an irradiance of  $1000\text{ W/m}^2$  with an AM 1.5 spectrum. These correspond to the irradiance and spectrum of incident sunlight on a clear day with the sun at an angle of  $41.8^\circ$  above the horizon, which is a reasonable approximation for the average insolation at mid latitudes.

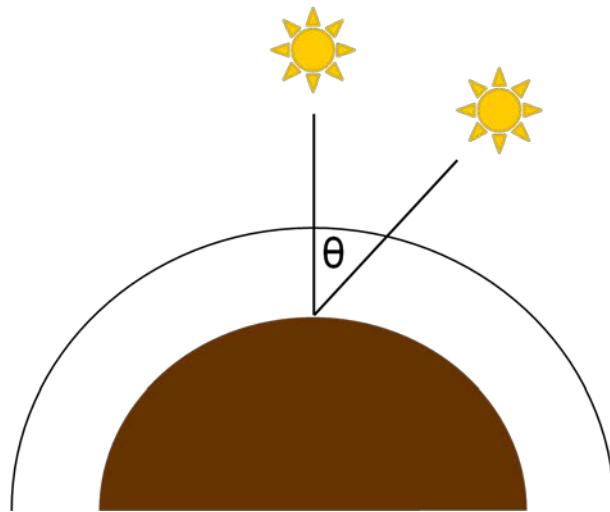


**Figure 2-17** The Air Mass through which radiation must pass before striking the Earth's surface (Wenham et al., 2007).

## 2.3. Theory of I-V characterisation in photovoltaic cells

### 2.3.1. The effect of light

Photovoltaic cells have been designed as a current source and to generate current when they absorb incident light, while photovoltaic cells acts like a diode when they are in the dark (Wenham, 2007, Nelson, 2003). Therefore, photovoltaic cells in the dark can be described using the ideal diode law below (2.2):

$$I = I_0 \left[ \exp\left(\frac{qV}{kT}\right) - 1 \right] \quad (2.2)$$

Where  $I$  is current,  $I_0$  is the saturation current (leakage current of the diode when there is no light),  $V$  is measured voltage,  $q$  is electric charge ( $1.6 \times 10^{-19}$

Coulombs),  $k$  is Boltzmann constant ( $1.38 \times 10^{-23}$  J/K), and  $T$  is the temperature in Kelvin. **Figure 2-18** shows I-V curve of photovoltaic cells as a diode in dark.

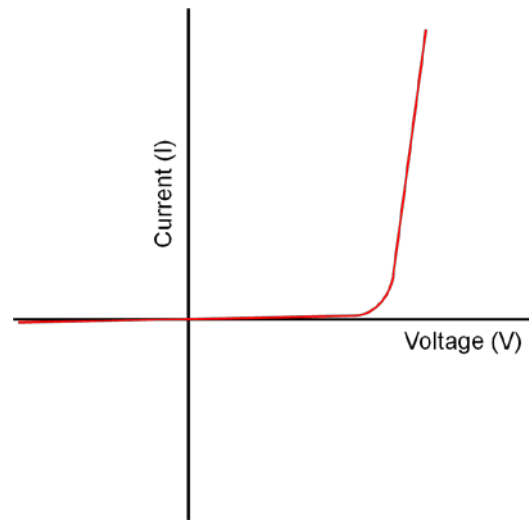


**Figure 2-18** The I-V curve of photovoltaic cells in dark.

However, when photovoltaic cells absorb the incident light, the light effect is added to the diode law. According to the equation (2.3):

$$I = I_0 \left[ \exp\left(\frac{qV}{nkT}\right) - 1 \right] - I_L \quad (2.3)$$

Where  $I_L$  is light generated current, and  $n$  is ideal factor ( $1 < n < 2$ ). As showing **Figure 2-19**, absorbed light shifts the I-V curve down into fourth quadrant.

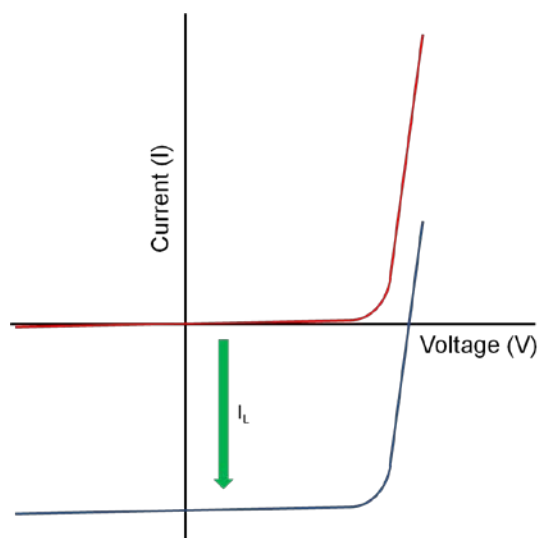


**Figure 2-19** The I-V curve of photovoltaic cells toward effect of incident light.

### 2.3.2. Short circuit current ( $I_{SC}$ ) and open circuit voltage ( $V_{OC}$ )

The equation (2.3) for the I-V curve in light can be re-defined so the direction of current flow is opposite such that the current produced is positive rather than negative and it can be written in first quadrant as shown below in equation (2.4):

$$I = I_L - I_0 \left[ \exp\left(\frac{qV}{nkT}\right) - 1 \right] \quad (2.4)$$

According to the equation (2.4), **Figure 2-20** shows I-V curve in first quadrant and  $I_{SC}$  and  $V_{OC}$  are described in the section below.

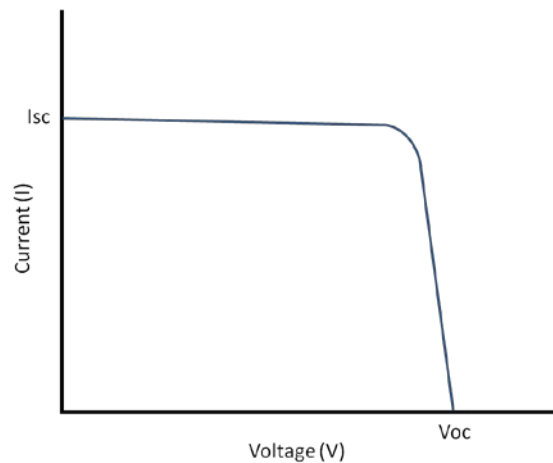


**Figure 2-20** The I-V curve of photovoltaic cells in light (first quadrant).

The short circuit current ( $I_{SC}$ ) is defined as the maximum current when the voltage across the photovoltaic cell equals 0. For an ideal cell, current value ( $I_{SC}$ ) equals  $I_L$  when  $V=0$ .  $I_{SC}$  value relates to the number of photons captured as the area of the photovoltaic cell is increased. To reduce any effects due to different the cell areas and allow comparison between cells, short circuit current density ( $J_{SC} = I_{SC}/\text{area}$  (mA/cm<sup>2</sup>)) is more useful than  $I_{SC}$ .

The open circuit voltage ( $V_{OC}$ ) is defined as the maximum voltage on a cell when no current flows.  $V_{OC}$  corresponds to the amount of voltage across the solar cell when no current is flowing in the solar cell in sunlight.  $V_{OC}$  is determined by the difference between the HOMO of the donor and LUMO of the acceptor components (Brabec et al., 2001).

### 2.3.3. Maximum power ( $P_{mp}$ ), maximum current ( $I_{mp}$ ), and maximum voltage ( $V_{mp}$ )

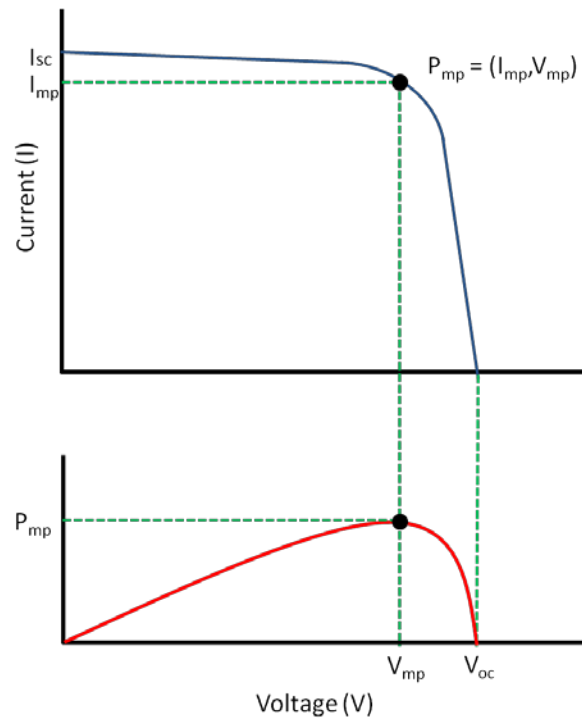


**Figure 2-21** Maximum power in I-V curve of photovoltaic cells.

The power of the photovoltaic cells is characterised by the equation  $P = IV$ . The maximum power point is shown in **Figure 2-21**. According to the equation, the theoretical maximum power ( $P_{mp}$ ) is the product of  $I_{sc}$  and  $V_{oc}$  when they have ideal conditions but it is not realistic due to resistivity in the devices. However, maximum power is generally the multiplication of some value for  $V_{mp}$  between zero and  $V_{oc}$  on the V-axis and another for  $I_{mp}$  between zero and  $I_{sc}$  on the I-axis. The maximum value of current and voltage at the  $P_{mp}$  are represented as  $V_{mp}$  and  $I_{mp}$  respectively.

### 2.3.4. Fill factor

The quality of the solar cell is evaluated by fill factor (FF). FF is the ratio of maximum power output ( $I_{mp}$ ,  $V_{mp}$  green rectangle) to theoretical power output ( $I_{sc}$ ,  $V_{oc}$  pink rectangle). The equation (2.5) and area of ratio are depicted below:

$$FF = \frac{P_{mp}}{P_T} = \frac{I_{mp}V_{mp}}{I_{sc}V_{oc}} \quad (2.5)$$

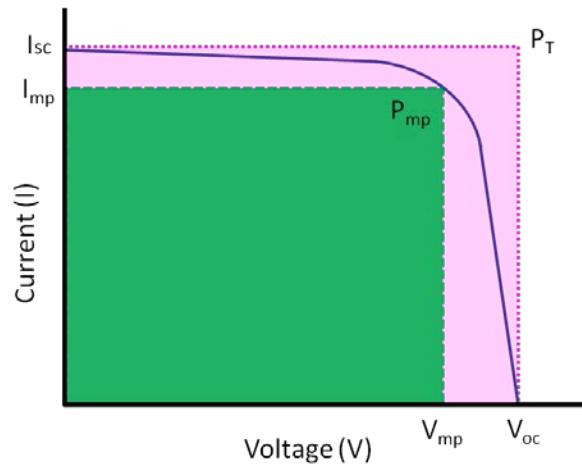


**Figure 2-22** The areas for calculation of FF (FF is the green region over pink region).

The quality of solar cells develops when FF is closer to 1.

### 2.3.5. The effects of parasitic (series and shunt) resistances

In general solar cells have parasitic resistances known as series ( $R_s$ ) and shunt ( $R_{sh}$ ). A simplified equivalent circuit for a photovoltaic cell is described in **Figure 2-23** and also the equation included resistances is shown below (2.6).

$$I = I_L - I_0 \left[ \exp \left( \frac{V + IR_s}{(nkT/q)} \right) - 1 \right] - \frac{V + IR_s}{R_{sh}} \quad (2.6)$$

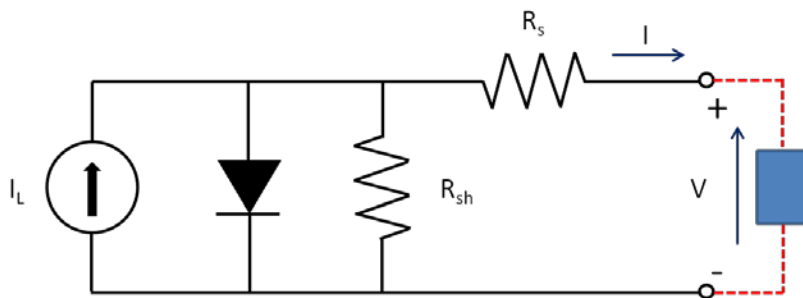


**Figure 2-23** Simplified equivalent circuit of a photovoltaic cell.

These two resistances cause reduction of the FF and the efficiency of solar cells. The main reason of series resistance is from bulk resistance which is from resistive contacts, carrier mobility through front surface to the contacts, and the resistance of semiconductor to metal current flow. The effect of series resistance is illustrated in **Figure 2-24**. According to the **Figure 2-24** and equation  $\Delta V = IR_s$ , medium  $R_s$  makes  $V$  is decreased, while large  $R_s$  causes  $I_{SC}$  to fall down.

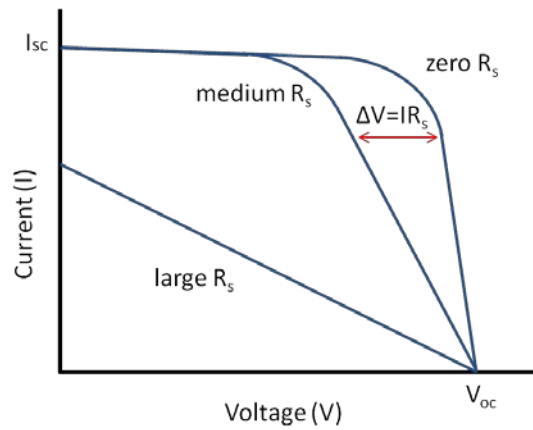


**Figure 2-24** The I-V curve from the effect of series resistance.

The main causes of shunt resistance are due to leakage across the p-n junction and impurities in the junction region like the edge of the cell. The effect of shunt resistance is shown by **Figure 2-25**. In **Figure 2-25**, if  $R_{sh}$  is largely decreased,  $V_{oc}$  will decline.

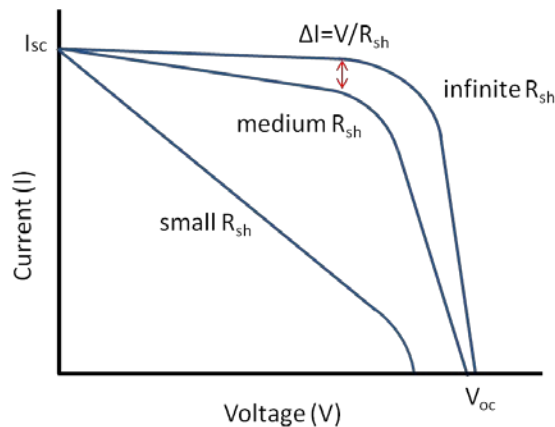


**Figure 2-25** The I-V curve from the effect of shunt resistance.

### 2.3.6. Power conversion efficiency (PCE, $\eta$ ) of photovoltaic cells

The PCE of photovoltaic cell is the ratio of power output from the solar cell to power input from the sun. The efficiency is considerably influenced by the spectrum and intensity of the sunlight and temperature. Therefore, the performance of solar cells must be measured in same condition to compare to other cells. The photovoltaic cells on the Earth are measured under AM 1.5 conditions (light output from solar simulator is  $100 \text{ mW/cm}^2$ ) and at  $25^\circ\text{C}$ . The equation of efficiency is defined as (2.7):

$$\eta = \frac{P_{\text{out}}}{P_{\text{in}}} \cong \frac{P_{\text{max}}}{P_{\text{in}}} = \frac{V_{\text{oc}} I_{\text{sc}} FF}{P_{\text{in}}} \quad (2.7)$$

Where,  $P_{\text{out}}$  is  $P_{\text{max}}$  when the cell can be worked up to its maximum power output to get maximum efficiency. In this section, general principles of which apply to all photovoltaic cells have been explained so far, but in the next section, the operation mechanism of BHJ in OPVCs and PPVCs will be explained because these are the device types used for this project.

## 2.4. Organic bulk-heterojunction (BHJ) photovoltaic cells

### 2.4.1. The operation of organic BHJ photovoltaic cells

A solar cell or photovoltaic cell is a device which absorbs light and then converts the energy from light to electricity by charge separation and transport (Thompson and Frechet, 2008a). Absorbed light generates excitons (bound state of an electron and an electron hole) that can dissociate to form electrons and holes. The electrons from the highest occupied molecular orbital (HOMO, valence band) are excited to the lowest unoccupied molecular orbital (LUMO, conduction band) and quickly relax upon illumination in the active layer. In order to generate a photocurrent the electrons and holes need to be separated from the active layer and transferred to the front contact and rear contact (e.g. metal layer and ITO layer), along percolating pathways, respectively. **Figure 2-26** shows the band structure of organic BHJ cells. A BHJ active layer has an interpenetrating nanostructure of donor and acceptor materials and this means that electrons and holes are easily dissociated.

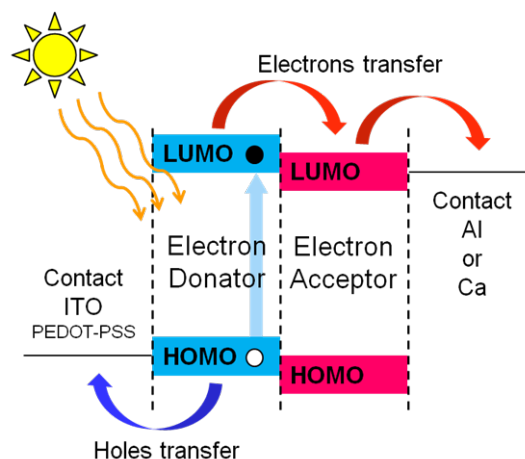


**Figure 2-26** The energy structure of an organic bulk-heterojunction cells.

## 2.4.2. How BHJ photovoltaic cells work

To date, OPVCs have shown lower PCE than that of IPVCs. Therefore, increasing PCE of OPVCs is an important issue to achieve effective conversion of solar energy into electricity and to replace IPVCs in industry, and also to improve their environmental sustainability. Bulk-heterojunction (BHJ) solar cells based on conjugated polymer are a promising technology to improve PCE of OPVCs.

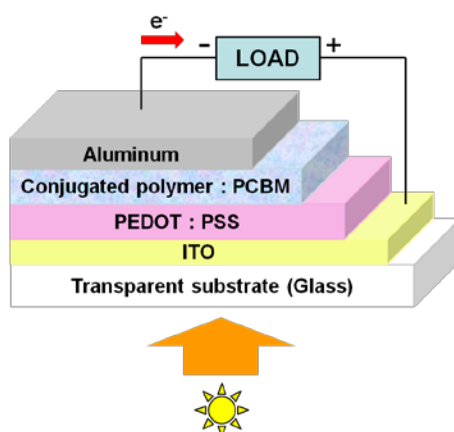


**Figure 2-27** The architecture of bulk-heterojunction photovoltaic cell.

The active layers in BHJ solar cells consist of mixtures of a polymer donor and acceptor. The two components in the active layer of a BHJ form an interpenetrating network which provides nanostructure and offers a large interfacial area for efficient exciton dissociation. This nanostructure of BHJ is important because exciton diffusion lengths of organic polymers are only a few nanometres (Tamai et al., 2015). The active layer polymer absorbs the incident light and then electrons are excited to conduction band then dissociated electrons move to metal cathode through PCBM; and holes move to ITO through PEDOT:PSS. PEDOT:PSS gives photovoltaic cells positive effects that PEDOT:PSS block the electron from active layer to ITO because it has higher LUMO level than materials in active layer and improve smoothness of the ITO contact (Arias et al., 1999, Kim et al., 2009). Conjugated polymers (Liang et al., 2010), oligomers (Sun et al., 2012b) and monomers (Sun et al., 2012a) can be applied as donors, in terms of acceptors, fullerene derivatives are most commonly employed. Fullerene is the best acceptor group so far as it is known to have a high electron affinity and ability to transport charges. The typical structure of BHJ solar cells is illustrated in **Figure 2-27**. The active layer is generally located between PEDOT:PSS and metal layer.

## 2.5. Low band gap polymers

The energy band gap of polymers is defined as the difference between HOMO and LUMO level (**Figure 2-28**). Low band gap polymers are generally defined as a polymer with a band gap less than 2 eV. Organic polymers for PVCs should have suitable energy band matched to that of fullerene which is used as the acceptor of electrons. It needs to have higher LUMO level than fullerene's LUMO level for efficient charge dissociation. In addition, polymers should absorb the whole visible spectrum and into near IR area, and retain high extinction coefficients (Bundgaard and Krebs, 2007).

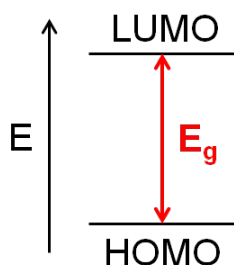


**Figure 2-28** Definition of (low) band gap.

**Figure 2-29** shows the effect of band gap (Nelson, 2003). Nelson suggested optimum band gap for solar cells.

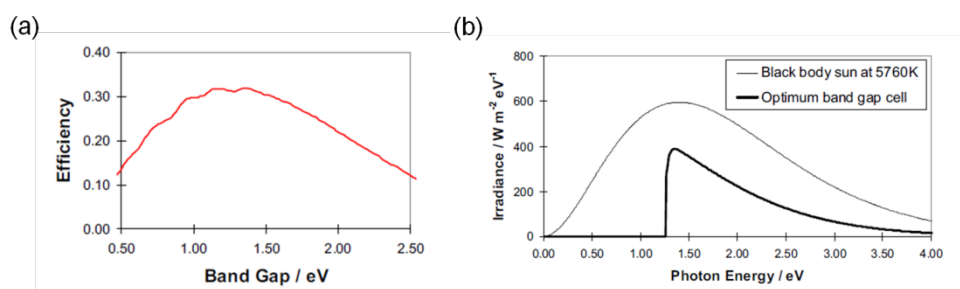


**Figure 2-29** The graph of (a) calculated limiting efficiency for a single band gap solar cell in AM 1.5, (b) power spectrum of a black body sun at 5760 K, and power available to the optimum band gap (Nelson, 2003). (This figure has got permission for use by World Scientific. Figure 2.8 and 2.9 'The Physics of Solar Cells', Jenny Nelson, Copyright @ 2003 by Imperial College Press).

According to **Figure 2-29(a)**, very small and very large band gaps will cause a reduction of efficiency. When the band gap is very small, it leads to small value of  $V$  ( $V_{OC}$  is always less than  $E_g$ ), and the band gap is very large, it causes a

photocurrent that is very small. The calculated S-Q limit on efficiency is around 33% when the band gap is around 1.4 eV. In **Figure 2-29(b)**, if a photon's energy is lower than the energy gap, it cannot contribute to generation of excitons because the photons cannot be absorbed by the active layer. If photon's energy is larger than energy gap, it can be absorbed but only  $\Delta\mu/E$  is available power.

In order to demonstrate why low band gap polymers are needed, E. Bundgaard (Bundgaard and Krebs, 2007) shows **Figure 2-30** and **Table 2-1** which include maximum integrated photon flux, current density and possibility to harvest photons with wavelength over 280 nm within solar cells. In **Figure 2-30**, black line shows the photon flux and red line shows the percentage of integrated photon flux and integrated current.

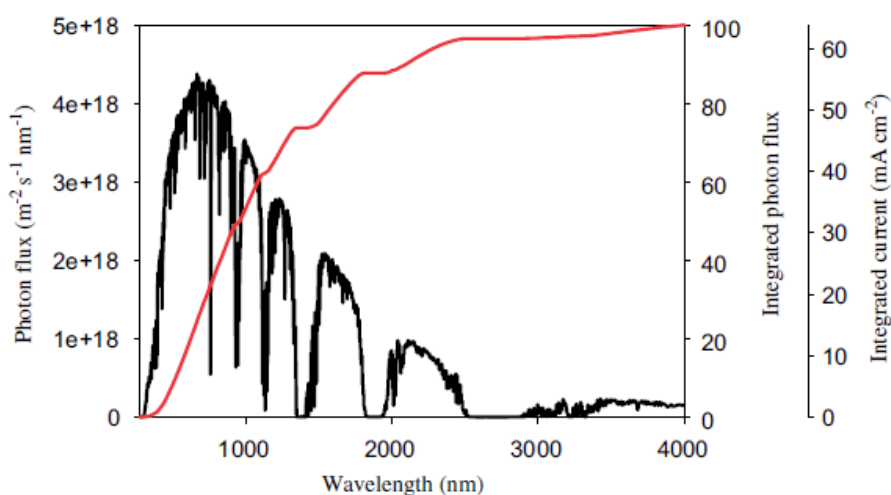


**Figure 2-30** Photon flux (black line) from the sun (AM 1.5) and the integral of the curve (red line) refers to the total number of photons and obtainable current density (Bundgaard and Krebs, 2007). (This figure has got permission for use by Elsevier. Figure 2 ‘Low band gap polymers for organic photovoltaics’, Eva Bundgaard, Frederik C. Krebs, Copyright @ 2007 by Elsevier.)

The data is summarised in **Table 2-2**. According to the table and figure, the polymer having 1.9 eV band gap (about 650 nm) is able to harvest only 22.4% photon flux and it has 14.3 mA/cm<sup>2</sup> current density. Therefore, low band gap polymers of 1.3-1.8 eV (650 nm to 1000 nm) are expected to harvest more photons and to have higher efficiencies.

**Table 2-2** The integrated maximum harvest and current density available of each wavelength for solar cells assumed that every photon is changed to one electron in the external circuit (Bundgaard and Krebs, 2007)

<b>Wavelength</b>	<b>Max % harvested</b>	<b>Current density</b>
<b>(nm)</b>	<b>( from 280 nm)</b>	<b>(mA/cm<sup>2</sup>)</b>
500	8.0	5.1
600	17.3	11.1
650	22.4	14.3
700	27.6	17.6
750	35.6	20.8
800	37.3	23.8
900	46.7	29.8
1000	53.0	33.9
1250	68.7	43.9
1500	75.0	47.9

Scharber et al. reported a calculation of the optimum band gap for BHJ solar cells using conjugated polymer with fullerene (Scharber et al., 2006). The ideal band gap of conjugated polymer is considered 1.3-1.8 eV for polymer-fullerene BHJ photovoltaic cells to achieve over 10% of PCE and the highest PCEs of OPVCs were approached by 1.5 eV of band gap of conjugated polymer in the report. In addition, organic conducting materials (donor) need electron acceptor compare to inorganic materials such as Si or Ge in order to increase charge carrier dissociation because quantum efficiency for charge generation in organic conducting materials is low (typically 1%). The sufficient energy difference between donor's LUMO and acceptor's LUMO is 0.3 eV (Bredas et al., 2004, Scharber et al., 2006).

Mismatch of absorption spectra will cause a reduction of exciton generation. To achieve high efficiency solar cells based on organic polymers, a low band gap

polymer, which absorbs in the long wavelength area and has a good match with high density photon area, is necessary. Many researchers have reported organic BHJ photovoltaic cells using various kinds of conjugated polymer. The structures of low band gap polymers are described later in section 3.2.2.

## 2.6. Perovskite photovoltaic cells

Perovskite when applied in photovoltaic cells has been a remarkable material and is of huge interest to the researchers due to rapid growth of their PCE. According to the NREL solar cell efficiency table (**Figure 1-1**), PCE of perovskite photovoltaic cells (PPVCs) has sharply increased from 2009 to 2015. It is very fast growth compared to other PVCs. In addition, PPVCs still have potential for further research because perovskites can be applied to various types of PVCs, such as dye-sensitised PVC and planar PVC, and fabrication and operation methods of PPVCs are still being developed.

### 2.6.1. Formation of perovskite

Three dimensional organic-inorganic hybrid perovskite (OIHP) are described by the formula  $ABX_3$ . A is a monovalent large cation (e.g. methylammonium (MA)) coordinated to 12 X anions (Mitzi, 1999, Liang et al., 1998, Baikie et al., 2013). B is a divalent metal halide cation (e.g. Pb, Sn, Ge) satisfying charge balancing and bonded to six X anions as  $BX_6$ . The  $BX_6$  adopts octahedral anion coordination, where X is a halogen (e.g. Br, I or Cl) (Mitzi, 1999, Liang et al., 1998). The inorganic layers form sheets of corner-sharing metal halide octahedron for full coordination.

**Figure 2-31** shows general procedure of forming perovskite crystals from perovskite precursors. As above mentioned, when the OIHP crystal crystallises in space the  $Pb^{2+}$  ion is coordinated with six surrounding halides and adopts the distorted octahedral coordination.  $PbX_6$  octahedra form the face or corner-sharing  $PbI_6$  octahedral chain and the organic cations are aligned into  $PbX_6$  octahedral chain (Manser et al., 2016, Yan et al., 2015, Gao et al., 2013).

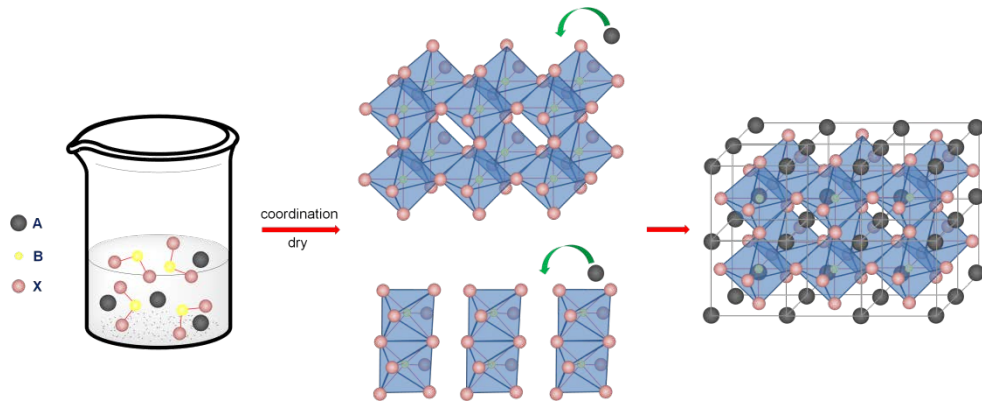


**Figure 2-31** The schematic illustration of forming perovskite from perovskite precursor.

## 2.6.2. How perovskite photovoltaic cells work

The perovskite is able to work as an active layer and it is easily merged into a standard OPVC structure. The PPVCs have generally two types of structure sensitised perovskite photovoltaic cell and planar perovskite photovoltaic cell.

The active layer in sensitised perovskite photovoltaic cells is composed of perovskite and mesoporous  $\text{TiO}_2$ . **Figure 2-32** shows architecture of sensitised perovskite PVC. Perovskite is coated onto the mesoporous  $\text{TiO}_2$ . The perovskite absorbs the incident light and then electrons and holes easily dissociate due to low exciton binding energy (Tanaka et al., 2003). Free electrons move to anode (FTO) through mesoporous and compact  $\text{TiO}_2$  layers. Free holes move to cathode (Au) through hole transporting material (Spiro-MeOTAD).

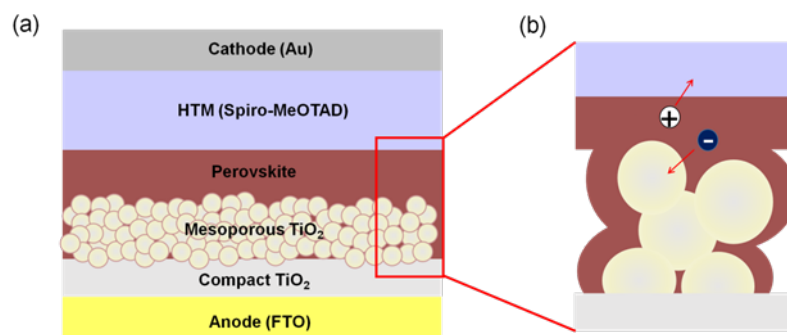


**Figure 2-32** (a) The architecture of sensitised perovskite photovoltaic cell and (b) magnification of rectangle area.

In planar perovskite photovoltaic cell, perovskite is used as donor in the active layer. The architecture of planar perovskite photovoltaic cell is illustrated in **Figure 2-33**. The architecture of planar perovskite photovoltaic cell is ITO/hole

transporting layer (PEDOT:PSS)/perovskite/electron transporting layer (PCBM)/electrode (Al). The active layer of planar perovskite photovoltaic cell has two layers contrast to organic BHJ photovoltaic cells. Perovskite does not need to form a BHJ because the exciton binding energy is much lower (about 35-150 meV) than that of conjugated polymer (Tanaka et al., 2003, Alvarado et al., 1998) and that results in a higher diffusion length (0.27-1.7  $\mu\text{m}$  of electrons and 0.46-6.3  $\mu\text{m}$  of holes) compared to that of conjugated polymer (few nanometres) (Tamai et al., 2015). The free electrons move to the cathode (Al) through the electron transporting layer (PCBM) and the free holes move to the anode (ITO) through hole transporting layer (PEDOT:PSS).

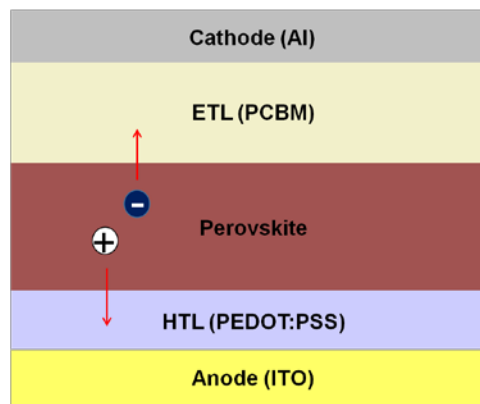


**Figure 2-33** The architecture of planar perovskite photovoltaic cell.

## 2.7. References

- ALVARADO, S. F., SEIDLER, P. F., LIDZEY, D. G. & BRADLEY, D. D. C. 1998. Direct determination of the exciton binding energy of conjugated polymers using a scanning tunneling microscope. *Physical Review Letters*, 81, 1082-1085.
- ARIAS, A. C., GRANSTROM, M., THOMAS, D. S., PETRITSCH, K. & FRIEND, R. H. 1999. Doped conducting-polymer-semiconducting-polymer interfaces: Their use in organic photovoltaic devices. *Physical Review B*, 60, 1854-1860.
- BRABEC, C. J., CRAVINO, A., MEISSNER, D., SARICIFTCI, N. S., FROMHERZ, T., RISPENS, M. T., SANCHEZ, L. & HUMMELEN, J. C. 2001. Origin of the open circuit voltage of plastic solar cells. *Advanced Functional Materials*, 11, 374-380.

- BREDAS, J. L., BELJONNE, D., COROPCEANU, V. & CORNIL, J. 2004. Charge-transfer and energy-transfer processes in pi-conjugated oligomers and polymers: A molecular picture. *Chemical Reviews*, 104, 4971-5003.
- BUNDGAARD, E. & KREBS, F. C. 2007. Low band gap polymers for organic photovoltaics. *Solar Energy Materials and Solar Cells*, 91, 954-985.
- CLAYDEN, J., GREEVES, N. & WARREN, S. G. 2012. *Organic chemistry*, Oxford, Oxford University Press.
- ERDMANN, H. 1888. Die Constitution der isomeren Naphtalinderivate. I. Die  $\alpha$ - $\alpha$ -disubstituirten Verbindungen. *Justus Liebigs Annalen der Chemie*, 247, 306-366.
- GAO, H., YUAN, G. J., LU, Y. N., ZHAO, S. P. & REN, X. M. 2013. Inorganic-organic hybrid compound with face-sharing iodoplumbate chains showing novel dielectric relaxation. *Inorganic Chemistry Communications*, 32, 18-21.
- JIANG, X. Z., LIU, S., MA, H. & JEN, A. K. Y. 2000. High-performance blue light-emitting diode based on a binaphthyl-containing polyfluorene. *Applied Physics Letters*, 76, 1813-1815.
- KEKUI, A. 1866. Untersuchungen über aromatische Verbindungen Ueber die Constitution der aromatischen Verbindungen. I. Ueber die Constitution der aromatischen Verbindungen. *Justus Liebigs Annalen der Chemie*, 137, 129-196.
- KEKUL, A. 1872. Ueber einige Condensationsproducte des Aldehyds. *Justus Liebigs Annalen der Chemie*, 162, 77-124.
- KIM, Y., BALLANTYNE, A. M., NELSON, J. & BRADLEY, D. D. C. 2009. Effects of thickness and thermal annealing of the PEDOT:PSS layer on the performance of polymer solar cells. *Organic Electronics*, 10, 205-209.
- KLEIN, D. R. A. 2015. *Organic chemistry*, Hoboken, NJ, Wiley.
- LECLERC, M. & MORIN, J.-F. O. 2010. *Design and synthesis of conjugated polymers*, Weinheim, Wiley-VCH.
- LIANG, Y. Y., XU, Z., XIA, J. B., TSAI, S. T., WU, Y., LI, G., RAY, C. & YU, L. P. 2010. For the Bright Future-Bulk Heterojunction Polymer Solar Cells with Power Conversion Efficiency of 7.4%. *Advanced Materials*, 22, E135-+.
- MANSER, J. S., SAIDAMINOV, M. I., CHRISTIANS, J. A., BAKR, O. M. & KAMAT, P. V. 2016. Making and Breaking of Lead Halide Perovskites. *Accounts of Chemical Research*, 49, 330-338.

- MCMURRY, J. 1996. *Organic chemistry*, Pacific Grove, CA ; London, Brooks/Cole.
- MONDAL, S. 2012. Recent Developments in the Synthesis and Application of Sultones. *Chemical Reviews*, 112, 5339-5355.
- NELSON, J. 2003. *The physics of solar cells*, London, Imperial College Press.
- NREL <http://rredc.nrel.gov/solar/spectra/am1.5/ASTMG173/ASTMG173.html>.
- ROGERS, D. W. & MCLAFFER, F. J. 1971. Heats of Hydrogenation - Physical-Organic Laboratory Experiment. *Journal of Chemical Education*, 48, 548-550.
- SCHARBER, M. C., WUHLBACHER, D., KOPPE, M., DENK, P., WALDAUF, C., HEEGER, A. J. & BRABEC, C. L. 2006. Design rules for donors in bulk-heterojunction solar cells - Towards 10 % energy-conversion efficiency. *Advanced Materials*, 18, 789-794.
- SUN, Y., WELCH, G. C., LEONG, W. L., TAKACS, C. J., BAZAN, G. C. & HEEGER, A. J. 2012a. Solution-processed small-molecule solar cells with 6.7% efficiency. *Nat Mater*, 11, 44-8.
- SUN, Y. M., WELCH, G. C., LEONG, W. L., TAKACS, C. J., BAZAN, G. C. & HEEGER, A. J. 2012b. Solution-processed small-molecule solar cells with 6.7% efficiency. *Nature Materials*, 11, 44-48.
- TAMAI, Y., OHKITA, H., BENTEN, H. & ITO, S. 2015. Exciton Diffusion in Conjugated Polymers: From Fundamental Understanding to Improvement in Photovoltaic Conversion Efficiency. *Journal of Physical Chemistry Letters*, 6, 3417-3428.
- TANAKA, K., TAKAHASHI, T., BAN, T., KONDO, T., UCHIDA, K. & MIURA, N. 2003. Comparative study on the excitons in lead-halide-based perovskite-type crystals CH<sub>3</sub>NH<sub>3</sub>PbBr<sub>3</sub>CH<sub>3</sub>NH<sub>3</sub>PbI<sub>3</sub>. *Solid State Communications*, 127, 619-623.
- THOMPSON, B. C. & FRECHET, J. M. 2008. Polymer-fullerene composite solar cells. *Angew Chem Int Ed Engl*, 47, 58-77.
- W. R. HODGKINSON, F. E. M. 1883. XXIII.—Note on some derivatives of fluorene, C<sub>13</sub>H<sub>10</sub>. *Journal of the Chemical Society, Transactions*, 43, 163-172.
- WENHAM, S. R. 2007. *Applied photovoltaics*, London, Earthscan.
- YAN, K. Y., LONG, M. Z., ZHANG, T. K., WEI, Z. H., CHEN, H. N., YANG, S. H. & XU, J. B. 2015. Hybrid Halide Perovskite Solar Cell Precursors: Colloidal Chemistry and Coordination Engineering behind Device

Processing for High Efficiency. *Journal of the American Chemical Society*, 137, 4460-4468.

YOHANNES, T., ZHANG, F., SVENSSON, A., HUMMELEN, J. C.,  
ANDERSSON, M. R. & INGANAS, O. 2004. Polyfluorene copolymer  
based bulk heterojunction solar cells. *Thin Solid Films*, 449, 152-157.

### **3. Literature review**

#### **3.1. Introduction**

The literature on OPVCs and PPVCs is large and rapidly growing. Therefore, the literature in this chapter does not seek to cover all the literature but instead to highlight some of the most relevant to the work carried out in this project. PVCs have been one of the most attractive devices to deal with the problems associated with increasing energy demands and the finite supply of fossil fuel. Sunlight provides natural, green and safe energy at the Earth's surface. Since the first modern p-n junction semiconductor solar cells were developed significantly and inorganic photovoltaic cells (IPVCs) have now achieved efficiencies over 40%. OPVCs show lower PCEs than that of inorganic solar cells. Some OPVCs have improved to about 10% PCE by incorporating a BHJ. However, even if OPVCs have lower PCEs than IPVCs, OPVCs have some advantages such as low cost, light weight, ease of manufacture and mechanical flexibility (Facchetti, 2011, Dennler et al., 2009, Gunes et al., 2007, Shaheen et al., 2005, Yu et al., 1995, Brabec, 2004). These are positive factors for the fabrication of OPVCs. In addition, hybrid organic and inorganic based PPVCs have rapidly developed since 2012. Their fabrication process is also short. This section focuses on BHJ solar cells based on conjugated polymer and conjugated polyelectrolytes and PPVCs.

#### **3.2. Photovoltaic cells via bulk-heterojunction**

Many researchers in the area of OPVCs have studied planar BHJs because of their advantages; the structure of BHJ cells is simple and they are easier to produce than planar PVCs. The active layer in planar PVCs is fabricated by coating several times but for an active layer in BHJs it is deposited all at once. It leads to low-cost fabrication and a reduction of production time. PEDOT:PSS has been typically used as HTL in OPVCs due to improved selectivity of the anode and higher work function relative to ITO. The active layer in OPVC typically consists of a blend of donor (e.g. conjugated polymer) and acceptor (e.g. fullerene) materials. Upon drying from the processing solution during fabrication the donor and acceptor materials undergo self-organised phase separation and form a BHJ nanostructure

which efficiently provides electrons and holes transportation. A lot of conjugated polymers have been used for OPVC and they are still being studied by many research teams because it is easy to change polymer structure and attach additive groups. In addition, even if the polymer structures are not changed, better results in PVC performance can be achieved by optimising processing conditions. To date, many researchers have reported various kinds of solar cells based on P3HT (Al-Ibrahim et al., 2005), poly[N-9''-hepta-decanyl-2,7-carbazole-alt-5,5-(4',7'-di-2-thienyl-2',1',3'-benzothiadiazole)] (PCDTBT) (Moon et al., 2012), and many other polymers (Liang et al., 2010, Zhang et al., 2006).

### **3.2.1. PEDOT:PSS for HTL in OPVCs**

Use of PEDOT:PSS as HTL in OPVC is apparently a benefit to achieve high efficiency, but specific properties of the ideal PEDOT:PSS layer have not yet been fixed (e.g. thickness, morphology, and conductivity). The thickness, and thermal annealing process of PEDOT:PSS has been reported by many researchers. Kim et al. reported PEDOT:PSS characteristics under various condition in the P3HT:PCBM PVC. In order for thickness dependence, they applied thickness of PEDOT:PSS varied from 0 (ITO only) to 165 nm and non-annealed (Kim et al., 2009). For the annealing temperature dependence, PEDOT:PSS films were non-annealed and annealed from 75 to 230 °C. According to the report, the performance of P3HT:PCBM devices was not strongly sensitive to film thickness of PEDOT:PSS (from 60 to 165 nm) apart from 0 nm (ITO only). While the conductivity of PEDOT:PSS increased when annealing temperature above 100 °C, but decreased as annealing temperature increased above 200 °C. According to the author, the change of conductivity is likely related to change of oxidation state in the polymer. The best annealing temperature between 100 and 200 °C was attributed to an increase of oxidation state but at temperatures above 200 °C over oxidation and degradation of the film occurs.

Dimitriev et al. reported an effect of organic solvent additive to PEDOT:PSS with thermal annealed films and effect of solvent vapour exposure (Dimitriev et al., 2009). They introduced ethylene glycol (EG) or dimethyl sulfoxide (DMSO) to PEDOT:PSS films in two ways. It was added directly to the PEDOT:PSS dispersion from which the film was cast or by exposure to the casted PEDOT:PSS film to the solvent vapours in a closed vessel. Their results showed that the conductivity of both pristine PEDOT:PSS and solvent added PEDOT:PSS films

which was prepared with organic solvent addition to the dispersion of polymer decreased as annealing temperature was increased. When the PEDOT:PSS film exposed to DMSO vapour, the conductivity of film was increased and it was easily controlled by exposure time to vapour.

The two literature reports above showed different conductivity behaviour upon thermal annealing. One showed that the conductivity of PEDOT:PSS film increased as annealing temperature increase above 100 °C but another showed a decrease in conductivity of PEDOT:PSS film as annealing temperature increase. However both these two literature reports showed low conductivity around 200 °C.

### **3.3. Use of conjugated polymer for BHJ photovoltaic cells**

Since the invention of conductive polyacetylene by Giulio Natta in 1958 (Ikeda, 1971), organic conjugated monomers and polymers have been recognised as an attractive class of novel conducting materials which has useful electrical and optical properties, in addition, to solution processing advantages. As demonstrated for the last few decades, conjugated polymers have attracted much attention due to their thermal stability, low cost, strong emission properties (Grimsdale et al., 2009, Hadziioannou and Hutten, 2000) and they have been utilised as the active materials in organic light emitting diodes (Gross et al., 2000), organic field effect transistor (Li et al., 2006), chemical sensors (Na et al., 2004), and organic photovoltaic cells (Yu et al., 1995). The main character of conjugated polymers is conductivity because of the conjugation system which has p-orbitals with alternating single and multiple bonds in the material's backbone. This character means that the conjugated polymers are stable, having fluorescence and use in electronic applications. In particular, the fluorescence emission is determined by the energy levels of conjugated polymers and as such can be tuned by changing various polymer main chains, and side groups with varying  $\pi$ -conjugation length, inter- or intramolecular charge transfer between electron donors and acceptors. This flexible character is a huge advantage as it allows the chemist within certain limits to design the polymers to have the properties desired.

### 3.3.1 Poly(3-hexylthiophene) based photovoltaic cells

Poly-thiophene (PT) has attracted attention since the 1980s because it is one of the most versatile, important types of  $\pi$ -conjugated polymer and organic electronic material due to its facile synthesis, processability, and charge carrier transport properties. T. Yamamoto et al. published a synthesis process of PT via Grignard cross-coupling (Yamamoto et al., 1980). The Grignard cross-coupling is a reaction using organomagnesium halides. They synthesised a regularly repeating polymer which had high regio-regularities and showed high electric conductivity when it has doped with iodine. However, it showed poor solubility in organic solvents. In order to improve solubility, an alkyl group was attached to the 3-position. Elsenbaumer et al. synthesised two series of soluble poly(3-alkylthiophene), poly(3-butylthiophene) and poly(3-methylthiophene) based copolymers, via Grignard cross-coupling (Elsenbaumer et al., 1986). After regioregular P3HT (band gap of 1.9 eV) was invented in the 1990s (Chen and Rieke, 1992), it has been used as the semiconducting material due to its large hole mobility ( $\sim 10^{-4} - 10^{-3} \text{ cm}^2 \text{ V}^{-1} \text{ s}^{-1}$ ) (C. Tanase, 2003).

Li et al. reported PVCs showing 4.4% efficiency (Li et al., 2005). They introduced thermally annealed devices, annealing at 110 °C. They dealt with four different annealing times 0, 10, 20 and 30 min. The best result was from the 10 min annealed device. The  $J_{\text{SC}}$  was slightly increased from 9.9 to 10.6  $\text{ mA/cm}^2$  and FF was changed from 60.3 to 67.4% which was the highest FF at that time. The annealing was also effective in reducing resistance from 2.41 to 1.56  $\Omega \text{ cm}^2$ . Ma et al. also suggested thermally annealed photovoltaic cells (Ma et al., 2005). They compared with three different conditions. The solar cell without annealing showed  $V_{\text{OC}}$  of 0.6 V,  $J_{\text{SC}}$  of 3.83  $\text{ mA/cm}^2$ , FF of 30% and PCE of 0.82%, while annealed solar cells at 150 °C for 30 min exhibited PCE of 5.1%,  $J_{\text{SC}}$  of 9.5  $\text{ mA/cm}^2$ , and FF of 68%. Almost all factors were improved, while  $V_{\text{OC}}$  remained at 0.63 V. Pearson et al. reported P3HT:PCBM PVC with different thermal annealing temperature and blend ratio of active layer (Pearson et al., 2012). They demonstrated two distinct compositional amorphous phases exist and proper annealing temperature to improve the PCE of OPVCs. According to the report, they suggested 40% concentration of PCBM in active layer showed the best PCE of 3.4% at 140 °C annealed temperature. However, the devices with lower and higher PCBM concentration than 40% in active layer appeared PCE of 0.2-2.5%. The good PCEs of devices with annealing temperature were shown at 130-150 °C. Even if the

components of the active layer were not changed, they revealed a good PCE via thermal annealing.

Some researchers reported different buffer layers instead of PEDOT:PSS. Irwin et al. introduced NiO, a cubic wide band gap semiconductor, which facilitates hole conduction (Irwin et al., 2008). The best PCE was 5.2% from 10 nm thickness of NiO buffer layer. It had  $J_{SC}$  of 11.3 mA/cm<sup>2</sup> and FF of 69.3%. Compared to the NiO buffer layer, a PEDOT:PSS buffer layer (40 nm thickness) solar cell resulted in a  $J_{SC}$  of 9.54 mA/cm<sup>2</sup>, FF of 40.4% and PCE of 2.40%. Most P3HT:PCBM solar cells have  $V_{OC}$  of 0.6 V. It is the main reason that P3HT:PCBM solar cells showed low efficiencies, although it had good hole mobility.

In order to improve  $V_{OC}$ , Zhao et al. reported P3HT donor with indene-C<sub>60</sub> bisadduct (ICBA) acceptor based solar cells (Zhao et al., 2010). The LUMO level was raised by ICBA (-3.74 eV) which was 0.17 eV higher than LUMO level of PCBM (-3.91 eV). As a result,  $V_{OC}$  of P3HT:ICBA solar cell increased from 0.6 to 0.84 V. They also tried to optimise the devices. The best result solar cell was blend ratio of P3HT:ICBA of 1:1 with pre-baking at 150 °C for 10 min. It was attained the PCE as high as 6.48% with  $V_{OC}$  of 0.84 V,  $J_{SC}$  of 10.61 mA/cm<sup>2</sup>, and FF of 72.7%. All of this result was the highest values suggested in the literatures by 2010 for P3HT based solar cells. **Figure 3-1** shows the structures of P3HT, PCBM and ICBA.

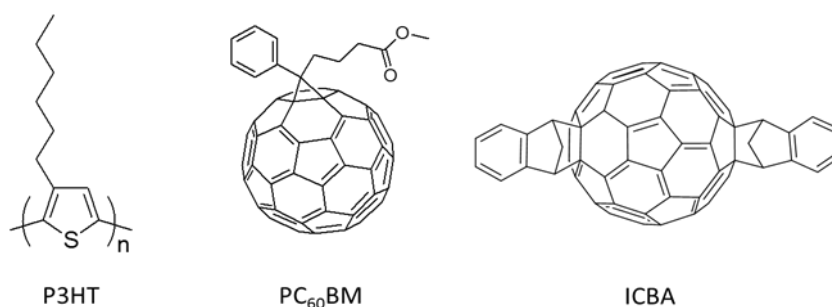


**Figure 3-1** The structures of P3HT, PC<sub>60</sub>BM, and ICBA

### 3.3.2. Low band gap polymer based photovoltaic cells

In order to synthesise low band gap polymers, many researchers introduced donor-acceptor parts in a polymer. Low band gap polymers are expected to harvest more photons (see **Figure 2-28** in **Chapter 2**). The inclusion of donor-acceptor groups

leads to electron delocalization over the polymer chain. The HOMO level of the donor and the acceptor build up two new HOMO levels and also the LUMO level of the donor and the acceptor form two new LUMO levels (Cheng et al., 2009). This facilitates control over the energy band gaps. The typical donating (electron-rich) groups are dithiophene (Wienk et al., 2008), cyclopentadithiophene (Li et al., 2011), carbazole (Park et al., 2009), dibenzosilole (Boudreault et al., 2007), dithienosilole (Hou et al., 2008), and dialkoxybenzodithiophene (Cabanetos et al., 2013). The typical accepting groups are benzothiadiazole (Wang et al., 2011), quinoxaline (Gadisa et al., 2007), thieno[3,4-c]pyrrole-4,6-dione (Zou et al., 2010), and diketo-pyrrolopyrrole (Bijleveld et al., 2009). **Figure 3-2** shows the donors and acceptors.

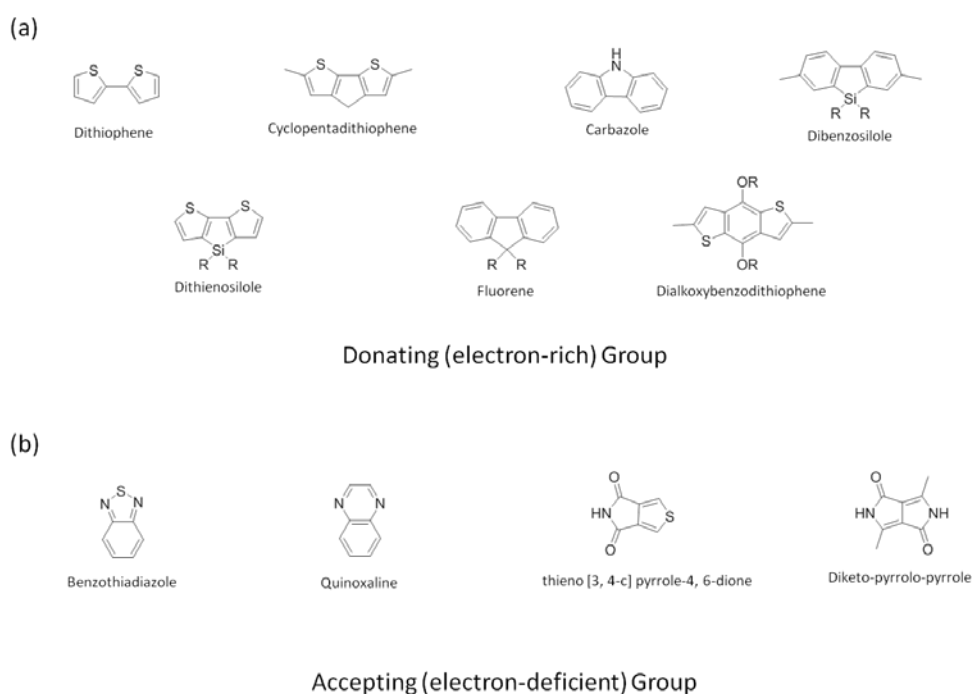


**Figure 3-2** Structures of (a) donors (electron-rich) and (b) acceptors (electron-deficient).

Bijleveld et al. reported conjugated polymer (P1 in **Figure 3-3**) based on dithiophene with diketo-pyrrolopyrrole (DPP) in 2009 (Bijleveld et al., 2009). P1 was synthesised via a Suzuki-cross coupling ( $M_n = 54$  kDa). The Suzuki-cross coupling is reaction in which the coupling partners are aryl- or vinyl- boronic acid with aryl- or vinyl- halide by catalyst palladium(0) which oxidation state is 0. The HOMO and LUMO levels were measured at  $-5.17$  eV and  $-3.61$  eV (energy band gap showed  $1.56$  eV in a thin film), respectively. In application to solar cells with PC<sub>71</sub>BM, the PCE showed 4.7% and it had  $V_{OC}$  of 0.65 V,  $J_{SC}$  of  $11.8$  mA/cm<sup>2</sup>, and FF of 60%. Woo et al. also suggested DPP based polymer (P2 in **Figure 3-3**) (Woo

et al., 2010). P1 incorporated dithiophene, whereas P2 introduced thiophenyl-furan instead. P2 was measured and showed an energy band gap of 1.41 eV in a film (HOMO of  $-5.4$  eV and LUMO of  $-3.8$  eV vs vacuum). The PCE of P2 achieved was up to 5.0% when 9% 1-chloronaphthalene (CN) was added in spin-coating process. It achieved  $V_{OC}$  of 0.74 V,  $J_{SC}$  of 11.2 mA/cm<sup>2</sup>, and FF of 60%.

A thieno[3,4-c]pyrrole-4,6-dione based copolymer (P3 in **Figure 3-3**) for solar cells was published by Zou et al. in 2010 (Zou et al., 2010). Thieno-pyrroledione is beneficial for electron delocalisation due to simple, compact, symmetric, and planar structure. The P3 was synthesised by Stille coupling polymerisation. 2-ethylhexyl group and octyl chain was attached to benzodithiophene and thienopyrrole moieties, respectively. It showed a band gap of 1.8 eV in a film. P3 with  $Pc_{71}BM$  solar cells obtained a PCE of 5.5%,  $V_{OC}$  of 0.85 V,  $J_{SC}$  of 9.81 mA/cm<sup>2</sup>, and FF of 66%. Cabanetos et al. also reported benzodithiophene with thienopyrrole copolymer (P4 in **Figure 3-3**) (Cabanetos et al., 2013). In comparison to P3, the side chain of pyrrole moiety in P4 is heptane and CN was added when spin coating. The best result of these series was P4 (PCE of 8.5%) and it had  $V_{OC}$  of 0.97 V,  $J_{SC}$  of 12.6 mA/cm<sup>2</sup>, and FF of 70%.

According to Liang et al., thienothiophene based polymer was reported (Liang et al., 2010, Liang et al., 2009). They suggested 7 polymers and the first 6 polymers were published in 2009, then, the last one was developed in 2010. The best PCE of the 6 polymers was from P5 (specified PTB4 in the paper). P5 has fluorine in thienothiophene. It played an important role to lower the HOMO level due to electron-withdrawing character. P5 has a 1.63 eV band gap and up to 6.10% PCE. It had  $V_{OC}$  of 0.74 V,  $J_{SC}$  of 13.0 mA/cm<sup>2</sup>, and FF of 61.4%. P6 was similar structure with P5, but, 2-ethylhexyl group was introduced to benzodithiophene. The HOMO and LUMO levels of P6 were  $-5.15$  eV and  $-3.31$  eV. The PCE of 7.4% was shown by P6 and it had  $V_{OC}$  of 0.74 V,  $J_{SC}$  of 14.16 mA/cm<sup>2</sup>, and FF of 68.97%. The structures of P1-P6 are illustrated in **Figure 3-3** and the device parameters of six polymers are summarised in **Table 3-1**.

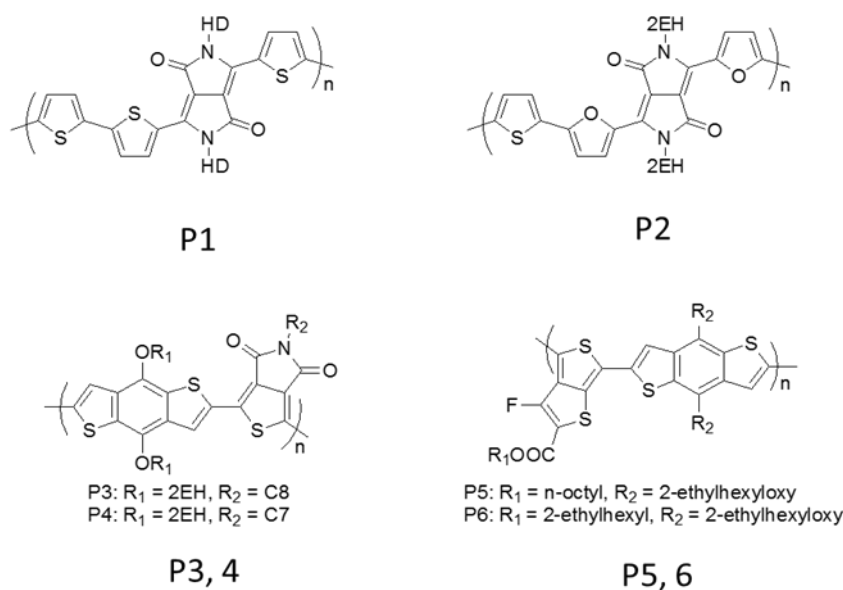


**Figure 3-3** The polymer structures of P1-P6.

**Table 3-1** The device parameters of 6 polymers

Polymers	PCE (%)	V <sub>oc</sub> (V)	J <sub>sc</sub> (mA/cm <sup>2</sup> )	FF (%)
<b>P1</b>	4.7	0.65	11.8	60
<b>P2</b>	5.0	0.74	11.2	60
<b>P3</b>	5.5	0.85	9.81	66
<b>P4</b>	8.5	0.97	12.6	70
<b>P5</b>	6.1	0.74	13.0	61.4
<b>P6</b>	7.4	0.74	14.16	68.97

Zhang et al. reported fluorine based polymers such as a poly[ $\{2,7-(9,9\text{-dialkylfluorene})\}_c\text{-alt-}\{5,5-(4,7\text{-di-}2'\text{-thienyl-}2,1,3\text{-benzothiadiazole})\}$ ] (P7 in **Figure 3-4**) (Zhang et al., 2006). The best performing device recorded PCE of 2.84%, V<sub>OC</sub> of 1.01 V, J<sub>SC</sub> of 6.3 mA/cm<sup>2</sup>, and FF of 44%. Even if P7 showed low efficiency due to low match with solar spectrum, it recorded high V<sub>OC</sub>. They also published work on polyfluorene with quinoxaline (P8 in **Figure 3-4**) (Gadisa et al., 2007). The 5',8'-di-2-thienyl-(2',3'-bis-(3''-octyloxyphenyl)-quinoxaline) moiety was introduced instead of benzothiadiazole. The device fabricated with PC<sub>60</sub>BM recorded a PCE of 3.7%, V<sub>OC</sub> of 1 V, J<sub>SC</sub> of 6 mA/cm<sup>2</sup>, and FF of 63%. P8 has a HOMO level of - 6.3 eV and and LUMO of - 3.6 eV.

Another series of polymers are reported by Muhlbacher et al. They presented cyclopenta-dithiophene and benzothiadiazole based polymer (P9 in **Figure 3-4**) (Muhlbacher et al., 2006). This polymer recorded the band gap of 1.40 eV in the solid state and HOMO and LUMO levels of  $-5.3$  eV and  $-3.7$  eV. The best result was a device made by P9 with PC<sub>71</sub>BM which was measured PCE of 3.4%, V<sub>OC</sub> of 0.7 V, J<sub>SC</sub> 10-11 mA/cm<sup>2</sup> and FF of 47%.

Hoven et al. suggested poly[(4,4-didodecyldithieno[3,2-b:20,30-d]silole)-2,6-diyl-alt-(2,1,3-benzoxadiazole)-4,7-diyl] (P10 in **Figure 3-4**) in 2010 (Hoven et al., 2010). The HOMO and LUMO of P10 are  $-5.5$  eV and  $-3.7$  eV, respectively. The average devices made by P10:PC<sub>71</sub>BM appeared different results with CN and without CN. The devices without CN was PCE of 1.8%, V<sub>OC</sub> of 0.70 V, J<sub>SC</sub> of 4.8mA/cm<sup>2</sup>, and FF of 55%, while the devices with CN recorded PCE of 5.4%, V<sub>OC</sub> of 0.68V, J<sub>SC</sub> of 13.7mA/cm<sup>2</sup>, and FF of 58%.

Park et al. achieved the PCE of 6.1% using Poly[N-9'-heptadecanyl-2,7-carbazole-alt-5,5-(4',7'-di-2-thienyl-2',1',3'-benzothiadiazole)] (PCDTBT) which is used in my research as well (P11 in **Figure 3-4**) with PC<sub>71</sub>BM (Park et al., 2009). The device has V<sub>OC</sub> of 0.88 V, J<sub>SC</sub> of 10.6 mA/cm<sup>2</sup>, and FF of 66%. Watters et al. also reported PCDTBT solar cell (Watters et al., 2012). They introduced dual metal cathode layer (Ca/Al) and it showed PCE of 5.01%, V<sub>OC</sub> of  $0.86 \pm 0.01$  V, J<sub>SC</sub> of  $9.4 \pm 0.1$  mA/cm<sup>2</sup>, and FF of  $60.6 \pm 0.3\%$ . The structures of P7-P11 are illustrated in **Figure 3-4** and the device performances of five polymers are summarised in **Table 3-2**.

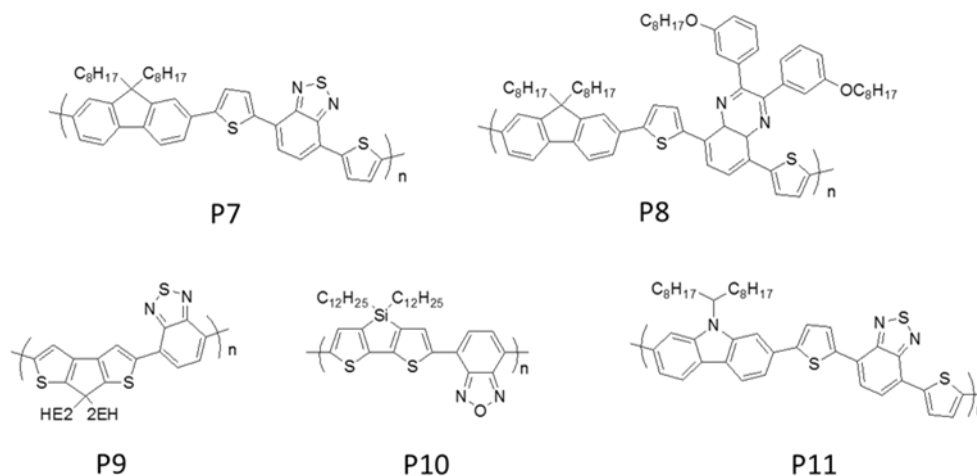


**Figure 3-4** The polymer structures of P7-P11.

**Table 3-2** The device parameters of 5 polymers

Polymers	PCE (%)	V <sub>oc</sub> (V)	J <sub>sc</sub> (mA/cm <sup>2</sup> )	FF (%)
<b>P7</b>	2.84	1.01	6.3	44
<b>P8</b>	3.7	1.0	6.0	63
<b>P9</b>	3.4	0.7	10-11	47
<b>P10 with CN</b>	5.4	0.68	13.7	58
<b>P11</b>	6.1 & 5.01	0.88 & 0.86	10.6 & 9.4	66 & 60.6

### 3.4. Use of conjugated polyelectrolytes for photovoltaic cells

Water-solubility is an important characteristic of conjugated polyelectrolytes. In order to dissolve in water, polar side chains such as negative (Vetrichelvan et al., 2006) or positive (Liu and Bazan, 2004) charged side chains and ethylene glycol (Pu et al., 2010) groups are added during synthesis.

When polyelectrolytes are dissolved in water, sometimes they show specific mobility of electrons in connection with water. As a result, their absorption or fluorescence spectral features may be red or blue shifted and increase or decrease in intensity when compared to conventional conjugated polymers in organic solvents due to hydrogen bonding with solvents or reagents, even though their backbone structure is the same (Seo et al., 2014, Huang et al., 2004). In addition, when conjugated polyelectrolytes combine other oppositely charged conjugated polyelectrolytes or materials, their emission and absorption peaks are changed by intermolecular charge transfer or fluorescence resonance energy transfer (FRET) (Bardeen, 2011, Pu et al., 2010, Kwak et al., 2010).

Conjugated polyelectrolytes are able to coat layer by layer with other materials using organic solvents in films. Therefore, it would be possible to be introduced to various layers such as HTL, ETL or active layer in the devices.

### 3.4.1. Synthesis of conjugated polyelectrolytes

Some of the literature which is related to synthesis of conjugated polyelectrolytes is discussed in this section. Although their results do not include the properties for photovoltaic cells, the band gaps of their polymers can be inferred from absorption and fluorescence peaks. To date, various conjugated polyelectrolytes have been reported since the early 1990s; for example poly(para-phenylene), polythiophene, polyfluorene. G. C. Bazan et al. reported a cationic poly(fluorene-co-phenylene) polymer chain having 2,1,3-benzothiadiazole (P12 in **Figure 3-5**) for DNA sensor (Liu and Bazan, 2004). The copolymer was synthesised by Suzuki cross coupling. Molecular weight by GPC was found to be ~ 11 kDa. A benzothiadiazole group was introduced in polymer backbone in order to attain two emission colours from polymer. The absorption and emission of P12 are  $\lambda_{\text{max}}$  of 380 nm and 400–500 nm below  $1 \times 10^{-6}$  M. However, green fluorescence (500-650 nm) is emitted over  $1 \times 10^{-6}$  M due to aggregation which shortened the distance between polymer and boosted energy transfer to lower energy benzothiadiazole group. They applied interpolymer interaction to detect target ss-DNA (5'-ATC TTG ACT ATG TGG GTG CT). The contraction and aggregation between polymer and DNA lead to efficient energy transfer to benzothiadiazole and as a result the colour changed.

Kim et al. studied water-soluble poly(p-phenyleneethynylene) (P13, P14) as a biosensor (Kim et al., 2005). P13 and P14 included negatively charged carboxylate side chain and it was synthesised via Sonogashira coupling. They have compared to two polymers (P13, and P14) and one oligomer attached protein. P13 has one water-soluble side chain, while P14 has a sugar group, as compared to P13, to give lower charge density. They compared fluorescence quenching of P13, P14 and the 6 protein oligomers. Both polymers showed good fluorescence quenching upon exposure to histone, whereas the fluorescence was increased by bovine serum albumin (BSA) exposure. These differences were because histone is positively charged, but BSA is negatively charged. Therefore, histone leads to charge transfer or induced aggregation which is responsible for the quenching processes with polymer. P13 also showed more quenching effect than P14 due to charge density in polymer.

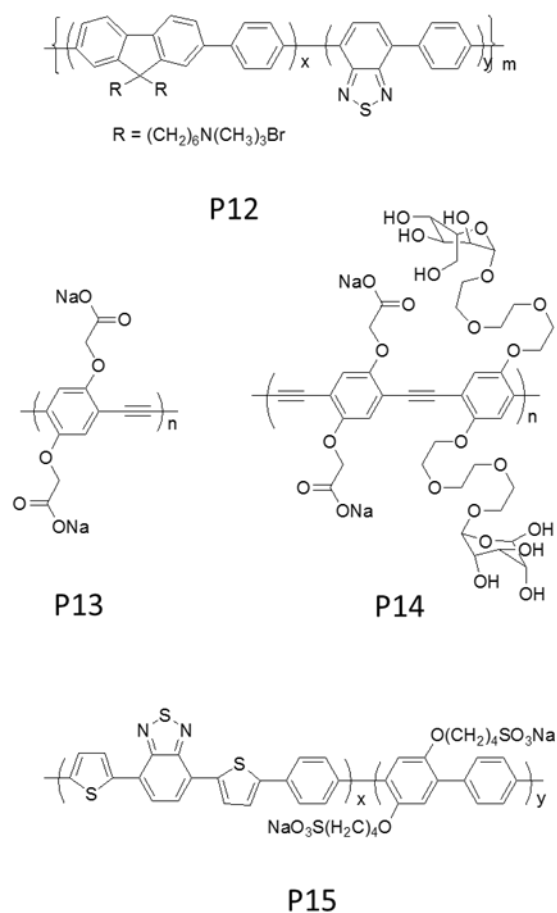


**Figure 3-5** The polymer structures of P12-P15.

Kwon et al. suggested water-soluble poly(bisthienylbenzothiadiazole-co-p-phenylene) (P15), which has sulfonate group, as a sensor (Kwon et al., 2011). P15 was synthesised by Suzuki-cross polymerisation and molecular weight of 1.24 kDa. P15 exhibited  $\lambda_{\text{max}}$  of 327 nm and small absorption peak showed (515 nm) in an aqueous solution. The P15 also showed similar absorption properties at 348 nm ( $\lambda_{\text{max}}$ ) and at 519 nm in solid state. However, the fluorescence in a solid state exhibited red emission at 653 nm due to intermolecular exciton migration to thienylbenzothiadiazole unit. This peak was not shown in an aqueous solution. This polymer detected mercury ions effectively. The colour of the polymer was changed from blue to red in both an aqueous solution and solid state. P12-P15 are illustrated in **Figure 3-5**.

### 3.4.2 Conjugated polyelectrolyte photovoltaic cells.

Conjugated polyelectrolytes (CPE) for photovoltaic cells have been studied by researchers for a decade. CPE has been used as an active layer or a buffer layer.

Water-soluble poly(thiophene), sodium poly[2-(3-thienyl)-ethoxy-4-butylsulfonate] (PTEBS:Na<sup>+</sup>) (P16) with fullerene was reported by Yang et al. in 2007 (Yang et al., 2007). P16 has butylsulfonate side chain instead of hexyl group. They reported bilayer photovoltaic cell and an architecture of devices was ITO/PTEBS:Na<sup>+</sup>/C60/2,9-dimethyl-4,7-diphenyl-1,10-phenanthroline (BCP)/Al. The device obtained PCE of 0.43 %, V<sub>OC</sub> of 0.58 ± 0.01 V, J<sub>SC</sub> of 0.95 ± 0.02 mA/cm<sup>2</sup>, and FF of 0.57 ± 0.01%.

J. T. McLeskey and Q. Qiao also reported PTEBS based solar cells (McLeskey and Qiao, 2006). They compared them to TiO<sub>2</sub> bilayer devices, TiO<sub>2</sub> BHJ devices, and carbon nanotubes (CNTs) BHJ cell. **Figure 3-6** illustrates polymer and device structure. All active layers in the devices were prepared by drop casting. The best result was achieved by the TiO<sub>2</sub> bilayer device. It showed PCE of 0.15%, V<sub>OC</sub> of 0.84 V, J<sub>SC</sub> of 0.15 mA/cm<sup>2</sup>, and FF of 91%. Attempting to use CNTs as an acceptor in polymer solar cell was expected to show good performances due to high electrons mobilities, however, it only showed a PCE of 1.35 × 10<sup>-4</sup>%.

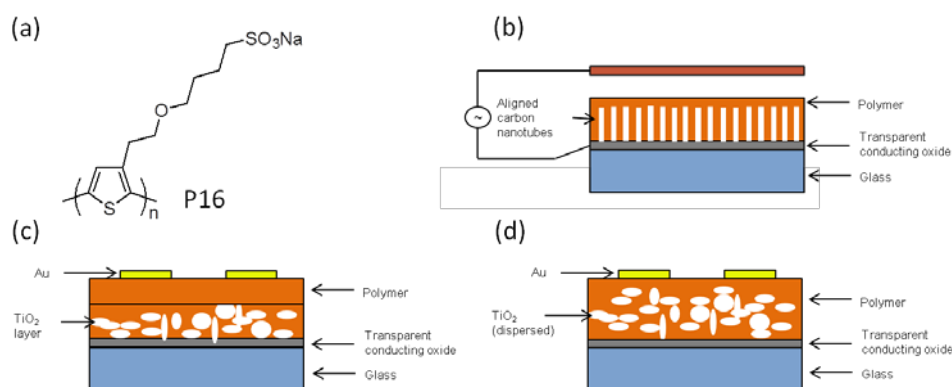


**Figure 3-6** The polymer and devices structure. (a) PTEBS, (b) aligned carbon nanotubes in BHJ cell, (c) bilayer heterojunction cell, and (d) bulk-heterojunction cell (Yang et al., 2007, McLeskey and Qiao, 2006)

### 3.4.3. Use of conjugated polyelectrolyte as interfacial layer in photovoltaic cells

The use of conjugated polyelectrolyte as an interfacial layer has improved the PCE of photovoltaic cells. In the past, CPEs have been introduced as ETLs to improve electron collecting ability and V<sub>OC</sub>. Seo et al. reported PCDTBT photovoltaic cell with poly[3-(6-trimethylammoniumhexyl)thiophene] (P3TMAHT, P17) or fluorene and thiophene based CPE poly(9,9-bis(2-ethylhexyl)-

fluorene]-b-poly[3-(6-trimethylammoniumhexyl)thiophene] (PF2/6-b-P3TMAHT, P18) in the ETL (Seo et al., 2011). The polymer structure is in **Figure 3-7**. P17 appeared HOMO of 4.98 eV and LUMO of 2.93 eV and P18 showed HOMO of 5.06 eV and LUMO of 3.04 eV. The device architecture was ITO/PEDOT:PSS/PCDTBT:PC<sub>71</sub>BM/CPE/Al. They improved the PCE of their devices up to 6.5 %. According to the report, the device's efficiencies were improved from 5 to over 6% and  $V_{OC}$  of  $0.89 \pm 0.01$  V,  $J_{SC}$  of  $10.6 \pm 0.3$  mA/cm<sup>2</sup>, and FF of  $67 \pm 1\%$  value were higher than general PCDTBT photovoltaic cell. Yao et al. also developed P17 and used it as an ETL for P3HT:PCBM photovoltaic cells (Yao et al., 2011). The best device's PCE was 3.28% and it was enhanced from 1.8%.

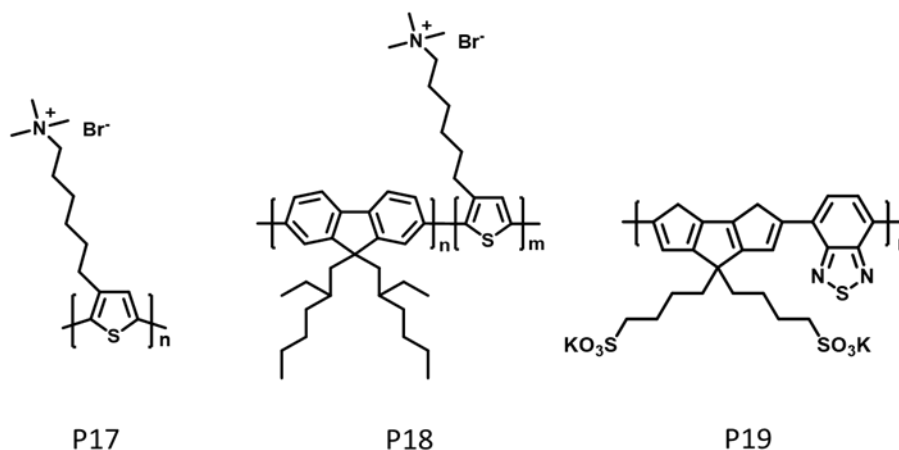


**Figure 3-7** The polymer structure of P17, P18 and P19.

Recently, CPE has been also utilised as HTL in organic photovoltaic cells. Zhou et al. reported the water/alcohol soluble CPE and it was used as HTL instead of PEDOT:PSS (Zhou et al., 2014). The CPE is poly[2,6-(4,4-bis-potassiumbutylsulfonate-4H-cyclopenta-[2,1-b;3,4-b']-dithiophene)-alt-4,7-(2,1,3-benzothiadiazole)] (PCPDTBT-SO<sub>3</sub>-K, P19). The CPE structure is in **Figure 3-7**. Their HOMO and LUMO levels were -4.9 eV and -3.5 eV. The architectures of their devices were ITO/CPE (P19)/PTB7:PC<sub>71</sub>BM/Al and the best PCE was 8.2%. When the device compared with general PEDOT:PSS HTL device, CPE HTL device showed a larger  $J_{SC}$ , a higher FF and a smaller  $V_{OC}$ . Smaller  $V_{OC}$  was caused by shallower HOMO for CPE (-4.9 eV) than that of PEDOT:PSS (-5.0 eV).

### 3.5. Perovskite photovoltaic cells

The relevant perovskite photovoltaic cells (PPVCs) literature is discussed in this chapter. Organic-metal halide perovskites have a structure of  $ABX_3$ , generally A is organic cations and X is halide anion. Organic cations, which have one or two ammonium groups, are placed between halide anions and it extends into the space between the inorganic layers. In general, methylammonium or formamidinium has been used as organic cation A, and lead (Pb) has been introduced as metal cation B. X halide anions are normally chloride ( $Cl^-$ ), bromide ( $Br^-$ ) and iodide ( $I^-$ ). These perovskites are good materials when used as a light harvester in solar cells, because of their bad gap, large absorption coefficients, high carrier mobility, and small exciton binding energy.

#### 3.5.1. Methylammonium lead trihalide based perovskite

Perovskite photovoltaic cells have achieved high PCE for last few years; therefore perovskites have become highly interesting materials for PVCs. The first perovskite photovoltaic cell was reported by Kojima et al.. They suggested  $MA(CH_3NH_3)PbI_3$  and  $MAPbBr_3$ -based cells. The architecture of devices was FTO/ $TiO_2$ /mp- $TiO_2$ /perovskite/electrode. The photovoltaic characteristics of  $MAPbI_3$  PVC were  $V_{OC}$  of 0.61 V,  $J_{SC}$  of 11  $mA/cm^2$ , FF of 57%, and PCE of 3.81%. The photovoltaic characteristics of  $MAPbBr_3$  PVC were  $V_{OC}$  of 0.96 V,  $J_{SC}$  of 5.57  $mA/cm^2$ , FF of 59%, and PCE of 3.13%. The band gap of  $MAPbI_3$  and  $MAPbBr_3$  was 1.44 eV and 2.02 eV respectively.

The first perovskite photovoltaic cells approached PCE up to 3.8%. However, PPVCs have been rapidly developed by myriad research groups. Kim et al. reported  $MAPbI_3$  sensitised PVC and it showed  $V_{OC}$  of 0.89 V,  $J_{SC}$  of 17  $mA/cm^2$ , FF of 62%, and PCE of 9.7%. The device's architecture was FTO/compact  $TiO_2$ /mp- $TiO_2$ /perovskite/spiro-MeOTAD/Au. Spiro-MeOTAD was used as hole transporting material and band gap of  $MAPbI_3$  was 1.5 eV.

Although PPVCs have approached high PCE over 20%, the perovskite active layer was applied to the cells with various methods in order to achieve theoretical values over 30%. Barrows and Kwak et al. reported  $MAPbI_{3-x}Cl_x$  PVC using spray coating. The PVC achieved  $V_{OC}$  of 0.92 V,  $J_{SC}$  of 16.8  $mA/cm^2$ , FF of 72%, and PCE of 11.1%. The architecture of PVC was ITO/PEDOT:PSS/perovskite/PCBM/Ca/Al.

Wu et al. reported two-step spin-coating procedure for MAPbI<sub>3</sub>. Therefore, the grain size of perovskite was increased and the performance of PVC was dramatically developed. The PCE of devices showed up to 15.3% and other characteristics of devices were V<sub>OC</sub> of 1.01 V, J<sub>SC</sub> of 21.8 mA/cm<sup>2</sup>, and FF of 69.8%.

### 3.5.2. Lead free perovskite

Reducing use of lead in the PPVCs is the one of the research aims of this work. Some research groups reported lead free perovskite PVCs due to toxicity of lead. Tin shows similar chemical characteristic with other 14 group metals such as germanium and lead. According to a recent report by Y. Ogomi et al., tin-lead mixed perovskite (CH<sub>3</sub>NH<sub>3</sub>Sn<sub>0.5</sub>Pb<sub>0.5</sub>I<sub>3</sub>) showed V<sub>OC</sub> of 0.42 V, J<sub>SC</sub> of 20.04 mA/cm<sup>2</sup>, FF of 50%, and PCE of 4.18%. The remarkable thing is that IPCE curve of CH<sub>3</sub>NH<sub>3</sub>Sn<sub>0.5</sub>Pb<sub>0.5</sub>I<sub>3</sub> reached 1060 nm. However, unfortunately they found that CH<sub>3</sub>NH<sub>3</sub>SnI<sub>3</sub> perovskite did not play a role as active layer.

N. K. Noel reported lead free perovskite (MASnI<sub>3</sub>) for photovoltaic applications (Noel et al., 2014). They approached PCE of 6.4% 1 sun illumination and V<sub>OC</sub> of 0.88 V, J<sub>SC</sub> of 16.8 mA/cm<sup>2</sup>, and FF of 42% with a band gap of 1.23 eV. The architecture of MASnI<sub>3</sub> sensitised PVC was FTO/compact TiO<sub>2</sub>/mp-TiO<sub>2</sub>/perovskite/Spiro-OMeTAD/Au.

Bismuth is one metal with lower toxicity than lead. Park et al. reported MA bismuth perovskite (MA<sub>3</sub>Bi<sub>2</sub>I<sub>9</sub>) and caesium (Cs) bismuth perovskite (Cs<sub>3</sub>Bi<sub>2</sub>I<sub>9</sub>) PVCs. In their study MA<sub>3</sub>Bi<sub>2</sub>I<sub>9</sub> showed a PCE of 0.12%, V<sub>OC</sub> of 0.68, J<sub>SC</sub> of 0.52 mA/cm<sup>2</sup>, and FF of 33%. Cs<sub>3</sub>Bi<sub>2</sub>I<sub>9</sub> appeared a PCE of 1.09%, V<sub>OC</sub> of 0.85 V, J<sub>SC</sub> of 2.15 mA/cm<sup>2</sup>, and FF of 60%. The energy band gap of MA<sub>3</sub>Bi<sub>2</sub>I<sub>9</sub> and Cs<sub>3</sub>Bi<sub>2</sub>I<sub>9</sub> was 2.1 eV and 2.2 eV respectively.

## 3.6. References

AL-IBRAHIM, M., AMBACHER, O., SENSFUSS, S. & GOBSCH, G. 2005.  
Effects of solvent and annealing on the improved performance of solar

- cells based on poly(3-hexylthiophene): Fullerene. *Applied Physics Letters*, 86.
- BARDEEN, C. 2011. Exciton Quenching and Migration in Single Conjugated Polymers. *Science*, 331, 544-545.
- BIJLEVELD, J. C., ZOOMBELT, A. P., MATHIJSEN, S. G. J., WIENK, M. M., TURBIEZ, M., DE LEEUW, D. M. & JANSSEN, R. A. J. 2009. Poly(diketopyrrolopyrrole-terthiophene) for Ambipolar Logic and Photovoltaics. *Journal of the American Chemical Society*, 131, 16616-+.
- BOUDREAU, P. L. T., MICHAUD, A. & LECLERC, M. 2007. A new poly(2,7-dibenzosilole) derivative in polymer solar cells. *Macromolecular Rapid Communications*, 28, 2176-2179.
- BRABEC, C. J. 2004. Organic photovoltaics: technology and market. *Solar Energy Materials and Solar Cells*, 83, 273-292.
- C. TANASE, E. J. M., P. W. M. BLOM, AND D. M. DE LEEUW 2003. Unification of the Hole Transport in Polymeric Field-Effect Transistors and Light-Emitting Diodes. *Physics Review Letters*, 91, 216601.
- CABANETOS, C., EL LABBAN, A., BARTELT, J. A., DOUGLAS, J. D., MATEKER, W. R., FRECHET, J. M. J., MCGEHEE, M. D. & BEAUJUGE, P. M. 2013. Linear Side Chains in Benzo[1,2-b:4,5-b']dithiophene-Thieno[3,4-c]pyrrole-4,6-dione Polymers Direct Self-Assembly and Solar Cell Performance. *Journal of the American Chemical Society*, 135, 4656-4659.
- CHEN, T. A. & RIEKE, R. D. 1992. The 1st Regioregular Head-to-Tail Poly(3-Hexylthiophene-2,5-Diyl) and a Regiorandom Isopolymer - Ni Vs Pd Catalysis of 2(5)-Bromo-5(2)-(Bromozincio)-3-Hexylthiophene Polymerization. *Journal of the American Chemical Society*, 114, 10087-10088.
- CHENG, Y. J., YANG, S. H. & HSU, C. S. 2009. Synthesis of Conjugated Polymers for Organic Solar Cell Applications. *Chemical Reviews*, 109, 5868-5923.
- DENNLER, G., SCHARBER, M. C. & BRABEC, C. J. 2009. Polymer-Fullerene Bulk-Heterojunction Solar Cells. *Advanced Materials*, 21, 1323-1338.
- DIMITRIEV, O. P., GRINKO, D. A., NOSKOV, Y. V., OGURTSOV, N. A. & PUD, A. A. 2009. PEDOT:PSS films-Effect of organic solvent additives and annealing on the film conductivity. *Synthetic Metals*, 159, 2237-2239.

- ELSENBAUMER, R. L., JEN, K. Y. & OBOODI, R. 1986. Processible and Environmentally Stable Conducting Polymers. *Synthetic Metals*, 15, 169-174.
- FACCHETTI, A. 2011. pi-Conjugated Polymers for Organic Electronics and Photovoltaic Cell Applications. *Chemistry of Materials*, 23, 733-758.
- GADISA, A., MAMMO, W., ANDERSSON, L. M., ADMASSIE, S., ZHANG, F., ANDERSSON, M. R. & INGANAS, O. 2007. A new donor-acceptor-donor polyfluorene copolymer with balanced electron and hole mobility. *Advanced Functional Materials*, 17, 3836-3842.
- GRIMSDALE, A. C., CHAN, K. L., MARTIN, R. E., JOKISZ, P. G. & HOLMES, A. B. 2009. Synthesis of Light-Emitting Conjugated Polymers for Applications in Electroluminescent Devices. *Chemical Reviews*, 109, 897-1091.
- GROSS, M., MULLER, D. C., NOTHOFFER, H. G., SCHERF, U., NEHER, D., BRAUCHLE, C. & MEERHOLZ, K. 2000. Improving the performance of doped pi-conjugated polymers for use in organic light-emitting diodes. *Nature*, 405, 661-665.
- GUNES, S., NEUGEBAUER, H. & SARICIFTCI, N. S. 2007. Conjugated polymer-based organic solar cells. *Chemical Reviews*, 107, 1324-1338.
- HADZIIOANNOU, G. & HUTTEN, P. F. V. 2000. *Semiconducting polymers : chemistry, physics and engineering*, Weinheim ; Chichester, Wiley-VCH.
- HOU, J. H., CHEN, H. Y., ZHANG, S. Q., LI, G. & YANG, Y. 2008. Synthesis, Characterization, and Photovoltaic Properties of a Low Band Gap Polymer Based on Silole-Containing Polythiophenes and 2,1,3-Benzothiadiazole. *Journal of the American Chemical Society*, 130, 16144-+.
- HOVEN, C. V., DANG, X. D., COFFIN, R. C., PEET, J., NGUYEN, T. Q. & BAZAN, G. C. 2010. Improved Performance of Polymer Bulk Heterojunction Solar Cells Through the Reduction of Phase Separation via Solvent Additives. *Advanced Materials*, 22, E63-+.
- HUANG, F., WU, H. B., WANG, D., YANG, W. & CAO, Y. 2004. Novel electroluminescent conjugated polyelectrolytes based on polyfluorene. *Chemistry of Materials*, 16, 708-716.
- IKEDA, H. S. A. S. 1971. Infrared Spectra of Poly(acetylene). *Polymer Journal*, 2, 231.
- IRWIN, M. D., BUCHHOLZ, B., HAINS, A. W., CHANG, R. P. H. & MARKS, T. J. 2008. p-Type semiconducting nickel oxide as an efficiency-enhancing anode interfacial layer in polymer bulk-heterojunction solar cells.

- Proceedings of the National Academy of Sciences of the United States of America*, 105, 2783-2787.
- KIM, I. B., DUNKHORST, A. & BUNZ, U. H. F. 2005. Nonspecific interactions of a carboxylate-substituted PPE with proteins. A cautionary tale for biosensor applications. *Langmuir*, 21, 7985-7989.
- KIM, Y., BALLANTYNE, A. M., NELSON, J. & BRADLEY, D. D. C. 2009. Effects of thickness and thermal annealing of the PEDOT:PSS layer on the performance of polymer solar cells. *Organic Electronics*, 10, 205-209.
- KWAK, C. K., KIM, D. G., KIM, T. H., LEE, C. S., LEE, M. & LEE, T. S. 2010. Simultaneous and Dual Emissive Imaging by Micro-Contact Printing on the Surface of Electrostatically Assembled Water-Soluble Poly(p-phenylene) Using FRET. *Advanced Functional Materials*, 20, 3847-3855.
- KWON, N. Y., KIM, D., SON, J. H., JANG, G. S., LEE, J. H. & LEE, T. S. 2011. Simultaneous detection and removal of mercury ions in aqueous solution with fluorescent conjugated polymer-based sensor ensemble. *Macromol Rapid Commun*, 32, 1061-5.
- LI, G., SHROTRIYA, V., HUANG, J. S., YAO, Y., MORIARTY, T., EMERY, K. & YANG, Y. 2005. High-efficiency solution processable polymer photovoltaic cells by self-organization of polymer blends. *Nature Materials*, 4, 864-868.
- LI, Y. N., WU, Y. L. & ONG, B. S. 2006. Polyindolo[3,2-b]carbazoles: A new class of p-channel semiconductor polymers for organic thin-film transistors. *Macromolecules*, 39, 6521-6527.
- LI, Z., TSANG, S. W., DU, X. M., SCOLES, L., ROBERTSON, G., ZHANG, Y. G., TOLL, F., TAO, Y., LU, J. P. & DING, J. F. 2011. Alternating Copolymers of Cyclopenta[2,1-b;3,4-b'] dithiophene and Thieno[3,4-c]pyrrole-4,6-dione for High-Performance Polymer Solar Cells. *Advanced Functional Materials*, 21, 3331-3336.
- LIANG, Y. Y., FENG, D. Q., WU, Y., TSAI, S. T., LI, G., RAY, C. & YU, L. P. 2009. Highly Efficient Solar Cell Polymers Developed via Fine-Tuning of Structural and Electronic Properties. *Journal of the American Chemical Society*, 131, 7792-7799.
- LIANG, Y. Y., XU, Z., XIA, J. B., TSAI, S. T., WU, Y., LI, G., RAY, C. & YU, L. P. 2010. For the Bright Future-Bulk Heterojunction Polymer Solar Cells with Power Conversion Efficiency of 7.4%. *Advanced Materials*, 22, E135-+.

- LIU, B. & BAZAN, G. C. 2004. Interpolyelectrolyte complexes of conjugated copolymers and DNA: Platforms for multicolor biosensors. *Journal of the American Chemical Society*, 126, 1942-1943.
- MA, W. L., YANG, C. Y., GONG, X., LEE, K. & HEEGER, A. J. 2005. Thermally stable, efficient polymer solar cells with nanoscale control of the interpenetrating network morphology. *Advanced Functional Materials*, 15, 1617-1622.
- MCLESKEY, J. T. & QIAO, Q. 2006. Hybrid solar cells from water-soluble polymers. *International Journal of Photoenergy*, 2006.
- MOON, J. S., JO, J. & HEEGER, A. J. 2012. Nanomorphology of PCDTBT:PC70BM Bulk Heterojunction Solar Cells. *Advanced Energy Materials*, 2, 304-308.
- MUHLBACHER, D., SCHARBER, M., MORANA, M., ZHU, Z. G., WALLER, D., GAUDIANA, R. & BRABEC, C. 2006. High photovoltaic performance of a low-bandgap polymer (vol 18, pg 2884, 2006). *Advanced Materials*, 18, 2931-2931.
- NA, J., KIM, Y. S., PARK, W. H. & LEE, T. S. 2004. Metal-induced optical sensing and optical switching in poly(pyridyl phenylene). *Journal of Polymer Science Part a-Polymer Chemistry*, 42, 2444-2450.
- NOEL, N. K., STRANKS, S. D., ABATE, A., WEHRENFENNIG, C., GUARNERA, S., HAGHIGHIRAD, A. A., SADHANALA, A., EPERON, G. E., PATHAK, S. K., JOHNSTON, M. B., PETROZZA, A., HERZ, L. M. & SNAITH, H. J. 2014. Lead-free organic-inorganic tin halide perovskites for photovoltaic applications. *Energy & Environmental Science*, 7, 3061-3068.
- PARK, S. H., ROY, A., BEAUPRE, S., CHO, S., COATES, N., MOON, J. S., MOSES, D., LECLERC, M., LEE, K. & HEEGER, A. J. 2009. Bulk heterojunction solar cells with internal quantum efficiency approaching 100%. *Nature Photonics*, 3, 297-U5.
- PEARSON, A. J., WANG, T., JONES, R. A. L., LIDZEY, D. G., STANIEC, P. A., HOPKINSON, P. E. & DONALD, A. M. 2012. Rationalizing Phase Transitions with Thermal Annealing Temperatures for P3HT:PCBM Organic Photovoltaic Devices. *Macromolecules*, 45, 1499-1508.
- PU, K. Y., LI, K. & LIU, B. 2010. Multicolor Conjugate Polyelectrolyte/Peptide Complexes as Self-Assembled Nanoparticles for Receptor-Targeted Cellular Imaging. *Chemistry of Materials*, 22, 6736-6741.

- SEO, J. H., GUTACKER, A., SUN, Y. M., WU, H. B., HUANG, F., CAO, Y., SCHERF, U., HEEGER, A. J. & BAZAN, G. C. 2011. Improved High-Efficiency Organic Solar Cells via Incorporation of a Conjugated Polyelectrolyte Interlayer. *Journal of the American Chemical Society*, 133, 8416-8419.
- SEO, S., KIM, J., JANG, G., KIM, D. & LEE, T. S. 2014. Aggregation-deaggregation-triggered, tunable fluorescence of an assay ensemble composed of anionic conjugated polymer and polypeptides by enzymatic catalysis of trypsin. *ACS Appl Mater Interfaces*, 6, 918-24.
- SHAHEEN, S. E., GINLEY, D. S. & JABBOUR, G. E. 2005. Organic-based photovoltaics. toward low-cost power generation. *Mrs Bulletin*, 30, 10-19.
- VETRICHELVAN, M., LI, H. R., RAVINDRANATH, R. & VALIYAVEETIL, S. 2006. Synthesis and comparison of the structure-property relationships of symmetric and asymmetric water-soluble poly(p-phenylene)s. *Journal of Polymer Science Part A-Polymer Chemistry*, 44, 3763-3777.
- WANG, B., TSANG, S. W., ZHANG, W. F., TAO, Y. & WONG, M. S. 2011. Naphthodithiophene-2,1,3-benzothiadiazole copolymers for bulk heterojunction solar cells. *Chemical Communications*, 47, 9471-9473.
- WATTERS, D. C., KINGSLEY, J., YI, H. N., WANG, T., IRAQI, A. & LIDZEY, D. 2012. Optimising the efficiency of carbazole co-polymer solar-cells by control over the metal cathode electrode. *Organic Electronics*, 13, 1401-1408.
- WIENK, M. M., TURBIEZ, M., GILOT, J. & JANSSEN, R. A. J. 2008. Narrow-bandgap diketo-pyrrolo-pyrrole polymer solar cells: The effect of processing on the performance. *Advanced Materials*, 20, 2556-+.
- WOO, C. H., BEAUJUGE, P. M., HOLCOMBE, T. W., LEE, O. P. & FRECHET, J. M. J. 2010. Incorporation of Furan into Low Band-Gap Polymers for Efficient Solar Cells. *Journal of the American Chemical Society*, 132, 15547-15549.
- YAMAMOTO, T., SANECHIKA, K. & YAMAMOTO, A. 1980. Preparation of Thermostable and Electric-Conducting Poly(2,5-Thienylene). *Journal of Polymer Science Part C-Polymer Letters*, 18, 9-12.
- YANG, J., GARCIA, A. & NGUYEN, T.-Q. 2007. Organic solar cells from water-soluble poly(thiophene)/fullerene heterojunction. *Applied Physics Letters*, 90, 103514-103514-3.
- YAO, K., CHEN, L., CHEN, Y. W., LI, F. & WANG, P. S. 2011. Influence of water-soluble polythiophene as an interfacial layer on the P3HT/PCBM

- bulk heterojunction organic photovoltaics. *Journal of Materials Chemistry*, 21, 13780-13784.
- YU, G., GAO, J., HUMMELEN, J. C., WUDL, F. & HEEGER, A. J. 1995. Polymer Photovoltaic Cells - Enhanced Efficiencies Via a Network of Internal Donor-Acceptor Heterojunctions. *Science*, 270, 1789-1791.
- ZHANG, F. L., JESPERSEN, K. G., BJORSTROM, C., SVENSSON, M., ANDERSSON, M. R., SUNDSTROM, V., MAGNUSSON, K., MOONS, E., YARTSEV, A. & INGANAS, O. 2006. Influence of solvent mixing on the morphology and performance of solar cells based on polyfluorene copolymer/fullerene blends. *Advanced Functional Materials*, 16, 667-674.
- ZHAO, G. J., HE, Y. J. & LI, Y. F. 2010. 6.5% Efficiency of Polymer Solar Cells Based on poly(3-hexylthiophene) and Indene-C-60 Bisadduct by Device Optimization. *Advanced Materials*, 22, 4355-+.
- ZHOU, H. Q., ZHANG, Y., MAI, C. K., COLLINS, S. D., NGUYEN, T. Q., BAZAN, G. C. & HEEGER, A. J. 2014. Conductive Conjugated Polyelectrolyte as Hole-Transporting Layer for Organic Bulk Heterojunction Solar Cells. *Advanced Materials*, 26, 780-785.
- ZOU, Y. P., NAJARI, A., BERROUARD, P., BEAUPRE, S., AICH, B. R., TAO, Y. & LECLERC, M. 2010. A Thieno[3,4-c]pyrrole-4,6-dione-Based Copolymer for Efficient Solar Cells. *Journal of the American Chemical Society*, 132, 5330-+.

## **4. Fabrication and characterisation of P3HT photovoltaic cells**

### **4.1. Introduction**

As previously mentioned in the introduction **Chapter 1**, organic photovoltaic cells (OPVCs) are an attractive technology due to potential source of renewable and clean energy and an alternative to fossil fuel. OPVCs are a type of solar cell which uses organic materials such as conductive conjugated polymers or small molecules. The most typical architecture for devices is bulk heterojunction (BHJ) based on an organic material:fullerene blend for the active layer. In general, organic materials used as active layer are conjugated polymers such as P3HT, PCDTBT, PTB7, and many others. Poly(3,4-ethylenedioxythiophene):Poly(styrenesulfonate) (PEDOT:PSS) is frequently used for the hole transporting layer (HTL), indium tin oxide (ITO) for the anode, and aluminium for the cathode (Iyer et al., 2006, Benanti and Venkataraman, 2006, Thompson and Frechet, 2008). In this chapter, to understand PEDOT:PSS as the HTL, thin films of PEDOT:PSS were fabricated and measured using a 4-probe sheet resistance measurement and UV-vis absorption experiments. In order to gain a general understanding of OPVCs, P3HT BHJ PVCs were also fabricated and characterised. Experiments comparing OPVCs with different blend ratios of P3HT:PCBM (1:0, 1:0.4, 1:0.6, 1:0.8, and 1:1), and comparing two fabrication conditions i.e. in glovebox and in atmosphere, and also a comparison of different cathode layers are reported. The experiments in this chapter were helpful to understand OPVCs and to increase fabrication technique for further experiments.

### **4.2. Experimental**

#### **4.2.1. Materials**

Regioregular poly(3-hexylthiophene) (P3HT, (M106) RR: 94.7%, Mw: 34,100), [6,6]-Phenyl-C61-butyric acid methyl ester (PCBM (M111)), encapsulation epoxy (E131) and poly(3,4-ethylenedioxythiophene) with poly(styrenesulfonate) (PEDOT:PSS – HC Stark Clevios P VP AI4083 (M121)) were purchased from

Ossila Ltd. Hellmanex, chlorobenzene, acetone and isopropanol (IPA) were purchased from Sigma-Aldrich. All organic components were used without any further purification. Pre-patterned ITO glass substrates (S171, 20  $\Omega$ /square) and encapsulation glass were provided by Ossila Ltd.

#### **4.2.2. Fabrication of thin films for characterisation of PEDOT:PSS**

In order to fabricate thin PEDOT:PSS films, PEDOT:PSS was spin coated on glass substrates using a Laurell WS-400BZ-6NPP/lite spin coater. First, the glass substrates were washed in Helmanex and then IPA for 10 min in an ultrasonic bath. After sonication, glass substrates were rinsed in DI water. For the research on conductivity of PEDOT:PSS thin films under various temperature, filtered (PVDF 0.45  $\mu$ m) PEDOT:PSS was spin coated at 5000 rpm for 40 sec and thermally annealed at 50, 75, 100, 125, 150, 175, and 200  $^{\circ}$ C for 15 min on the hot plate and as cast. For the research on UV-vis absorption of PEDOT:PSS thin films under different thickness, filtered PEDOT:PSS was spin coated at 2500, 5000, 7500, and 10000 rpm for 40 sec and then thermally annealed at 150  $^{\circ}$ C for 15 min.

#### **4.2.3. Fabrication of photovoltaic cells**

Pre-patterned ITO substrates were loaded into the substrate rack. In order to wash the ITO substrates, the rack was submerged in Hellmanex and was cleaned for 10 min in ultrasonic bath with hot water followed by immersing into hot DI water twice and once in cool. The ITO substrates were washed using Iso-propyl alcohol (IPA) followed by dump rinse in cool DI water twice. The substrates were blown dry using nitrogen before use. A substrate was transferred to spin coater and then PEDOT:PSS filtered through PVDF 0.45  $\mu$ m was coated at 5000 rpm for 40 sec. After the deposition of the PEDOT:PSS layer, the PEDOT:PSS film covering the edge part of ITO substrates was removed by a damp cotton bud and then the samples were annealed at 150  $^{\circ}$ C for 10 min. The PEDOT:PSS coated films were brought into the glovebox and thermally annealed 5 min more due to absorption of moisture on the PEDOT:PSS layer (This step is omitted when devices are fabricated in atmosphere). Solutions of P3HT and PCBM, 25 mg/ml in chlorobenzene, were prepared separately in chlorobenzene and heated at 70  $^{\circ}$ C overnight. The two solutions were then mixed by various volume. A blend of P3HT and PCBM solution was heated at 70  $^{\circ}$ C over 3 h to fully dissolve and then filtered before use. The blend (various blend ratio) of P3HT:PCBM was deposited

on the PEDOT:PSS layer at 2000 rpm for 40 sec and then P3HT:PCBM on the edge of substrates was wiped off with cotton bud soaked in chlorobenzene. P3HT and PCBM solution were heated at 70 °C over 3 h to fully dissolve. Aluminum (Al) (100 nm) or calcium (Ca) (5 nm)/Al (100 nm) was coated onto the P3HT:PCBM by vacuum evaporation under  $<10^{-6}$  mbar. The devices were thermally annealed for 30 min at 150 °C and then encapsulated with glass using UV-epoxy under UV light for 30 min.

#### **4.2.4. Instruments for characterisation of thin films and devices**

UV-vis absorption spectra were obtained using an Ocean Optics USB2000+ spectrometer and a DT-MINI-2-GS combined with a Deuterium-Halogen light source. Photoluminescence spectra were collected by a silicon diode detector and a Keithley 2700 multimeter under illumination by a Laser- LDCU CW 450nm diode laser. Samples were measured under vacuum at approximately  $1 \times 10^{-3}$  mbar. Sheet resistance and conductivity were measured by Keithley 2612 and four-point probe, which is 20  $\mu\text{m}$  gold coated nickel, was used with 1.07 mm probe tip diameter and 1.27 mm tip spacing. Film thickness was measured by J. A. Woollam Co. M-2000 ellipsometer with a charge-coupled device (CCD) camera as the detector. The atomic force microscope (AFM) images were obtained by a Veeco Dimension 3100 AFM with a Nanoscope IIIa controller and basic extender. Tapping mode was operated with Bruker TESPAs tapping mode cantilevers with a nominal spring constant of 42 N/m and a nominal resonant frequency of 320 kHz. The performance of devices were measured using a Newport 92251A-1000 solar simulator in ambient conditions under simulated AM 1.5 sunlight at an intensity of 100 mW/cm as determined using an NREL calibrated silicon photovoltaic reference cell. The devices were masked with an aperture ( $0.025 \text{ cm}^2$ ) to define the active area during the J-V measurement to minimize any edge effects. The PCE was subsequently calculated from the J-V curve and the known illumination intensity.

### **4.3. Study of PEDOT:PSS**

This section aims to better understand PEDOT:PSS as a hole transporting layer. PEDOT:PSS is the most commonly used hole transporting (electron blocking) layer in OPVCs. Thermal annealing of PEDOT:PSS layer is an important step in

the process because PEDOT:PSS can readily absorb moisture from the air (Elschner, 2011) and annealing will dry it removing the moisture in the PEDOT:PSS layer. Also the influence of oxygen on solar cells is not perfectly understood (Nam et al., 2009). Oxygen exposure in some reports was shown to increase charge carrier mobility in the organic semiconductors (Fan et al., 2008) but other reports showed a decrease of charge carrier mobility (Sze, 1981, Schafferhans et al., 2008). In order to understand the HTL in OPVCs, PEDOT:PSS has been characterised as a HTL. Firstly, how the conductivity of PEDOT:PSS under various conditions is described in this chapter. Secondly, UV-vis absorption of PEDOT:PSS deposited under different spin speeds is also described in this chapter. The absorption measurement provides detail of the transmittance of the HTL.

#### **4.3.1. Conductivity of PEDOT:PSS films in various annealing temperatures**

Sheet conductivities of various films were measured using a 4-point probe developed by Ossila Ltd. and Keithley 2612 source meter. The probe has linear tips with an equal tip diameter of 1.07 mm and spacing of 1.27 mm. Outer probes deliver a current to the sample whilst the inner probes measure the resulting voltage drop.

The experiment has been conducted using eight different annealing temperatures namely as cast, 50, 75, 100, 125, 150, 175, and 200 °C. To reduce effects from other materials such as ITO and P3HT, only PEDOT:PSS was coated on the clean glass substrates without ITO. The conductivity of all the PEDOT:PSS samples were measured using Keithley 2612 by sourcing either 200 pA or 1nA current (with a compliance of 20 V). The sheet resistance was calculated using equation (4.1) below (Smits, 1958).

$$R_S = 4.53 \frac{V}{I} \quad (4.1)$$

Where,  $R_S$  is sheet resistance,  $V$  is voltage,  $I$  is current, and 4.53 is correction factor.  $R_S$  is also related with resistivity (ohm) and film thickness (cm) and its equation (4.2) followed by,

$$R_S = \text{resistivity}/\text{thickness} \quad (4.2)$$

The thickness ( $t$ ) of the film and sheet resistance ( $R_s$ ) is related to conductivity ( $\sigma$ ) and the equation (4.3) is below.

$$\sigma = \frac{1}{R_s \cdot t} \quad (4.3)$$

The first conductivity measurement result of each two PEDOT:PSS thin films under various temperature are shown in **Figure 4-1**.

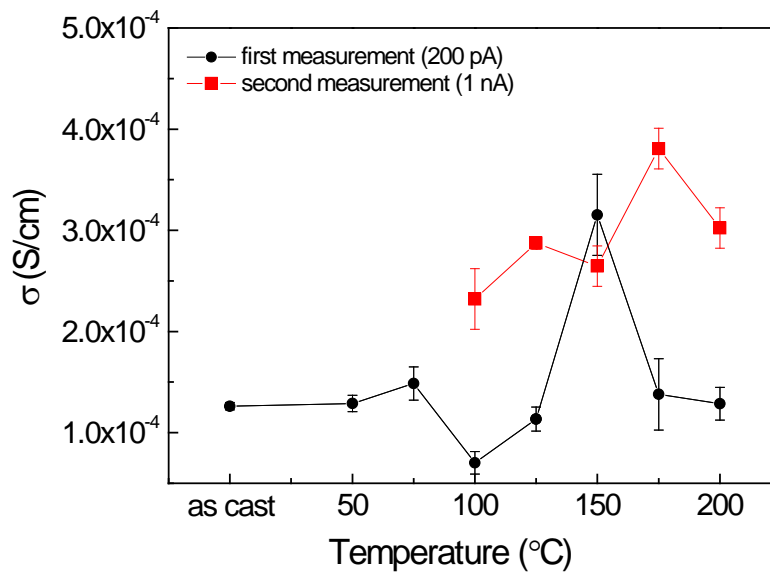


**Figure 4-1** The average conductivity of each two PEDOT:PSS thin films as cast, 50, 75, 100, 125, 150, 175, and 200 °C by sourcing at 200 pA current (black line and circle) and 1 nA current (red line and square).

Two PEDOT:PSS films were made for each fabrication condition (as cast, 50, 75, 100, 125, 150, 175, and 200 °C) so 16 films were fabricated. All the each films were measured three times with the probes located at different random position and then average values were shown in **Figure 4-1**. The black line and circle were first measured by sourcing a current of 200 pA and the red line and squares in the second measurement were found when sourcing a current of 1 nA. The second set of experiments attempted to reduce noise in the experiment by adopting a higher current than first set. In the first measurements, the as casted PEDOT:PSS film had a higher conductivity than the 100 °C and 125 °C annealed PEDOT:PSS films. The highest conductivity is shown at 150 °C ( $3.15 \times 10^{-4}$  S/cm). 75 and 175 °C annealed films showed similar high conductivity. The conductivity then decreased as annealed temperature increased above 175 °C. Although the conductivity of PEDOT:PSS at 100 and 125 °C were lower than expected (conductivity of

PEDOT:PSS provided by Ossila Ltd. is  $1.5 \times 10^{-3} - 1.5 \times 10^{-4}$  S/cm or 600 - 6000  $\Omega$ /cm), the behaviour shown was similar to a previous report (Kim et al., 2009). According to the report, the conductivity of PEDOT:PSS increases as annealing temperature is increased above 100 °C, then conductivity is decreased as annealing temperature goes above 200°C. The change of conductivity is likely due to a change of oxidation state of PEDOT:PSS or decomposition of polymer in high temperature (Kim et al., 2009).

The second conductivity measurement result (red line and square) of each of two freshly prepared PEDOT:PSS thin films annealed at various temperature are shown in **Figure 4-1**. The fabrication process of the PEDOT:PSS films was the same as the former experiment.

The result of the second measurement did not yield stable results below 100 °C annealing temperature, so only the results over 100 °C are shown in the **Figure 4-1**. As shown in **Figure 4-1**, the PEDOT:PSS film annealed at 175 °C showed the highest conductivity and the conductivity of PEDOT:PSS films annealed over 200 °C was decreased. The second measurement showed slightly different results compared to the first measurement. However, second results showed reasonable conductivity values of PEDOT:PSS above 100 °C. The conductivity of PEDOT:PSS above 100 °C was from  $2.32 \times 10^{-4}$  to  $3.8 \times 10^{-4}$  S/cm. These values are in the range of conductivity from supplier ( $5 \times 10^{-3} - 1.5 \times 10^{-4}$  S/cm (600 - 6000  $\Omega$ /cm)).

According to a previous report by Dimitriev et al. (Dimitriev et al., 2009). Conductivity of pristine PEDOT:PSS films was decreased as annealing temperature increased above 100 °C. In the report, 50 °C showed the highest conductivity of PEDOT:PSS films. This is conflict with the results shown here and also those of Kim et al (Kim et al., 2009).

From this conductivity measurement and the previous reports, the conductivity of PEDOT:PSS film are evidently very sensitive and it can be dramatically changed by surface conditions and circumstance such as temperature and humidity. Therefore, uncontrolled changes of the PEDOT:PSS films may well be occurring during device fabrication/degradation if care is not taken. In order to get consistent results, constant temperature and humidity are needed and the process time after

annealing and before conductivity measurement should be kept similar because PEDOT:PSS is able to absorb moisture quickly.

#### 4.3.2. Absorption of PEDOT:PSS thin film under different thickness

The UV-vis absorbance of PEDOT:PSS thin films is an important parameter for PVCs. If there is significant absorbance, the sunlight cannot reach the active layers. Therefore, it should be as small as possible. Increasing the absorption of light by PEDOT:PSS is more probable with increasing thickness. To determine the dependence of thickness, UV absorption spectrometry of PEDOT:PSS films was measured. The results are shown in **Figure 4-2**. The film thickness of PEDOT:PSS film at 2500, 5000, 7500, and 10000 rpm is about 57, 41, 32, and 26 nm, respectively.

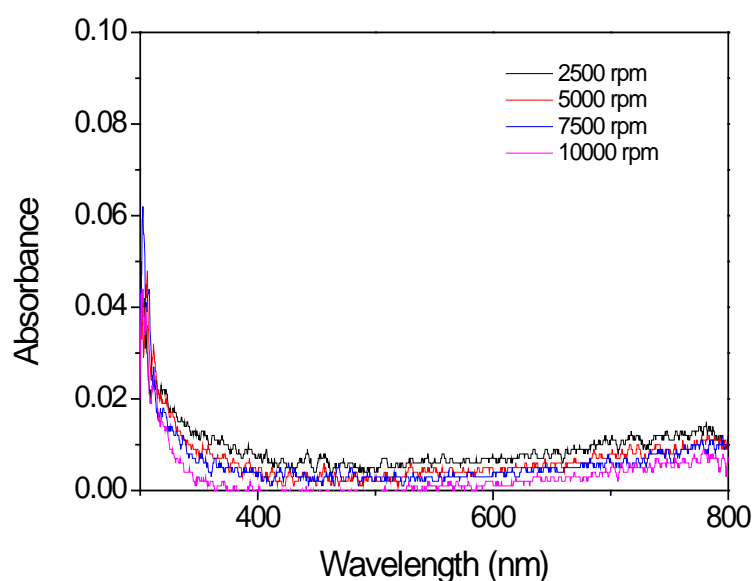


**Figure 4-2** The absorbance of PEDOT:PSS films with different spin speed at 2500 (57 nm), 5000 (41 nm), 7500 (32 nm), and 10000 (26 nm) rpm annealed at 150 °C. The values in brackets are thickness.

In **Figure 4-2**, a weak absorption feature associated with the PEDOT:PSS films appeared about 300 nm for all films. A small broad rise in absorbance is also observed over 700 nm for all films. The films fabricated in lower speed showed higher absorption in both around 300 nm and 780 nm. Although the absorption of the films slightly increased as film thickness increased, in accordance with the Beer Lambert law it should not significantly affect the amount of light entering the

active layer in a device due to the very absorbance observed. Therefore, PEDOT:PSS does not obstruct an active layer harvesting the sunlight due to its very small absorption.

#### 4.4. Study on BHJ OPVCs using P3HT:PCBM

P3HT:PCBM is the one of the fundamental materials in organic (polymer) bulk-heterojunction photovoltaic cell. P3HT:PCBM organic photovoltaic cells based on bulk-heterojunction were studied in order to understand device structure and improve the skills for device preparation. These experiments were performed using various blend ratio of P3HT:PCBM and two different cathode layers. Then, it was also fabricated in standard atmospheric condition at room temperature and in nitrogen filled glovebox.

##### 4.4.1. Different blend ratio of P3HT:PCBM based OPVCs

A series of OPVCs were fabricated to optimise the blend solution ratio of P3HT:PCBM. The different blend ratio of P3HT:PCBM (1:0.4, 1:0.6, 1:0.8, and 1:1) were applied to devices. The P3HT and PCBM solutions in chlorobenzene were heated over 3 h at 70 °C then each solution were mixed following four different volume blend ratio. The device structure is ITO/PEDOT:PSS/P3HT:PCBM/(Ca)/Al, with PEDOT:PSS and PCBM performing as hole- and electron- transporting layers respectively. The pre-patterned ITO/Glass substrate which has 6 pixels in one substrate is illustrated in **Figure 4-3**.

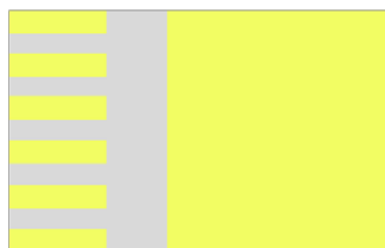


**Figure 4-3** The pre-patterned ITO/Glass architecture in use (yellow patterned region is where there is an ITO coating on the glass substrate and grey is uncoated glass).

The performance of P3HT PVCs with different blend ratios made in glovebox were measured using a Newport Lot Oriel 91159 Solar Simulator, with light filtered to approximate the AM 1.5G solar spectrum.

#### 4.4.1.1. Optical properties of P3HT:PCBM

In order to understand light harvesting system of P3HT:PCBM, UV-vis absorption and photoluminescence (PL) spectra were measured. **Figure 4-4** shows the absorption of P3HT:PCBM blend films. P3HT shows strong absorption at 500 and 552 nm and shoulder peak at 602 nm. The absorption at 552 nm is caused by extended conjugation of P3HT in the film and the shoulder at 602 nm comes from the intermolecular  $\pi$ - $\pi$  stacking of P3HT suggesting improved crystallinity (Lin et al., 2012, Chang and Wang, 2008, Liu et al., 2010). When the PCBM concentration of the blend ratio is increased, the absorbance was decreased from 500 to 600 nm due to reduction of P3HT concentration. However the absorbance at 337 nm was increased as much as PCBM concentration increased.

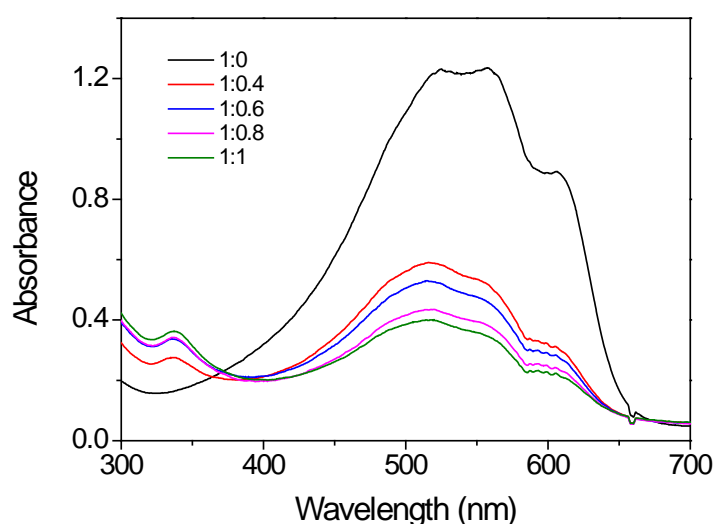


**Figure 4-4** The absorbance of P3HT:PCBM films with blend ratios of 1:0 (black), 1:0.4 (red), 1:0.6 (blue), 1:0.8 (magenta), and 1:1 (green).

Fluorescence of P3HT:PCBM films are shown in **Figure 4-5**. As shown in **Figure 4-5**, a strong emission peak from P3HT (1:0) is apparent between 650 and 750 nm. P3HT films showed significant emission quenching after mixing with PCBM. When PCBM concentration increased, the emission peak of P3HT was decreased because increasing PCBM concentration enables P3HT and PCBM to make interface in the BHJ and then more excited electrons in P3HT to move more easily. 1:0.8 blend ratio of P3HT:PCBM showed sufficient quenching but 1:0.4 blend ratio of P3HT:PCBM showed not enough quenching for electron transfer. From the PL

spectra, it showed that electron charge transfer was appeared and PCBM is used as electron acceptor for P3HT.

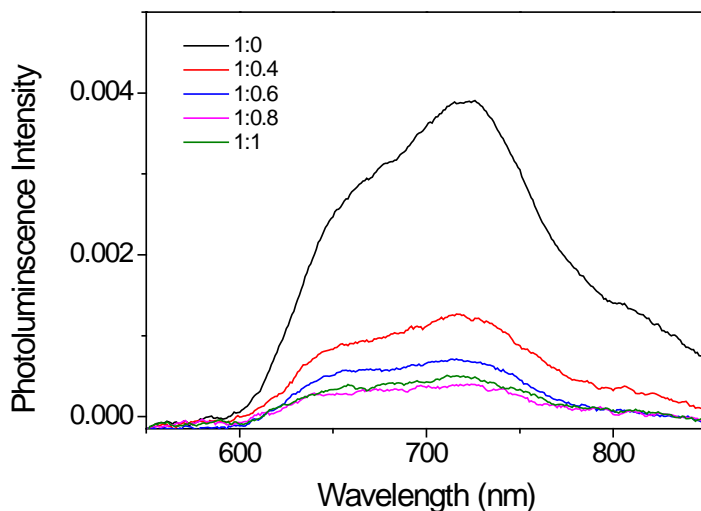


**Figure 4-5** PL spectra of the P3HT:PCBM films with blend ratios of 1:0 (black), 1:0.4 (red), 1:0.6 (blue), 1:0.8 (magenta), and 1:1 (green).

#### 4.4.1.2. Morphology of P3HT:PCBM films

To understand nanoscale morphology of bulk heterojunction active layer, P3HT:PCBM films were measured by atomic force microscopy (AFM). AFM is good technology to see the phase separation of nanocomposites. The AFM images of P3HT:PCBM with different blend ratios were shown in **Figure 4-6**. As shown in **Figure 4-6(a)**, AFM image of the P3HT film shows root mean square (RMS) of 11.14 nm. However, AFM images of P3HT:PCBM films shows RMS of 1.62 (1:0.4), 0.88 (1:0.6), 1.58 (1:0.8), and 1.65 (1:1) nm, this values are about 10% of RMS of P3HT surface. Therefore this result indicates that surface of P3HT:PCBM blended films appeared smoother than only P3HT film and also from the AFM images, P3HT and PCBM blend forms the nanoscale bulk heterojunction. Exciton diffusion length of P3HT is 2 – 8 nm (Shaw et al., 2008, Goh et al., 2007, Kroeze et al., 2003), so electrons in P3HT were likely to transfer well to PCBM in nanoscale BHJ. P3HT forms ordered crystalline domains, and PCBM molecules also aggregate to form nanocrystals. The phase separation between P3HT and PCBM forms a bi-continuous network enabling charge transfer to the electrodes.

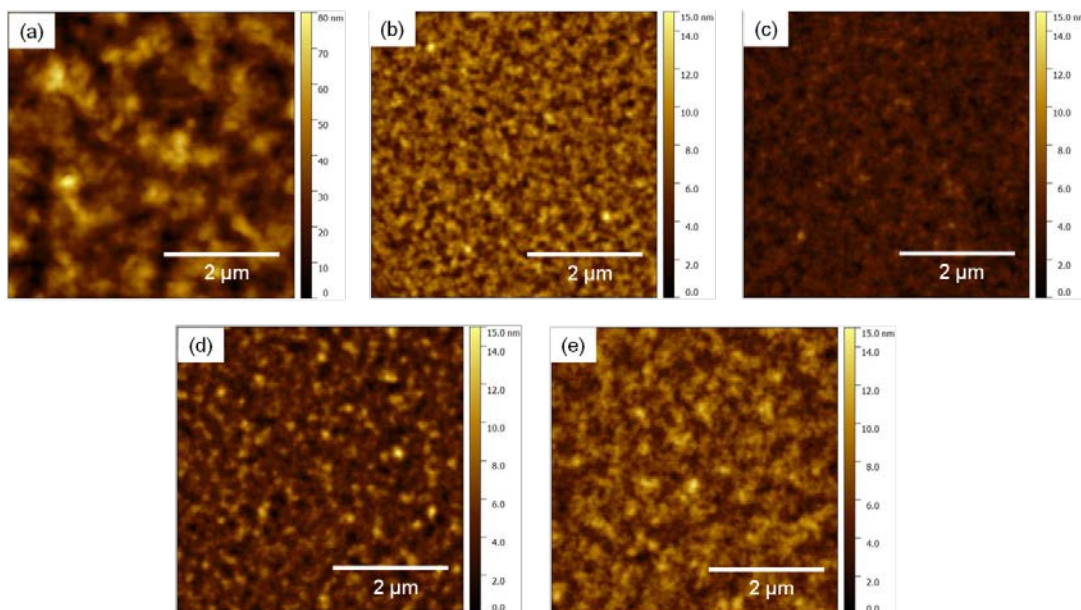


**Figure 4-6** AFM images of the P3HT:PCBM films with blend ratios of (a) 1:0, (b) 1:0.4, (c) 1:0.6, (d) 1:0.8, and (e) 1:1. (scale bar is 2  $\mu\text{m}$ )

#### 4.4.1.3. Photovoltaic device characterisation

**Figure 4-7** shows the J-V curves from best performing pixel of each of the 6-pixel devices. The four samples showed PCE between 1.62 and 2.73%. The device of 1:0.4 blend ratios shows the PCE of 1.6%. 1:0.6 blend ratio device exhibits the best PCE of 2.73% in all the devices 1:0.8 and 1:1 blend ratio shows the PCE of 2.39 and 2.35% respectively. Corresponding data is shown in **Figure 4-8**.

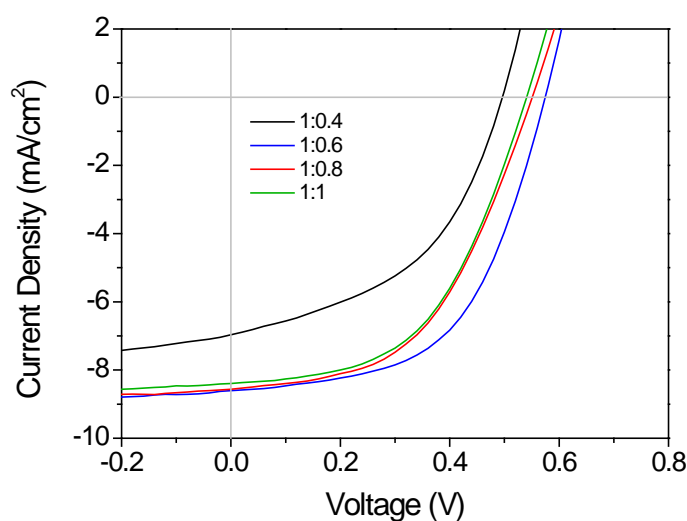


**Figure 4-7** J-V curves of P3HT:PCBM devices. Blend ratio of P3HT:PCBM is 1:0.4 (black line), 1:0.6 (blue line), 1:0.8 (red line), and 1:1 (green line).

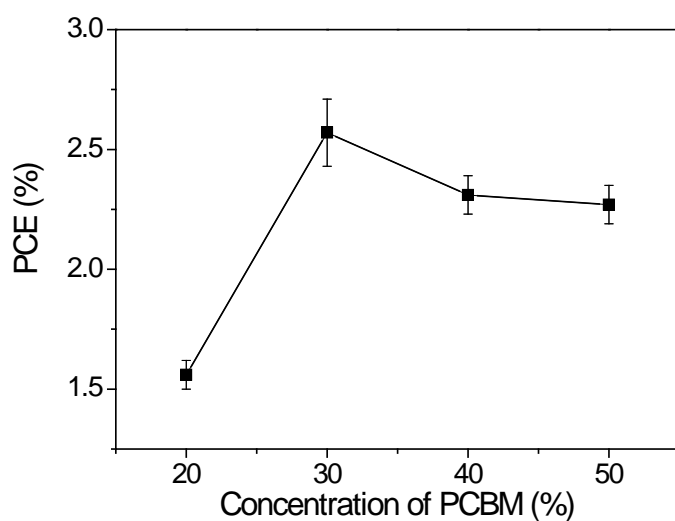


**Figure 4-8** PCE (%) of devices depend on PCBM concentration.

External quantum efficiency (EQE) spectra of all devices are shown in **Figure 4-9**. It shows that device of 1:0.4 blend ratio appeared lower EQE from 450 to 620 nm than other devices and it showed lower short-circuit current density ( $J_{SC}$ ) as shown in the **Figure 4-9**. However, other devices having 1:0.6, 1:0.8, and 1:1 blend ratio showed similar EQE spectra and appeared similar  $J_{SC}$  value.

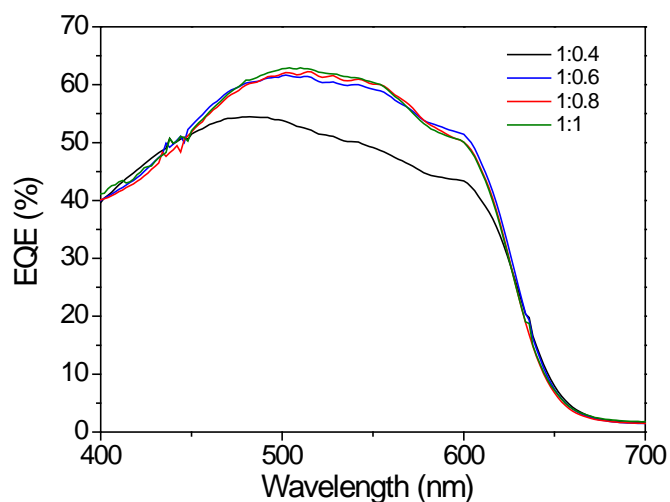


**Figure 4-9** EQE spectra of P3HT:PCBM devices. Blend ratio of P3HT:PCBM is 1:0.4 (black line), 1:0.6 (blue line), 1:0.8 (red line), and 1:1 (green line).

The characteristics of all devices are described in **Table 4-1**. As shown in **Table 4-1**, 1:0.4 blend devices appeared the lowest values with  $J_{SC}$  of  $-6.84 \pm 0.12$  mA/cm<sup>2</sup>,

open-circuit voltage ( $V_{oc}$ ) of  $0.5 \pm 0.01$  V, and fill factor (FF) of  $46.72 \pm 0.14$  % then that of other devices. Because, lower concentrated PCBM in active layer could not show sufficient exciton dissociation and transfer electrons to cathode layer due to insufficient PCBM, so it shows low  $J_{sc}$  (Bavel et al., 2010, Baek et al., 2010, Pearson et al., 2012). It is corresponded with PL data in the **Figure 4-5**. Lower concentrated PCBM in active layer also led to lower  $V_{oc}$ , because much P3HT directly contacts cathode layer. While 1:1 blend ratio devices showed lower PCE than 1:0.6 and 1:0.8 blended devices. There are not specific changes of surface in the **Figure 4-7(b)-(e)**. However, according to the previous report, it could not extract well and transport holes because of large-scale phase separation and it reduce absorption ability of P3HT due to covering of active layer in higher concentrated PCBM in active layer (Pearson et al., 2012, Baek et al., 2010). 1:0.6 blend ratio devices showed the highest characteristics in J-V curves with  $J_{sc}$  of  $-8.39 \pm 0.21$  mA/cm<sup>2</sup>,  $V_{oc}$  of  $0.57 \pm 0.01$  V, and FF of  $54.56 \pm 0.34$  %.

**Table 4-1** The characteristics of P3HT:PCBM photovoltaic cells with various blend ratio of active layer (1:0.4, 1:0.6, 1:0.8, and 1:1) All data was collected from 5 devices with 6 pixels each, and the average results for the higher 50% taken

P3HT:PCBM Blend ratio	$J_{sc}$ (mA/cm <sup>2</sup> )	$V_{oc}$ (V)	FF (%)	PCE (%)	
				Average	Best
<b>1:0.4</b>	$-6.84 \pm 0.12$	$0.5 \pm 0.01$	$46.72 \pm 0.14$	1.56	1.62
<b>1:0.6</b>	$-8.39 \pm 0.21$	$0.57 \pm 0.01$	$54.56 \pm 0.34$	2.57	2.73
<b>1:0.8</b>	$-8.36 \pm 0.2$	$0.54 \pm 0.01$	$51.35 \pm 0.72$	2.31	2.39
<b>1:1</b>	$-8.84 \pm 0.53$	$0.53 \pm 0.01$	$51.62 \pm 0.62$	2.27	2.35

#### 4.4.2. Comparing fabrication of OPVCs in the glovebox and atmosphere

In order to compare performance of OPVCs fabricated in the glovebox and atmosphere, the blend ratio of 1:0.6 and 1:0.8 P3HT:PCBM devices, which is chosen from two higher performance by above results in, were fabricated in the two different environments. The architecture of devices was ITO/PEDOT:PSS/P3HT:PCBM/Ca/Al. The PCE of devices were also measured using the same solar simulator.

#### 4.4.2.1. Photovoltaic device characterisation

Two devices (1:0.6 and 1:0.8 of P3HT:PCBM blend ratio) were fabricated by the same procedure above mentioned in a glovebox. Another two devices (1:0.6 and 1:0.8 of P3HT:PCBM blend ratio) were also fabricated by same procedure, this time in an air atmosphere. In the **Figure 4-10**, J-V curves of the devices are shown. As shown in the **Figure 4-10**, all PCE of devices shows between 2.65 and 3.06%. Interestingly, devices in atmosphere appeared higher or similar PCE compared to those devices made in the glovebox against expectation. While it is not fully understood, it could be because the solvent used was not sufficiently anhydrous. Therefore, devices made in the glovebox also included small amounts of moisture in the active layer and showed similar results with devices fabricated in atmosphere. In addition, according to the previous report by Nam et al., suitable post annealing process causes the devices improving good PCE resulting from a reduction in electron and hole trap densities and growth of thin Al oxide hole blocking layer at the top metal contact interface (Nam et al., 2009). The best PCE is from 1:0.8 (A) device. It approached the PCE of 3.06%.

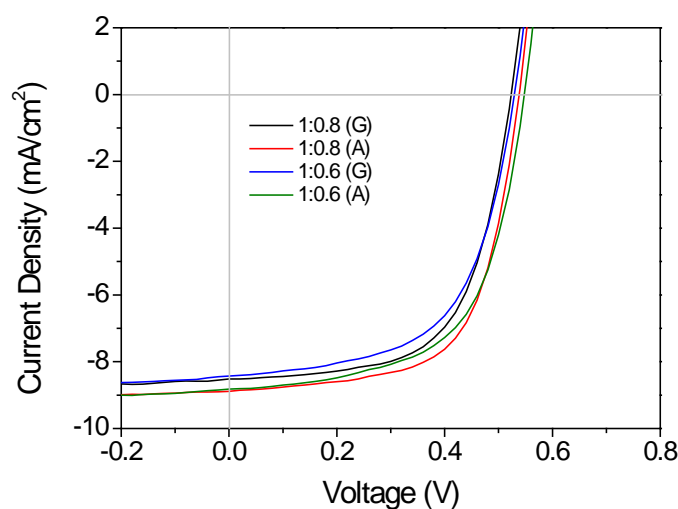


**Figure 4-10** J-V curves of P3HT:PCBM fabricated in the glovebox or air. 1:0.8 (black and red line) 1:0.6 (blue and green line) is the blend ratio of P3HT:PCBM. (G) indicates the devices made in the glovebox and (A) indicates the devices made in atmosphere.

It is summarized that the average of PCE,  $J_{SC}$ ,  $V_{OC}$  and FF of four devices are represented in **Table 4-2**. This result is different with above result with different blend ratio devices. In this experiment, 1:0.8 blend ratio devices were shown better performance than 1:0.6 blend ratio devices. 1:0.8 (A) device showed the highest

values than that of others. It has  $J_{sc}$  of  $-8.78 \pm 0.11$  mA/cm<sup>2</sup>,  $V_{oc}$  of  $0.53 \pm 0.01$  V, and FF of  $63.6 \pm 0.4\%$ . As mentioned above, the devices fabricated in suitable condition process such as annealing or moisture and oxygen concentration in air may also show the good PCE compare to the devices fabricated in the glovebox.

**Table 4-2** The characteristics of P3HT:PCBM photovoltaic cells fabricated in the glovebox or atmosphere (1:0.8 (G), 1:0.8 (A), 1:0.6 (G), and 1:0.6 (A), (G) and (A) refer to glovebox and atmosphere, respectively) All data was collected from 5 devices with 6 pixels each, and the average results for the higher 50% taken

Device's fabrication condition	$J_{sc}$ (mA/cm <sup>2</sup> )	$V_{oc}$ (V)	FF (%)	PCE (%)	
				Average	Best
<b>1:0.8 (G)</b>	$-8.38 \pm 0.13$	$0.51 \pm 0.01$	$63.1 \pm 0.4$	2.74	2.79
<b>1:0.8 (A)</b>	$-8.78 \pm 0.11$	$0.53 \pm 0.01$	$63.6 \pm 0.4$	2.98	3.06
<b>1:0.6 (G)</b>	$-8.31 \pm 0.14$	$0.53 \pm 0.01$	$58.9 \pm 0.3$	2.63	2.65
<b>1:0.6 (A)</b>	$-8.73 \pm 0.08$	$0.53 \pm 0.01$	$60.1 \pm 0.5$	2.78	2.93

#### 4.4.3. Fabrication of OPVCs with only Al cathode layer

In order to eliminate any cathode layer effects, a layer of only Al was used in the OPVCs as a cathode layer in this section. All the devices were fabricated in same condition with above experiment apart from cathode layer. The architecture of devices is ITO/PEDOT:PSS/P3HT:PCBM/Al/.

##### 4.4.3.1. Photovoltaic device characterisation

The J-V curves of devices are shown in **Figure 4-11**. The best performance of photovoltaic effect was from 1:0.8 (G) device. It showed the PCE of 3.29% and other devices 1:0.8 (A), 1:0.6 (G), and 1:0.6 (A) appeared 3.24, 3.11, and 3.11 respectively. All the PCE of devices are higher than devices which has Ca/Al cathode layers in above section 4.4.2. It could be possible that although the devices were fabricated in the glovebox, the Ca layer was easily oxidised by residual oxygen in the glovebox after thermal evaporation coating was deposited. In addition according to Eo et al., calcium forms a Schottky type contact and a non-

spontaneous electron extraction process due to high work function (- value) of calcium. It is significantly lower than LUMO of PCBM. In this case, PCE was decreased due to space charge limited current and it was about 40% reduction in PCE of aluminium cathode device (Eo et al., 2009).

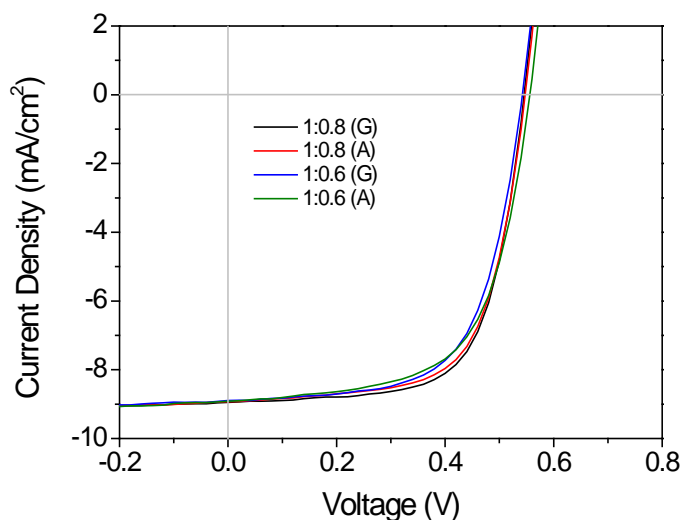


**Figure 4-11** J-V curves of P3HT:PCBM which has ITO/PEDOT:PSS/P3HT:PCBM/Al device structure. 1:0.8 (black and red line) 1:0.6 (blue and green line) is the blend ratio of P3HT:PCBM. (G) indicates the devices made in the glovebox and (A) indicates the devices made in atmosphere. Device's structure is ITO/PEDOT:PSS/P3HT:PCBM/Al.

EQE spectra of all devices are shown in **Figure 4-12**. All devices showed EQE values over 60 % from 480 to 530 nm. Using this data, the theoretical  $J_{SC}$  for devices was  $8.0 \text{ mA/cm}^2$  and it was slightly different value with measured  $J_{SC}$  of  $8.7 \text{ mA/cm}^2$  because it was measured from 400 nm.

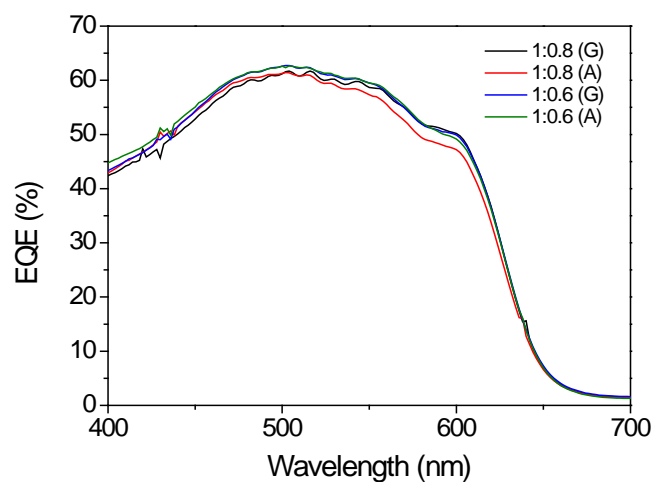


**Figure 4-12** EQE spectra of P3HT:PCBM devices. Blend ratio of P3HT:PCBM is 1:0.8 (G) (black line), 1:0.8 (A) (red line), 1:0.6 (G) (blue line), and 1:0.6 (A) (green line).

The characteristics of all photovoltaic cells are summarised in **Table 4-3**. When the devices use only Al cathode layer, PCE of 1:0.8 (G) device was increased from 2.78 to 3.29%. This is an 18% increase in PCE. As shown in **Table 4-3** compared with **Table 4-2**, PCEs of all devices (only Al cathode) are higher than the PCE of devices (Ca/Al cathode layer). Voc was not shown much specific change, but Jsc and FF were increased. Therefore, it means that devices using Al cathode layer move electrons well and reduce resistivity.

**Table 4-3** The characteristics of P3HT:PCBM photovoltaic cells fabricated with only Al cathode layer (1:0.8 (G), 1:0.8 (A), 1:0.6 (G), and 1:0.6 (A), (G) and (A) refer to glovebox and atmosphere, respectively) All data was collected from 5 devices with 6 pixels each, and the average results for the higher 50% taken

Device's fabrication condition	J <sub>SC</sub> (mA/cm <sup>2</sup> )	V <sub>OC</sub> (V)	FF (%)	PCE (%)	
				Average	Best
<b>1:0.8 (G)</b>	-8.76 ± 0.21	0.54 ± 0.01	66.3 ± 0.9	3.19	3.29
<b>1:0.8 (A)</b>	-8.75 ± 0.17	0.54 ± 0.01	65.4 ± 0.9	3.11	3.24
<b>1:0.6 (G)</b>	-8.71 ± 0.22	0.54 ± 0.01	63.2 ± 0.8	3.02	3.11
<b>1:0.6 (A)</b>	-8.71 ± 0.2	0.55 ± 0.01	62.4 ± 0.5	3.02	3.11

None of the PCEs of P3HT PVCs reported in the experiments were above the PCE of 4-5% previously reported. However, the results showed similar results to the report by Pearson et al. under very similar fabrication condition. From this result, it was determined that the fabrication process and technique of device testing is robust and reliable.

#### 4.5. Conclusions

In this chapter, in order to understand each layer, architecture, characteristic, and fabrication process of general OPVCs, thin films of PEDOT:PSS and photovoltaic devices of P3HT:PCBM were fabricated and analysed. The effects of annealing PEDOT:PSS at various temperatures and its influence on its conductivity were studied for the HTL. The conductivity measurements were performed after

applying various annealing temperatures. From the conductivity measurement, my understanding is that PEDOT:PSS is a high resistive material and sensitive to moisture. In order to get repeatable results, it would be necessary that all PEDOT:PSS films are fabricated in same atmosphere (e.g. temperature, and humidity) before annealing. After annealing, it is necessary to minimise side effects by preventing the reabsorption of moisture in air. While from the UV-vis absorption spectra of PEDOT:PSS thin films, it was more clear than conductivity experiment. Absorption of PEDOT:PSS increased as thickness increased, but absorption intensity was very small. All the PEDOT:PSS films fabricated at 2500, 5000, 7500, and 10000 rpm were very small absorbing sunlight from 300 to 800 nm so it does not obstruct the active layer to harvest incident light.

The effect of different blend ratios of the active layer and its fabrication process in the glovebox and air were studied. In the active layer, the blend ratio of P3HT:PCBM played an important role to achieve high performance. The PL peak of P3HT appeared between 650 and 750 nm and it was quenched by PCBM. The PL intensity of P3HT was reduced as PCBM concentration increased. The morphology of P3HT was changed when mixed with PCBM. The RMS roughness of P3HT was 11.14 nm but RMS roughness of P3HT:PCBM blend was 0.88-1.65 nm. In low PCBM concentration blend, the device PCE was low due to recombination of dissociated electrons and holes. In P3HT:PCBM PVCs, 1:0.8 and 1:0.6 blend ratio showed good results and it achieved PCEs up to 3.29%. All the characteristics of PVCs fabricated with 1:0.8 and 1:0.6 blend ratios were higher than other blend ratio devices. The devices fabricated in an air atmosphere also showed good PCEs of over 3%. In Ca/Al cathode devices, due to significantly higher work function of calcium than LUMO of PCBM (Eo et al., 2009), and the possible oxidation of the Ca, the PCE of Ca/Al cathode devices were reduced compared to those with Al only cathodes. In addition, Ca is very reactive to O<sub>2</sub>, so thin layer of Ca and controlled O<sub>2</sub> may help to improve device performance but if not, it would decrease device performance.

The results from this Chapter, have helped to understand OPVC fabrication further. The device fabrication is very sensitive to circumstance and the results can be easily affected by the device fabrication conditions and the composition of the materials in each layer.

#### 4.6. References

- BAEK, W. H., YOON, T. S., LEE, H. H. & KIM, Y. S. 2010. Composition-dependent phase separation of P3HT:PCBM composites for high performance organic solar cells. *Organic Electronics*, 11, 933-937.
- BAVEL, S. S. V., BARENKLAU, M., DE WITH, G., HOPPE, H. & LOOS, J. 2010. P3HT/PCBM Bulk Heterojunction Solar Cells: Impact of Blend Composition and 3D Morphology on Device Performance. *Advanced Functional Materials*, 20, 1458-1463.
- BENANTI, T. L. & VENKATARAMAN, D. 2006. Organic solar cells: An overview focusing on active layer morphology. *Photosynthesis Research*, 87, 73-81.
- CHANG, Y. M. & WANG, L. 2008. Efficient Poly(3-hexylthiophene)-Based Bulk Heterojunction Solar Cells Fabricated by an Annealing-Free Approach. *Journal of Physical Chemistry C*, 112, 17716-17720.
- DIMITRIEV, O. P., GRINKO, D. A., NOSKOV, Y. V., OGURTSOV, N. A. & PUD, A. A. 2009. PEDOT:PSS films—Effect of organic solvent additives and annealing on the film conductivity. *Synthetic Metals*, 159, 2237-2239.
- ELSCHNER, A. 2011. *PEDOT : principles and applications of an intrinsically conductive polymer*, Boca Raton, Fla., CRC Press ; London : Taylor & Francis [distributor].
- EO, Y. S., RHEE, H. W., CHIN, B. D. & YU, J. W. 2009. Influence of metal cathode for organic photovoltaic device performance. *Synthetic Metals*, 159, 1910-1913.
- FAN, B., HANY, R., MOSER, J. E. & NUESCH, F. 2008. Enhanced cyanine solar cell performance upon oxygen doping. *Organic Electronics*, 9, 85-94.
- GOH, C., SCULLY, S. R. & MCGEHEE, M. D. 2007. Effects of molecular interface modification in hybrid organic-inorganic photovoltaic cells. *Journal of Applied Physics*, 101.
- IYER, S. S. K., BAJAJ, D. & BHAT, A. 2006. Photovoltaic behaviour of organic polymer - PCBM bulk hetero junctions solar cells. *Iete Journal of Research*, 52, 391-399.
- KIM, Y., BALLANTYNE, A. M., NELSON, J. & BRADLEY, D. D. C. 2009. Effects of thickness and thermal annealing of the PEDOT:PSS layer on the performance of polymer solar cells. *Organic Electronics*, 10, 205-209.

- KROEZE, J. E., SAVENIJE, T. J., VERMEULEN, M. J. W. & WARMAN, J. M. 2003. Contactless determination of the photoconductivity action spectrum, exciton diffusion length, and charge separation efficiency in polythiophene-sensitized TiO<sub>2</sub> bilayers. *Journal of Physical Chemistry B*, 107, 7696-7705.
- LIN, Y., LIM, J. A., WEI, Q. S., MANNSFELD, S. C. B., BRISENO, A. L. & WATKINS, J. J. 2012. Cooperative Assembly of Hydrogen-Bonded Diblock Copolythiophene/Fullerene Blends for Photovoltaic Devices with Well-Defined Morphologies and Enhanced Stability. *Chemistry of Materials*, 24, 622-632.
- LIU, J. G., SHAO, S. Y., WANG, H. F., ZHAO, K., XUE, L. J., GAO, X., XIE, Z. Y. & HAN, Y. C. 2010. The mechanisms for introduction of n-dodecylthiol to modify the P3HT/PCBM morphology. *Organic Electronics*, 11, 775-783.
- NAM, C. Y., SU, D. & BLACK, C. T. 2009. High-Performance Air-Processed Polymer-Fullerene Bulk Heterojunction Solar Cells. *Advanced Functional Materials*, 19, 3552-3559.
- PEARSON, A. J., WANG, T., JONES, R. A. L., LIDZEY, D. G., STANIEC, P. A., HOPKINSON, P. E. & DONALD, A. M. 2012. Rationalizing Phase Transitions with Thermal Annealing Temperatures for P3HT:PCBM Organic Photovoltaic Devices. *Macromolecules*, 45, 1499-1508.
- SCHAFFERHANS, J., BAUMANN, A., DEIBEL, C. & DYAKONOV, V. 2008. Trap distribution and the impact of oxygen-induced traps on the charge transport in poly(3-hexylthiophene). *Applied Physics Letters*, 93.
- SHAW, P. E., RUSECKAS, A. & SAMUEL, I. D. W. 2008. Exciton diffusion measurements in poly(3-hexylthiophene). *Advanced Materials*, 20, 3516-+.
- SMITS, F. M. 1958. Measurement of Sheet Resistivities with the 4-Point Probe. *Bell System Technical Journal*, 37, 711-718.
- SZE, S. M. 1981. *Physics of semiconductor devices*, New York, Wiley.
- THOMPSON, B. C. & FRECHET, J. M. 2008. Polymer-fullerene composite solar cells. *Angew Chem Int Ed Engl*, 47, 58-77.

## 5. Synthesis of conjugated polyelectrolyte

### 5.1 Introduction

Conjugated polyelectrolytes (CPEs, water-soluble conjugated polymers) have been studied for the last two decades. Here they are used in order to reduce the use of organic solvents which will help to reduce the need for environmentally toxic organic solvents and reduce risks to human health in the manufacture of PVCs. CPEs are promising materials for chemical (Son et al., 2013, Kwon et al., 2011) and biological (Pu and Liu, 2010, Kwak et al., 2010, Yu et al., 2008, Liu and Bazan, 2004) sensors, thin film transistors, (Yang et al., 2010) organic light emitting diodes, (Grimsdale et al., 2009) and organic solar cells (Duan et al., 2013, Yang et al., 2007, Seo et al., 2011, Cheng et al., 2009). For the last decade, some conjugated polyelectrolytes have been used as an active layer (Qiao et al., 2005), a hole transporting layer (Zhou et al., 2014), and an electron transporting layer (Yao et al., 2011) in photovoltaic cells.

#### 5.1.1. Synthesis of conjugated polyelectrolyte

The chemical structures and synthesis methods of polyelectrolyte poly[(9,9-bis(4-sulfonatobutyl sodium) fluorene-alt-phenylene)-ran-(4,7-di-2-thienyl-2,1,3-benzothiadiazole-alt-phenylene)] (PSFP-DTBTP) are described in **Scheme 5-1**. The PSFP-DTBTP was designed based on the concept that it can dissolve in water and serve as a low energy band gap polyelectrolyte which is significant because such a material can reduce organic solvent use and match the electronic properties required for solar cell manufacture. In order to fabricate the low band gap polymer, fluorene and phenylene groups were used as electron donors and di-thienyl-benzothiadiazole groups were introduced as electron acceptors in the polyelectrolyte. In addition, to absorb a wide range of wavelengths, fluorene which can absorb from 300 to 400 nm and di-thienyl-benzothiadiazole which can absorb from 450 to 550 nm groups were introduced. The negatively charged sulfonatobutyl side chain in fluorene was applied to produce the electrolytic property of the polymer, thereby enhancing water solubility. In addition, fluorene groups were applied to absorb short wavelengths. The 2,7-dibromo-9,9-bis(4-sulfonatobutyl)fluorene disodium (1) was synthesised from 2,7-dibromofluorene

and 1,4-butane sultone in the presence of tetrabutylammonium bromide (TBAB) in a mixture of dimethyl sulfoxide (DMSO) and 50 wt % aqueous sodium hydroxide (NaOH). The 4,7-dibromo-2,1,3-benzothiadiazole (2) was prepared by the bromination of benzothiadiazole with bromine in hydrobromic acid (HBr). The 4,7-di-2-thienyl-2,1,3-benzothiadiazole (3) was synthesised via the Suzuki cross-coupling of (2) and thiophene-2-boronic acid pinacol ester with Pd(OAc)<sub>2</sub>/tri(o-tolyl)phosphine catalyst in toluene and 2M aqueous Na<sub>2</sub>CO<sub>3</sub>. The 4,7-Bis(5-bromo-2-thienyl)-2,1,3-benzothiadiazole (4) was prepared through the bromination of (3) with N-bromosuccinimide (NBS) in a mixture of chloroform and acetic acid. For the synthesis of conjugated polyelectrolyte PSFP-DTBTP, Suzuki cross-coupling was carried out with (1), (4), and 1,4-phenylene-bisboronic acid pinacol ester at a molar ratio of 9:1:10 in N,N-dimethylformamide (DMF) and 2M aqueous Na<sub>2</sub>CO<sub>3</sub> in the presence of Pd(OAc)<sub>2</sub>/Tri(o-tolyl)phosphine catalyst. Purification of PSFP-DTBTP was performed by dialysis using a dialysis cellulose membrane (molecular weight cut-off: 12.4 KDa) for 3 d. The molar ratio 9:1 of sulfonatobutyl attached fluorene and di-thienyl-benzothiadiazole in PSFP-DTBTP afforded good solubility in water.

In order to study the use of conducting polyelectrolytes in organic photovoltaic cells, the conjugated polyelectrolyte PSFP-DTBTP was synthesised. In this chapter, the synthesis method, analysis, and material characterisation of the polymer are described.

## 5.2 Experimental

### 5.2.1. Materials

2,7-dibromofluorene (97%), 1,4-butane sultone (99%), tetrabutylammonium bromide (98%), 2,1,3-benzothiadiazole (98%), bromine (99%), thiophene-2-boronic acid pinacol ester (98%), sodium carbonate (99.5%), magnesium sulphate (97%), 1,4-phenylene-bisboronic acid pinacol ester (97%), and N-bromosuccinimide (99%) were purchased from Sigma-Aldrich and used without any further purification. Palladium (II) acetate trimer (99.98%), and tri(o-tolyl)phosphine (98%) were purchased from Alfa Aesar and used without further purification. All solvents used in the synthesis of the monomers and polymer were

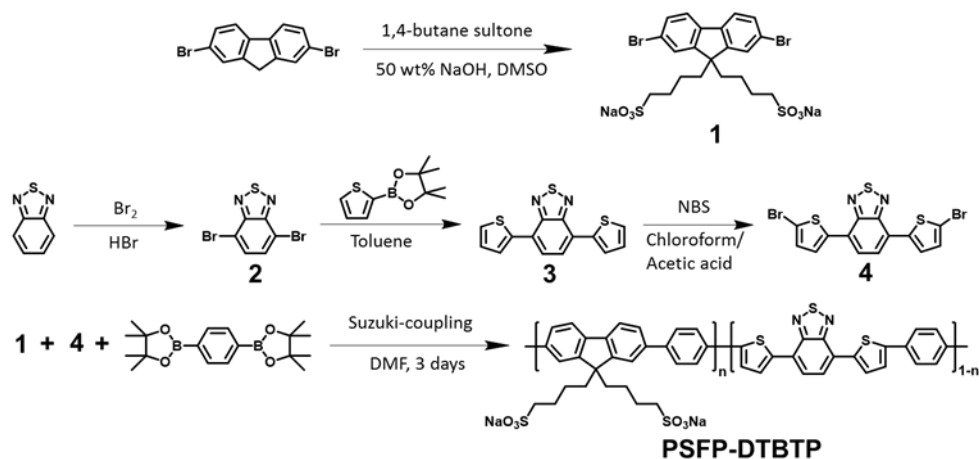
purchased from Sigma-Aldrich, Acros Organics, and Fisher scientific, and used as supplied.

## 5.2.2. Instruments for characterisation of monomers and a polymer

$^1\text{H}$  and  $^{13}\text{C}$  nuclear magnetic resonance (NMR) spectra were recorded using a Bruker DRX-500 NMR spectrometer and deuterium oxide ( $\text{D}_2\text{O}$ ) or chloroform-d ( $\text{CDCl}_3$ ) as the solvent. Elemental analysis (EA) results were measured using a Perkin Elmer 2400 series II CHN analyzer. UV-vis absorption spectra were obtained by an Ocean Optics USB2000+ spectrometer and DT-MINI-2-GS combined Deuterium-Halogen light source. Fourier transform infrared (FT-IR) spectra were recorded by Perkin Elmer Frontier MID ATR FT-IR Spectrometer. Photoluminescence (PL) spectra were collected under vacuum at  $1 \times 10^{-3}$  mbar using a Laser- LDCU CW 450nm diode laser and silicon diode detector and recorded by a Keithley 2700 multimeter. Cyclic voltammetry (CV) measurement was carried out with a Princeton Applied Research model 263A Potentiostat/Galvanostat with 10 ml of 0.1 M tetrabutylammonium perchlorate in acetonitrile used as the electrolyte solution. A three electrodes system of  $\text{Ag}/\text{Ag}^+$  reference electrode (Ag wire in 0.01 M  $\text{AgNO}_3$  solution in the electrolyte solution), Pt working electrode (2mm diameter smooth Pt disc, area =  $3.14 \times 10^{-2}$   $\text{cm}^2$ ) and Pt counter electrode (Pt wire) was used for the measurement.

## 5.2.3. Synthesis of monomers and conjugated polyelectrolyte

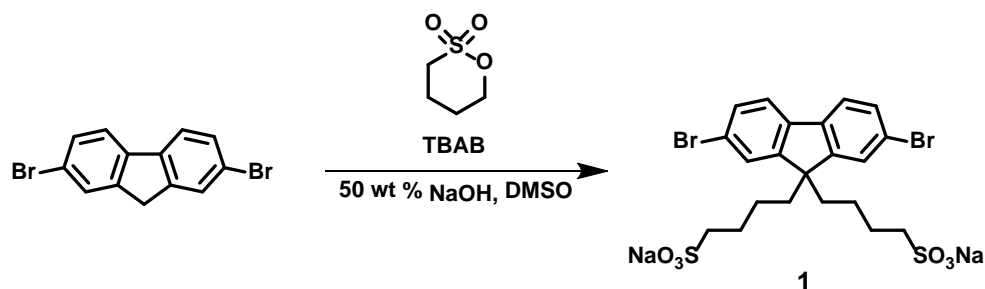
### 5.2.3.1. The overall plan of synthesis for conjugated polyelectrolyte



**Scheme 5-1** The overall plan in synthesis of conjugated polyelectrolyte.

The synthesis followed the steps in the scheme above. Firstly, water-soluble fluorene for donor material in the polymer was synthesised. The other monomers for the acceptor in the polymer were synthesised. Finally, the CPE was synthesised using Suzuki-coupling.

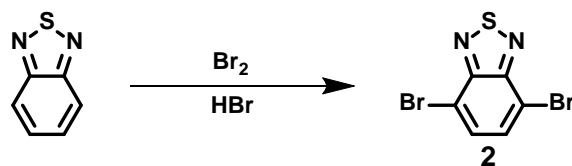
### 5.2.3.2. Synthesis of 2,7-dibromo-9,9-bis(4-sulfonatobutyl)fluorene disodium (1) (Pu et al., 2010)



**Scheme 5-2** Synthesis of 2,7-dibromo-9,9-bis(4-sulfonatobutyl)fluorene disodium.

Following the procedure described by Pu et al. 100 mg of tetrabutylammonium bromide (TBAB) was dissolved in 50 wt % sodium hydroxide solution (NaOH) (10 ml) and dimethyl sulfoxide (DMSO) (70 ml) in a 250 ml 3-necked round-bottomed flask under nitrogen. 5 g (15.43 mmol) of 2,7-Dibromofluorene was added into the mixture in the flask (the colour changed from white to orange). A solution of 1,4-butane sultone (5.25g, 38.58 mmol) and DMSO (26 ml) was added dropwised into the mixture. The mixture was reacted for 3 h at room temperature under nitrogen (the mixture's colour changed from orange to dark purple) and then the reacted mixture was precipitated into 500 ml of acetone. The crude product was isolated by vacuum filtration and washed with ethanol. The product was re-crystallised twice in acetone/H<sub>2</sub>O in order to purify it then dried in vacuum at 40 °C for 24 h. White crystals were obtained. Yield 6.28 g (63.56 %). <sup>1</sup>H NMR (500 MHz, D<sub>2</sub>O, δ ppm): 7.62 (d, 2H), 7.59 (d, 2H), 7.47 (dd, 2H), 2.58-2.42 (m, 4H), 2.05-1.88 (m, 4H), 1.47-1.26 (m, 4H), 0.6-0.41 (m, 4H). <sup>13</sup>C NMR (125 MHz, D<sub>2</sub>O, δ ppm): 167.75, 152.15, 138.88, 130.31, 126.47, 121.44, 121.26, 55.18, 50.76, 38.57, 24.24, 22.39. Element Anal. Calcd. for C<sub>21</sub>H<sub>22</sub>Br<sub>2</sub>Na<sub>2</sub>O<sub>6</sub>S<sub>2</sub>: C, 39.39; H, 3.46; Br, 24.96; S, 10.01; found: C, 34.93; H, 3.67; Br, 21.18; S, 8.71.

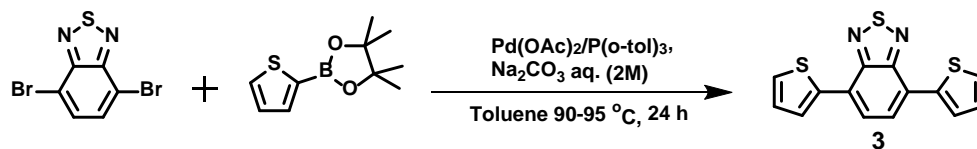
### 5.2.3.3. Synthesis of 4,7-dibromo-2,1,3-benzothiadiazole (2) (Yang et al., 2005)



**Scheme 5-3** Synthesis of 4,7-dibromo-2,1,3-benzothiadiazole.

Following the procedure described by Yang et al., 10 g (73.4 mmol) of 2,1,3-benzothiadiazole and 150 ml of hydrobromic acid (HBr) were added into a 500 ml two-necked round-bottomed flask and stirred (2,1,3-benzothiadiazole did not dissolve in HBr). A mixture of bromine (35.19 g, 220.2 mmol) and HBr (100 ml) was very slowly added dropwise into the flask (the colour changed to dark brown and no solids appeared immediately after bromine added). The mixture was heated under reflux for 6 h at 100 °C. Dark orange coloured solids were appeared after the reaction. The mixture was cooled down and then neutralised with sodium bisulfite solution (~40 %, 250 ml) to remove excess bromine. The crude product was filtered and washed well in deionised water over 1 h then washed with diethyl ether. The product was recrystallised in chloroform/methanol and dried in vacuum at 40 °C for 24 h. Yellowish needled crystals were obtained. Yield 15.9 g (73.7 %). <sup>1</sup>H NMR (500 MHz, CDCl<sub>3</sub>, δ ppm): 7.75 (s, 2H). <sup>13</sup>C NMR (125 MHz, CDCl<sub>3</sub>, δ ppm) 152.99, 132.38, 113.94. Element Anal. Calcd. for C<sub>6</sub>H<sub>2</sub>Br<sub>2</sub>N<sub>2</sub>S: C, 24.52; H, 0.69; Br, 54.36; N, 9.53; S, 10.91; found: C, 24.55; H, 0.73; Br, 53.36; N, 9.4; S, 10.22.

### 5.2.3.4. Synthesis of 4,7-di-2-thienyl-2,1,3-benzothiadiazole (3) (Liu et al., 2013)

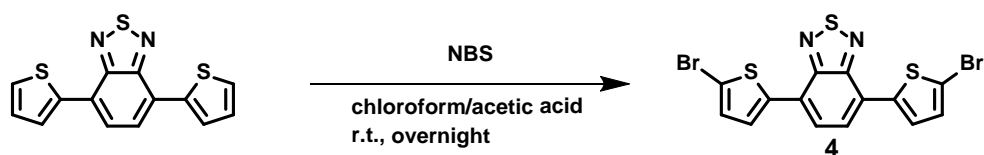


**Scheme 5-4** Synthesis of 4,7-di-2-thienyl-2,1,3-benzothiadiazole.

Using the method of Liu et al., The yellow crystals of 1 g (3.4 mmol) of 4,7-dibromo-2,1,3-benzothiadiazole (2) produced as described above and 1.79 g (8.5 mmol) of thiophene-2-boronic acid pinacol ester were added into a 100 ml three-necked round-bottomed flask. The mixture was dissolved in toluene (30 ml) and 2M aqueous Na<sub>2</sub>CO<sub>3</sub> (10 ml) under nitrogen. A catalyst of Pd(OAc)<sub>2</sub> (20 mg, 0.09

mmol)/Tri(o-tolyl)phosphine (54.2 mg, 0.18 mmol) (1:2 molar ratio, 4 mol % of mixture) was added into the flask (the colour was yellow) and then the mixture was strongly stirred at 95 °C under reflux for 24 h (the colour changed to red). The mixture was cooled down to room temperature and then deionised water was added to the mixture. The organic phase was separated and then washed with deionised water and brine three times respectively. The organic phase was dried over MgSO<sub>4</sub> and then filtered. The organic phase solvent was evaporated using a rotary evaporator. The crude product was purified by column chromatography using dichloromethane (DCM)/hexane (1/3, v/v). The product was crystallised in toluene/ethanol (1/1, v/v). Red crystals were obtained. Yield 0.33 g (32.3 %). <sup>1</sup>H NMR (500 MHz, CDCl<sub>3</sub>, δ ppm): 8.11 (dd, 2H), 7.88 (s, 2H), 7.45 (dd, 2H), 7.21 (dd, 2H). <sup>13</sup>C NMR (125 MHz, CDCl<sub>3</sub>, δ ppm): 152.5, 139.3, 128.1, 127.5, 126.8, 126, 125.8. Element Anal. Calcd. for C<sub>14</sub>H<sub>8</sub>N<sub>2</sub>S<sub>3</sub>: C, 55.97; H, 2.68; N, 9.33; S, 32.02; found: C, 56.15; H, 3.06; N, 9.07; S, 30.85.

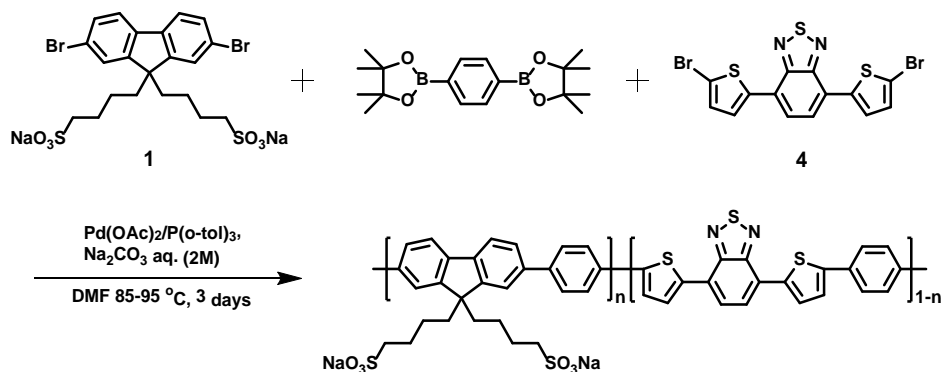
#### 5.2.3.5. Synthesis of 4,7-bis(5-bromo-2-thienyl)-2,1,3-benzothiadiazole (4) (Yang et al., 2005, Hou et al., 2009)



**Scheme 5-5** Synthesis of 4,7-bis(5-bromo-2-thienyl)-2,1,3-benzothiadiazole.

The procedures described by Yang et al. and Hou et al. were used to synthesise 4,7-Bis(5-bromo-2-thienyl)-2,1,3-benzothiadiazole. Starting with 0.3 g (1 mmol) of 4,7-di-2-thienyl-2,1,3-benzothiadiazole (3) which was dissolved in a mixture of chloroform (7 ml) and acetic acid (7 ml) in a 250 ml round-bottomed flask (the material was well dissolved in the solvent). N-bromosuccinimide (NBS) (0.4 g, 2.2 mmol) was then slowly added into the mixture. The mixture was stirred at room temperature overnight (about 24 h). Dark red solids were precipitated in the flask and filtered off. The product was washed with methanol and recrystallised in N,N-dimethylformamide (DMF). Dark red crystals were obtained. Yield 0.29 g (63.8 %). <sup>1</sup>H NMR (500 MHz, CDCl<sub>3</sub>, δ ppm): 7.80 (dd, 2H), 7.78 (s, 2H), 7.15 (dd, 2H). Element Anal. Calcd. for C<sub>14</sub>H<sub>6</sub>Br<sub>2</sub>N<sub>2</sub>S<sub>3</sub>: C, 36.70; H, 1.32; Br, 34.88; N, 6.11; S, 20.99; found: C, 29.93; H, 1.08; Br, 48.66; N, 4.92; S, 17.10.

**5.2.3.6. The polymerisation reaction used to synthesise Poly[(9,9-bis(4-sulfonatobutyl sodium) fluorene-alt-phenylene)-ran-(4,7-di-2-thienyl-2,1,3-benzothiadiazole-alt-phenylene)] (PSFP-DTBTP) (Lee et al., 2011, Kwak et al., 2010)**



**Scheme 5-6** Synthesis of conjugated polyelectrolyte.

The final stage of the synthesis was similar to the synthesis method previously described by Lee et al. and Kwak et al.. 0.63 g (0.98 mmol) of 2,7-dibromo-9,9-bis(4-sulfonatobutyl)fluorene disodium (1), 0.05 g (0.11 mmol) of 4,7-Bis(5-bromo-2-thienyl)-2,1,3-benzothiadiazole (4), and 0.36 g (1.09 mmol) of 1,4-phenylene-bisboronic acid pinacol ester purchased from Sigma-Aldrich were dissolved in the solvents of anhydrous DMF (10 ml) and 2M aqueous Na<sub>2</sub>CO<sub>3</sub> (15 ml) and placed in a 100 ml round-bottomed flask. After the monomers fully dissolved in the solvents, 1.23 mg (0.006 mmol) of Pd(OAc)<sub>2</sub> and 6.7 mg (0.022 mmol) of Tri(o-tolyl)phosphine (molar ratio of 1/4, 5 mol %) was added into the mixture then degassed with argon (if the solids were not well dissolved, the temperature was slightly increased to 40 °C). The reaction mixture was stirred at 85-90 °C under reflux for 3 d. The mixture was cooled down to room temperature and then poured into acetone. The precipitate was re-dissolved in deionised water. The solution was then dialysed using a cellulose membrane (MWCO 12,400) for 3 d (deionised water for dialysis was changed every day). A red product was obtained through freeze-drying, yield 0.22 g (37%). <sup>1</sup>H NMR (500 MHz, D<sub>2</sub>O, δ ppm): 8.39-6.78 (br, 10H), 3.88-3.51 (br, 3.6H), 2.68-2.02 (br, 3.6H), 1.58-1.09 (br, 3.6H), 0.83-0.6 (br, 3.6H).

## 5.3 Results and discussion

### 5.3.1. NMR analysis of monomers and PSFP-DTBTP

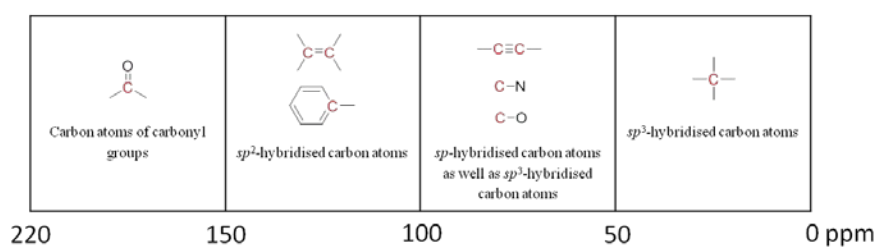
Nuclear magnetic resonance spectroscopy (NMR spectroscopy) is a powerful research technique to get information about the structure, dynamics, reaction state, and chemical environment of molecules. It uses the magnetic properties of certain atomic nuclei, which possesses intrinsic angular momentum or spin, immersed in a strong magnetic field. It deals with the phenomenon of nuclear magnetic resonance and provides specific information about the molecules as mentioned above. In order to know that the conjugated polyelectrolyte was synthesised properly NMR spectroscopy was carried out. This was done at many stages during the synthesis so the state of the products was checked at each stage. **Table 5-1**(a) and (b) show tables of correlation of  $^1\text{H}$  and  $^{13}\text{C}$  NMR chemical shift.

**Table 5-1** Correlation of (a)  $^1\text{H}$  and (b)  $^{13}\text{C}$  NMR chemical shift (Klein, 2015)

(a)

Type of Proton	Chemical Shift ( $\delta$ )	Type of Proton	Chemical Shift ( $\delta$ )
Methyl $\text{R}-\text{CH}_3$	$\sim 0.9$	Alkyl halide $\begin{array}{c} \text{H} \\   \\ \text{R}-\text{C}-\text{X} \\   \\ \text{R} \end{array}$	2-4
Methylene $>\text{CH}_2$	$\sim 1.2$	Alcohol $\text{R}-\text{O}-\text{H}$	2-5
Methine $-\text{CH}-$	$\sim 1.7$	Vinyl $\text{C}=\text{CH}_2$	4.5-6.5
Allylic $\text{CH}_2=\text{CH}-\text{CH}_2$	$\sim 2$	Aryl $\text{C}_6\text{H}_5$	6.5-8
Alkynyl $\text{R}-\text{C}\equiv\text{C}-\text{H}$	$\sim 2.5$	Aldehyde $\text{R}-\text{C}(=\text{O})-\text{H}$	$\sim 10$
Aromatic methyl $\text{C}_6\text{H}_5-\text{CH}_3$	$\sim 2.5$	Carboxylic acid $\text{R}-\text{C}(=\text{O})-\text{OH}$	$\sim 12$

(b)



The structure of all monomers and PSFP-DTBTP were confirmed by  $^1\text{H}$  and  $^{13}\text{C}$  NMR.

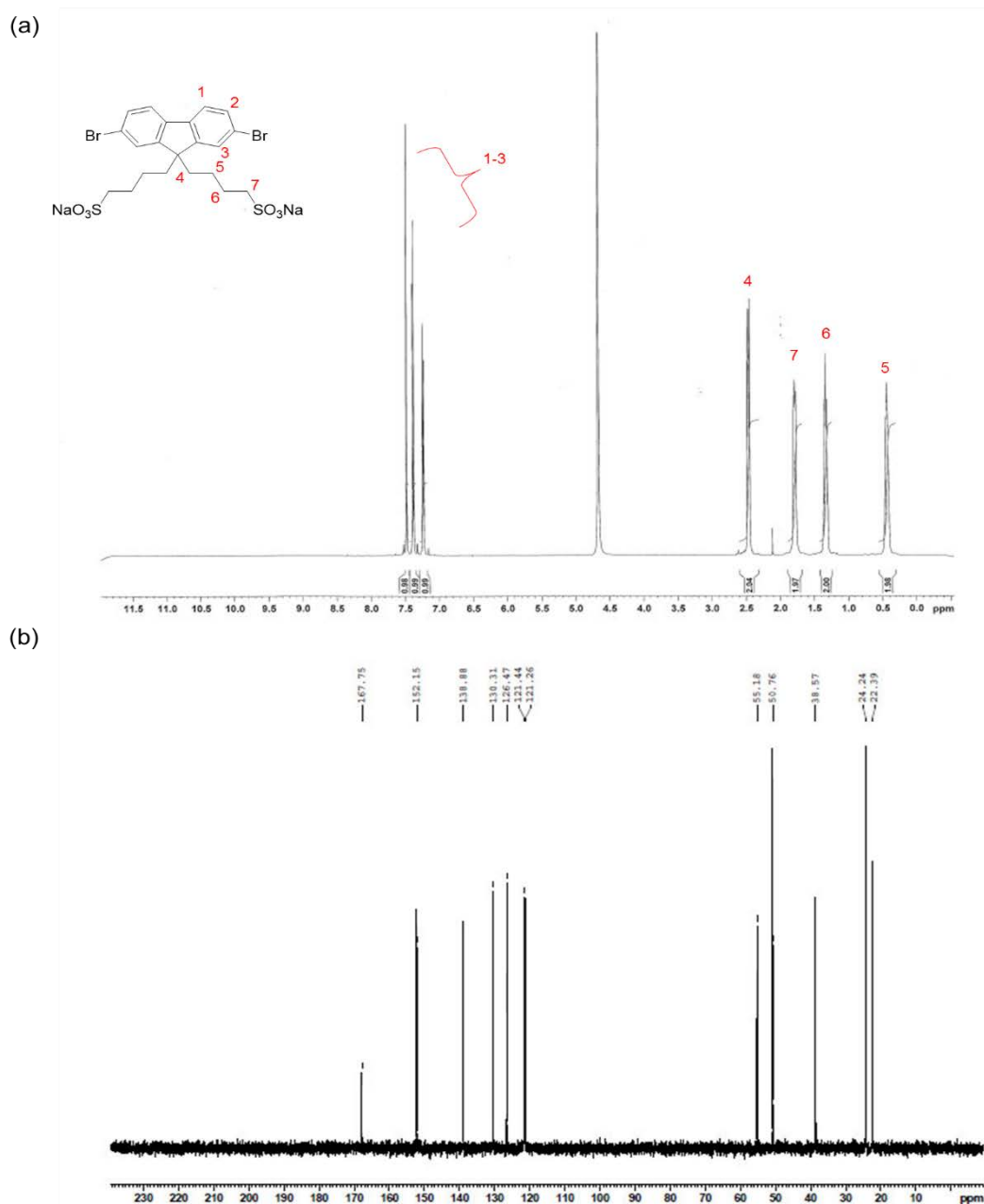


**Figure 5-1** (a)  $^1\text{H}$  NMR and (b)  $^{13}\text{C}$  NMR spectra of 2,7-dibromo-9,9-bis(4-sulfonatobutyl) fluorene disodium.

All NMR data from the monomers and PSFP-DTBTP are shown in **Figures 5-1 to 5-5**. **Figure 5-1**(a) and (b) shows the  $^1\text{H}$  and  $^{13}\text{C}$  NMR of synthesis of 2,7-Dibromo-9,9-bis(4-sulfonatobutyl)fluorene disodium (1). In  $^1\text{H}$  NMR, proton peaks of aromatic compounds are shown between 7.7 and 7.4 ppm and proton peaks of alkyl chains appear from 2.6 to 0.4 ppm (the deuterium oxide (solvent) peak appears at 4.8 ppm). In  $^{13}\text{C}$  NMR, carbon peaks of aromatic rings are indicated between 168 and 120 ppm and alkyl chains' peaks are shown from 55 to 22 ppm.

All the peaks are well matched with expected peaks chemical shift, confirming a successful synthesis.

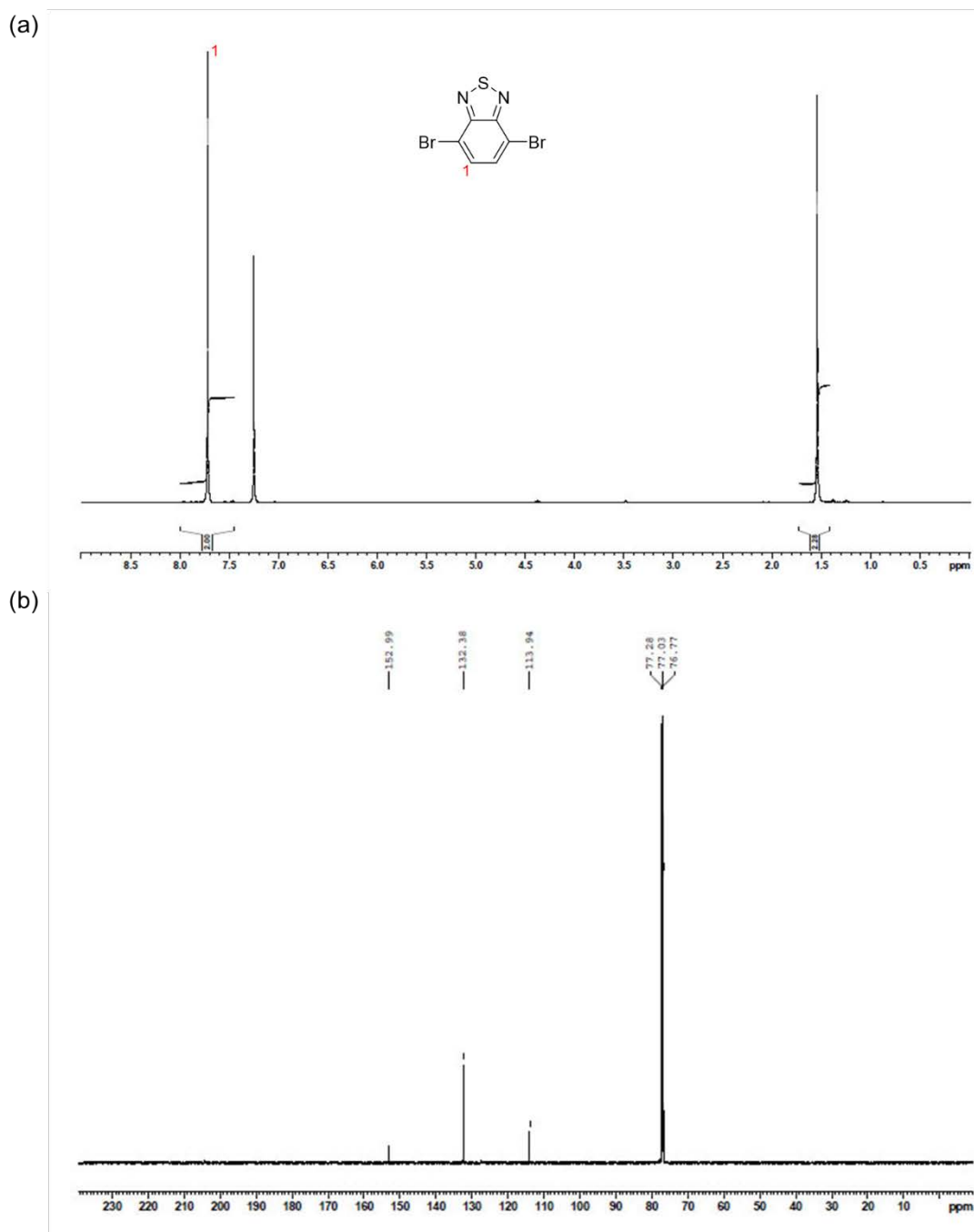
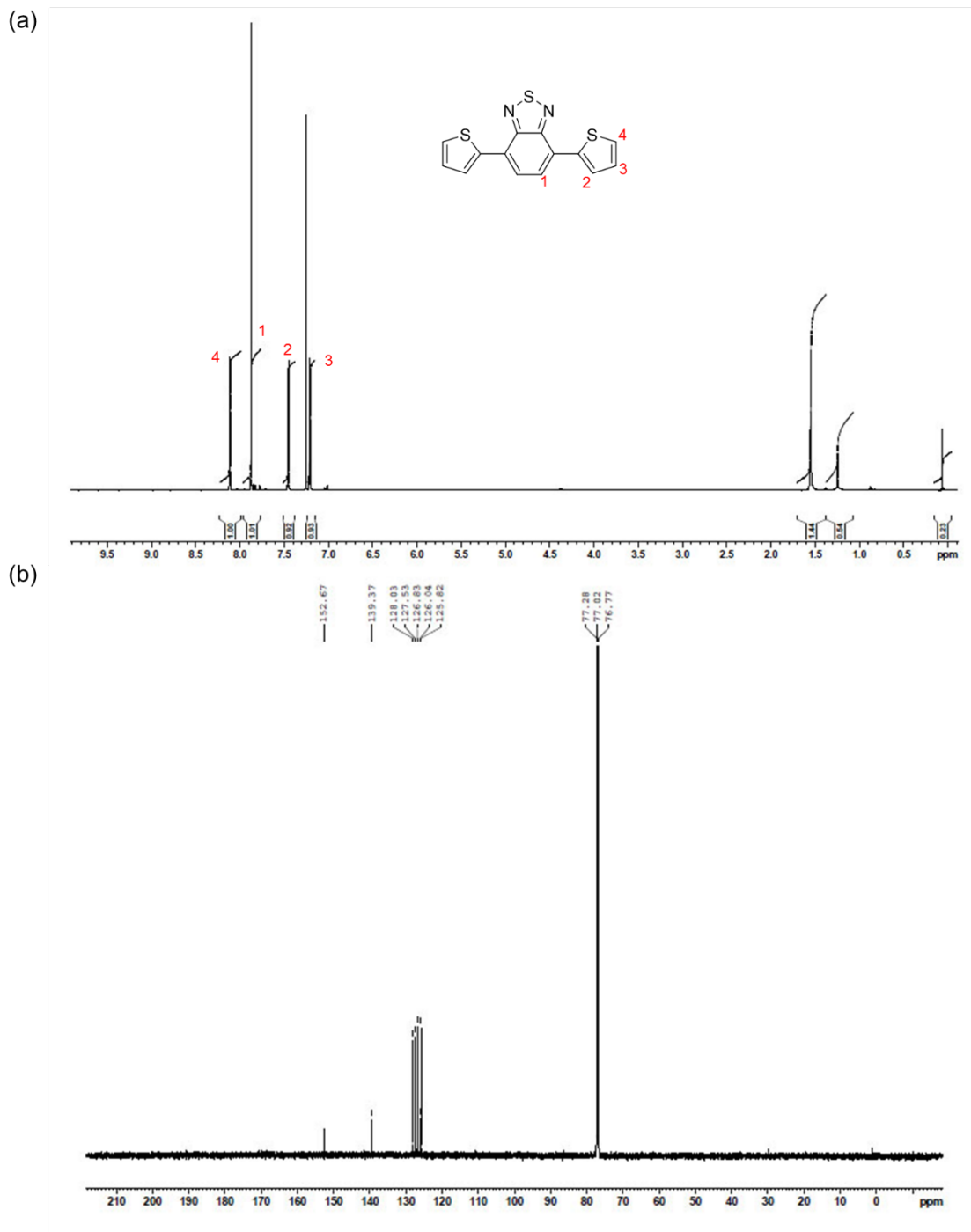


Figure 5-2(a) and (b) shows the  $^1\text{H}$  and  $^{13}\text{C}$  NMR spectra of 4,7-dibromo-2,1,3-benzothiadiazole (2). For this molecule (2), only one proton is in the aromatic group, so only one proton peak shows at 7.75 ppm (other peaks are chloroform-d (solvent) peak at 7.24 ppm and water peak at 1.5 ppm). In the  $^{13}\text{C}$  NMR spectrum, three carbon peaks from the aromatic group appear at 152.99, 132.38, and 113.94

ppm (the chloroform-d (solvent) peak is shown at 77.23 ppm). The solvent peak is always shown in the NMR spectrum and this peak appears at a specific point (77.23 ppm). Therefore, the solvent peak will be shown in further NMR data.



**Figure 5-3** (a) <sup>1</sup>H NMR and (b) <sup>13</sup>C NMR spectra of 4,7-di-2-thienyl-2,1,3-benzothiadiazole

**Figure 5-3(a)** and (b) is the <sup>1</sup>H and <sup>13</sup>C NMR spectra of 4,7-di-2-thienyl-2,1,3-benzothiadiazole (3). The proton peaks of the material appeared at 8.11, 7.88, 7.45,

and 7.21 ppm corresponding to aromatic rings in  $^1\text{H}$  NMR. Three more peaks are shown in comparison with (2) in the spectrum. The seven carbon peaks are shown between 152.5 and 125.8 ppm in  $^{13}\text{C}$  NMR and four more peaks appeared in the spectrum. From the two NMR data, it is evident that the molecule is well synthesised.

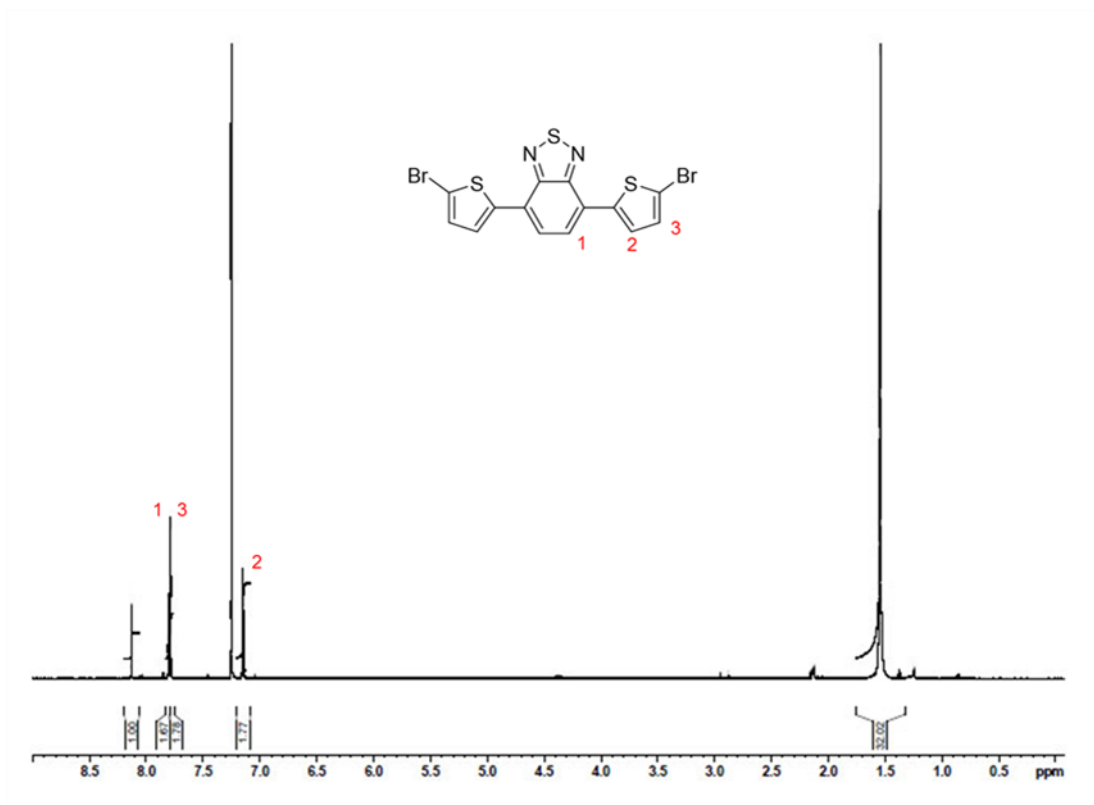


**Figure 5-4**  $^1\text{H}$  NMR spectrum of 4,7-bis(5-bromo-2-thienyl)-2,1,3-benzothiadiazole.

**Figure 5-4** shows the  $^1\text{H}$  NMR spectrum of 4,7-bis(5-bromo-2-thienyl)-2,1,3-benzothiadiazole (4). Three proton peaks in the aromatic group emerged at 7.80, 7.78, and 7.15 ppm. One proton peak was removed due to bromine attached to the ring in this material and the peaks are slightly shifted by a change of electron density due to the bromine within the molecule. Small impurity peaks also appeared as well as a big water peak. This indicated the sample was not well purified and dried.

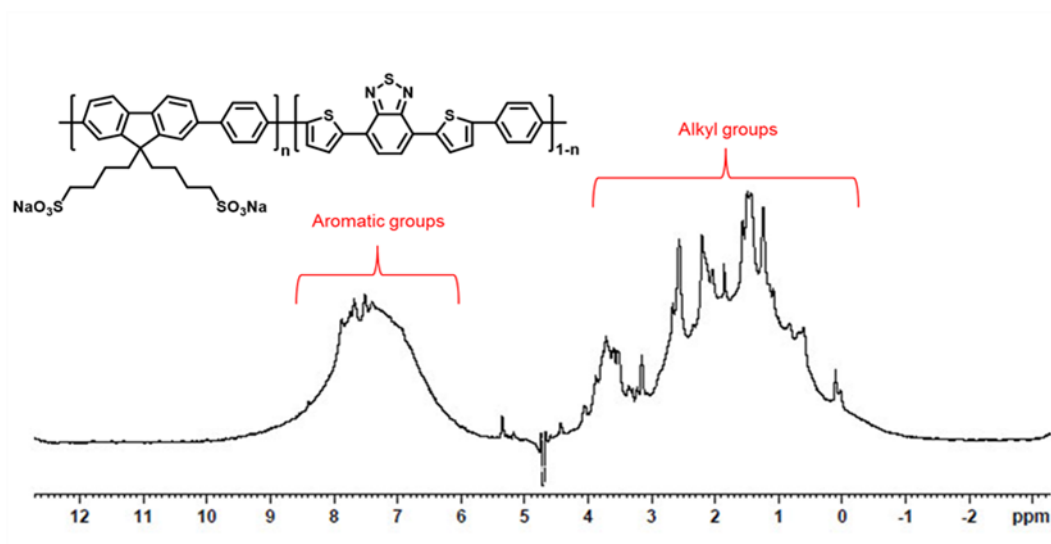


**Figure 5-5**  $^1\text{H}$  NMR spectrum of conjugated polyelectrolyte PSFP-DTBTP.

The  $^1\text{H}$  NMR spectrum of PSFP-DTBTP is shown in **Figure 5-5**. In  $^1\text{H}$  NMR, proton peaks of aromatic compounds are broadly present between 8.39 and 6.78 ppm and proton peaks of alkyl chains appear from 3.88 to 0.6 ppm.

All the synthesised materials are analysed by  $^1\text{H}$  and  $^{13}\text{C}$  NMR spectra. In the analysis, the molecular weight of PSFP-DTBTP was not measured by gel permeation chromatography (GPC) due to this technique generating inaccurate data for water soluble polymers. In general, for water-soluble polymers it is hard to measure molecular weight ( $M_w$ ) because it is not well dissolved in the organic solvent required for GPC and even if it is dissolved in protic solvent such as DMSO, the molecular weight of the polymer is not accurate. Therefore, the  $M_w$  of PSFP-DTBTP was predicted by dialysis membrane molecular weight cut-off (MWCO). The molecular weight of dialysis membrane in this experiment was 12,400, so the  $M_w$  of polyelectrolyte should be over 12,400.

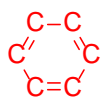
In addition, PSFP-DTBTP was synthesised three times in three different batches. However, the polyelectrolyte from a single batch was used for all experiments in the research to ensure consistency.

### 5.3.2. FT-IR spectrum of PSFP-DTBTP

Infrared (IR) spectroscopy measures the transmittance within the infrared region of the electromagnetic spectrum. This technique is used to identify and study chemicals by identifying what functional groups they have. To understand the

components of the polymer backbone and its functional groups, PSFP-DTBTP solid was measured by FT-IR spectroscopy. **Table 5-2** shows the IR spectroscopy correlation table of some functional groups.

**Table 5-2** Correlation IR absorption signals of some functional groups (McMurry, 1996)

Functional group class	Band position (cm <sup>-1</sup> )	Intensity of absorption
Alkanes, alkyl groups		
C-H	2850-2960	Medium to strong
Alkenes		
=C-H	3020-3100	Medium
C=C	1640-1680	Medium
Alkynes		
≡C-H	3300	Strong
—C≡C—	2100-2260	Medium
Alkyl halides		
C-Cl	600-800	Strong
C-Br	500-600	Strong
C-I	500	Strong
Alcohols		
O-H	3400-3650	Strong and broad
C-O	1050-1150	Strong
Aromatics		
	3030	Medium
	1600, 1500	Strong
Amines		
N-H	3300-3500	Medium
C-N	1030, 1230	Medium
Carbonyl compounds		
C=O	1680-1750	Strong
Carboxylic acids		
O-H	2500-3100	Strong and very broad
Nitriles		
C≡N	2210-2260	Medium
Nitro compounds		
NO <sub>2</sub>	1540	Strong

The FT-IR spectrum of PSFP-DTBTP is illustrated in **Figure 5-6**. Vibration bands of sulfonate groups in PSFP-DTBTP are confirmed at 1042 and 1167  $\text{cm}^{-1}$  and this is well matched with previous reports at approximately 1040 and 1180  $\text{cm}^{-1}$  (Borozenko et al., 2014, Martins et al., 2003). The bands of aromatic rings in PSFP-DTBTP were evident at 1462 and 1600  $\text{cm}^{-1}$ . Aromatic C-C stretch peaks appeared at 1462 and 1602  $\text{cm}^{-1}$ . C-H stretch peak of alkyl chain in polyelectrolyte also appeared at 2870  $\text{cm}^{-1}$ . All the peaks are well matched with previous reports and the correlating IR functional peaks. Therefore, we can confirm the all functional groups expected are present in the PSFP-DTBTP.

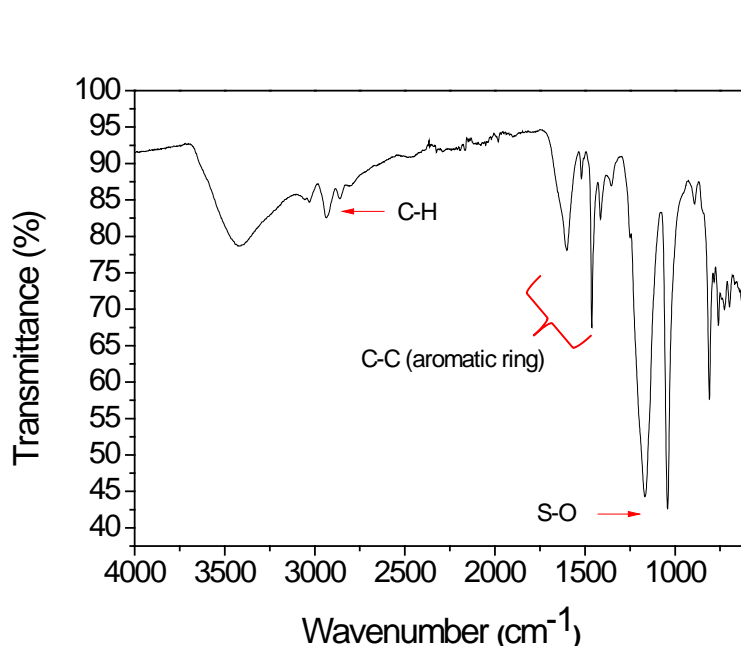


**Figure 5-6** ATR FT-IR spectrum of PSFP-DTBTP.

### 5.3.3. Optical properties of PSFP-DTBTP

To characterise the optical properties, a thin film of the conjugated polyelectrolyte was prepared on a clean glass substrate. 5 mg of the conjugated polyelectrolyte was dissolved in 1 ml of deionised water. The solution was spin-cast on the glass substrate at 6000 rpm for 40 sec and thermally annealed at 150 °C for 15 min. **Figure 5-7(a)** shows UV-vis absorption spectra and PL spectrum of PSFP-DTBTP solution in water and a thin film of PSFP-DTBTP. Corresponding photos of the solution and the films are shown in the **Figure 5-7(b)**.

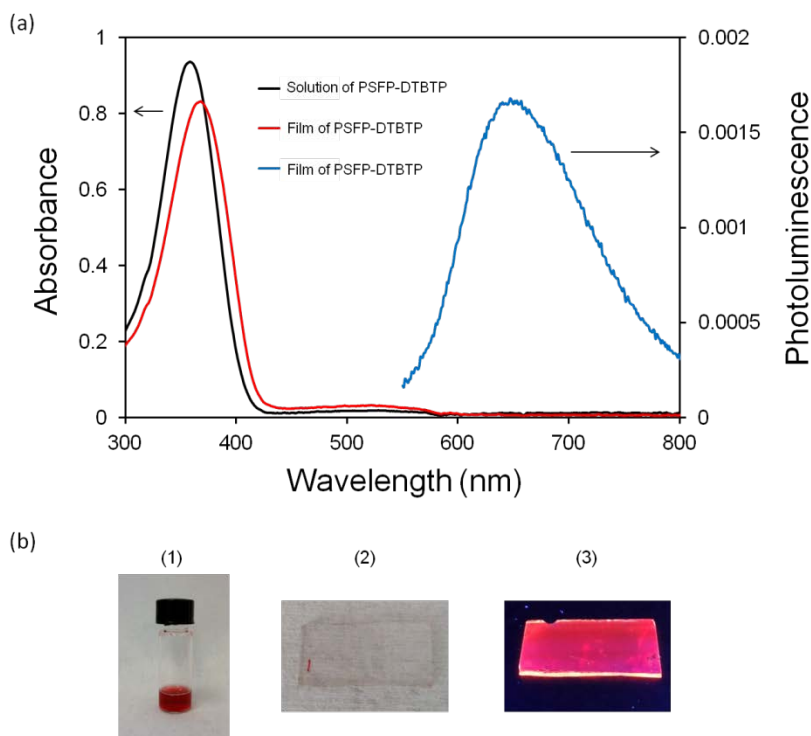


**Figure 5-7** (a) UV-vis absorption spectra of PSFP-DTBTP solution in water ( $2.76 \times 10^{-5}$  M [R. U.]) (black) and PSFP-DTBTP film (red) and PL spectrum of PSFP-DTBTP film (blue), (b) photographs of PSFP-DTBTP solution (1) and film (2) and film (3) taken under uv illumination.

The PSFP-DTBTP film shows a strong absorption peak at 366 nm from the fluorene-phenylene groups and a very weak absorption peak at around 530 nm with a shoulder edge around 590 nm from di-thienyl benzothiadiazole-phenylene groups. This result was red-shifted by about 8 nm from the PSFP-DTBTP solution peak at 358 nm due to a conjugation length change of rigid conjugated polymer backbone in the thin film. The number of aromatic rings along the backbone of the polymer determines its conjugation length. In the solution, the aromatic rings easily rotate relative to each other through the single bond in the polymer backbone. In the solid state, however, fewer twists of the polymer backbone increases co-planarity. Therefore, conjugation length of the polymer is increased in the solid state and the absorbance of the polymer film is slightly red-shifted. It was not possible to confirm that the peak of DTBTP group around 530 nm was changed from solution because of the weak signal strength, however the absorption peak strength of the film around 530 nm was increased compared to the solution peak. The PL spectrum of PSFP-DTBTP film showed a strong fluorescence peak at 647 nm, even though they had a strong absorption peak at 366 nm. The emission peak of molecules normally shows an absorbance edge peak due to the energy band gap of the system.

Excited electrons which are generated by absorption of light in molecules move to the conduction band edge and they emit fluorescence when they relax down from lowest conduction band (LUMO) to the valence band (HOMO). In such cases, the band gap energy is matched with the absorption band edge of the molecules. However, PSFP-DTBTP shows red fluorescence. This is because of exciton migration effects, they migrate from the electron donating fluorene group to the electron accepting benzothiadiazole group in the polyelectrolyte (Bardeen, 2011, Lee et al., 2011). These results were as expected because similar UV-vis absorption and PL peaks have been observed in previous reports.

#### 5.3.4. Cyclic voltammetry (CV) measurement of PSFP-DTBTP

The intention was to use PSFP-DTBTP as both an active layer and interfacial layer in photovoltaic cells, therefore CV was carried out to measure its electronic energy levels. A CV measurement is used to study the oxidation and reduction properties of the material and it is a useful technique to understand the HOMO and LUMO level of materials. The CV measurement of PSFP-DTBTP was performed in the presence of tetrabutylammonium perchlorate (0.1 M) as an electrolyte in acetonitrile and Ag/Ag<sup>+</sup> reference electrode (Ag wire in 0.01 M AgNO<sub>3</sub> solution). For calibration, the energy level of HOMO and LUMO was calculated using the equations below (Liang et al., 2009).

$$E_{\text{HOMO}} = -(\phi_{\text{ox}} + 4.8 - 0.082) \text{ eV}$$

$$E_{\text{LUMO}} = -(\phi_{\text{red}} + 4.8 - 0.082) \text{ eV}$$

Where  $\phi_{\text{ox}}$  and  $\phi_{\text{red}}$  are the onset oxidation point and onset reduction point vs. Ag/Ag<sup>+</sup> respectively. This equation is based on the redox potential of ferrocene/ferrocenium being -4.8 eV in absolute energy level below the vacuum level (located at 0.082 V to the Ag/Ag<sup>+</sup> electrode).

A CV curve of PSFP-DTBTP is shown in **Figure 5-8**. The onset point of oxidation  $\phi_{\text{ox}}$  is determined to be 0.66 V, which is determined by intersection point of two tangents (red lines in the **Figure 5-8**), and the energy level of highest occupied molecular orbital (HOMO) was calculated at -5.38 eV using the equation above. The reduction onset point is -1.33 V and the energy level of lowest unoccupied molecular orbital (LUMO) was calculated at -3.39 eV. Therefore, PSFP-DTBTP has band gap of 1.99 eV and it is well matched with UV-vis absorption spectrum,

although it was very weak peak at around 530 nm in PSFP-DTBTP, the spectral edge of PSFP-DTBTP absorption is around 600 nm. To convert wavelength to energy, it is calculated by Plank-Einstein relation below;

$$E = h\nu$$

$$\nu = \frac{c}{\lambda}$$

$$E = \frac{hc}{\lambda}$$

From the equation, where E is the energy of photon,  $\nu$  is frequency, h is the Plank constant, and c is speed of light.

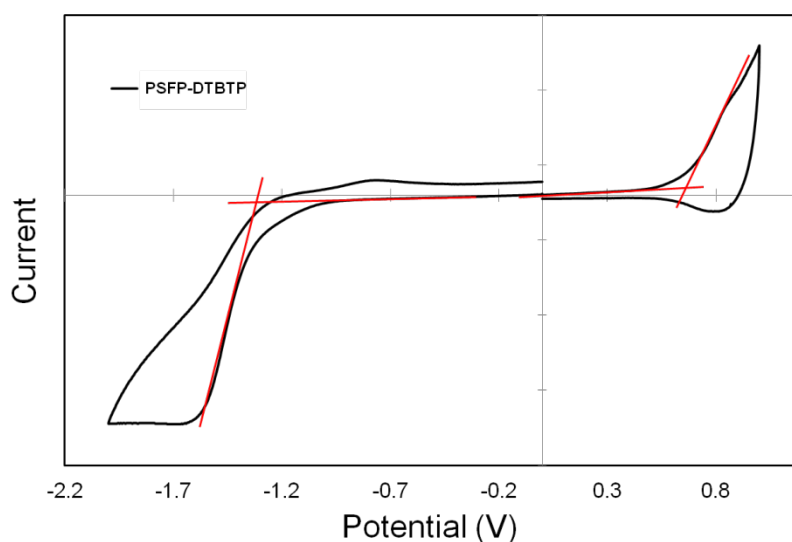


**Figure 5-8** Cyclic Voltammetry (CV) diagram of PSFP-DTBTP.

These results were compared to a similar CPE material poly[(9,9-bis(3'-(N,N-dimethylamino)propyl)-2,7-fluorene)-alt-2,7-(9,9-dioctylfluorene)] (PFN, fluorene groups are included). The energy levels compared reasonably well with PFN (HOMO of -5.61 eV and LUMO of -2.14 eV) (Zhang et al., 2010). The effect of the fluorene side group and the donor and acceptor nature of PSFP-DTBTP resulted in a lower oxidation and reduction potential than PFN. The ionic sulfonyl groups of PSFP-DTBTP lead to easier oxidation than the general fluorine. The DTBTP groups gave the polymer a lower reduction potential and lower band gap than PFN due to the donor and acceptor structure of the polymer (Cheng et al., 2009). Hou et al. reported fluorene-based red-emitting copolymer (9,9-dioctylfluorene and 4,7-di-2-thienyl-2,1,3-benzothiadiazole, PFO-DBT) (Hou et al., 2002). In the report, the HOMO and LUMO levels were slightly altered by

different ratios of fluorene and benzothiadiazole parts but generally the HOMO was -5.47 to -5.61 eV and the LUMO was -3.46 to -3.54 eV. As mentioned above, PSFP-DTBTP showed a slightly higher HOMO and LUMO level than PFO-DBT. However, PSFP-DTBTP showed higher band gap than PCDTBT (HOMO of -5.4 eV and LUMO of -3.6 eV). This is attributed to PSFP-DTBTP (blocked copolymer) consisting of 90% of fluorene groups (donor) and 10% of dithienyl-benzothiadiazole groups (acceptor). There is a relatively small amount of the acceptor groups compared to the donor groups. However, in comparison PCDTBT has alternating 1:1 donor and acceptor groups, so in PCDTBT the electrons are more readily moved from donors to acceptors.

#### **5.4. Conclusions**

The low band gap conjugated polyelectrolyte PSFP-DTBTP was synthesised and its structure was confirmed by NMR and IR. It dissolves easily at a concentration of <30 mg/ml in water. The CPE had sulfonate side chains in the fluorene groups to aid dissolution in water and this CPE had donor and acceptor groups in the polymer backbone. PSFP-DTBTP showed a strong absorption peak at 366 nm and a weak absorption peak at 530 nm. It showed red fluorescence and the PL peak was at 647 nm due to intramolecular charge transfer from the fluorene groups (donor) to the benzothiadiazole groups (acceptor) within the polymer backbone. The HOMO and LUMO energy levels were determined by CV to be -5.38 and -3.39 eV and the band gap of the CPE was found to be 1.99 eV. This CPE was synthesised in order to address the challenge of applying CPEs in PVCs and the electronic energy levels measured were suitable for application in PVCs.

#### **5.5. References**

- BARDEEN, C. 2011. Exciton Quenching and Migration in Single Conjugated Polymers. *Science*, 331, 544-545.
- BOROZENKO, O., MACHADO, V., SKENE, W. G. & GIASSON, S. 2014. Organophosphonic acids as viable linkers for the covalent attachment of polyelectrolyte brushes on silica and mica surfaces. *Polymer Chemistry*, 5, 5740-5750.

- CHENG, Y. J., YANG, S. H. & HSU, C. S. 2009. Synthesis of Conjugated Polymers for Organic Solar Cell Applications. *Chemical Reviews*, 109, 5868-5923.
- DUAN, C. H., CAI, W. Z., HSU, B. B. Y., ZHONG, C. M., ZHANG, K., LIU, C. C., HU, Z. C., HUANG, F., BAZAN, G. C., HEEGER, A. J. & CAO, Y. 2013. Toward green solvent processable photovoltaic materials for polymer solar cells: the role of highly polar pendant groups in charge carrier transport and photovoltaic behavior. *Energy & Environmental Science*, 6, 3022-3034.
- GRIMSDALE, A. C., CHAN, K. L., MARTIN, R. E., JOKISZ, P. G. & HOLMES, A. B. 2009. Synthesis of Light-Emitting Conjugated Polymers for Applications in Electroluminescent Devices. *Chemical Reviews*, 109, 897-1091.
- HOU, J. H., CHEN, H. Y., ZHANG, S. Q. & YANG, Y. 2009. Synthesis and Photovoltaic Properties of Two Benzo[1,2-b:3,4-b']dithiophene-Based Conjugated Polymers. *Journal of Physical Chemistry C*, 113, 21202-21207.
- HOU, Q., XU, Y. S., YANG, W., YUAN, M., PENG, J. B. & CAO, Y. 2002. Novel red-emitting fluorene-based copolymers. *Journal of Materials Chemistry*, 12, 2887-2892.
- KWAK, C. K., KIM, D. G., KIM, T. H., LEE, C. S., LEE, M. & LEE, T. S. 2010. Simultaneous and Dual Emissive Imaging by Micro-Contact Printing on the Surface of Electrostatically Assembled Water-Soluble Poly(p-phenylene) Using FRET. *Advanced Functional Materials*, 20, 3847-3855.
- KWON, N. Y., KIM, D., SON, J. H., JANG, G. S., LEE, J. H. & LEE, T. S. 2011. Simultaneous Detection and Removal of Mercury Ions in Aqueous Solution with Fluorescent Conjugated Polymer-Based Sensor Ensemble. *Macromolecular Rapid Communications*, 32, 1061-1065.
- LEE, J. H., KIM, D. G., KWON, N. Y., JANG, G. S., SON, J. H., LEE, M., CHO, H. J., KWEON, H. S. & LEE, T. S. 2011. Protein-Induced Aggregation of Fluorescent Conjugated Polyelectrolytes with Sulfonate Groups: Synthesis and Its Sensing Application. *Journal of Polymer Science Part a-Polymer Chemistry*, 49, 138-146.
- LIANG, Y. Y., FENG, D. Q., WU, Y., TSAI, S. T., LI, G., RAY, C. & YU, L. P. 2009. Highly Efficient Solar Cell Polymers Developed via Fine-Tuning of Structural and Electronic Properties. *Journal of the American Chemical Society*, 131, 7792-7799.

- LIU, B. & BAZAN, G. C. 2004. Interpolyelectrolyte complexes of conjugated copolymers and DNA: Platforms for multicolor biosensors. *Journal of the American Chemical Society*, 126, 1942-1943.
- LIU, M. F., CHEN, Y. L., ZHANG, C., LI, C. H., LI, W. W. & BO, Z. S. 2013. Synthesis of thiophene-containing conjugated polymers from 2,5-thiophenebis(boronic ester)s by Suzuki polycondensation. *Polymer Chemistry*, 4, 895-899.
- MARTINS, C. R., RUGGERI, G. & DE PAOLI, M. A. 2003. Synthesis in pilot plant scale and physical properties of sulfonated polystyrene. *Journal of the Brazilian Chemical Society*, 14, 797-802.
- MCMURRY, J. 1996. *Organic chemistry*, Pacific Grove, CA ; London, Brooks/Cole.
- PU, K. Y., LI, K. & LIU, B. 2010. Multicolor Conjugate Polyelectrolyte/Peptide Complexes as Self-Assembled Nanoparticles for Receptor-Targeted Cellular Imaging. *Chemistry of Materials*, 22, 6736-6741.
- PU, K. Y. & LIU, B. 2010. Fluorescence Turn-on Responses of Anionic and Cationic Conjugated Polymers toward Proteins: Effect of Electrostatic and Hydrophobic Interactions. *Journal of Physical Chemistry B*, 114, 3077-3084.
- QIAO, Q. Q., SU, L. Y., BECK, J. & MCLESKEY, J. T. 2005. Characteristics of water-soluble polythiophene: TiO<sub>2</sub> composite and its application in photovoltaics. *Journal of Applied Physics*, 98.
- SEO, J. H., GUTACKER, A., SUN, Y. M., WU, H. B., HUANG, F., CAO, Y., SCHERF, U., HEEGER, A. J. & BAZAN, G. C. 2011. Improved High-Efficiency Organic Solar Cells via Incorporation of a Conjugated Polyelectrolyte Interlayer. *Journal of the American Chemical Society*, 133, 8416-8419.
- SON, J. H., JANG, G. & LEE, T. S. 2013. Synthesis of water-soluble, fluorescent, conjugated polybenzodiazaborole for detection of cyanide anion in water. *Polymer*, 54, 3542-3547.
- YANG, J. H., GARCIA, A. & NGUYEN, T. Q. 2007. Organic solar cells from water-soluble poly(thiophene)/fullerene heterojunction. *Applied Physics Letters*, 90.
- YANG, N. J., LIAO, C. S. & CHEN, S. A. 2010. Hysteresis in Conjugated Polymer Thin Film Transistors Generated by Chain Relaxation. *Advanced Functional Materials*, 20, 1000-1004.

- YANG, R. Q., TIAN, R. Y., YAN, J. G., ZHANG, Y., YANG, J., HOU, Q., YANG, W., ZHANG, C. & CAO, Y. 2005. Deep-red electroluminescent polymers: Synthesis and characterization of new low-band-gap conjugated copolymers for light-emitting diodes and photovoltaic devices. *Macromolecules*, 38, 244-253.
- YAO, K., CHEN, L., CHEN, Y. W., LI, F. & WANG, P. S. 2011. Influence of water-soluble polythiophene as an interfacial layer on the P3HT/PCBM bulk heterojunction organic photovoltaics. *Journal of Materials Chemistry*, 21, 13780-13784.
- YU, D. Y., ZHANG, Y. & LIU, B. 2008. Interpolyelectrolyte complexes of anionic water-soluble conjugated polymers and proteins as platforms for multicolor protein sensing and quantification. *Macromolecules*, 41, 4003-4011.
- ZHANG, L. J., HE, C., CHEN, J. W., YUAN, P., HUANG, L. A., ZHANG, C., CAI, W. Z., LIU, Z. T. & CAO, Y. 2010. Bulk-Heterojunction Solar Cells with Benzotriazole-Based Copolymers as Electron Donors: Largely Improved Photovoltaic Parameters by Using PFN/A1 Bilayer Cathode. *Macromolecules*, 43, 9771-9778.
- ZHOU, H. Q., ZHANG, Y., MAI, C. K., COLLINS, S. D., NGUYEN, T. Q., BAZAN, G. C. & HEEGER, A. J. 2014. Conductive Conjugated Polyelectrolyte as Hole-Transporting Layer for Organic Bulk Heterojunction Solar Cells. *Advanced Materials*, 26, 780-785.

## 6. Polymer photovoltaic cells with conjugated polyelectrolyte

### 6.1. Introduction

Conjugated polyelectrolytes (CPEs) are conjugated polymers that contain ionic charged side chains which give it water-solubility (Huang et al., 2005, Tran-Van et al., 2004, Huang et al., 2004, Stork et al., 2002, Gaylord et al., 2001). During the past decade, CPEs have been used within the active layer (Yang et al., 2007, McLeskey and Qiao, 2006), electron transporting layers (ETLs) or hole transporting layers (HTLs) in OPVCs. CPEs when used as interlayers helped to improve the PCE of devices (Zhou et al., 2014, Duan et al., 2013, Seo et al., 2011, Zhang et al., 2010, He et al., 2011).

Yang et al. and McLeskey and Qiao reported water-soluble polythiophene based photovoltaic cells. Poly[2-(3-thienyl)-ethoxy-4-butylsulfonate] (PTEBS) was used as a water-soluble polythiophene. Yang et al. applied PTEBS and C60 as the electron donor and hole transporting layer and 2,9-dimethyl-4,7-diphenyl-1,10-phenanthroline (BCP) was used as the exciton blocking layer. They achieved a PCE of 0.43%. McLeskey and Qiao reported organic solar cells made from PTEBS and TiO<sub>2</sub>. PTEBS was used as the electron donor and TiO<sub>2</sub> as the electron acceptor. The highest PCE of the devices produced was 0.13%.

Seo et al. and Zhou et al. reported fluorene and cyclopenta-dithiophene based CPE as materials for application in thin ETLs and HTLs, respectively and showed an improvement of J<sub>SC</sub>, V<sub>OC</sub>, FF and PCE. Seo et al. reported that PCDTBT based PVCs achieved a PCE of over 6% with a positively charged poly[3-(6-trimethylammoniumhexyl)thiophene] (P3TMAHT) or poly(9,9-bis(2-ethylhexyl)-fluorene)-b-poly[3-(6-trimethylammoniumhexyl)thiophene] (PF2/6-b-P3TMAHT) interlayer where the employed device architecture was ITO/PEDOT:PSS/PCDTBT:PC<sub>71</sub>BM/CPE/Al (Seo et al., 2011). Zhou et al. showed an improvement of J<sub>SC</sub>, V<sub>OC</sub>, FF and PCE using CPE-K negatively charged conjugated polyelectrolyte as a HTL instead of PEDOT:PSS. The solar cell performance was increased up to 8.2% and their device structure was ITO/CPE-K/PTB7:PC<sub>71</sub>BM/Ca/Al (Zhou et al., 2014).

The use of a PSFP-DTBTP as both as an active layer and hole transporting layer is described in this chapter. Conjugated polyelectrolyte was synthesised as described in **Chapter 5** for use both as an active layer material therefore avoiding the need for organic solvents and also as an additive in the hole transporting layer so as to improve the efficiency of OPVCs. Improving the device efficiency is expected to improve the overall sustainability of OPVC fabrication by reducing the quantities of materials needed per Watt of power produced. Unfortunately, PSFP-DTBTP did not show any photovoltaic behaviour as an active layer material, but it did show an increase of the PCE and reproducibility of OPVC performance as an additive in the PEDOT:PSS layer.

## **6.2. Experimental**

### **6.2.1. Materials**

Poly(3,4-ethylenedioxythiophene) with poly(styrenesulfonate) (PEDOT:PSS – HC Stark Clevios P VP AI4083 (M121)), poly[N-9''-hepta-decanyl-2,7-carbazole-alt-5,5-(4',7'-di-2-thienyl-2',1',3'-benzothiadiazole)] (PCDTBT, (M1311) Mw: 34,900), [6,6]-phenyl-C71-butyric acid methyl ester (PC<sub>71</sub>BM), Poly(3-hexylthiophene-2,5-diyl) (P3HT, (M106) RR: 94.7%, Mw: 34,100), [6,6]-phenyl-C61-butyric acid methyl ester (PCBM), Indium tin oxide (ITO) glass substrates (S171, 20 Ω/square), and UV-epoxy resin were purchased from Ossila Ltd. Water-soluble C60 (C60-(N,N-dimethyl pyrrolidinium iodide)) was purchased from Solaris Chem Inc..

### **6.2.2. Organic photovoltaic cell fabrication (PSFP-DTBTP used as active layer)**

PSFP-DTBTP was synthesised as explained in **Chapter 5** for use as an active layer. Pre-patterned ITO glass substrates were washed with Hellmanex solution, isopropyl alcohol (IPA), and deionised (DI) water in an ultrasonic bath for 10 min each. The substrates were then dump rinsed twice in hot deionised water and once in cold deionised water. For the ITO/PEDOT:PSS/PSFP-DTBTP:W-C60/Ca/Al structured devices, PEDOT:PSS (filtered by 0.45 µm PVDF filter) was spin coated on the ITO glass substrate and thermally annealed for 15 min at 150 °C. A blend of PSFP-DTBTP and W-C60 (1:4 volume ratio) was spin coated at 2000 rpm on the PEDOT:PSS and thermally annealed at 150 °C for 15 min. For the

ITO/PEDOT:PSS:PSFP-DTBTP:W-C60/Ca/Al structured devices, PEDOT:PSS and PSFP-DTBTP:W-C60 were mixed in a 1:1 volume ratio. The mixture of PEDOT:PSS and PSFP-DTBTP:W-C60 was then spin coated at 2000 rpm and thermally annealed at 150 °C for 15 min. For ITO/PEDOT:PSS/PSFP-DTBTP/PCBM/Ca/Al, PEDOT:PSS was spin coated at 5000 rpm and annealed at 150 °C for 15 min on the ITO glass substrate and then PSFP-DTBTP was spin coated at 2000 rpm on the PEDOT:PSS layer and annealed at 150 °C. The substrate was then moved into the glovebox and PCBM (25 mg/ml) was spin coated at 2000 rpm on the PSFP-DTBTP layer. All the cathode layers for these various devices structures were deposited onto the active layer in a vacuum evaporator. Calcium (2.5 nm) and aluminium (100 nm) cathodes were deposited under  $1 \times 10^{-6}$  mbar. Devices were subsequently thermally annealed on a hot plate at 80 °C 15 min. All devices were finally encapsulated using uv-epoxy resin and a glass cover slide.

### **6.2.3. Organic photovoltaic cells fabrication (PSFP-DTBTP used as HTL or additive in HTL)**

All materials for device fabrication were purchased from Ossila Ltd. and used without further treatment apart from CPE and metals for electrodes. The device architecture used was glass substrate/ITO/hole transporting layer (HTL)/polymer:PC<sub>71</sub>BM/calcium (Ca)/aluminium (Al). PCDTBT:PC<sub>71</sub>BM (1:4 by weight, 20 mg/ml) or P3HT:PCBM (1:0.8 by weight, 25 mg/ml) were used as active layer materials. Pre-patterned ITO glass substrates were cleaned with the same process above mentioned. The HTL solution was filtered by PVDF filter (0.45 µm) and was spin-coated on the ITO substrate at 6000 rpm then annealed at 150 °C on a hot plate for 15 min. For the PCDTBT solar cells, PCDTBT (4 mg) was dissolved in chlorobenzene and the solution was heated at 80 °C with stirring overnight to fully solubilise. This was then mixed with PC<sub>71</sub>BM (16 mg) and the blend solution was heated at 80 °C for 2 h. The blend solution was filtered with PTFE (0.45 µm) before use. The blended mixture of PCDTBT:PC<sub>71</sub>BM was spin coated on the HTL at 700 rpm to achieve a thickness of ~75 nm as measured by J. A. Woollam Co. M-2000 ellipsometer. For the P3HT solar cells, solutions (25 mg/ml in chlorobenzene) of P3HT and PCBM were prepared separately in chlorobenzene and heated at 70 °C overnight. The P3HT and PCBM solutions were then mixed by volume portion of 1:0.8. A blend of P3HT and PCBM solution was heated at 70 °C over 3 h to fully dissolve and then filtered before use. The blended mixture of P3HT:PCBM was spin coated on the HTL at 2000 rpm to give a

thickness of ~70 nm. Calcium (2.5 nm) and aluminium (100 nm) cathodes (for PCDTBT solar cell) or aluminium (100 nm) cathode (for P3HT solar cells) were deposited onto the active layer in a vacuum evaporator. The base pressure of evaporation chamber was less than  $1 \times 10^{-6}$  mbar. Devices were thermally annealed on a hot plate at 80 °C (for PCDTBT PVCs) for 15 min or 150 °C (for P3HT PVCs) for 30 min. All devices were finally encapsulated by UV-epoxy resin and a glass cover slide.

#### **6.2.4. Preparation of films for characterisation**

In order to measure UV-vis absorption, thickness, AFM, and PL of the HTL, PEDOT:PSS or PEDOT:PSS:PSFP-DTBTP thin films similar samples were spin-coated at 6000 rpm for 40 sec on to glass substrates, silicon wafer or ITO patterned glass substrates. The glass substrates were cleaned using the same procedure used to prepare ITO substrates and the thin films were thermally annealed on a hotplate at 150 °C for 15 min after spinning. For the PL measurement of PSFP-DTBTP and PCDTBT, PSFP-DTBTP solution of 15 mg/ml in water were spin-coated at 6000 rpm for 40 sec on glass substrates and thermally annealed at 150 °C for 15 min then, PCDTBT (4 mg/ml in chlorobenzene) was spin-coated at 700 rpm for 30 sec and thermally annealed at 80 °C for 15 min.

#### **6.2.5. Instruments**

NMR, EA, UV-vis, PL, FT-IR, and CV for analysis of polymer are described in synthesis **Chapter 5**. The Ultraviolet photoemission spectroscopy (UPS) data was collected using the Kratos Axis Ultra DLD instrument with a helium (He) source. A 5 eV pass energy was set, and an area of 110  $\mu\text{m}$  diameter analysed. The data was collected between 25 eV to 0 eV in steps of 0.025 eV and for a 200 ms dwell time. The thickness of the HTL thin films were measured using a J. A. Woollam Co. M-2000 ellipsometer with a charge-coupled devices (CCD) camera detector. Atomic force microscope (AFM) images were obtained using a Veeco Dimension 3100 AFM with a Nanoscope IIIa controller and basic extender. It was operated in tapping mode with Bruker TESPA tapping mode cantilevers with a nominal spring constant of 42 N/m and a nominal resonant frequency of 320 kHz. Photoluminescence spectra were collected by Keithley 2700 multimeter with Laser- LDCU CW 450nm diode laser and detector was silicon diode. Samples were measured under vacuum at approximately  $1 \times 10^{-3}$  mbar.

### 6.3. Use PSFP-DTBTP in active layer

In order to reduce the usage of organic solvents for devices, a CPE was synthesised and applied as part of the active layer. As mentioned in the synthesis **Chapter 5**, the CPE has donor and acceptor parts and it showed low band gap about 2.0 eV.

#### 6.3.1. Thickness change of PEDOT:PSS HTL caused by spin casting subsequent water soluble layers

Before using PSFP-DTBTP as an active layer, it was necessary to test the thickness of the PEDOT:PSS after spin casting water on top of the HTL to check whether the PEDOT:PSS is entirely washed away during the process or not. Water was spin cast on top of both an annealed and as cast PEDOT:PSS films. Because both materials can be dissolved in water the PEDOT:PSS may be washed away by spin coating subsequent water based solutions. Thin films of PEDOT:PSS were fabricated on the pieces of silicon wafer and the film thickness was measured by ellipsometry. To measure thickness before and after water casting on the PEDOT:PSS film, PEDOT:PSS was spin coated at 5000 rpm on the silicon wafer then one sample was not annealed and another sample was annealed at 150 °C for 15 min. Two of each type of film was made. Water was spin coated on each PEDOT:PSS film at 2000 rpm. The thickness of all four films was measured. **Table 6-1** shows the change of thickness before and after water casting with non-annealed and annealed at 150 °C PEDOT:PSS.

**Table 6-1** The average film thickness of non-annealed and annealed PEDOT:PSS before and after water casting (the data was collected by 2 films of each condition)

Samples	Thickness of film	
	Before water drop	After water drop
Non-annealed	45 ± 1 nm	3 ± 1.5 nm
Annealed at 150 °C	42 ± 0.6 nm	31 ± 1 nm

As shown in **Table 6-1**, almost all PEDOT:PSS was washed out by water at non-annealed film, but the PEDOT:PSS film annealed at 150 °C showed 42 and 31 nm thickness before and after water dropping respectively.

### 6.3.2. Fabrication of water-based photovoltaic cells

To fabricate a water based BHJ photovoltaic cell, both PCBM and water-soluble C60 (W-C60) (C60-(N,N-dimethyl pyrrolidinium iodide)) was used as an electron acceptor. The molecular structures of materials are shown in **Figure 6-1**.

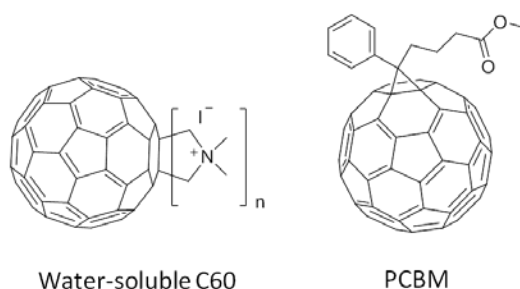


**Figure 6-1** Structures of water-soluble C60 and PCBM.

Four types of device structure were produced as shown in **Figure 6-2**. The architecture shown in **Figure 6-2(a)** is similar to the usual BHJ OPVC with an active layer consisting of a blend of CPE and W-C60 and the concentration of CPE and W-C60 was 25 mg/ml (1:4 volume blend ratio). The blend of CPE:W-C60 and PEDOT:PSS used in **Figure 6-2(b)** was prepared in a 1:1 volume ratio. This device architecture required only one spin-casting step for all the organic materials. In **Figure 6-2(c)** the blend of CPE and PEDOT:PSS was 1:1 by volume ratio and PCBM (25 mg/ml) was used as an electron transporting layer. In order to avoid aggregation of CPE and W-C60, PCBM was applied in the device as a separate layer. In **Figure 6-2(d)**, the concentrations of CPE and PCBM were 25 mg/ml. This architecture of device has a bi-layer structure rather than a BHJ active layer in the device to compare to device's architectures in **Figure 6-2(a)** and (c).

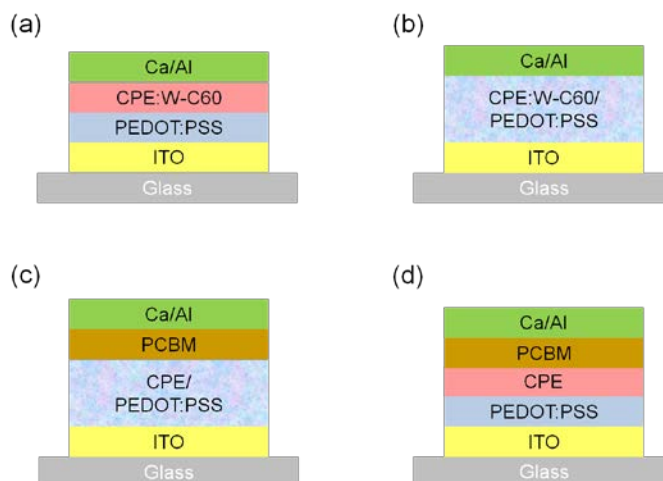


**Figure 6-2** Four kinds of architecture of devices using PSFP-DTBTP as an active layer.

Unfortunately, none of these devices showed any photovoltaic behaviour. There were two possible reasons for this. First, when making the blend of CPE and W-C60, many aggregations of solids appeared. It may be that because CPE and W-C60 are negatively and positively charged materials respectively they are bind well together to form aggregates and therefore fall out of solution prior to spin casting. Even if CPE and W-C60 were dissolved in solvent separately, they still made precipitates after mixing them. As a result, the solution was much too transparent after filtering. Filtering is needed to fabricate uniform films free of defects by removing undissolved or large particles. Therefore, it was not possible to make a proper functioning bulk-heterojunction layer from the materials due to their aggregation. Secondly, the absorption wavelength of the CPE is short. As shown in **Figure 5-9** in **Chapter 5**, the main absorption peak of PSFP-DTBTP is around 370 nm and only a weak absorption peak is shown around 530 nm. Therefore, although CPE absorbs the short wavelengths, a lot of photons pass thorough the active layer at longer wavelength so the devices cannot harvest large amounts of photons. In order to increase of absorption around 530 nm, CPE was synthesised using 1:1 ratio of donor (fluorene group) and acceptor (dithienyl-benzothiadiazole group). However, when the relative fraction of acceptor groups was increased, the polymer would not dissolve in water.

#### **6.4. Use PSFP-DTBTP in HTL**

In order to study the PCE of devices made using CPE as an additive in the HTL or as a replacement HTL, photovoltaic cells with typical blends of PCDTBT and PC<sub>71</sub>BM and P3HT with PCBM as the active layer BHJ were fabricated. ITO and calcium/aluminium (Ca/Al) were used as the anode and cathode materials, respectively. Device architecture of the OPVCs was ITO/PEDOT:PSS:PSFP-DTBTP /Active layer/(Ca)/Al and they were compared to more standard ITO/PEDOT:PSS/Active layer/(Ca)/Al reference devices. In this Chapter, a Ca/Al cathode layer was used for PCDTBT PVCs to allow direct comparison to the P3HT PVCs. According to previous reports (Watters et al., 2012), PCDTBT PVCs with a Ca/Al cathode showed high  $V_{OC}$ , relatively high  $J_{SC}$  and significant enhanced FF.

#### 6.4.1. Optical characterisation of conjugated polyelectrolyte with PEDOT:PSS and PCDTBT:PC<sub>71</sub>BM

Hole transporting layer blends of PEDOT:PSS:PSFP-DTBTP (with 2 mg/ml or 5 mg/ml or 8 mg/ml of the CPE dissolved in the as acquired PEDOT:PSS solution) were named as HTL2, HTL5, and HTL8 respectively in this chapter. HTL2 related to 2 mg of PSFP-DTBTP per 1 ml of PEDOT:PSS solution. HTL5 related to 5 mg of PSFP-DTBTP per 1 ml of PEDOT:PSS solution. HTL8 related to 8 mg of PSFP-DTBTP per 1 ml of PEDOT:PSS solution. **Figure 6-3(a)** shows the UV-vis absorption spectra of the PSFP-DTBTP, PEDOT:PSS, HTL2, HTL5, and HTL8 thin films after spin casting onto glass substrates. To measure the UV-vis absorption of the thin films, PSFP-DTBTP, PEDOT:PSS, HTL2, HTL5, and HTL8 were spin coated at 6000 rpm on glass substrates for 40 sec and then thermally annealed at 150 °C for 15 min. The PSFP-DTBTP film shows a strong  $\pi$ - $\pi^*$  absorption peak at 367 nm from fluorene-phenylene groups and a very weak absorption peak at around 530 nm from intramolecular charge transfer between donor and acceptor units along polymer chains. The 367 nm absorption peak observed in the PSFP-DTBTP film was shifted by about 9 nm compared to the solution spectra where the peak was at about 358 nm. The number of co-planar rings along the backbone of the polymer determines its conjugation length. The longer the conjugation length, the smaller the separation between adjacent energy levels due to quantum confinement effects. Fewer twists in the polymer increase the co-planarity and can result from changes in the environment. Therefore the absorbance shift is attributed to increasing the conjugation length of the rigid backbone in the film, when the polymer is in the solid state. However, we could not confirm whether the peak from the DTBTP group around 530 nm was changed from solution because of the weak signal strength. The pristine PEDOT:PSS film did not show any specific absorption features. HTL films showed a small absorption peak at 372 nm which increased with increasing concentration (2 mg/ml, and 5 mg/ml) and it has a very small trace of an absorption peak at around 530 nm from PSFP-DTBTP. The absorption peaks of HTL2 and HTL5 were slightly red shifted from the PSFP-DTBTP peak at 367 to 372 nm. However, HTL8 was blue shifted and had an absorption peak at 362 nm.

Although it was very weak peak at around 530 nm in PSFP-DTBTP, the spectral edge of PSFP-DTBTP absorption is around 600 nm which equates to a band gap

for PSFP-DTBTP of 2.0 eV from the UV-vis absorption spectra and it was (1.99 eV) in the CV measurement in synthesis **Chapter 5**.

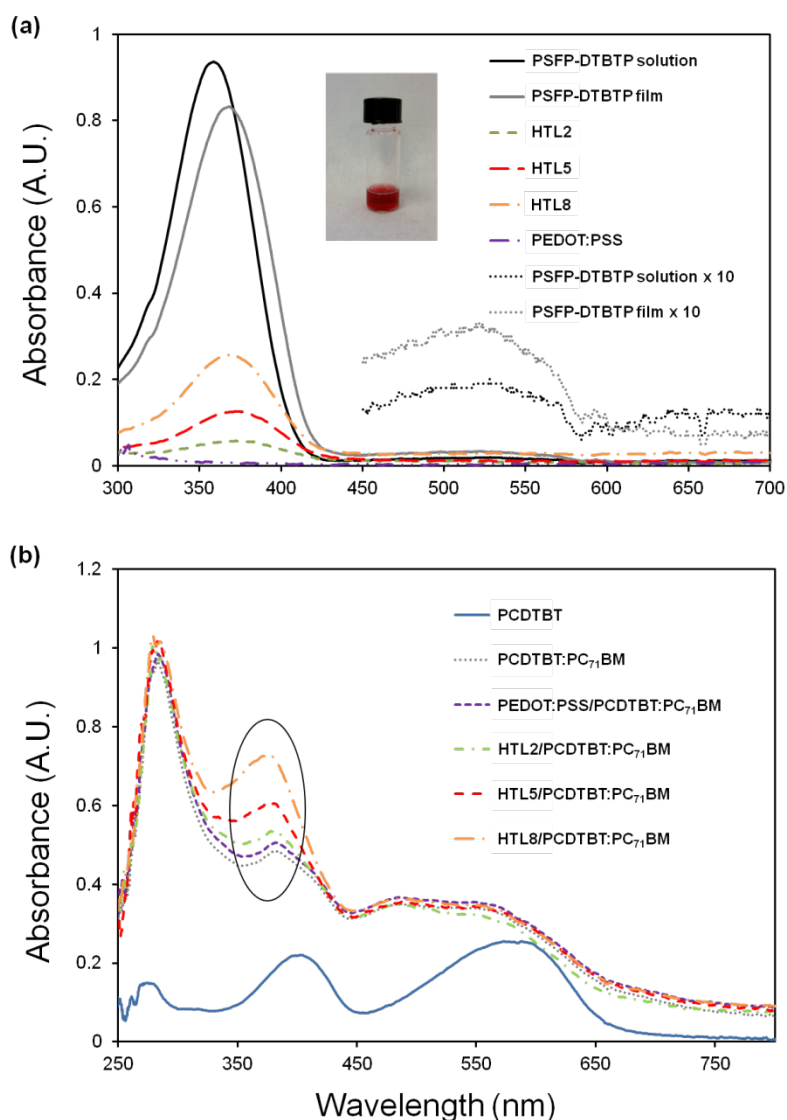


**Figure 6-3** UV-vis absorption spectra of (a) PSFP-DTBTP film (black), PEDOT:PSS (red), HTL2 (blue), HTL5 (purple), and HTL8 (green) and (b) PCDTBT (black), PCDTBT:PC<sub>71</sub>BM (red), PEDOT:PSS/PCDTBT:PC<sub>71</sub>BM (blue), and HTL2 (purple), or HTL5 (green), HTL8/PCDTBT:PC<sub>71</sub>BM (orange) (HTL is hole transporting layer of PEDOT:PSS:PSFP-DTBTP).

In order to understand the combined absorption abilities of the active layer and the HTLs, UV-vis absorption spectra of PCDTBT, PCDTBT:PC<sub>71</sub>BM (blend ratio of 1:4) and HTL/PCDTBT:PC<sub>71</sub>BM were measured and are shown in **Figure 6-3(b)**. All HTLs were spin coated on glass substrates at 6000 rpm and the HTLs were thermally annealed at 150 °C for 15 min then PCDTBT:PC<sub>71</sub>BM was spin coated at

700 rpm on the HTL and thermally annealed at 80 °C for 15 min. The PCDTBT film showed a strong absorption peak at 403 nm and strong broad absorption band from 560 to 590 nm (Yi et al., 2011). The blended PCDTBT:PC<sub>71</sub>BM film showed increased absorption ability from 300 to 580 nm due to absorption by PC<sub>71</sub>BM. PEDOT:PSS/PCDTBT:PC<sub>71</sub>BM did not show any specific difference with PCDTBT:PC<sub>71</sub>BM. However, HTL2, HTL5, and HTL8/PCDTBT:PC<sub>71</sub>BM films showed a peak around 370 nm which increased with increasing CPE concentration in the HTL and this corresponds with the results for the PSFP-DTBTP absorption peak in **Figure 6-3(a)**.

#### 6.4.2. FT-IR spectra of CPE and HTL layers

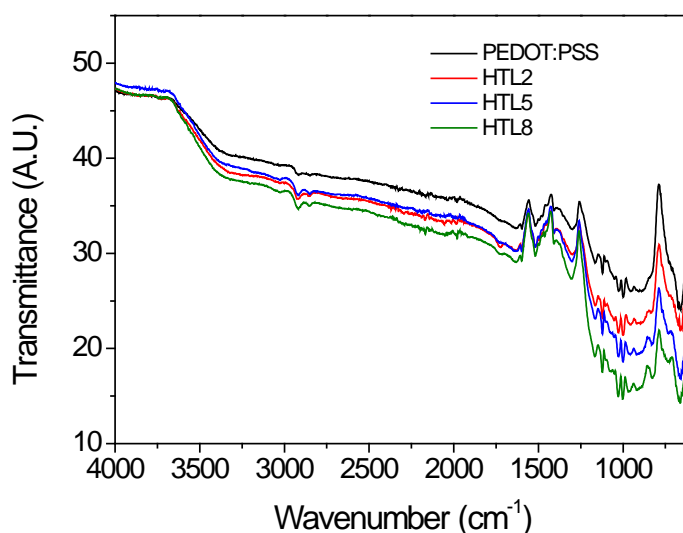


**Figure 6-4** ATR FT-IR transmittance of PEDOT:PSS (black), HTL2 (red), HTL5 (blue), and HTL8 (green).

The FT-IR spectra of polymers PEDOT:PSS, HTL2, HTL5, and HTL8 are shown in **Figure 6-4**. They were measured to better understand the components within the HTL. Comparing the spectra of PEDOT:PSS and PSFP-DTBTP, it is hard to determine whether PSFP-DTBTP was left in the films because PEDOT:PSS has a similar structure and functional groups and therefore similar FT-IR spectrum. However, when PSFP-DTBTP is included in PEDOT:PSS, the amounts of the absorbance due to the functional groups and molecules present increased and the transmittance at these specific bands decreased. As shown in **Figure 6-4**, the spectra show an increase in absorption around 1300-1000 cm<sup>-1</sup> when the PSFP-DTBTP concentration was increased and the spectra were normalised for

comparison. A weak C-H stretch peak of alkyl chain in CPE was observed at  $2870\text{ cm}^{-1}$  in the HTL peaks.

### 6.4.3. The characterisation of the band gaps of each layer

**Figure 6-5(a)** summarises the energy levels of ITO, PEDOT:PSS, PSFP-DTBTP, P3HT, PCDTBT, PC<sub>71</sub>BM, PCBM, Ca, and Al and is similar to those reported elsewhere (Yao et al., 2011, Thompson and Frechet, 2008, da Silva et al., 2015). As shown in **Figure 6-5(a)**, the HOMO level of PSFP-DTBTP is located between the HOMO level of PCDTBT and PEDOT:PSS, so holes generated in PCDTBT should be able to easily move to the ITO electrode. Also electrons will be blocked from going to ITO anode. In addition, absorption by the PSFP-DTBTP means it is possible to make excitons in the PSFP-DTBTP. Therefore, it would be possible that more electrons move to the cathode via PCDTBT and PC<sub>71</sub>BM and holes move to anode ITO via PEDOT:PSS. However, in comparison the HOMO and LUMO levels of PSFP-DTBTP are lower than HOMO and LUMO levels of P3HT, respectively, so in the P3HT devices the PSFP-DTBTP would interrupt the flow of holes to the anode. As a result, it is unsurprising that the P3HT device with PSFP-DTBTP showed a reduction of PCE as described in **Figure 6-7(c)** and **Table 6-1**.

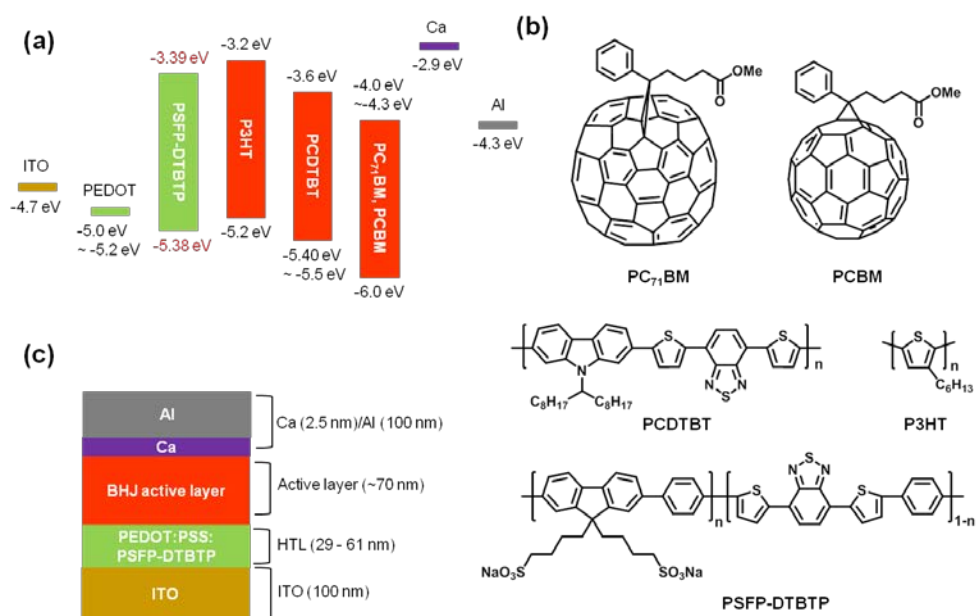


**Figure 6-5** (a) The energy diagram of materials in a photovoltaic cell (PSFP-DTBTP band gap is measured by CV, others are from previous report (Yao et al., 2011, Thompson and Frechet, 2008, da Silva et al., 2015)), (b) the structure of PSFP-DTBTP, PCDTBT, and PC<sub>71</sub>BM, and (c) the architecture of BHJ organic photovoltaic cell.

#### 6.4.4. Work function of HTLs

In order to confirm the electronic properties of the HTLs with CPE additive, the work functions of thin films of pristine PEDOT:PSS, and blends of PSFP-DTBTP mixed with PEDOT:PSS were measured by ultraviolet photoemission spectra (UPS) (helium lamp at 21.2 eV). UPS spectra of PEDOT:PSS, HTL2, HTL5 and HTL8 were measured three times. All 3 data sets showed similar trends. The data from one of these measurements are shown in **Figure 6-6**. The work function is seen as a "cut-off" in the UPS spectrum at the low kinetic energy side. As shown in **Figure 6-6**, the work function of PEDOT:PSS, HTL2, HTL5, and HTL8 are 4.95, 5.07, 5.14, and 5.11 eV, respectively. The HTL5 has higher work function compare to the others.

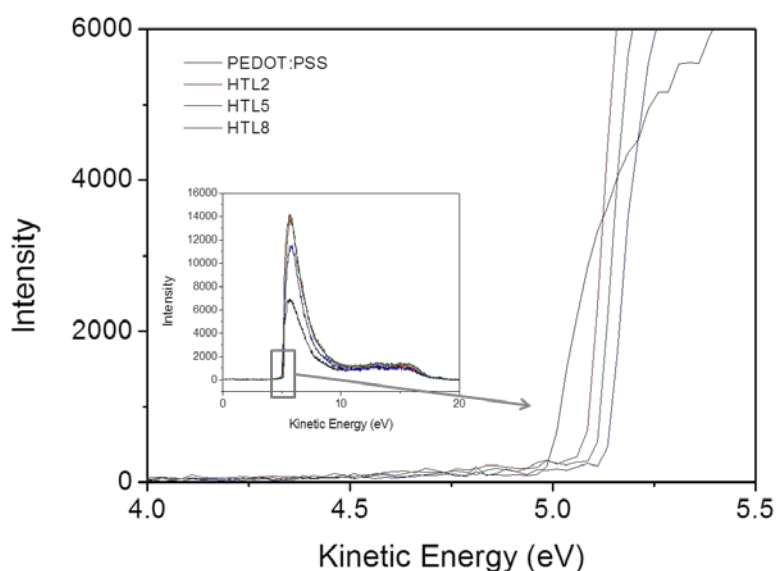


**Figure 6-6** The UPS spectra of PEDOT:PSS, HTL2, HTL5, and HTL8 thin films.

#### 6.4.5. Photovoltaic properties of devices with CPE additive in HTL

The architecture of the PCDTBT BHJ PVCs was ITO/PEDOT:PSS, or HTL2, or HTL5, or HTL8/PCDTBT:PC<sub>71</sub>BM/Ca/Al and P3HT BHJ PVCs were ITO/PEDOT:PSS, or HTL5/P3HT:PCBM/Al. In order to investigate the performance of the CPE additive in P3HT PVCs, HTL5 (the best HTL for PCDTBT) was chosen for comparison with HTL5 in PCDTBT PVCs. The device's structure, materials, and energy level of each material are described in **Figure 6-5(c)**. The corresponding J-V curves and external quantum efficiency (EQE) of the

devices are shown in **Figure 6-7** and their photovoltaic characteristics are described in **Table 6-2**. The J-V curves of the BHJ PCDTBT photovoltaic cell devices were measured using a solar simulator under AM 1.5G irradiation. Reference PCDTBT devices showed  $J_{SC}$  of  $-8.63 \pm 1.7$  mA/cm<sup>2</sup>,  $V_{OC}$  of  $0.84 \pm 0.03$  V, and FF of  $62.28 \pm 7.85\%$ . The average PCE was 4.63% and the best PCE was 5.36%. HTL2 devices and HTL8 devices showed better average efficiency, but the reference devices recorded a better champion PCE than HTL2 and HTL8. However, the HTL5 devices recorded an improved  $J_{SC}$  of  $-9.46 \pm 0.88$  mA/cm<sup>2</sup>,  $V_{OC}$  of  $0.88 \pm 0.03$  V, FF of  $66.25 \pm 2.85\%$ , average PCE of 5.26% and the best PCE of 5.67%, which are evidently better results than other devices. In general, enhancement of all parameters  $J_{SC}$ ,  $V_{OC}$ , and FF for the HTL5 device resulted in an improvement of both average and best efficiency. The devices with CPE added showed higher  $V_{OC}$  by 0.02 – 0.1 V than the reference device. The ideal maximum  $V_{OC}$  in photovoltaic cells is defined as the difference between the HOMO level of the donor and the LUMO level of the acceptor, but the  $V_{OC}$  in actual devices showed a lower value than the  $V_{OC}$  of ideal devices. Because the actual  $V_{OC}$  is affected by the work function of electrodes and interfacial layer (Zhao et al., 2015, Ratcliff et al., 2013, Greiner and Lu, 2013). The devices with CPE added have a lower work function (-5.14 eV) than pristine PEDOT:PSS (-4.95 eV) which gave the devices with CPE added a higher  $V_{OC}$  than the reference device. The PCE of reference PCDTBT devices delivered higher performance when compared to previous reports under similar experimental condition (Watters et al., 2012, Yi et al., 2011). As mentioned in the introduction section, Seo et al. reported the PCE of PCDTBT PVCs were increased by an interlayer of fluorene and thiophene based conjugated copolymer deposited from a methanol solution beneath the Al cathode (Seo et al., 2011). The PCE of the devices increased from 5.3 to 6.5%. When compared to this research, it showed a PCE 0.8% higher than reported here. However, it should not be directly compared to this research because the CPE was used in a different layer. In addition, they used methanol as the CPE solvent, but water to deposit the CPE in this research. Therefore, the device in this research is more environmental friendly.

In **Figure 6-7(b)**, the HTL5 based device showed a lower EQE below 390 nm. This is attributed to some of the light <390 nm being absorbed by the CPE rather than PCDTBT and therefore not undergoing efficient charge separation at the interfaces within the BHJ. However, as demonstrated below in our PL experiments significant energy transfer can occur between the CPE and PCDTBT which minimises this effect. Above 390 nm the EQE of the HTL5 device is higher than

the PEDOT:PSS device, which is attributed to improved charge transfer into the HTL because of the improved match between the work function of the HTL and the PCDTBT BHJ layer HOMO level. The HTL5 device has a higher  $J_{SC}$  than the pristine PEDOT:PSS based device because the charge transport is more efficient. Fewer generated charges are lost to recombination processes.

P3HT PVCs were also fabricated, with CPE added to the HTL. The reference P3HT PVC showed  $J_{SC}$  of  $-8.99 \pm 0.18$  mA/cm<sup>2</sup>,  $V_{OC}$  of  $0.56 \pm 0.01$  V, FF of  $66.55 \pm 0.81\%$ , average PCE of 3.35% and the best PCE of 3.55%. However, the HTL5 based P3HT PVC showed lower performance characteristics with a  $J_{SC}$  of  $-6.83 \pm 0.98$  mA/cm<sup>2</sup>,  $V_{OC}$  of  $0.57 \pm 0.01$  V, FF of  $40.54 \pm 9.46\%$ , average PCE of 1.68%, and the best PCE of 2.18%. HTL5 based P3HT exhibited a similar  $V_{OC}$  (0.01 V increased) to the reference P3HT PVC due to the lower HOMO level of HTL5. However,  $J_{SC}$  was significantly reduced because the energy level of PSFP-DTBTP is lower than the P3HT HOMO level and so would act as a barrier to hole transport across this interface, reducing the efficiency of charge transport. Therefore the series resistance in P3HT PVC was increased resulting in a decrease of  $J_{SC}$  as is explained in **Figure 2-23** in **Chapter 2**.

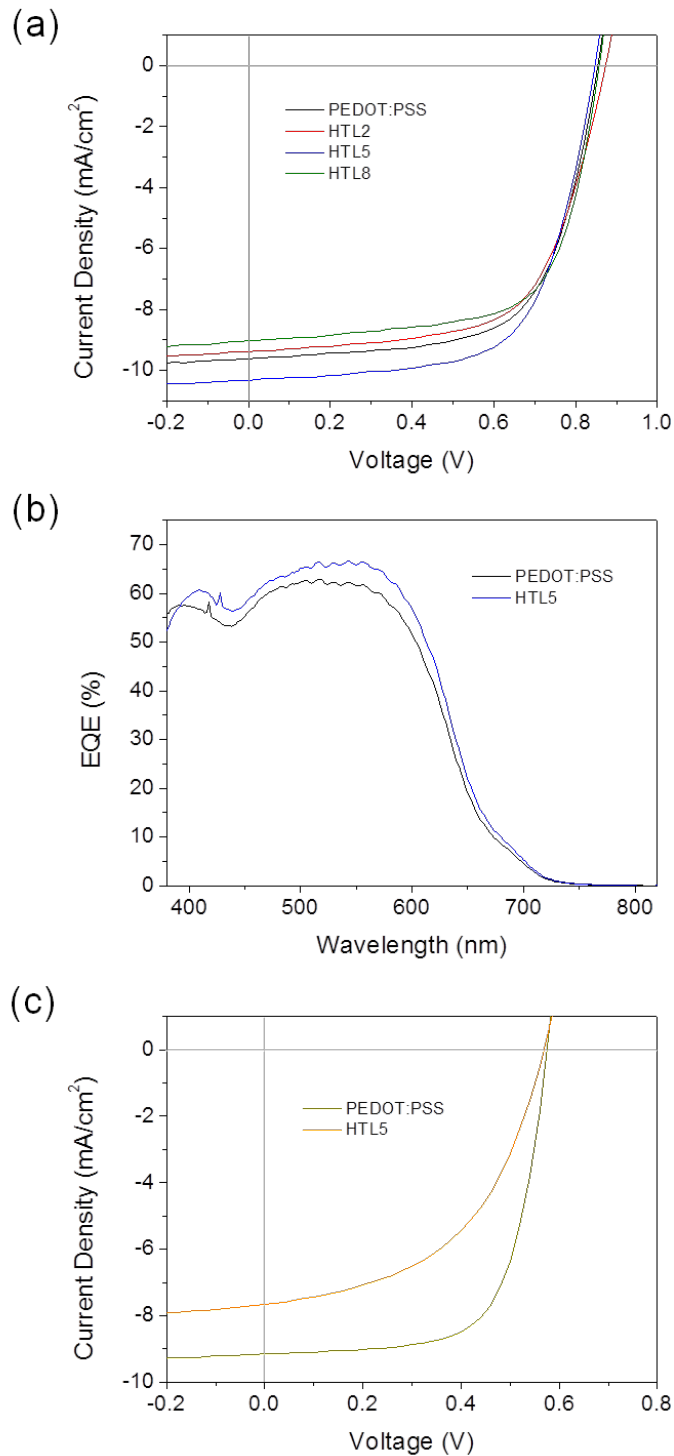


**Figure 6-7** (a) J-V curves of the PCDTBT photovoltaic cells with PEDOT:PSS (black), HTL2 (red), HTL5 (blue), and HTL8 (green). (b) EQE of the PCDTBT photovoltaic cells with PEDOT:PSS (black) and HTL5 (blue) the PEDOT:PSS/PCDTBT:PC<sub>71</sub>BM photovoltaic cell, and HTL5/PCDTBT:PC<sub>71</sub>BM photovoltaic cell. (c) J-V curves of the P3HT photovoltaic cells with PEDOT:PSS (dark yellow) and HTL5 (orange).

**Table 6-2** Photovoltaic properties of PCDTBT and P3HT photovoltaic cells with various HTL (The average value was calculated with the best 50% of pixels of over 6 devices)

HTL	HTL Thickness	$J_{sc}$ (mA/cm <sup>2</sup> )	$V_{oc}$ (V)	FF (%)	PCE (%)	
					Ave.	Best
<b>PCDTBT photovoltaic cells</b>						
PEDOT:PSS	29 nm	$-8.63 \pm 1.7$	$0.84 \pm 0.03$	$62.28 \pm 7.85$	4.63	5.32
HTL2	35 nm	$-8.88 \pm 0.54$	$0.86 \pm 0.04$	$62.51 \pm 6.79$	4.83	5.18
HTL5	47 nm	$-9.46 \pm 0.88$	$0.88 \pm 0.03$	$66.25 \pm 2.85$	5.26	5.67
HTL8	61 nm	$-8.84 \pm 0.53$	$0.86 \pm 0.03$	$63.62 \pm 4.42$	4.85	5.18
<b>P3HT photovoltaic cells</b>						
PEDOT:PSS	29 nm	$-8.99 \pm 0.18$	$0.56 \pm 0.01$	$66.55 \pm 0.81$	3.35	3.55
HTL5	47 nm	$-6.83 \pm 0.98$	$0.57 \pm 0.01$	$40.54 \pm 9.46$	1.68	2.18

#### 6.4.6. Conductivity of HTLs

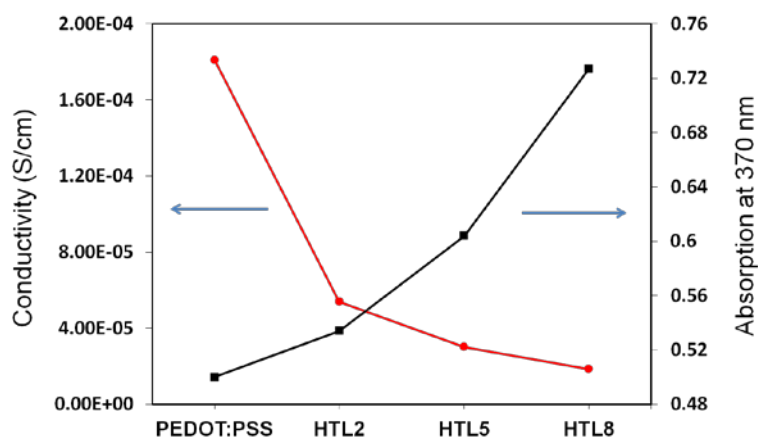


**Figure 6-8** Effect of PSFP-DTBTP concentration on the film conductivity for the hole transporting layers (blue) and the film UV-vis absorption at 370 nm for the hole transporting layers. (Conductivity measurement was performed by same condition with previous Chapter 4.)

The conductivity and absorption values of the HTL are described in **Figure 6-8**. In **Figure 6-8**, the PEDOT:PSS shows the highest sheet conductivity  $1.8 \times 10^{-4}$  S/cm and HTL2, HTL5, and HTL8 showed decreased of conductivities of  $5.4 \times 10^{-5}$  S/cm,

$3.0 \times 10^{-5}$  S/cm, and  $1.8 \times 10^{-5}$  S/cm respectively with increasing concentration of PSFP-DTBTP in the films. Therefore assuming the carrier conductivity vertically through the HTL film follows the same trend as the sheet conductivity the presence of CPE in the HTL would be expected to reduce performance. The PSFP-DTBTP acted as an insulator in the HTL, but yet the HTL5 based photovoltaic cell showed the best efficiency. Considering the absorbance of these devices the incident light will be absorbed more efficiently between 330 nm and 420 nm in those devices with CPE in the HTL layers compared to the pristine PEDOT:PSS. Therefore, although the CPE mixed with PEDOT:PSS showed lower conductivity than that of PEDOT:PSS, the HTL5 based solar cell had a higher PCE than that of pristine PEDOT:PSS based solar cell because, the presence of CPE improved the energy transfer that occurred between the active layer and HTL and therefore it helped charge transport to be more efficient. There is a trade-off between reduced conductivity through the HTL layer and improved carrier generation and charge transport across the interface into the HTL layer which is optimised at a CPE concentration close to 5 mg/ml.

#### 6.4.7. Photoluminescence (PL) characterisation of HTL and active layer

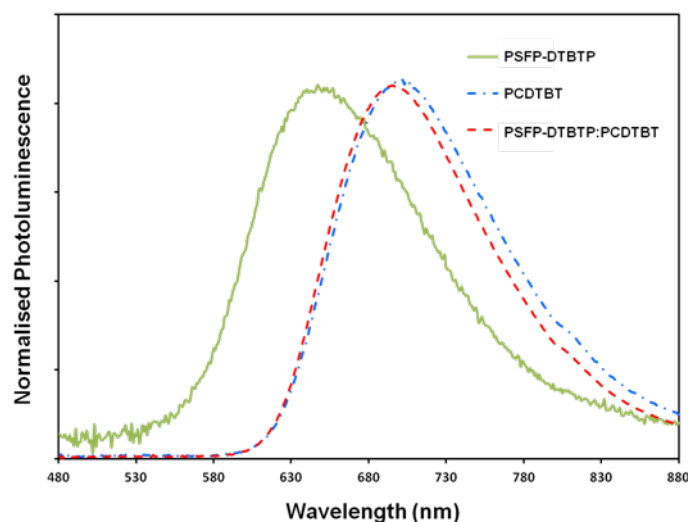


**Figure 6-9** Normalized PL spectra of PSFP-DTBTP, PCDTBT and bi-layer of PSFP-DTBTP and PCDTBT.

**Figure 6-9** shows the photoluminescence (PL) spectra of PSFP-DTBTP (15 mg/ml in H<sub>2</sub>O) film, PCDTBT (4 mg/ml in chlorobenzene) film, and PSFP-DTBTP and PCDTBT bi-layer film. The PL spectrum of PCDTBT shows emission peak at 698 nm and small shoulder peak at 810 nm. It is similar to the emission peak of

PCDTBT from a previous report (Duan et al., 2013). The PL spectrum of PSFP-DTBTP film has an emission peak at 647 nm, even though they had strong absorption peak at 367 nm. It was red emission due to exciton migration from the electron donating fluorene groups to the electron accepting benzothiadiazole groups in the polyelectrolyte (Bardeen, 2011).

To understand the correlation of HTL5 with PCDTBT, PSFP-DTBTP and PCDTBT a bi-layer film was prepared. The spectra of the PSFP-DTBTP and PCDTBT bi-layer film did not exhibit an emission peak at 647 nm (**Figure 6-9**) and it showed an emission peak at 695 nm. This is attributed to the overlapping of the PSFP-DTBTP emission peak with absorption peak of PCDTBT around 600 nm to 650 nm and the resulting quenching of the PSFP-DTBTP emission by PCDTBT. It implies that intermolecular charge transfer was occurring from the CPE to the PCDTBT (Mataga and Tanimoto, 1969, Hutchison et al., 2005). Therefore, much of the light absorbed by CPE in our devices will likely be transferred to the PCDTBT minimising losses.

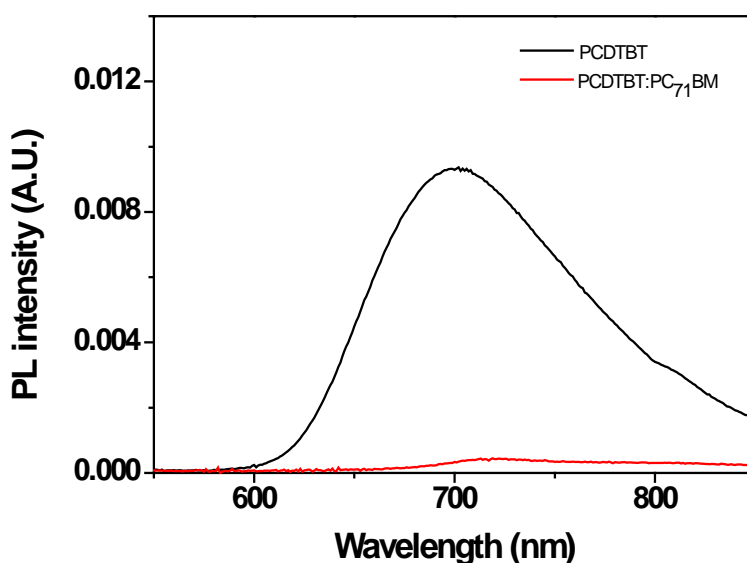


**Figure 6-10** PL spectra of PCDTBT (black) and PCDTBT:PC<sub>71</sub>BM in a blend ratio of 1:4 (red).

PCDTBT PL was well quenched when mixed with PC<sub>71</sub>BM in a blend (1:4 weight ratio) film in **Figure 6-10**.

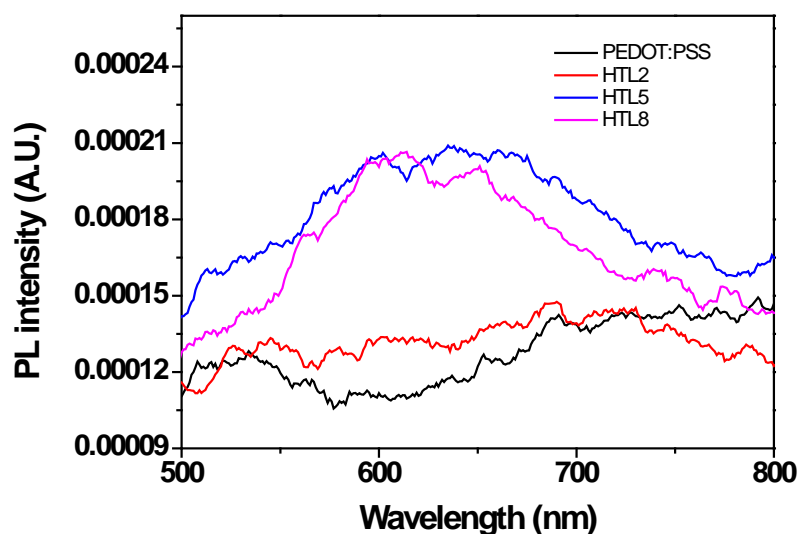


**Figure 6-11** PL spectra of PEDOT:PSS (black), HTL2 (red), HTL5 (blue), and HTL8 (pink).

The PL spectra of PEDOT:PSS with PSFP-DTBTP are illustrated in **Figure 6-11**. PEDOT:PSS thin films with CPE included showed a weak PL peak around 647 nm. The PL intensity around 640 nm increases slightly with CPE concentration increase.

#### 6.4.8. AFM characterisation of HTLs

Changes in the surface morphology of the HTL between the ITO and active layer were imaged by atomic force microscopy (AFM) in tapping mode. A HTL was spin-coated on an ITO surface. Resulting AFM height images are illustrated in **Figure 6-12**. The height images (**Figure 6-12**(b), (c), and (d)) of HTL2, HTL5 and HTL8 were not visibly different from the pristine PEDOT:PSS image (**Figure 6-12**(a)). However their root-mean-square (RMS) roughness values showed small changes. The RMS roughness of pristine PEDOT:PSS was 1.12 nm and the RMS roughness was reduced when the PSFP-DTBTP were added into the PEDOT:PSS (HTL2 and HTL8). On the other hand, the RMS roughness of HTL5 was increased to 1.22 nm. The correlation between RMS roughness of all HTLs and PCE of the corresponding devices are shown in graph **Figure 6-13** and RMS roughness has a coincident trend with PCE. The PCE of HTL5 based device showed the highest value and it corresponded with the highest RMS roughness HTL surface. The other HTL2 and HTL8 based devices had lower PCE than pristine PEDOT:PSS based device and also showed lower RMS roughness.

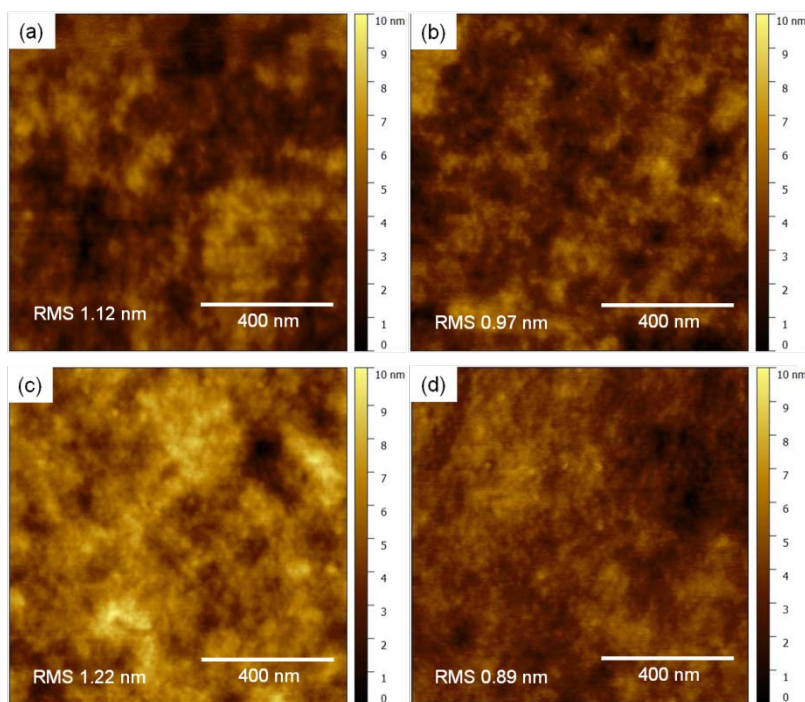


**Figure 6-12** AFM images (1 x 1  $\mu\text{m}$ ) of hole transporting layer (a) PEDOT:PSS, (b) HTL2, (c) HTL5, and (d) HTL8.

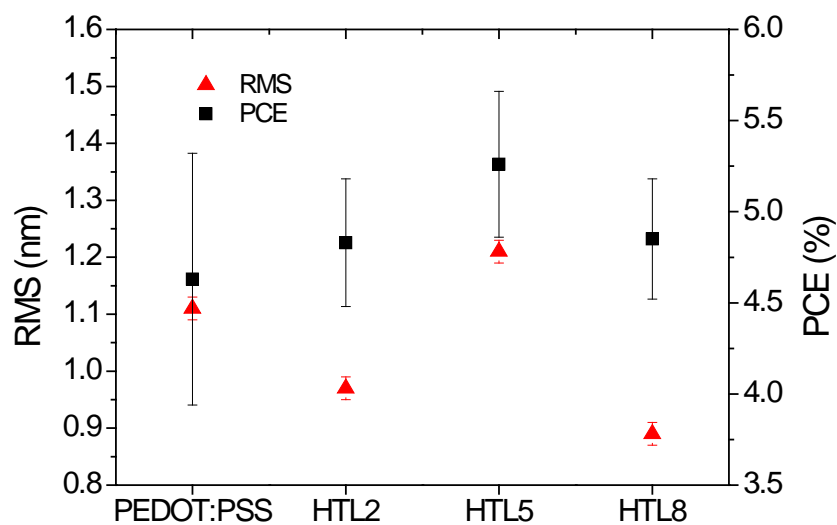


**Figure 6-13** RMS values and the best device PCE of each hole transporting layers.

#### 6.4.9. Photovoltaic properties of devices with PSFP-DTBTP HTL

BHJ PCDTBT PVCs were fabricated without a PEDOT:PSS layer, instead using a PSFP-DTBTP layer as the HTL. Their device structure is ITO/PSFP-DTBTP/PCDTBT:PC<sub>71</sub>BM/Ca/Al. PSFP-DTBTP was applied as the HTL with

various thicknesses. The thickness 2, 8, and 15 nm were adjusted by varying the concentration of PSFP-DTBTP solution in DI water from 2, 10, and 15 mg/ml used for spin coating respectively. The J-V curves of all devices are shown in **Figure 6-14**. The devices were all measured using the same solar simulator previously mentioned.

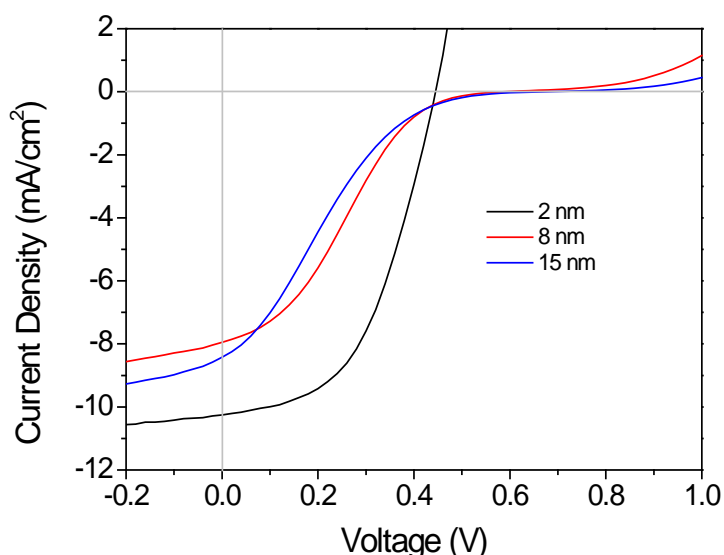


**Figure 6-14** J-V curves of PCDTBT photovoltaic cells with only PSFP-DTBTP HTL. The thickness of HTLs is 2 (black), 8 (red), and 15 nm (blue).

PSFP-DTBTP ( $3.6 \times 10^{-5} - 4 \times 10^{-5}$  S/cm) is high resistively material, so holes did not well pass through the HTL easily. Therefore, the thinner HTL devices showed higher PCE than thicker HTL devices. As shown in **Figure 6-14**, the efficiency results are lower than the those for the devices with a PEDOT:PSS HTL and also they showed S-shaped J-V curves for the 8 and 15 nm thick HTL devices which critically reduces the FF and PCE. S-kink behaviour can be attributed to an imbalanced charge carrier mobility of electrons and holes in the planar heterojunction photovoltaic cells and is caused by energy barriers at the interfaces between the active layer and the electrode (Wagner et al., 2012, Zhang et al., 2011, Tress et al., 2011, Huh et al., 2014). There is a barrier to charge extraction due to the close HOMO energy level of CPE (-5.38 eV) and PCDTBT (-5.4 eV). Therefore, it would be possible that holes in the active layer did not easily move into the HTL and therefore accumulated around the contact between PCDTBT and PSFP-DTBTP before recombining with electrons. The photovoltaic properties of devices are in the **Table 6-3**. The 2 nm thickness of HTL based PVC showed the

best result with PCE of 2.28%,  $J_{SC}$  of  $-9.72 \pm 0.52$  mA/cm<sup>2</sup>,  $V_{OC}$  of  $0.42 \pm 0.02$  V, and FF of  $46.39 \pm 3.71\%$ .

**Table 6-3** Photovoltaic properties of PCDTBT photovoltaic cells with PSFP-DTBTP HTL (The average value was calculated with the best 50% of pixels of over 6 devices).

PSFP-DTBTP Thickness (nm)	$J_{SC}$ (mA/cm <sup>2</sup> )	$V_{OC}$ (V)	FF (%)	PCE (%)	
				Ave.	Best
$2 \pm 0.5$	$-9.72 \pm 0.52$	$0.42 \pm 0.02$	$46.39 \pm 3.71$	1.94	2.28
$8 \pm 0.6$	$-7.74 \pm 0.37$	$0.49 \pm 0.07$	$25.51 \pm 6.48$	1.05	1.12
$15 \pm 0.5$	$-8.46 \pm 0.58$	$0.56 \pm 0.11$	$22.45 \pm 7.15$	0.72	0.9

## 6.5. Conclusions

Poly[(9,9-bis(4-sulfonatobutyl sodium) fluorene-alt-phenylene)-ran-(4,7-di-2-thienyl-2,1,3-benzothiadiazole-alt-phenylene)] (PSFP-DTBTP) synthesised as described in Chapter 4 showed a strong absorption peak at 370 nm with small absorption features around 550 nm, and a PL emission peak at 645 nm. When PSFP-DTBTP was used as an active layer, the devices did not show any photovoltaic abilities due to a much too transparent film being produced as a result of aggregation and an unsuitable absorption wavelength. When the conjugated polyelectrolyte was used as an additive in the hole transporting layer of OPVCs, the PSFP-DTBTP HTL5 based PCDTBT:PC<sub>71</sub>BM photovoltaic cell had a PCE of 5.67%. It was a significant improvement over the control device without CPE. All characteristics of the photovoltaic cell with CPE were higher than that of the reference device without the additive. The repeat ability of the device performance was also improved. Although the HTL with the conjugated polyelectrolyte had a lower conductivity, the improved charge transport into the HTL and absorption ability of polyelectrolyte more than compensated for this because it improved generation of carriers which subsequently transferred to the ITO or active layer. From the PL spectrum it is evident that energy transfer can occur from the CPE to PCDTBT. The work function of the HTLs with CPE added is lower than the pristine PEDOT:PSS, so the HTL5 devices had a higher  $V_{OC}$  by about 0.02-0.04 compared to the reference devices. The improved match between the HTL with CPE work function and the PCDTBT BHJ layer is shown to improved charge

transfer into the HTL. For these reasons, the photovoltaic cells with the CPE showed an average PCE improvement of 13% compared to the reference devices. This 13% improvement would mean a 13% reduction in materials and energy required to make the devices and deliver the same energy output.

When the PSFP-DTBTP was used as the HTL without any PEDOT:PSS, the PCE of devices was decreased and in some cases they showed S-shaped J-V curves due to imbalanced charge carrier mobility of electrons and holes due to energy barriers at the interface between the active layer and HTL.

## 6.6. References

- BARDEEN, C. 2011. Exciton Quenching and Migration in Single Conjugated Polymers. *Science*, 331, 544-545.
- DA SILVA, W. J., SCHNEIDER, F. K., YUSOFF, A. B. & JANG, J. 2015. High performance polymer tandem solar cell. *Scientific Reports*, 5, 18090.
- DUAN, C. H., CAI, W. Z., HSU, B. B. Y., ZHONG, C. M., ZHANG, K., LIU, C. C., HU, Z. C., HUANG, F., BAZAN, G. C., HEEGER, A. J. & CAO, Y. 2013. Toward green solvent processable photovoltaic materials for polymer solar cells: the role of highly polar pendant groups in charge carrier transport and photovoltaic behavior. *Energy & Environmental Science*, 6, 3022-3034.
- GAYLORD, B. S., WANG, S. J., HEEGER, A. J. & BAZAN, G. C. 2001. Water-soluble conjugated oligomers: Effect of chain length and aggregation on photoluminescence-quenching efficiencies. *Journal of the American Chemical Society*, 123, 6417-6418.
- GREINER, M. T. & LU, Z. H. 2013. Thin-film metal oxides in organic semiconductor devices: their electronic structures, work functions and interfaces. *Npg Asia Materials*, 5.
- HE, Z. C., ZHONG, C. M., HUANG, X., WONG, W. Y., WU, H. B., CHEN, L. W., SU, S. J. & CAO, Y. 2011. Simultaneous Enhancement of Open-Circuit Voltage, Short-Circuit Current Density, and Fill Factor in Polymer Solar Cells. *Advanced Materials*, 23, 4636-+.
- HUANG, F., WANG, X. H., WANG, D. L., YANG, W. & CAO, Y. 2005. Synthesis and properties of a novel water-soluble anionic polyfluorenes for highly sensitive biosensors. *Polymer*, 46, 12010-12015.

- HUANG, F., WU, H. B., WANG, D., YANG, W. & CAO, Y. 2004. Novel electroluminescent conjugated polyelectrolytes based on polyfluorene. *Chemistry of Materials*, 16, 708-716.
- HUH, Y. H., PARK, B. & HWANG, I. 2014. Investigating the origin of S-shaped photocurrent-voltage characteristics of polymer:fullerene bulk-heterojunction organic solar cells. *Journal of Applied Physics*, 115.
- HUTCHISON, G. R., RATNER, M. A. & MARKS, T. J. 2005. Intermolecular charge transfer between heterocyclic oligomers. Effects of heteroatom and molecular packing on hopping transport in organic semiconductors. *Journal of the American Chemical Society*, 127, 16866-16881.
- MATAGA, N. & TANIMOTO, O. 1969. Possible Mechanisms of Intermolecular Charge Transfer and Electron Transfer Processes in Excited Electronic State. *Theoretica Chimica Acta*, 15, 111-&.
- MCLESKEY, J. T. & QIAO, Q. Q. 2006. Hybrid solar cells from water-soluble polymers. *International Journal of Photoenergy*.
- RATCLIFF, E. L., GARCIA, A., PANIAGUA, S. A., COWAN, S. R., GIORDANO, A. J., GINLEY, D. S., MARDER, S. R., BERRY, J. J. & OLSON, D. C. 2013. Investigating the Influence of Interfacial Contact Properties on Open Circuit Voltages in Organic Photovoltaic Performance: Work Function Versus Selectivity. *Advanced Energy Materials*, 3, 647-656.
- SEO, J. H., GUTACKER, A., SUN, Y. M., WU, H. B., HUANG, F., CAO, Y., SCHERF, U., HEEGER, A. J. & BAZAN, G. C. 2011. Improved High-Efficiency Organic Solar Cells via Incorporation of a Conjugated Polyelectrolyte Interlayer. *Journal of the American Chemical Society*, 133, 8416-8419.
- STORK, M., GAYLORD, B. S., HEEGER, A. J. & BAZAN, G. C. 2002. Energy transfer in mixtures of water-soluble oligomers: Effect of charge, aggregation, and surfactant complexation. *Advanced Materials*, 14, 361-366.
- THOMPSON, B. C. & FRECHET, J. M. J. 2008. Organic photovoltaics - Polymer-fullerene composite solar cells. *Angewandte Chemie-International Edition*, 47, 58-77.
- TRAN-VAN, F., CARRIER, M. & CHEVROT, C. 2004. Sulfonated polythiophene and poly (3,4-ethylenedioxythiophene) derivatives with cations exchange properties. *Synthetic Metals*, 142, 251-258.

- TRESS, W., PETRICH, A., HUMMERT, M., HEIN, M., LEO, K. & RIEDE, M. 2011. Imbalanced mobilities causing S-shaped IV curves in planar heterojunction organic solar cells. *Applied Physics Letters*, 98.
- WAGNER, J., GRUBER, M., WILKE, A., TANAKA, Y., TOPCZAK, K., STEINDAMM, A., HORMANN, U., OPITZ, A., NAKAYAMA, Y., ISHII, H., PFLAUM, J., KOCH, N. & BRUTTING, W. 2012. Identification of different origins for s-shaped current voltage characteristics in planar heterojunction organic solar cells. *Journal of Applied Physics*, 111.
- WATTERS, D. C., KINGSLEY, J., YI, H. N., WANG, T., IRAQI, A. & LIDZEY, D. 2012. Optimising the efficiency of carbazole co-polymer solar-cells by control over the metal cathode electrode. *Organic Electronics*, 13, 1401-1408.
- YANG, J. H., GARCIA, A. & NGUYEN, T. Q. 2007. Organic solar cells from water-soluble poly(thiophene)/fullerene heterojunction. *Applied Physics Letters*, 90.
- YAO, K., CHEN, L., CHEN, Y. W., LI, F. & WANG, P. S. 2011. Influence of water-soluble polythiophene as an interfacial layer on the P3HT/PCBM bulk heterojunction organic photovoltaics. *Journal of Materials Chemistry*, 21, 13780-13784.
- YI, H. N., AL-FAIFI, S., IRAQI, A., WATTERS, D. C., KINGSLEY, J. & LIDZEY, D. G. 2011. Carbazole and thienyl benzo[1,2,5]thiadiazole based polymers with improved open circuit voltages and processability for application in solar cells. *Journal of Materials Chemistry*, 21, 13649-13656.
- ZHANG, L. J., HE, C., CHEN, J. W., YUAN, P., HUANG, L. A., ZHANG, C., CAI, W. Z., LIU, Z. T. & CAO, Y. 2010. Bulk-Heterojunction Solar Cells with Benzotriazole-Based Copolymers as Electron Donors: Largely Improved Photovoltaic Parameters by Using PFN/A1 Bilayer Cathode. *Macromolecules*, 43, 9771-9778.
- ZHANG, M. L., WANG, H. & TANG, C. W. 2011. Hole-transport limited S-shaped I-V curves in planar heterojunction organic photovoltaic cells. *Applied Physics Letters*, 99.
- ZHAO, Z. Q., WU, Q. L., XIA, F., CHEN, X., LIU, Y. W., ZHANG, W. F., ZHU, J., DAI, S. Y. & YANG, S. F. 2015. Improving the Conductivity of PEDOT:PSS Hole Transport Layer in Polymer Solar Cells via Copper(II) Bromide Salt Doping. *Acs Applied Materials & Interfaces*, 7, 1439-1448.
- ZHOU, H. Q., ZHANG, Y., MAI, C. K., COLLINS, S. D., NGUYEN, T. Q., BAZAN, G. C. & HEEGER, A. J. 2014. Conductive Conjugated

Polyelectrolyte as Hole-Transporting Layer for Organic Bulk Heterojunction Solar Cells. *Advanced Materials*, 26, 780-785.

## 7. Perovskite photovoltaic cell

### 7.1. Introduction

The abundance of sunlight makes it a highly attractive source of green energy. Within the field of photovoltaic (PV) technologies, silicon is the dominant technology due to its mature manufacturing methods and moderate processing costs (Shaheen et al., 2005). Recently, hybrid perovskite photovoltaics have attracted great interest due to their outstanding efficiency, a composition that is based on inexpensive materials and their ease of fabrication (Liu and Kelly, 2014, Liu et al., 2013, Burschka et al., 2013, Ball et al., 2013, Lee et al., 2012, Eperon et al., 2014). As a consequence of these promising characteristics, hybrid perovskites are showing strong potential to drive the next wave of widespread PV adoption; both in areas currently dominated by silicon and in innovative applications such as building integrated PV.

Among the challenges facing the scale-up of perovskite PVCs, the toxicity of the semiconductors has been raised as a potential issue owing to the presence of lead (Landrigan, 1989, Flora et al., 2012). Specifically, beyond the hazards present during solar cell fabrication and end-of-life recycling, the ability to deploy such cells in real world applications may be prohibited by the potential risk for lead seepage that occurs due to encapsulation failure (the solubility of organo-lead halide perovskites in water has been well-documented) (Babayigit et al., 2016). To overcome this, research into reduced lead or lead-free perovskites has gained traction over the past few years and amongst the possible substitute metals, tin has showed reasonable promise (Ogomi et al., 2014, Hao et al., 2014, Noel et al., 2014). Notable highlights include the demonstration of  $\text{CH}_3\text{NH}_3\text{SnI}_3$  solar cells with an initial PCE above 6% (Noel et al., 2014), however the efficient photovoltaic functionality of Sn rich phases in mixed Sn/Pb perovskites has been questioned (Ogomi et al., 2014). Additional issues that include semiconductor oxidation and the mitigation of hysteresis effects in devices continues to drive the development of reduced lead perovskites with the ultimate goal of matching the performance characteristics of the original lead-based semiconductors. Another study considered other metals that match the requirements on electron valency and size tolerance within the perovskite lattice (Travis et al., 2016). In order to reduce the use of lead,

Park et al. have introduced bismuth as substitute for lead (Park et al., 2015). Bismuth has much lower toxicity than lead (Mohan, 2010) and they found that caesium-bismuth perovskite showed a PCE of 1.09%, however, Cs is still considered mildly toxic. They also reported methylammonium Bi-perovskite which was assigned a  $MA_3Bi_2I_9$  structure and measured a PCE of 0.12%. Slavney et al. studied a double-perovskite structure  $Cs_2Ag^+Bi^{3+}Br_6$  finding lattice a unit-cell axis of 11.25 Å is roughly double that of  $CH_3NH_3PbBr_3$  however they did not test any photovoltaic devices (Slavney et al., 2016).

In this work the use of bismuth was explored as a low toxicity alternative to lead in hybrid perovskite semiconductors. A control sample of  $CH_3NH_3PbI_{3-x}Cl_x$  was investigated alongside a range of perovskites with the composition  $CH_3NH_3(Pb_yBi_{1-y})I_{3-x}Cl_x$  where y varies between 0 and 1 and x is small, with such samples prepared from a range of precursors (including  $BiCl_3$  and  $BiI_3$ ) and using various precursor blend ratios. This study places particular focus on the crystallinity and phase purity of each perovskite, with scanning electron microscopy (SEM), energy-dispersive X-ray spectroscopy (EDS), and grazing incidence wide angle X-ray scattering (GIWAXS) measurements used to characterize their nanoscale structure and composition. Although their initial performance in solar cell devices is not promising, the structural data presented helps us to understand why this is the case. In general the results provide important insight into the processability of bismuth perovskites, thereby helping to refine the choice of materials and processing methods used for developing high performance hybrid perovskites with low toxicity.

The presentation of results proceeds as follows. The UV-vis absorption spectra of each perovskite sample is considered first, before discussing composition and microstructure characteristics in depth via SEM, EDS and GIWAXS analysis. The GIWAXS data is modelled in order to help explain how the perovskite film forms for bismuth perovskites. In addition this provides insight into the ability for binary-metal compositions (i.e. Pb/Bi mixtures) to form crystalline semiconductor structures of high phase purity. Lastly, the results from initial solar cell devices are presented. This study concludes by considering engineering strategies for improving bismuth perovskite film quality.

## 7.2. Experimental

### 7.2.1. Materials

Perovskite precursors were made from methylamine (33 wt % in ethanol, Sigma-Aldrich Company Ltd.), hydriodic acid (57 wt % in water, Acros Organics), PbCl<sub>2</sub> (98%, Acros Organics), BiI<sub>3</sub> (99%, Sigma-Aldrich Company Ltd.), BiCl<sub>3</sub> (98%, Acros Organics), and anhydrous DMF (Sigma-Aldrich Company Ltd.). Phenyl-C<sub>61</sub>-butyric acid methyl ester (PCBM), PEDOT:PSS (Heraeus Clevious™ P VP AI 4083), and encapsulating UV-epoxy were purchased from Ossila Ltd.. These materials were used as purchased without any further purification. Pre-patterned ITO glass substrates (20 Ω sq<sup>-1</sup>) were purchased from Ossila Ltd.

### 7.2.2. Synthesis of methylamine iodide (MAI)



**Scheme 7-1** The procedure of making MAI.

48 ml (0.386 mol) of methylamine solution (CH<sub>3</sub>NH<sub>2</sub>, 33 wt % in absolute ethanol) and 200 ml of ethanol were added into a 500 ml 2-necked round-bottomed flask. 20 ml (0.152 mol) of hydriodic acid (HI, 57 wt % in deionised water) was added dropwise into the flask and then degassed with nitrogen. The mixed solution was stirred at room temperature for 2 h then all solvent was evaporated using a rotary evaporator. The resulting solid was washed with acetone and dried in vacuum at 40 °C for 2 d. A white coloured crystal was obtained. <sup>1</sup>H NMR (500MHz, DMSO-d<sub>6</sub>, δ): 7.52-7.39 (m, 3H), 2.36 (3H). Anal. Calcd. for CH<sub>3</sub>NH<sub>3</sub>I: C, 7.55; H, 3.81; N, 8.8; I, 79.82. Found: C, 7.67; H, 3.63; N, 8.71; I, 79.80.

### 7.2.3. Mixed perovskite precursor of various blend ratios

#### 7.2.3.1. Methylammonium lead iodide chloride (MAPbI<sub>3-x</sub>Cl<sub>x</sub>, MAI:PbCl<sub>2</sub> = 3:1) precursor

A blend of 419.4 mg (2.63 mmol) of MAI and 244.6 mg (0.88 mmol) of PbCl<sub>2</sub> was dissolved in 1 ml of anhydrous N,N-dimethyl-formamide (DMF) with a solid concentration of 664 mg/ml.

### **7.2.3.2. Methylammonium bismuth iodide chloride (MABi<sub>3-x</sub>Cl<sub>x</sub>, MAI:BiCl<sub>3</sub> = 3:1) precursor**

A blend of 419.4 mg (2.63 mmol) of MAI and 277.3 mg (0.88 mmol) of BiCl<sub>3</sub> was dissolved in 1 ml of anhydrous DMF with a solid concentration of 938 mg/ml.

### **7.2.3.3. Mixed metal methylammonium lead bismuth iodide chloride precursors**

Three mixed metal precursor solutions were made by mixing the prepared MAPbI<sub>3-x</sub>Cl<sub>x</sub> and MABiI<sub>3-x</sub>Cl<sub>x</sub> solutions in different ratios. The MA(Pb<sub>0.75</sub>Bi<sub>0.25</sub>)I<sub>3-x</sub>Cl<sub>x</sub> was made up of 0.75 ml of MAPbI<sub>3-x</sub>Cl<sub>x</sub> and 0.25 ml of MABiI<sub>3-x</sub>Cl<sub>x</sub>. The MA(Pb<sub>0.5</sub>Bi<sub>0.5</sub>)I<sub>3-x</sub>Cl<sub>x</sub> was made from 0.50 ml of MAPbI<sub>3-x</sub>Cl<sub>x</sub> and 0.50 ml of MABiI<sub>3-x</sub>Cl<sub>x</sub>. Finally, the MA(Pb<sub>0.25</sub>Bi<sub>0.75</sub>)I<sub>x</sub>Cl<sub>y</sub> was made from 0.25 ml of MAPbI<sub>3-x</sub>Cl<sub>x</sub> and 0.75 ml of MABiI<sub>3-x</sub>Cl<sub>x</sub>.

### **7.2.3.4. Methylammonium bismuth iodide (MABiI<sub>3</sub>, MAI:BiI<sub>3</sub> = 1:1) precursor**

A mixture of 139.8 mg (0.88 mmol) of MAI and 518.6 mg (0.88 mmol) of BiI<sub>3</sub> was dissolved in 1 ml of anhydrous DMF and its resulting solid concentration was 658.4 mg/ml.

### **7.2.3.5. Methylammonium bismuth iodide (MABiI<sub>3</sub>, MAI:BiI<sub>3</sub> = 3:1) precursor**

A mixture of 419.4 mg (2.63 mmol) of MAI and 518.6 mg (0.88 mmol) of BiI<sub>3</sub> was dissolved in 1 ml of anhydrous DMF with total solid concentration of 938 mg/ml.

All the precursor solutions were heated overnight at 70 °C to ensure fully dissolution of mixture solids. The precursor solutions were cooled to room temperature and then filtered using a 0.45 μm PTFE filter before use.

## **7.2.4. Thin films fabrication for SEM, EDS, and GIWAXS**

For the SEM, EDS, and GIWAXS characterisation approximately 15 mm x 15 mm pieces of Si wafer were used as the substrates. Pieces of silicon wafers were cleaned with acetone and isopropyl alcohol (IPA) in turn in the ultrasonic bath for 10 min each and then exposed to oxygen plasma for 10 min to remove any organic

residues. The perovskite layer was spin coated on the silicon wafer at 5000 rpm then thermally annealed at 90 °C for 90 min. The films were fabricated in air.

### **7.2.5. Thin films fabrication for UV-vis absorption spectroscopy**

For the UV-vis absorption spectroscopy 25 mm x 25 mm pieces of glass were used. Glass substrates were cleaned in Helmanex solution, IPA and deionized water in an ultrasonic bath for 10 min for each rinse respectively. The films were fabricated by spin coating on the glass substrates. The films were thermally annealed at 90 °C for 90 min. The films were fabricated in air.

### **7.2.6. Device fabrication and characterisation**

The planar heterojunction architecture used in this work is a relatively easy and fast way to fabricate perovskite solar cells. The perovskite layer is sandwiched between PEDOT:PSS and fullerene layers which act as hole and electron transporting layers, respectively. An advantage of this system is the relative ease with which the thickness of films produced is controlled using spin-coating. Pre-patterned substrates were washed for 10 min each in Helmanex solution, IPA, and deionized water in an ultrasonic bath to remove any dirt on the ITO substrates. After washing, the substrates are blown dry using clean dry nitrogen. PEDOT:PSS (Heraeus Clevios™ P VP AI 4083) filtered through a 0.45 µm PVDF filter was then spin-coated at 5000 rpm for 30 sec on the substrates resulting in a thin film of ~40 nm thickness. The PEDOT:PSS coated ITO substrates were then annealed on a hot plate at 130 °C for 15-30 min. The perovskite precursor was subsequently deposited on top of the PEDOT:PSS layer by spin coating at 5000 rpm for 30 sec. A small strip of the perovskite film on the edge of substrates was wiped off with a cotton bud to leave an area of the ITO electrodes exposed for contacting. The perovskite coated films were annealed on a hot plate for 90 min at 90 °C. PCBM solution (50 mg/ml in chlorobenzene filtered through a 0.45 µm PTFE filter before use) was heated to 70 °C for 12 h. It was then spin-coated on top of the perovskite layers in an oxygen and moisture free glovebox. Again some of the ITO electrode was exposed by wiping off a strip of the PCBM on the edge of substrates using a cotton bud. Calcium and aluminium were deposited onto the PCBM layer through a mask to form cathodes in a vacuum evaporator. The thicknesses of the calcium

and aluminium layers were nominally 5 and 100 nm respectively. The devices were then encapsulated with glass using UV-cured epoxy under UV light for 30 min.

### 7.2.7. Instruments

$^1\text{H}$  NMR was collected using a Bruker DRX 500 spectrometer. Elemental analysis was performed by Perkin Elmer 2400 series II CHN analyzer. The spin coater used to deposit for films and devices was a Laurell WS-400BZ-6NPP/lite. UV-vis absorption spectra were measured using an Ocean Optics USB2000+ spectrometer and DT-MINI-2-GS combined Deuterium-Halogen light source. SEM images and EDS analysis were obtained using JEOL JSM6010LA (thermionic emission gun) scanning electron microscope (10kV, Multi-segment secondary electron detector). GIWAXS analysis was performed at beamline I07 at the Diamond Light Source (10keV, Pilatus 2M detector, sample-detector distance of  $\sim 40$  cm). 2D GIWAXS images were taken by detector and the line profiles were obtained by radial integral of the 2D GIWAXS images. The line profiles were calibrated using a 2D GIWAXS image of silver behenate. All the images and line profiles were processed using Dawn software from Diamond Light Source. The photovoltaic characteristics of the devices were measured using a Newport 92251A-1000 solar simulator in ambient conditions under  $100 \text{ mW cm}^{-2}$  of simulated AM 1.5 sunlight as determined using an NREL calibrated silicon photovoltaic reference cell. The devices were masked with an aperture ( $0.025 \text{ cm}^2$ ) to define the active area during the J-V measurement to minimize any edge effects.

## 7.3. Results and discussion

The general route for preparing hybrid perovskite films involves the coordination of an organic cation within a metal-halide lattice structure. This process can take place in solution, or *via* thermal annealing of a precursor film with an appropriate starting stoichiometry (i.e. relative concentrations of organic and inorganic material). To synthesise organo-bismuth halide perovskites,  $\text{CH}_3\text{NH}_3\text{I}$  (methylammonium iodide, hereafter referred to as MAI),  $\text{BiI}_3$  and  $\text{BiCl}_3$  were used as precursor materials to form  $\text{MABiI}_3$  and  $\text{MABi}_{3-x}\text{Cl}_x$ . The role of starting stoichiometry for the pure tri-iodide perovskite  $\text{MABiI}_3$  was investigated by considering 1:1 or 3:1 mol% mixtures of MAI and  $\text{BiI}_3$  respectively. Finally, The precursors for  $\text{MABi}_{3-x}\text{Cl}_x$  and  $\text{MAPb}_{3-x}\text{Cl}_x$  were mixed to form three mixed metal

cation perovskites with nominal compositions  $\text{MA}(\text{Pb}_{0.25}\text{Bi}_{0.75})\text{I}_{3-x}\text{Cl}_x$ ,  $\text{MA}(\text{Pb}_{0.5}\text{Bi}_{0.5})\text{I}_{3-x}\text{Cl}_x$  and  $\text{MA}(\text{Pb}_{0.75}\text{Bi}_{0.25})\text{I}_{3-x}\text{Cl}_x$ . A total of seven perovskite samples are considered in this study, with full preparation details provided in the experimental methods.

### 7.3.1. UV-vis absorption of perovskites

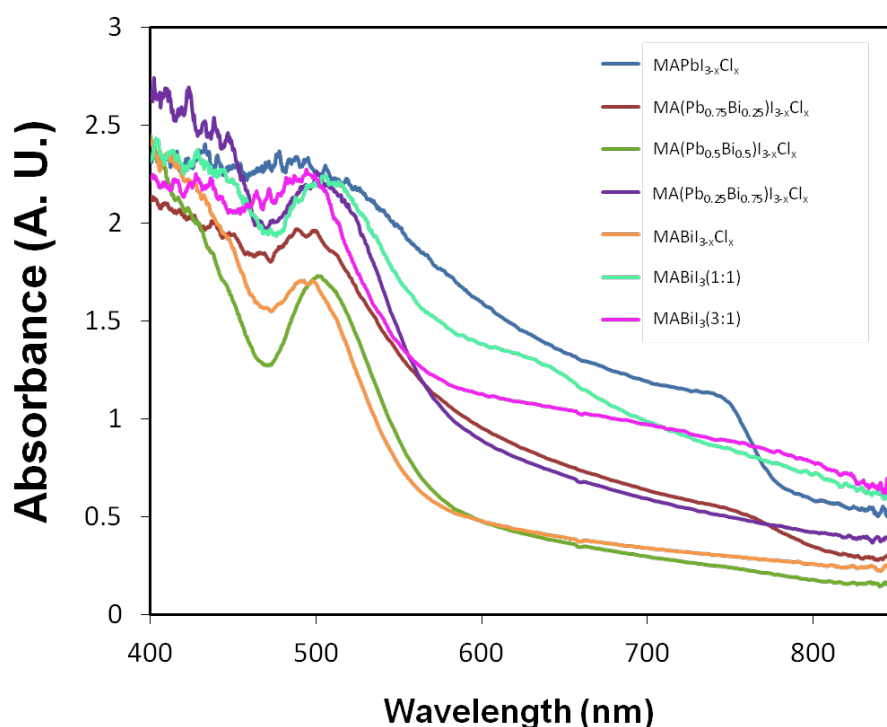


**Figure 7-1** Absorbance spectra of  $\text{MAPbI}_{3-x}\text{Cl}_x$ ,  $\text{MABiI}_{3-x}\text{Cl}_x$ ,  $\text{MABiI}_3(1:1)$ ,  $\text{MABiI}_3(3:1)$ ,  $\text{MA}(\text{Pb}_{0.25}\text{Bi}_{0.75})\text{I}_{3-x}\text{Cl}_x$ ,  $\text{MA}(\text{Pb}_{0.5}\text{Bi}_{0.5})\text{I}_{3-x}\text{Cl}_x$  and  $\text{MA}(\text{Pb}_{0.75}\text{Bi}_{0.25})\text{I}_{3-x}\text{Cl}_x$  films prepared on glass substrates. All samples were annealed at  $90^\circ\text{C}$  after spin casting the precursor solution.

**Figure 7-1** shows the UV-vis absorption spectra for each perovskite film, where it can be seen that each sample exhibits a relatively strong absorption peak centred around 500 nm. The signal to noise ratio was very large at less than 400 nm because the absorption is very strong so the intensity of light measured was very small therefore the data was truncated at 400 nm. For our control sample  $\text{MAPbI}_{3-x}\text{Cl}_x$ , its optical absorption extends to long wavelengths  $>750$  nm where there is a distinct edge which when extrapolated meets the x-axis at approximately 820 nm, equating to a band gap of 1.51 eV in reasonable agreement with earlier reports (Colella et al., 2013, Lee et al., 2012). This is close to the value reported for  $\text{MAPbI}_3$  (Kulkarni et al., 2014, Bi et al., 2014), suggesting there are low / trace levels of Cl in this perovskite. Among the mixed metal perovskites only

MA(Pb<sub>0.75</sub>Bi<sub>0.25</sub>)I<sub>3-x</sub>Cl<sub>x</sub> showed a weaker absorption shoulder in the near-IR region of the light spectrum, at a wavelength similar to that observed for the control sample (> 750 nm). This feature was tentatively attributed to the presence of pure lead perovskite phases within the sample, given the 3x difference in lead molar content compared to bismuth in the precursor. Further increases in bismuth content within the sample, from Pb<sub>0.75</sub>Bi<sub>0.25</sub> to Pb<sub>0.25</sub>Bi<sub>0.75</sub>, results in the eventual disappearance of this feature. For the pure bismuth perovskites, MABiI<sub>3</sub> (1:1) prepared from a 1:1 precursor stoichiometry shows a weak absorption edge at approximately 605 nm, whereas MABiI<sub>3</sub>(3:1) prepared from a 3:1 precursor stoichiometry and MABiI<sub>3-x</sub>Cl<sub>x</sub> do not. The MABiI<sub>3-x</sub>Cl<sub>x</sub> was estimated to have an optical band gap of 2.1 eV *via* extrapolation of the absorption edge observed beyond 510 nm. Note however that this method does not readily extend to every perovskite considered here, as the slow and incomplete drop-off in absorption (likely an indication of pronounced light scatter) will introduce unintended artefacts (Tian and Scheblykin, 2015).

### 7.3.2. SEM and EDS characterisation

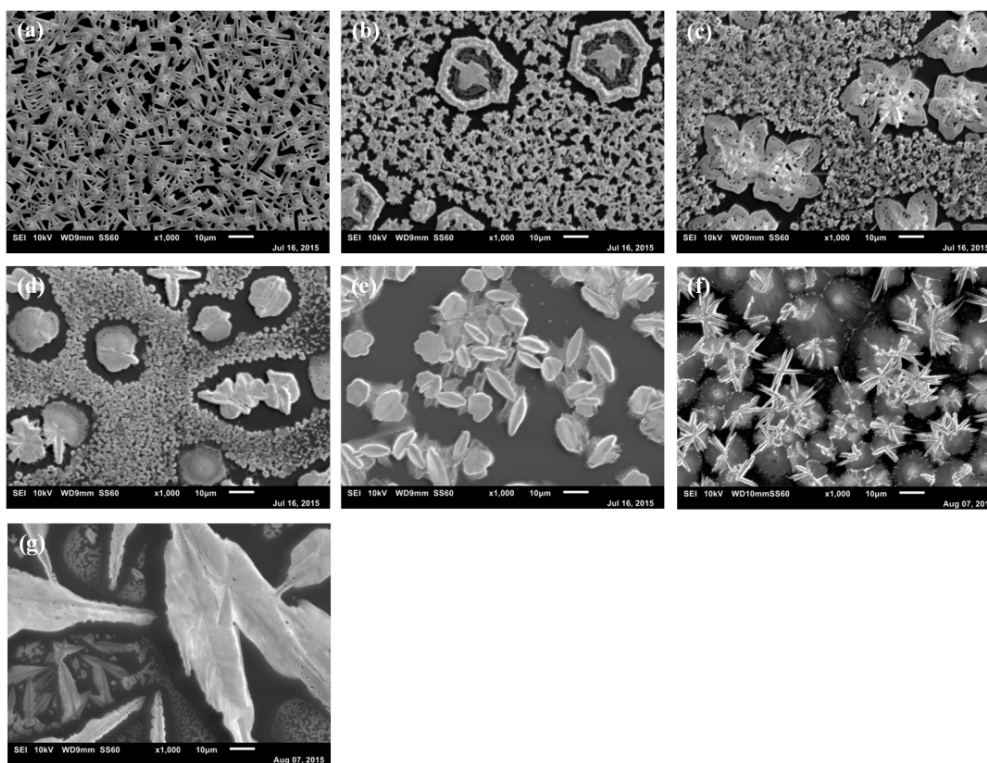


**Figure 7-2** SEM images of (a) MAPbI<sub>3-x</sub>Cl<sub>x</sub>, (b) MA(Pb<sub>0.75</sub>Bi<sub>0.25</sub>)I<sub>3-x</sub>Cl<sub>x</sub>, (c) MA(Pb<sub>0.5</sub>Bi<sub>0.5</sub>)I<sub>3-x</sub>Cl<sub>x</sub>, (d) MA(Pb<sub>0.25</sub>Bi<sub>0.75</sub>)I<sub>3-x</sub>Cl<sub>x</sub>, (e) MABiI<sub>3-x</sub>Cl<sub>x</sub>, (f) MABiI<sub>3</sub>(1:1), and (g) MABiI<sub>3</sub>(3:1) films prepared on silicon substrates. Scale bar corresponds to 10 µm.

To study in detail the microstructure of each perovskite film, in addition to confirming their composition, a series of SEM images and EDS chemical surveys were recorded. **Figure 7-2** shows representative SEM images for each perovskite.

From **Figure 7-2(a)**, which corresponds to our control sample, it can be seen that  $\text{MAPbI}_{3-x}\text{Cl}_x$  consists of a relatively dense distribution of elongated crystals, each having a characteristic length between 3 and 10  $\mu\text{m}$ . Quantitative analysis of this image suggests a surface coverage of 60%. For the mixed metal perovskites, shown here in **Figure 7-2(b)-(d)**, two distinct structure types are present; a compact distribution of micron-sized crystallites that cover a sizable fraction of the substrate, and dispersed structures with a size between 20 and 30  $\mu\text{m}$ . Note that these relatively large features are often surrounded by a region void of any material, suggesting that mass transport and/or substrate de-wetting has taken place during their formation (Barrows et al., 2014, Colella et al., 2013, Yu et al., 2014). In general, these structures are present in greater number when the relative concentration of Bi in the sample increases. Although this might suggest the presence of separate perovskite phases in the sample (i.e. regions of pure  $\text{MAPbI}_{3-x}\text{Cl}_x$  that are spatially distinct from regions of pure  $\text{MABiI}_{3-x}\text{Cl}_x$ ), EDS mapping indicates that the distribution of Bi throughout the sample is reasonably uniform. As a consequence we suggest that the formation of either crystallite structure is not determined primarily by metal content, and is instead governed by factors that include halide composition, the dynamics of precursor conversion and the local presence of defects / impurities in the sample that act as possible nucleation sites for crystal formation.

The SEM image for  $\text{MABiI}_{3-x}\text{Cl}_x$  is shown in **Figure 7-2(e)**. Here it can be seen that multiple ‘flower’ shaped features are present, many of which appear to sit edge on from the substrate surface. These features are often surrounded by regions of what appears to be less structured material, however their total surface coverage is low (c. 50%).

In **Figure 7-2(f)** the film corresponding to  $\text{MABiI}_3(1:1)$  shows a mixture of short needle like crystals protruding from central points (about 10  $\mu\text{m}$  long) sitting on top of round unstructured regions that are between 10 and 35  $\mu\text{m}$  in diameter. For this sample the total surface coverage is much higher than for  $\text{MABiI}_{3-x}\text{Cl}_x$ . The  $\text{MABiI}_3(3:1)$  perovskite film is principally characterized by large crystals (> 50  $\mu\text{m}$  in length) alongside local regions containing smaller structures as shown in **Figure**

7-2(g). Connectivity between these regions is however poor, with many areas of the substrate containing no material whatsoever.

Having established that the bismuth perovskite films were comprised of multiple crystal structures with characteristically distinct sizes, EDS mapping was employed to determine their chemical composition. **Table 7-1** summarises the results of these measurements, where values correspond to the stoichiometric ratio of each element

**Table 7-1** The stoichiometric ratio of elements as determined by EDS for the  $\text{MAPbI}_{3-x}\text{Cl}_x$ , mixed metal perovskites,  $\text{MABi}_{3-x}\text{Cl}_x$ , and  $\text{MABiI}_3$  films as determined by EDS. The numbers in parenthesis shows correspond to the target stoichiometric ratio determined by the composition of the precursor solutions used

Materials	C	N	Pb	Bi	I	Cl
$\text{MAPbI}_{3-x}\text{Cl}_x$	3.12 (1)	0.33 (1)	1 (1)	-	2.58 (3-x)	0.03 (x)
$\text{MA}(\text{Pb}_{0.75}\text{Bi}_{0.25})\text{I}_{3-x}\text{Cl}_x$	2.96 (1)	0.55 (1)	0.72 (0.75)	0.28 (0.25)	2.76 (3.5-x)	0.46 (x)
$\text{MA}(\text{Pb}_{0.5}\text{Bi}_{0.5})\text{I}_{3-x}\text{Cl}_x$	2.59 (1)	0.72 (1)	0.38 (0.50)	0.62 (0.50)	2.94 (3.5-x)	0.76 (x)
$\text{MA}(\text{Pb}_{0.25}\text{Bi}_{0.75})\text{I}_{3-x}\text{Cl}_x$	2.61 (1)	0.97 (1)	0.26 (0.25)	0.74 (0.75)	2.5 (3.5-x)	1.01 (x)
$\text{MABiI}_{3-x}\text{Cl}_x$	3.34 (1)	0.91 (1)	-	1 (1)	2.47 (4-x)	1.47 (x)
$\text{MABiI}_3$ (1:1)	2.76 (1)	0.30 (1)	-	1 (1)	3.43 (4)	-
$\text{MABiI}_3$ (3:1)	4.70 (3)	1.71 (3)	-	1 (1)	4.27 (6)	-

The corresponding images are presented in the **Figures 7-3 to 7-9**.

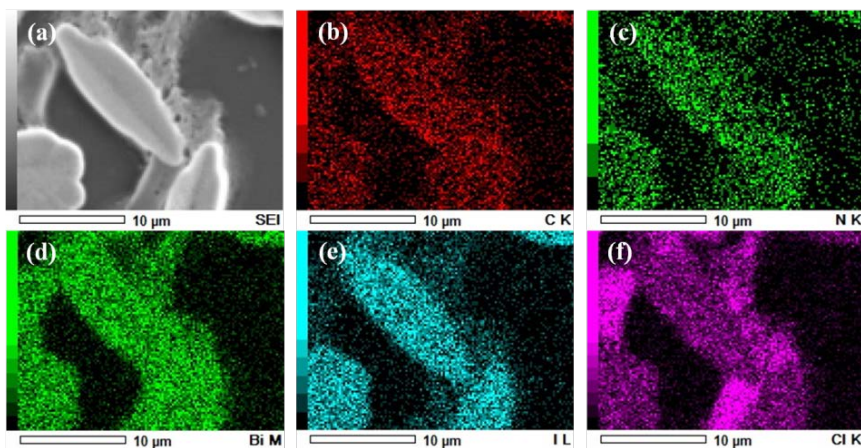


**Figure 7-3** SEM image of (a)  $\text{MABi}_{3-x}\text{Cl}_x$  and corresponding EDS analysis with elemental mapping of (b) carbon, (c) nitrogen, (d) bismuth, (e) iodine, and (f) chlorine.

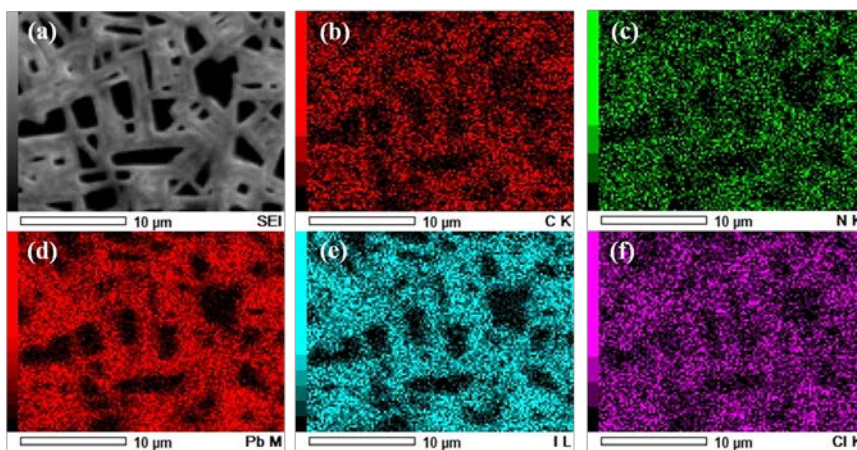


**Figure 7-4** SEM image of (a)  $\text{MAPbI}_{3-x}\text{Cl}_x$ , and EDS analysis with elemental mapping of (b) carbon, (c) nitrogen, (d) lead, (e) iodine, and (f) chlorine.

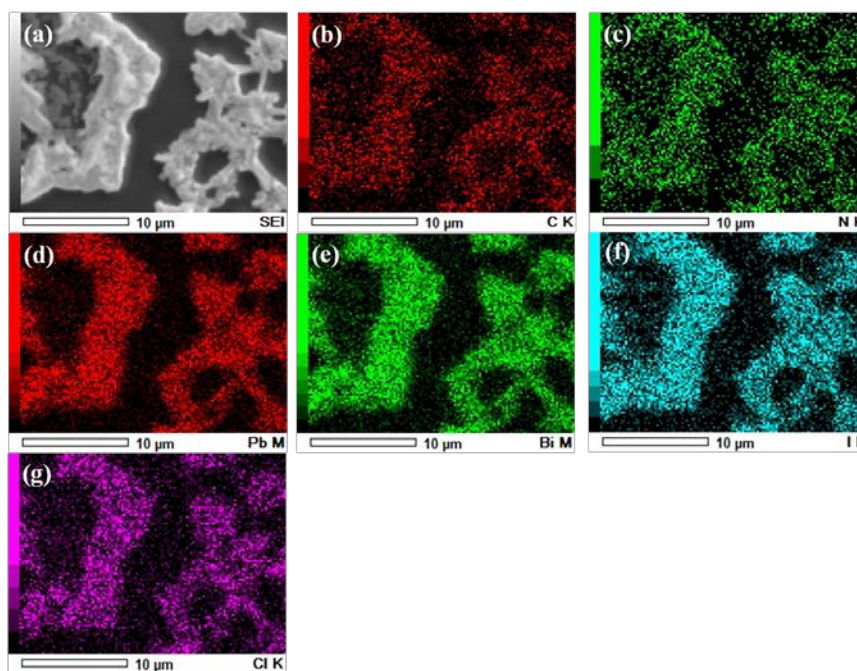


**Figure 7-5** SEM image of (a)  $\text{MA}(\text{Pb}_{0.75}\text{Bi}_{0.25})\text{I}_{3-x}\text{Cl}_x$ , and EDS analysis with elemental mapping of (b) carbon, (c) nitrogen, (d) lead, (e) bismuth, (f) iodine, and (g) chlorine.

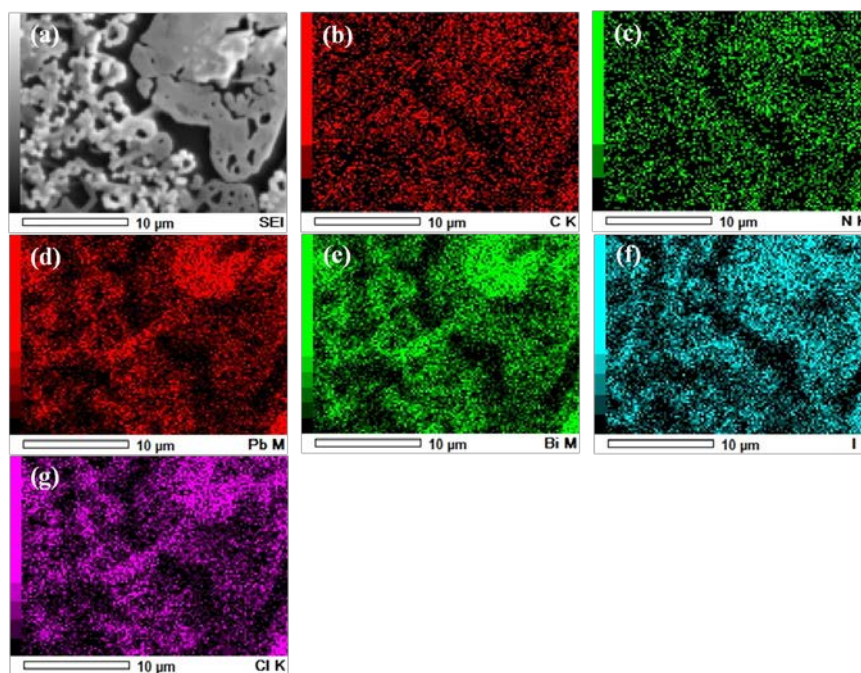


**Figure 7-6** SEM image of (a)  $\text{MA}(\text{Pb}_{0.5}\text{Bi}_{0.5})\text{I}_{3-x}\text{Cl}_x$ , and EDS analysis with elemental mapping of (b) carbon, (c) nitrogen, (d) lead, (e) bismuth, (f) iodine, and (g) chlorine.

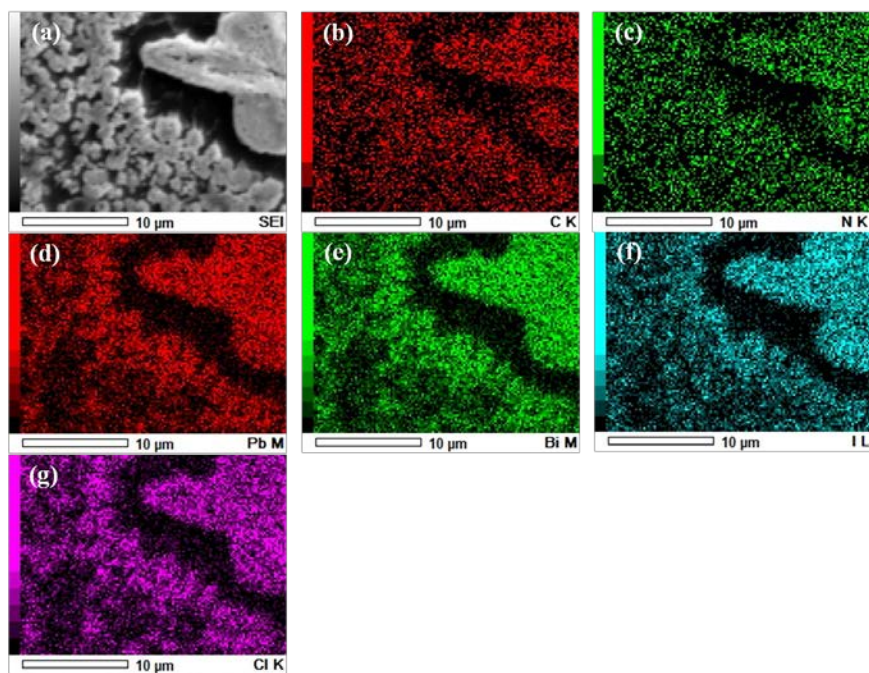


**Figure 7-7** SEM image of (a)  $\text{MA}(\text{Pb}_{0.25}\text{Bi}_{0.75})\text{I}_{3-x}\text{Cl}_x$ , and EDS analysis with elemental mapping of (b) carbon, (c) nitrogen, (d) lead, (e) bismuth, (f) iodine, and (g) chlorine.

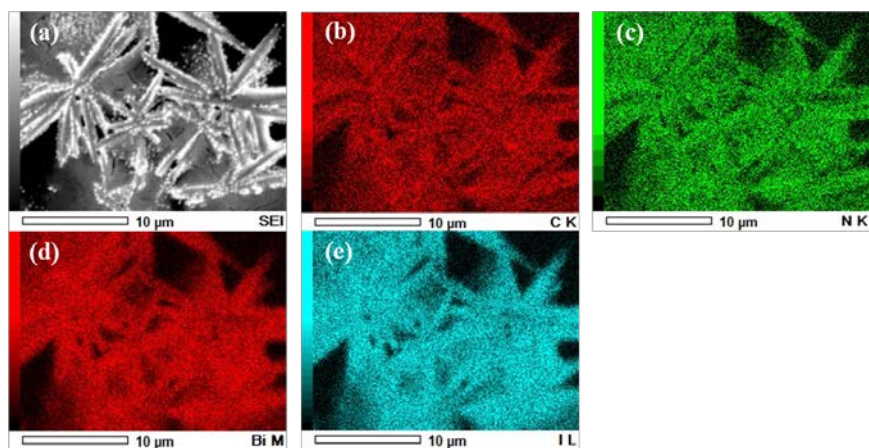


**Figure 7-8** SEM image of (a)  $\text{MABiI}_3(1:1)$  and EDS analysis with elemental mapping of (b) carbon, (c) nitrogen, (d) bismuth, and (e) iodine.

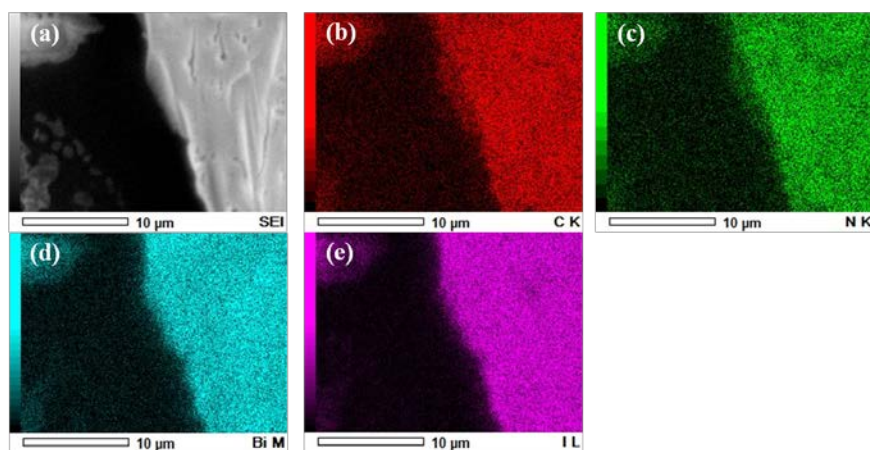


**Figure 7-9** SEM image of (a)  $\text{MABi}_3(3:1)$  and EDS analysis with elemental mapping of (b) carbon, (c) nitrogen, (d) bismuth, and (e) iodine.

As reported previously, Cl was almost completely absent in the  $\text{MAPbI}_{3-x}\text{Cl}_x$  film, (Zhao and Zhu, 2014) indicating its removal from the sample during processing (i.e. *via* sublimation with excess MAI) (Yu et al., 2014, Unger et al., 2014, Zhang et al., 2015) or its preferential location at the substrate interface. As the ratio of Bi is increased in the mixed metal perovskite the Cl content rises from 0.46 (25% Bi) up to 1.47 (100% Bi). Spatially averaged EDS data for  $\text{MABi}_{3-x}\text{Cl}_x$  indicates a halide ratio of approximately 2.5:1.5 I:Cl, however this result masks important local variations that will be discussed later. In line with the choice of starting precursor stoichiometries,  $\text{MABi}_3(3:1)$  shows the highest concentration of iodine. Although carbon was found to exist in a 1:1 ratio with nitrogen during elemental analysis of MAI, its relative concentration in each film is increased. This enhanced carbon content was attributed to combination of sample contamination by carbon caused by electron beam exposure in the SEM and residual levels of trapped precursor solvent (DMF).

To identify the origin(s) for the different crystal structures present in the mixed Pb/Bi perovskite films, we note that EDS maps show a generally homogenous distribution of these specific elements throughout each sample. Cl and I are also similarly distributed in both the large and small structures. In contrast, from **Figure 7-3** where noticeable differences in the distribution of the halides in the  $\text{MABi}_{3-x}\text{Cl}_x$  film are determined. I closely maps to the large flower shaped structures present and Cl maps to the thin layer than lies beneath. It appears therefore that in these films there are two different stoichiometries which we subsequently refer to as I-rich and Cl-rich. To determine their molar ratio in each region we conducted a series of point EDS chemical surveys.

As summarised in **Table 7-2**, in the I-rich regions bismuth preferentially binds to iodine when forming crystalline structures. Unlike in the lead-halide perovskite, a significant amount of chlorine is present in the film, suggesting that its removal during perovskite formation is less efficient when bismuth is present. In the I-rich regions the Bi:Cl:I ratio 1:0.67:2.67. Within the Cl-rich regions the Bi:Cl:I ratio is 1:1.37:1.64. These ratios indicate that the bismuth to halide ratio in both cases is almost 1:3, as one would expect for an ABX<sub>3</sub> perovskite.

**Table 7-2** The EDS point analysis for the MABi<sub>3-x</sub>Cl<sub>x</sub> film highlighting the distribution of iodine and chlorine rich regions areas

Materials	C	N	Bi	I	Cl
I-Rich Region	2.02	0.71	1	2.67	0.67
Cl-Rich Region	2.57	0.97	1	1.64	1.37

### 7.3.3. GIWAXS characterization of perovskite thin films

Given the difference in ionic radii for lead, bismuth, chlorine and iodine, it suggests that the various structures imaged using SEM will also have different crystal lattice parameters. To test this hypothesis, and to also verify the presence of crystallites with a perovskite unit cell structure, samples were measured using GIWAXS. Radially integrated 1D X-ray scattering patterns from each sample are shown in **Figure 7-10**, alongside patterns from films prepared using the precursor materials MAI, BiCl<sub>3</sub> and BiI<sub>3</sub>.

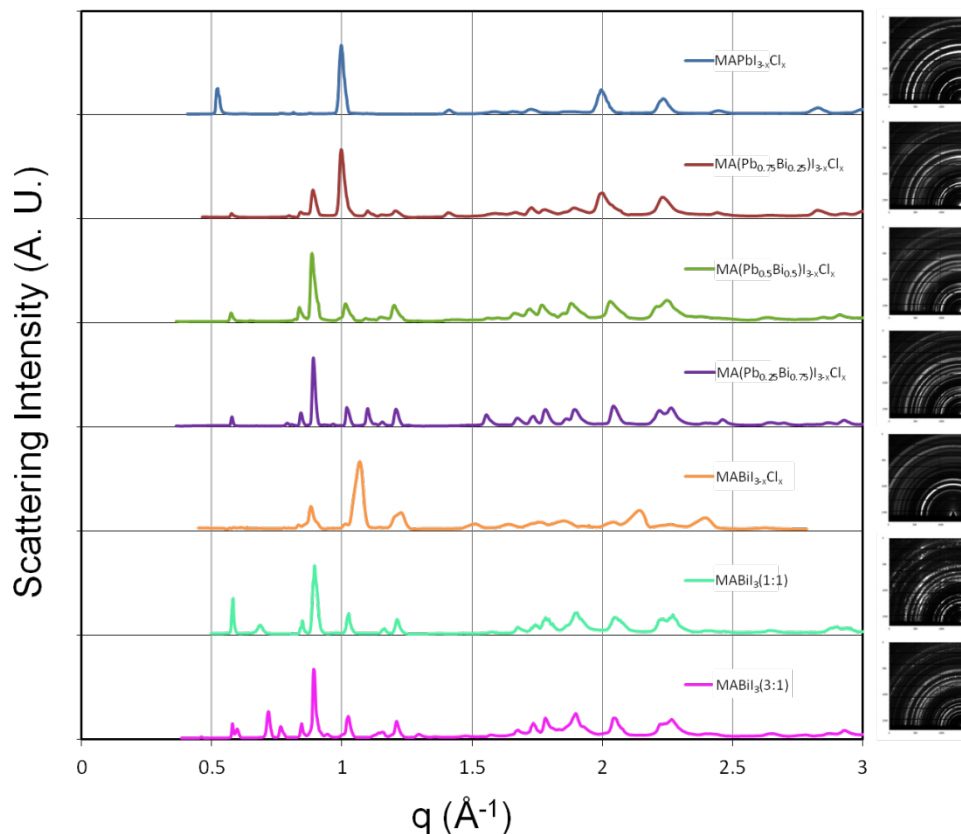


**Figure 7-10** The 1D radially integrated GIWAXS patterns of  $\text{MAPbI}_{3-x}\text{Cl}_x$ ,  $\text{MA}(\text{Pb}_{0.75}\text{Bi}_{0.25})\text{I}_{3-x}\text{Cl}_x$ ,  $\text{MA}(\text{Pb}_{0.5}\text{Bi}_{0.5})\text{I}_{3-x}\text{Cl}_x$ ,  $\text{MA}(\text{Pb}_{0.25}\text{Bi}_{0.75})\text{I}_{3-x}\text{Cl}_x$ ,  $\text{MABiI}_{3-x}\text{Cl}_x$ ,  $\text{MABiI}_3(1:1)$ , and  $\text{MABiI}_3(3:1)$  films prepared on silicon substrates. 2D GIWAXS images are illustrated by each GIWAXS patterns. The GIWAXS patterns are taken by 2D GIWAXS image's radial integral.

Immediately it can be seen that the diffraction pattern of each perovskite is not a simple linear combination of its precursor ingredients, thereby confirming the precursor components have combined to form new crystalline phases. The GIWAXS data for  $\text{MABiI}_{3-x}\text{Cl}_x$  shown in **Figure 7-10** demonstrates minimal evidence for X-ray scattering from MAI and  $\text{BiCl}_3$ , supporting the idea that the perovskite has a stoichiometry close to its target value. Nevertheless the presence of X-ray scattering peaks other than those attributable to the perovskite suggests more than one crystalline phase has been formed. For  $\text{MABiI}_3(1:1)$  and  $\text{MABiI}_3(3:1)$ , there are clear indications that unreacted  $\text{BiI}_3$  is present within the film as well as unreacted MAI. This result implies that for these blends the precursors do not undergo complete conversion possibly because they are not stoichiometrically well matched and also the annealing conditions may not be optimal. Despite the different mixing ratios used the X-ray scatter pattern from both these new crystal phases are very similar. This is in stark contrast to the

different structures observed using SEM (see **Figure 7-3**), demonstrating a strong sensitivity of sample microstructure to precursor composition (Yu et al., 2014, Colella et al., 2013).

The X-ray scattering from  $\text{MAPbI}_{3-x}\text{Cl}_x$  is similar to previously published data, (Tan et al., 2014, Park et al., 2014, Colella et al., 2013) allowing us attribute the scattering peaks at  $q = 0.99$  to  $1.00 \text{ \AA}^{-1}$ ,  $q = 1.41$  to  $1.42 \text{ \AA}^{-1}$ , and  $q = 1.99$  to  $2.00 \text{ \AA}^{-1}$  to X-ray scatter from the (002) and (110), (112) and (200), and (004) and (220) features of tetragonal  $\text{MAPbI}_{3-x}\text{Cl}_x$  respectively. For this system the corresponding lattice parameters are  $a = b = 8.85 \text{ \AA}$  and  $c = 12.69 \text{ \AA}$ , close to the values reported for the pure tri-iodide perovskite (Baikie et al., 2013, Im et al., 2011, Stoumpos et al., 2013). The GIWAXS pattern for  $\text{MA}(\text{Pb}_{0.75}\text{Bi}_{0.25})\text{I}_{3-x}\text{Cl}_x$  is broadly similar to  $\text{MAPbI}_{3-x}\text{Cl}_x$ , albeit with the addition of new scattering peaks at  $q = 0.89 \text{ \AA}^{-1}$ ,  $q = 1.21 \text{ \AA}^{-1}$  and peaks of relatively weak intensity between  $1.50$  and  $2.00 \text{ \AA}^{-1}$ . This is consistent with the UV-vis data presented in **Figure 7-1** that indicated a similar absorption onset for the two samples. For  $\text{MA}(\text{Pb}_{0.5}\text{Bi}_{0.5})\text{I}_{3-x}\text{Cl}_x$ , the relative intensity of the peaks at  $0.89$  and  $1.21 \text{ \AA}^{-1}$  is higher, however the peaks corresponding to the (110) and (220) reflections from  $\text{MAPbI}_{3-x}\text{Cl}_x$  are found to undergo both a reduction in relative intensity alongside a small shift (c. 1%) to higher  $q$  values. This not only implies a reduction in Pb-rich perovskite content within the sample, consistent with the sample preparation conditions and UV-vis / EDS data discussed earlier, but also a contraction in the unit cell size that may result from compressive strain. Further reductions in Pb content within the sample (i.e.  $\text{MA}(\text{Pb}_{0.25}\text{Bi}_{0.75})\text{I}_{3-x}\text{Cl}_x$ ), results in an X-ray scattering pattern that is consistent with the observed trend.

In agreement with the SEM data presented in **Figure 7-2**, the presence of X-ray scattering peaks that can be partly attributed to  $\text{MAPbI}_{3-x}\text{Cl}_x$  in the mixed metal samples suggests the formation of distinct crystal phases rather than the formation of an alloy. We suggest that prior to mixing precursor solutions for  $\text{MAPbI}_{3-x}\text{Cl}_x$  and  $\text{MABiI}_{3-x}\text{Cl}_x$ , the partial formation of metal halide complexes has already taken place that favours the eventual formation of crystals containing either (but not both) metals. Interestingly, the observed peaks in the  $\text{MABiI}_{3-x}\text{Cl}_x$  GIWAXS pattern at  $0.89$  and  $1.90 \text{ \AA}^{-1}$  match those from  $\text{BiI}_3$ , despite the fact that  $\text{BiI}_3$  was not present as precursor material. It appears therefore that for these mixed Pb/Bi samples significant halide ion exchange has taken place during sample processing that result in the formation of  $\text{BiI}_3$ . Furthermore, from **Figure 7-10** it can also be

seen that the mixed Pb/Bi samples follow a trend that more closely resembles a transition from MAPbI<sub>3</sub> to MABiI<sub>3</sub>, rather than to MABiI<sub>3-x</sub>Cl<sub>x</sub>, even though the precursors for MABiI<sub>3-x</sub>Cl<sub>x</sub> were used for mixing, further indicating that halide exchange occurs (Yoon et al., 2016).

To better understand the origin of each new feature observed in our GIWAXS measurements, X-ray scattering patterns of single phase powder samples were simulated using CrystalDiffract 6 software package (Crystallmaker). Crystal structures (.cif files) for MAPbI<sub>3</sub> and BiI<sub>3</sub> were taken from a previous report. (Stoumpos et al., 2013) The MAPbI<sub>3</sub> scattering pattern measured was in good agreement with the previously reported structure. Crystal structures for bismuth perovskites have not been widely reported; therefore we started from a generic ABX<sub>3</sub> structure file (A= methylammonium, B=Bi and X=halide) and iteratively adjusted the lattice parameters until it matched the experimental data. The fitted lattice parameters for MABiI<sub>3</sub> (prepared from both the 1:1 and 3:1 precursor mixtures) correspond to a tetragonal structure. **Figure 7-11** shows the simulated GIWAXS pattern of a perovskite with unit cell dimensions  $a = b = 8.67 \text{ \AA}$  and  $c = 12.41 \text{ \AA}$  and a mixture of this simulated pattern BiI<sub>3</sub> and MAI. This mixture is compared to the measured data for MABiI<sub>3</sub> and as shown, there is reasonable agreement between the mixture and the experimentally measured data. Specifically, the simulated ABX<sub>3</sub> pattern shows two peaks at  $q = 1.01$  and  $1.02 \text{ \AA}^{-1}$ , corresponding to the (002) and (110) reflections respectively. The experimental pattern for MABiI<sub>3</sub> also shows a peak at the  $q = 1.02 \text{ \AA}^{-1}$ , alongside a shoulder at  $q = 1.01 \text{ \AA}^{-1}$ .

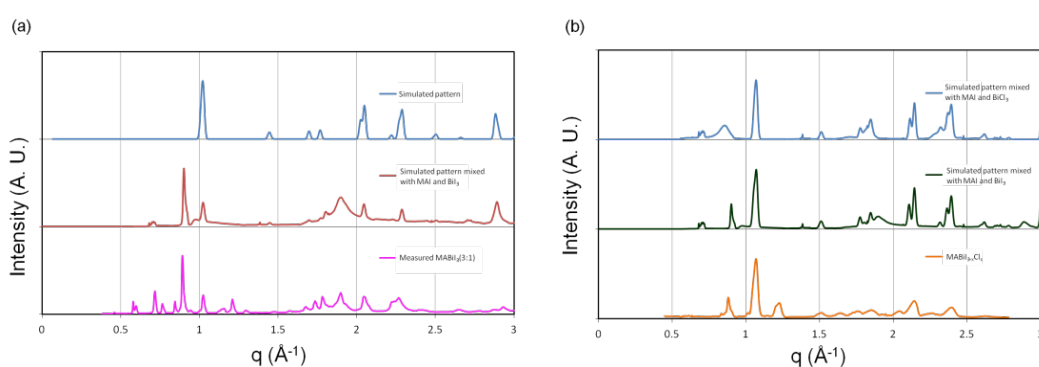


**Figure 7-11** The GIWAXS patterns from (a) the simulated ABX<sub>3</sub> (tetragonal  $a = b = 8.67 \text{ \AA}$  and  $c = 12.41 \text{ \AA}$ ), simulated mixture of ABX<sub>3</sub>, MAI, and BiI<sub>3</sub>, and the experimentally observed pattern from MABiI<sub>3</sub>(3:1) and (b) the simulated ABX<sub>3</sub> (tetragonal  $a = b = 8.67 \text{ \AA}$  and  $c = 12.41 \text{ \AA}$ ), simulated mixture of ABX<sub>3</sub>, MAI, BiCl<sub>3</sub> and BiI<sub>3</sub>, and the experimentally observed pattern from MABiI<sub>3-x</sub>Cl<sub>x</sub>.

The mixture and the experimental pattern both show several peaks between  $q = 1.5$  and  $2.3 \text{ \AA}^{-1}$ . Therefore, the relatively intense peaks observed can be modelled using a mixture of a generic  $ABX_3$  crystal lattice, MAI and  $\text{BiI}_3$ , allowing us to conclude that  $\text{MABiI}_3$  forms a perovskite structure. However, between  $q = 0.5$  and  $1 \text{ \AA}^{-1}$  there are several weak features that cannot be readily identified, alongside a peak shown at  $q = 1.21 \text{ \AA}^{-1}$  that is present in the GIWAXS data for every bismuth containing perovskite. These features are tentatively attributed to the presence of unreacted  $\text{BiCl}_3$  and other impurities.

We also adapted our model to simulate the X-ray scattering pattern for  $\text{MABiI}_{3-x}\text{Cl}_x$ , based on a generic  $ABX_3$  structure, and combined it with data for MAI,  $\text{BiI}_3$  and  $\text{BiCl}_3$ . The results are presented in **Figure 7-11(b)**. In order to match the experimental data the best fit lattice parameters used in the simulated  $ABX_3$  structure were  $a = b = 8.29 \text{ \AA}$  and  $c = 11.89 \text{ \AA}$ . Weak X-ray scattering features at  $q = 1.21, 1.64,$  and  $2.04 \text{ \AA}^{-1}$  were not well matched by our model suggesting the presence of unidentified residual phases that are in addition to the perovskite, MAI,  $\text{BiI}_3$  and  $\text{BiCl}_3$ .

#### **7.3.4. Photovoltaic properties of perovskite PVCs**

Our measurements of methylammonium bismuth- and methylammonium mixed Pb/Bi-perovskite films have evidenced systems with limited phase purity (relative to our control sample for  $\text{MAPbI}_{3-x}\text{Cl}_x$ ), in addition to the presence of crystalline structures that have incomplete surface coverage and a range of length-scales. To determine whether such films exhibit any photovoltaic functionality, we fabricated a series of inverted architecture solar cell devices according to the structure ITO/PEDOT:PSS/Perovskite/PCBM/Ca/Al. Light J-V curves and tabulated metrics for each device are shown in **Figure 7-12** and **Table 7-3** respectively

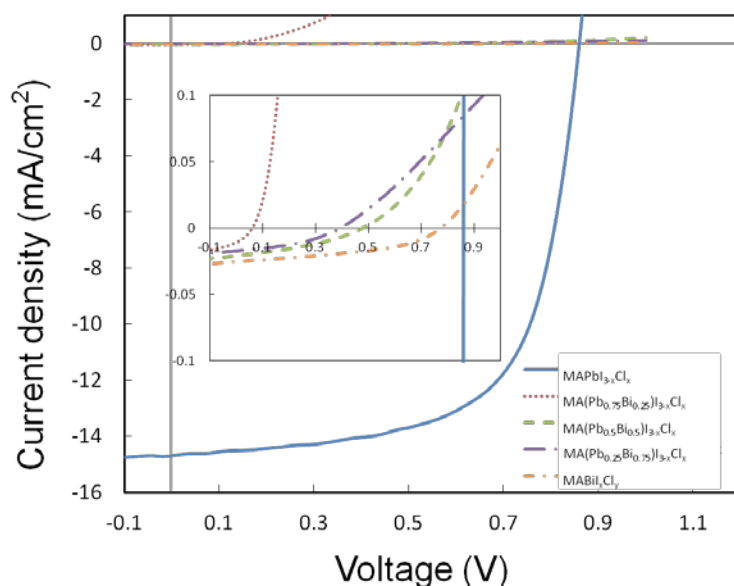


**Figure 7-12** J-V curves for photovoltaic cell devices based on  $\text{MAPbI}_{3-x}\text{Cl}_x$ ,  $\text{MA}(\text{Pb}_{0.25}\text{Bi}_{0.75})\text{I}_{3-x}\text{Cl}_x$ ,  $\text{MA}(\text{Pb}_{0.5}\text{Bi}_{0.5})\text{I}_{3-x}\text{Cl}_x$ ,  $\text{MA}(\text{Pb}_{0.75}\text{Bi}_{0.25})\text{I}_{3-x}\text{Cl}_x$ , and  $\text{MABiI}_{3-x}\text{Cl}_x$ .

Here it can be seen that as expected the control devices based on  $\text{MAPbI}_{3-x}\text{Cl}_x$  exhibited the best photovoltaic cell performance by a considerable margin, recording average efficiencies of 8.25% ( $J_{\text{SC}} = -14.7 \text{ mA cm}^{-2}$ ,  $V_{\text{OC}} = 0.86 \text{ V}$ ,  $\text{FF} = 65.3\%$ ). This result is similar to our previous work using the same materials and processing routes (Barrows et al., 2014). In comparison, and in agreement with Park et al. (Park et al., 2015) PCE values for the Bi-containing devices were very low. Mixed Pb/Bi perovskite solar cells exhibited  $J_{\text{SC}}$  and  $V_{\text{OC}}$  below  $0.03 \text{ mA/cm}^2$  and  $0.5 \text{ V}$  respectively. For the  $\text{MABiI}_{3-x}\text{Cl}_x$  PVCs (data shown inset graph in the Figure 6) a maximum PCE of 0.009% was determined ( $J_{\text{SC}}$  of  $-0.03 \text{ mA cm}^{-2}$ ,  $V_{\text{OC}} = 0.78 \text{ V}$ ,  $\text{FF} = 44.8 \%$ ). Although its performance was poor, the J-V curve shows the distinctive shape for a photovoltaic device; furthermore a  $V_{\text{OC}}$  of  $0.78 \text{ V}$  was high compared to the other Bi containing perovskite solar cells. Lastly, for  $\text{MABiI}_3$ , a relatively high  $J_{\text{SC}}$  of  $0.08 \text{ mA cm}^{-2}$  was measured when the perovskite was prepared from a 1:1 mixture of precursor materials. This was offset however by a low  $V_{\text{OC}}$  value of  $0.22 \text{ V}$ .  $\text{MABiI}_3$  prepared from a 3:1 precursor mixture did not show any measureable photovoltaic effect. The J-V curves of  $\text{MABiI}_3(1:1)$  and  $\text{MABiI}_3(3:1)$  are shown in **Figure 7-13**.

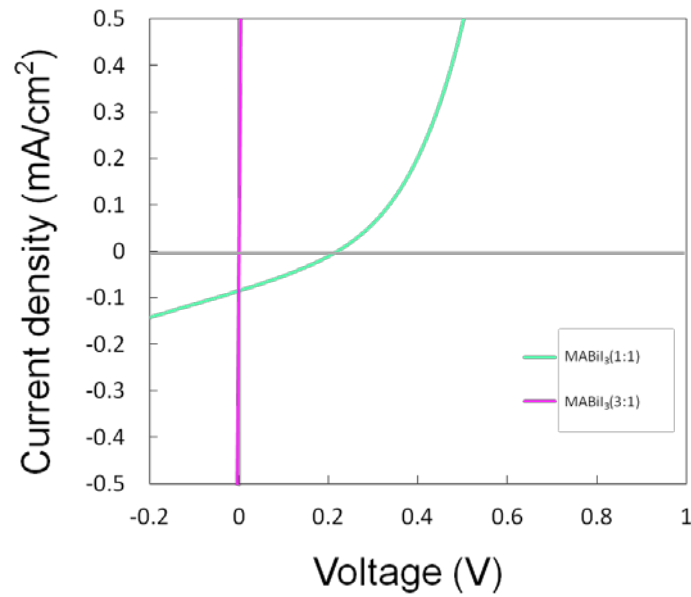


**Figure 7-13** J-V curves for photovoltaic cell devices based on MABi<sub>3</sub>(1:1) and MABi<sub>3</sub>(3:1).

**Table 7-3** Photovoltaic performance parameters of the devices produced for this study

Materials	<b>J<sub>sc</sub></b>	<b>V<sub>oc</sub></b>	<b>FF</b>	<b>PCE</b>
	(mA/cm <sup>2</sup> )	(V)	(%)	(%)
MAPbI <sub>3-x</sub> Cl <sub>x</sub>	-14.7	0.86	65.3	8.25
MA(Pb <sub>0.75</sub> Bi <sub>0.25</sub> )I <sub>3-x</sub> Cl <sub>x</sub>	-0.01	0.06	31.1	0
MA(Pb <sub>0.5</sub> Bi <sub>0.5</sub> )I <sub>3-x</sub> Cl <sub>x</sub>	-0.02	0.47	35.9	0.003
MA(Pb <sub>0.25</sub> Bi <sub>0.75</sub> )I <sub>3-x</sub> Cl <sub>x</sub>	-0.02	0.39	39.4	0.003
MABiI <sub>3-x</sub> Cl <sub>x</sub>	-0.03	0.78	44.9	0.009
MABi <sub>3</sub> (1:1)	-0.08	0.22	29.3	0.005
MABi <sub>3</sub> (3:1)	N/A	N/A	N/A	N/A

Despite the disappointing device efficiencies reported for the Bi perovskite solar cells it is still noteworthy that these materials can produce a measurable photovoltaic effect. From our SEM, EDS and GIWAXS data some of the reasons why the performances of these devices are poor can be understood. The material characterisation data suggests that both the mixed Pb/Bi and the 100% bismuth based perovskite films contain a significant amount of impurity phases from

compounds including  $\text{BiI}_3$  and MAI. It is assumed that these are responsible for the dramatically reduced  $J_{\text{SC}}$ ,  $V_{\text{OC}}$  and FF values relative to our control device as they may act to increase the internal resistance of the devices. In addition, the inhomogeneous surface coverage of these perovskites will also limit photocurrent efficiency due a reduced effective active area. Given the promising  $V_{\text{OC}}$  value for  $\text{MABi}_{3-x}\text{Cl}_x$ , we believe sufficient incentive exists to continue our studies into this material with a focus on the optimization of the semiconductor phase purity and microstructure. By eliminating impurities from the material as well as maximizing its coverage on a substrate layer (potentially *via* a refined precursor conversion process), it should be possible to realize hybrid perovskite solar cells with improved quantum efficiencies and PCEs, thereby providing a potential low-toxicity alternative to lead-based perovskites for solar cell applications.

#### 7.4. Conclusions

In this work, we studied bismuth as a substitute metal cation for lead in hybrid perovskite semiconductors. We show that significant halide ion exchange takes place during sample processing and conclude that  $\text{MABiI}_3$  and  $\text{MABi}_{3-x}\text{Cl}_x$  adopt a tetragonal perovskite structure with unit cell parameters  $a = b = 8.67 \text{ \AA}$  and  $c = 12.41 \text{ \AA}$  and  $a = b = 8.29 \text{ \AA}$  and  $c = 11.89 \text{ \AA}$  respectively. Composition and structural analysis of these perovskites evidence the presence of large ( $> 20 \mu\text{m}$  lateral size) crystallites, alongside regions of smaller crystallites and apparently amorphous material. GIWAXS measurements confirm the inhomogeneous phase composition of these samples, which in combination with their poor surface coverage, large band gap and presence of residual precursor materials as impurities provide a clear explanation for their inefficient photovoltaic behaviour in a photovoltaic cell device. The inhomogeneous composition implies that the film composition is not optimal. The low surface coverage means that a significant fraction of the incident light will not be captured. The large band gap means that only the high energy photons will be captured. Finally, the presence of impurities will introduce loss mechanisms within the devices whereby excited carriers can relax without passing through the external circuit. The promising  $V_{\text{OC}}$  for  $\text{MABi}_{3-x}\text{Cl}_x$  solar cells (0.78 V) however suggests that efficient solar cells can be realised, with optimisation of the perovskite precursor conversion process being an obvious focus for future studies.

## 7.5. References

- BABAYIGIT, A., ETHIRAJAN, A., MULLER, M. & CONINGS, B. 2016. Toxicity of organometal halide perovskite solar cells. *Nat Mater*, 15, 247-251.
- BAIKIE, T., FANG, Y. N., KADRO, J. M., SCHREYER, M., WEI, F. X., MHAISALKAR, S. G., GRAETZEL, M. & WHITE, T. J. 2013. Synthesis and crystal chemistry of the hybrid perovskite (CH<sub>3</sub>NH<sub>3</sub>) PbI<sub>3</sub> for solid-state sensitised solar cell applications. *Journal of Materials Chemistry A*, 1, 5628-5641.
- BALL, J. M., LEE, M. M., HEY, A. & SNAITH, H. J. 2013. Low-temperature processed meso-superstructured to thin-film perovskite solar cells. *Energy & Environmental Science*, 6, 1739-1743.
- BARROWS, A. T., PEARSON, A. J., KWAK, C. K., DUNBAR, A. D. F., BUCKLEY, A. R. & LIDZEY, D. G. 2014. Efficient planar heterojunction mixed-halide perovskite solar cells deposited via spray-deposition. *Energy & Environmental Science*, 7, 2944-2950.
- BI, C., SHAO, Y. C., YUAN, Y. B., XIAO, Z. G., WANG, C. G., GAO, Y. L. & HUANG, J. S. 2014. Understanding the formation and evolution of interdiffusion grown organolead halide perovskite thin films by thermal annealing. *Journal of Materials Chemistry A*, 2, 18508-18514.
- BURSCHEKA, J., PELLET, N., MOON, S. J., HUMPHRY-BAKER, R., GAO, P., NAZEERUDDIN, M. K. & GRATZEL, M. 2013. Sequential deposition as a route to high-performance perovskite-sensitized solar cells. *Nature*, 499, 316-+.
- COLELLA, S., MOSCONI, E., FEDELI, P., LISTORTI, A., GAZZA, F., ORLANDI, F., FERRO, P., BESAGNI, T., RIZZO, A., CALESTANI, G., GIGLI, G., DE ANGELIS, F. & MOSCA, R. 2013. MAPbI<sub>3</sub>(1-x)Cl<sub>x</sub> Mixed Halide Perovskite for Hybrid Solar Cells: The Role of Chloride as Dopant on the Transport and Structural Properties. *Chemistry of Materials*, 25, 4613-4618.
- CRYSTALMAKER. <http://www.crystallmaker.com/crystaldiffract/> [Online].
- EPERON, G. E., STRANKS, S. D., MENELAOU, C., JOHNSTON, M. B., HERZ, L. M. & SNAITH, H. J. 2014. Formamidinium lead trihalide: a broadly tunable perovskite for efficient planar heterojunction solar cells. *Energy & Environmental Science*, 7, 982-988.

- FLORA, G., GUPTA, D. & TIWARI, A. 2012. Toxicity of lead: A review with recent updates. *Interdiscip Toxicol*, 5, 47-58.
- HAO, F., STOUMPOS, C. C., CAO, D. H., CHANG, R. P. H. & KANATZIDIS, M. G. 2014. Lead-free solid-state organic-inorganic halide perovskite solar cells. *Nature Photonics*, 8, 489-494.
- IM, J. H., LEE, C. R., LEE, J. W., PARK, S. W. & PARK, N. G. 2011. 6.5% efficient perovskite quantum-dot-sensitized solar cell. *Nanoscale*, 3, 4088-4093.
- KULKARNI, S. A., BAIKIE, T., BOIX, P. P., YANTARA, N., MATHEWS, N. & MHAISALKAR, S. 2014. Band-gap tuning of lead halide perovskites using a sequential deposition process. *Journal of Materials Chemistry A*, 2, 9221-9225.
- LANDRIGAN, P. J. 1989. Toxicity of Lead at Low-Dose. *British Journal of Industrial Medicine*, 46, 593-596.
- LEE, M. M., TEUSCHER, J., MIYASAKA, T., MURAKAMI, T. N. & SNAITH, H. J. 2012. Efficient Hybrid Solar Cells Based on Meso-Superstructured Organometal Halide Perovskites. *Science*, 338, 643-647.
- LIU, D. Y. & KELLY, T. L. 2014. Perovskite solar cells with a planar heterojunction structure prepared using room-temperature solution processing techniques. *Nature Photonics*, 8, 133-138.
- LIU, M. Z., JOHNSTON, M. B. & SNAITH, H. J. 2013. Efficient planar heterojunction perovskite solar cells by vapour deposition. *Nature*, 501, 395-+.
- MOHAN, R. 2010. Green bismuth. *Nature Chemistry*, 2, 336.
- NOEL, N. K., STRANKS, S. D., ABATE, A., WEHRENFENNIG, C., GUARNERA, S., HAGHIGHIRAD, A. A., SADHANALA, A., EPERON, G. E., PATHAK, S. K., JOHNSTON, M. B., PETROZZA, A., HERZ, L. M. & SNAITH, H. J. 2014. Lead-free organic-inorganic tin halide perovskites for photovoltaic applications. *Energy & Environmental Science*, 7, 3061-3068.
- OGOMI, Y., MORITA, A., TSUKAMOTO, S., SAITHO, T., FUJIKAWA, N., SHEN, Q., TOYODA, T., YOSHINO, K., PANDEY, S. S., MA, T. L. & HAYASE, S. 2014. CH<sub>3</sub>NH<sub>3</sub>Sn<sub>x</sub>Pb(1-x)I<sub>3</sub> Perovskite Solar Cells Covering up to 1060 nm. *Journal of Physical Chemistry Letters*, 5, 1004-1011.
- PARK, B. W., PHILIPPE, B., GUSTAFSSON, T., SVEINBJORNSSON, K., HAGFELDT, A., JOHANSSON, E. M. J. & BOSCHLOO, G. 2014.

- Enhanced Crystallinity in Organic-Inorganic Lead Halide Perovskites on Mesoporous TiO<sub>2</sub> via Disorder-Order Phase Transition. *Chemistry of Materials*, 26, 4466-4471.
- PARK, B. W., PHILIPPE, B., ZHANG, X. L., RENSMO, H., BOSCHLOO, G. & JOHANSSON, E. M. J. 2015. Bismuth Based Hybrid Perovskites A(3)Bi(2)I(9) (A: Methylammonium or Cesium) for Solar Cell Application. *Advanced Materials*, 27, 6806-+.
- SHAHEEN, S. E., GINLEY, D. S. & JABBOUR, G. E. 2005. Organic-based photovoltaics. toward low-cost power generation. *Mrs Bulletin*, 30, 10-19.
- SLAVNEY, A. H., HU, T., LINDENBERG, A. M. & KARUNADASA, H. I. 2016. A Bismuth-Halide Double Perovskite with Long Carrier Recombination Lifetime for Photovoltaic Applications. *J Am Chem Soc*, 138, 2138-41.
- STOUMPOS, C. C., MALLIAKAS, C. D. & KANATZIDIS, M. G. 2013. Semiconducting Tin and Lead Iodide Perovskites with Organic Cations: Phase Transitions, High Mobilities, and Near-Infrared Photoluminescent Properties. *Inorganic Chemistry*, 52, 9019-9038.
- TAN, K. W., MOORE, D. T., SALIBA, M., SAI, H., ESTROFF, L. A., HANRATH, T., SNAITH, H. J. & WIESNER, U. 2014. Thermally Induced Structural Evolution and Performance of Mesoporous Block Copolymer-Directed Alumina Perovskite Solar Cells. *Acs Nano*, 8, 4730-4739.
- TIAN, Y. & SCHEBLYKIN, I. G. 2015. Artifacts in Absorption Measurements of Organometal Halide Perovskite Materials: What Are the Real Spectra? *The Journal of Physical Chemistry Letters*, 6, 3466-3470.
- TRAVIS, W., GLOVER, E. N. K., BRONSTEIN, H., SCANLON, D. O. & PALGRAVE, R. G. 2016. On the application of the tolerance factor to inorganic and hybrid halide perovskites: a revised system. *Chemical Science*.
- UNGER, E. L., BOWRING, A. R., TASSONE, C. J., POOL, V. L., GOLD-PARKER, A., CHEACHAROEN, R., STONE, K. H., HOKE, E. T., TONEY, M. F. & MCGEHEE, M. D. 2014. Chloride in Lead Chloride-Derived Organo-Metal Halides for Perovskite-Absorber Solar Cells. *Chemistry of Materials*, 26, 7158-7165.
- YOON, S. J., STAMPLECOSKIE, K. G. & KAMAT, P. V. 2016. How Lead Halide Complex Chemistry Dictates the Composition of Mixed Halide Perovskites. *Journal of Physical Chemistry Letters*, 7, 1368-1373.

- YU, H., WANG, F., XIE, F. Y., LI, W. W., CHEN, J. & ZHAO, N. 2014. The Role of Chlorine in the Formation Process of "CH<sub>3</sub>NH<sub>3</sub>PbI<sub>3-x</sub>Cl(x)" Perovskite. *Advanced Functional Materials*, 24, 7102-7108.
- ZHANG, L. Q., ZHANG, X. W., YIN, Z. G., JIANG, Q., LIU, X., MENG, J. H., ZHAO, Y. J. & WANG, H. L. 2015. Highly efficient and stable planar heterojunction perovskite solar cells via a low temperature solution process. *Journal of Materials Chemistry A*, 3, 12133-12138.
- ZHAO, Y. X. & ZHU, K. 2014. CH<sub>3</sub>NH<sub>3</sub>Cl-Assisted One-Step Solution Growth of CH<sub>3</sub>NH<sub>3</sub>PbI<sub>3</sub>: Structure, Charge-Carrier Dynamics, and Photovoltaic Properties of Perovskite Solar Cells. *Journal of Physical Chemistry C*, 118, 9412-9418.

## 8. Conclusions and further work

### 8.1. Conclusions

Photovoltaic cells are one of the most remarkable technologies for renewable energy in a future. The research aim was the development of improved photovoltaic abilities and improved sustainability for device fabrication, by reducing the use of harmful materials in their processing. There is still much work needed in order to produce more sustainable, less toxic organic and inorganic materials for photovoltaic cells. In order to reduce the usage of toxic organic solvents and toxic materials, water-soluble conjugated polymer and less toxic bismuth based perovskite have been studied.

In **Chapter 4**, a general overview of photovoltaic cells was studied to understand structure, fabrication methods, characterisation, and principle of photovoltaic cells. PEDOT:PSS was investigated to understand how it performs as a HTL in devices, conductivity and UV-vis absorption were measured. The conductivity measurements were performed on samples processed at various annealing temperatures. From the experiment it was evident PEDOT is a highly resistive material, so sheet conductivity was very low. It was hard to measure accurately conductivity of PEDOT:PSS thin films and they did not show repeatable results due to it being highly sensitive to moisture and temperature. Therefore, moisture and temperature need to be well controlled during the fabrication of devices. The UV-vis absorption measurement was performed for different spin speeds and a 150 °C annealing temperature. However, UV-vis absorption spectra showed very small differences in absorption ability with different spin speed, so the thickness has insignificant impact on their transparency. PEDOT:PSS showed some absorption ability around 300 nm and but this is not thought likely to interrupt the active layer's ability to absorb incident light. P3HT based PVCs were investigated to understand their fabrication methods, and the principles of device processing. All the devices were fabricated as ITO/PEDOT:PSS/P3HT:PCBM/(Ca)/Al. P3HT showed absorption ability from 500 to 600 nm due to extended conjugation length and pi-pi stacking of polymer. The PL peak of P3HT appeared around 720 nm and it was quenched by PCBM. The PL intensity of P3HT was reduced as PCBM concentration increased. Therefore, electrons and holes are being dissociated by

intermolecular charge transfer. The devices showed good performance with 1:0.6 and 1:0.8 blend ratios of P3HT:PCBM and they showed PCEs over 3%. When a cathode layer including Ca was used the performance of devices was reduced because Ca is sensitive to oxygen. So if oxygen is not well controlled, Ca is not good for the cathode layer. From this experiment, fabrication processes, structures and the principles of organic photovoltaic cells were understood.

In **Chapter 5 and 6**, water-soluble conjugated polyelectrolyte PSFP-DTBTP containing sulfonyl-fluorene and dithienyl-benzothiadiazole was synthesised using Suzuki cross coupling. The polyelectrolyte had a strong absorption peak at 370 nm, but it showed emission at 645 nm due to exciton migration. Although, this conjugated polyelectrolyte did not show any photovoltaic abilities as an active layer in a device, it improved the PCE of PCDTBT photovoltaic cell when it was used as an additive in the HTL because the work function of the HTL was changed. When PSFP-DTBTP was mixed with PEDOT:PSS, the work function was lower than pristine PEDOT:PSS. Therefore, the improved PCE of the devices is attributed to improved charge transfer to anode through the HTL with CPE added. In addition, the HTL with CPE added showed lower conductivity but improved absorption ability. Because intermolecular charge transfer was occurring from the CPE to the PCDTBT in the active layer and the hole transfer into the HTL was improved the presence of CPE increased the amount of energy transfer and increased device PCE. The HTL with added CPE resulted in a PCE improvement of 13% relative to the PCE of the PCDTBT reference device without any CPE.

In **Chapter 7**, bismuth was introduced to perovskite instead of lead due to its lower toxicity. The lattice structure of bismuth perovskite was successfully modelled using an  $ABX_3$  structure. Bismuth perovskite  $MABiI_3$  and  $MABi_{3-x}Cl_x$  showed a tetragonal perovskite structure with unit cell parameters  $a = b = 8.67 \text{ \AA}$  and  $c = 12.41 \text{ \AA}$  and  $a = b = 8.29 \text{ \AA}$  and  $c = 11.89 \text{ \AA}$  respectively. However, unreacted MAI and bismuth halide were left within the perovskite films due to imperfectly matched stoichiometric oxidation states of bismuth. Bismuth perovskite photovoltaic cells showed very low PCE, as seen in other reports published during this project. This is because the active layer was not fully covered and many unreacted impurities were included on the surface.

New materials such as conjugated polyelectrolyte and bismuth were introduced into photovoltaic cell processing in order to improve the sustainability of PVC

fabrication. Although the PVCs based on these materials did not always improve the PCE of the PVCs in this PhD research, the research demonstrated the significant challenge in producing PVCs that do not require materials damaging to the environment and human health. It was shown that the sustainability of PCDTBT devices can be improved by increasing their PCE by using conjugated polyelectrolytes as additives within the hole transport layer.

## 8.2. Further work

In order to further the improvement of the CPE-based devices, different negative charged  $C_{60}$  could be applied to avoid aggregation of the CPE and  $C_{60}$ . If these materials dissolve well together in water, it would be possible to coat them on the surface uniformly. Another improvement to the methods reported here is an increase in the concentration of acceptor groups (e.g. benzothiadiazole in PSFP-DTBTP) within the CPE polymer backbone. If the concentration of acceptor groups is increased, UV-vis absorption ability of polymer around 600 nm might be increased and it would be possible to then apply it as an active layer. In order to increase the acceptor groups within the polymer, water-soluble functional side groups should be attached to the acceptor groups.

In addition, the CPE additive in the HTL could be easily applied to different active layer devices such as PTB7 to compare to PCDTBT. The development of the work in **Chapter 5 and 6** would undertake an investigation of composition and nanostructure of the HTL with added CPE. For example, it is not fully understood where exactly the CPE is within the HTL. If it is known where the CPE is in the HTL when they are mixed with PEDOT:PSS, it would allow easy control of the concentrations of PEDOT, PSS, and CPE to be blended and it would be known how exactly the CPE plays a role within the HTL in the devices. Finally, the introduction of various functional materials to the polymer backbone and side groups of the CPE would facilitate the use of that polymer as either a HTL, ETL, or active layer and also it would be possible to use it with alcohol solvents such as methanol and ethanol.

In order to extend the study of the bismuth perovskite precursor in photovoltaic cells in **Chapter 7**, the precursor solution of MAI and bismuth halide could be undertaken by investigating suitable blend ratios in order to reduce the amount of

unreacted MAI and bismuth halide. In the **Chapter 7**, DMF was used as solvent for the perovskite precursor. However, to improve the surface coverage, changing the solvent, changing the annealing time and the temperature, and using different coating methods could be investigated. Different solvents such as DMSO would be applied as the solvent and it would show different behaviours. In addition application of various annealing temperatures and annealing durations for the bismuth perovskite films after spin-casting would be helpful to help improve absorption ability. An alternative approach to improving surface coverage would be to grind the Bi perovskite crystals after mixing the MAI and bismuth halide and then coating it on the surface. Finally, further investigation of the effect of adjusting the lattice parameters of the perovskite crystals could be interesting because it is still novel challenge. Formamidinium iodide (FAI) might be able to use instead of MAI. The lattice parameters of bismuth perovskite would be changed and it would influence performance of devices.

In order to improve the PCE of bismuth perovskite devices, transition to inverted architecture and changing the interface layer from PEDOT:PSS to  $\text{TiO}_2$  and from PCBM to Spiro-MeOTAD might increase the PCE of devices.